



THE UNIVERSITY *of* EDINBURGH

This thesis has been submitted in fulfilment of the requirements for a postgraduate degree (e.g. PhD, MPhil, DClinPsychol) at the University of Edinburgh. Please note the following terms and conditions of use:

This work is protected by copyright and other intellectual property rights, which are retained by the thesis author, unless otherwise stated.

A copy can be downloaded for personal non-commercial research or study, without prior permission or charge.

This thesis cannot be reproduced or quoted extensively from without first obtaining permission in writing from the author.

The content must not be changed in any way or sold commercially in any format or medium without the formal permission of the author.

When referring to this work, full bibliographic details including the author, title, awarding institution and date of the thesis must be given.

Reliable detection and characterisation of dim targets via track-before-detect

Kimin Kim



A thesis submitted for the degree of Doctor of Philosophy.

The University of Edinburgh

March 2021

Abstract

Detection of manoeuvring and small objects is a challenging task in radar surveillance applications. Small objects in high noise background induce low signal to noise ratio (SNR) reflections. Conventional methods detect such objects by integrating multiple reflections in the same range-bearing and doppler bins in sampled versions of received signals. When the objects manoeuvre, however, these methods are likely to fail to detect them because the integration is performed without taking into account the possibility of the object movements across resolution bins. Furthermore, slowly manoeuvring objects create detection difficulties in discriminating them from radar clutter. Reflections of such objects contain micro-Doppler shifts generated by their propulsion devices. These shifts can characterise specific types of objects. In this case, estimation of these shifts is a challenging task because the front-end signals at the receiver are low SNR reflections and are the superposition of all reflections from the entire object and the noise background. Conventional estimators for this purpose only use reflections collected in a coherent processing interval (CPI) and produce poor estimate outputs. In order to achieve the desired accuracy, one requires more reflections than those collected in a CPI.

This thesis mainly considers the aforementioned two difficulties and aims to develop efficient algorithms, which can detect low SNR and manoeuvring objects by incorporating long-time pulse integration and micro-doppler estimation. Main contributions in this thesis are based on the following two algorithms. The first work considers the detection of manoeuvring and small objects with radars. The radar systems are considered both co-located and separated transmitter/receiver pairs, i.e., monostatic and bistatic configurations, respectively, as well as multistatic settings involving both types. The proposed detection algorithm is capable of coherently integrating reflected signals within a CPI in all these configurations and continuing integration for an arbitrarily long time across consecutive CPIs. This approach estimates the complex value of the reflection coefficients for the integration while simultaneously estimating the object trajectory. Compounded with this simultaneous tracking and reflection coefficient estimation is the estimation of the unknown time reference shift of the separated transmitters necessary for coherent processing. The detection is made by using the resulting integration value in a Neyman-Pearson test against a constant false alarm rate threshold.

The second work focuses on micro-Doppler signature estimation of manoeuvring and small rotor based unmanned aerial vehicle (UAV) systems with a monostatic radar. The micro-Doppler signature is considered rotation frequencies generated by rotating rotor blades of the UAVs. This estimation uses a maximum likelihood (ML) approach that finds rotation frequencies to maximise a likelihood function conditioned on an object trajectory, complex reflection coefficients, and rotation frequencies. In particular, the proposed algorithm uses an expectation-maximisation (EM) approach such that the expectation of the likelihood mentioned above is approximated by using the state distributions generated from Bayesian recursive filtering for the trajectory estimation. The reflection coefficients and the rotation frequencies are estimated by maximising this approximated expectation. As a result, this algorithm is capable of simultaneously tracking the trajectory and estimating the reflection coefficients and the rotation frequencies of the UAVs before the decision on the object presence is made.

Lay Summary

Small aircraft detection and object-related parameter estimation in high noise background environmental conditions are challenging in radar surveillance applications. That is because small aircraft have low reflectivity, which makes a level of reflected signals similar to noise only signals. In order to detect such objects, conventional detection techniques use a sum of multiple reflected signals from the same location over time. When this integrated value exceeds a threshold, a conventional detector decides on the object presence. However, when these objects move to another location, this detector is likely to fail to detect them because the integrated value does not follow their movements. Another problem scenario would be slowly manoeuvring aircraft when flying at nearly zero velocity, such as hovering drones. In this scenario, the conventional detector might detect them but cannot discriminate them from stationary background objects. That is because the integrated value cannot specify the reflections from the object of interest or stationary background objects. Therefore, this thesis mainly focuses on these two difficulties. It aims to develop efficient algorithms to detect small aircraft and estimate their object-related parameters.

The main contributions are based on the following two algorithms: The first focus is on detecting manoeuvring and small objects and proposes a detection algorithm that is capable of coherently integrating reflected signals collected by simultaneously estimating the object trajectory. Its benefit produces high integrated value for a long time while simultaneously estimating the object trajectory. The second work considers the micro-Doppler signature estimation of slowly manoeuvring rotary-wing aircraft, such as drones, for object identification/classification. The micro-Doppler signature considers rotation frequencies generated by rotating rotor blades of such objects. This work proposes a novel algorithm that can estimate the micro-Doppler signature and discriminate the objects of interest from stationary background objects. In particular, this estimator uses a maximum likelihood (ML) approach that finds both a rotation frequency and an object trajectory to maximise a likelihood function conditioned on an object trajectory and a rotation frequency. As a result, this algorithm can simultaneously track the object trajectory and estimate the rotation frequency of drones.

Declaration of originality

I hereby declare that this thesis and the work reported herein was composed and originated entirely by myself in the School of Engineering at the University of Edinburgh.

Kimin Kim

March 2021

Acknowledgements

This work is funded by university defence research collaboration (UDRC) phase 2 programme. Without this financial support, I would have been difficult to finish this work. I would also like to thank the following people:

- Prof. Bernard (Bernie) Mulgrew and Dr. Murat Üney for their advice and guidance. Without their support, none of this work would have been completed. I have learned many things from them over the years and would like to thank them again.
- My family for everything they have done for me. They have supported and encouraged me to finish my PhD study.
- My wife (Bomi Park) for her support and encouragement. Her support has been invariable during my PhD study.
- My friends in the Institute for Digital Communications (IDCOM). I have spent a great time with them and discussed many different topics including my research work. I have learned many things from these discussions.

Contents

	Abstract	ii
	Lay Summary	iii
	Declaration of originality	iv
	Acknowledgements	v
	List of figures	ix
	List of tables	xvi
	List of abbreviations	xvii
	Nomenclature	xviii
1	Introduction	1
1.1	Motivation and objectives	2
1.1.1	Objectives	7
1.2	Assumptions	7
1.3	Contributions	8
1.4	Thesis outline	10
2	Background	11
2.1	Introduction	11
2.2	Radar fundamentals	12
2.2.1	Monostatic configuration	19
2.2.2	Bistatic and multistatic configurations	22
2.3	Conventional object detection in array receivers	25
2.3.1	Beam-forming	31
2.3.2	Doppler processing	32
2.3.3	Space-time filtering	33
2.3.4	Object detection	35
2.4	Micro-Doppler signatures	38
2.5	Pulse integration	47
2.6	Track-before-detect	48
2.7	Summary	53
3	Detection via simultaneous trajectory estimation and long time integration	55
3.1	Introduction	55
3.2	Problem statement	58
3.2.1	Spatio-temporal signal model in reflection channels	59

3.2.2	Spatio-temporal signal model in direct channels	61
3.2.3	Problem definition	62
3.2.4	Sufficient statistics for the likelihood ratio	64
3.3	Simultaneous tracking and reflection coefficient estimation	66
3.4	Maximum Likelihood estimation of unknown parameters	73
3.4.1	ML estimation of the reflection coefficients	73
3.4.2	Synchronisation of the local processor with remote transmitters .	77
3.5	Long time integration for detection	81
3.5.1	Constant false alarm rate threshold for the detection test	82
3.5.2	Signal to noise ratio (SNR) in the radar data cube	84
3.6	Example	87
3.6.1	Detection test via long time integration	92
3.6.2	Performance in estimating the unknowns	99
3.7	Summary	104
4	Joint micro-Doppler signature estimation and track-before-detect in an array receiver	106
4.1	Introduction	106
4.2	Problem statement	109
4.2.1	Received signal model and baseband processing	109
4.2.2	Problem definition	113
4.2.3	Sufficient statistics of the likelihood functions	114
4.3	Spatio-temporal signal model components	116
4.3.1	MF Output due to rotating blades: The micro-Doppler model . .	116
4.3.2	Measurement model	122
4.4	Trajectory estimation with Bayesian filtering of the radar data cubes .	123
4.5	Maximum likelihood estimation of the micro-Doppler shift and the reflectivity	126
4.5.1	ML estimation for the reflection coefficients	131
4.5.2	ML estimation for the angular rotation frequencies	134
4.6	Detection via long time integration using the proposed estimator	135
4.6.1	Signal to noise ratio (SNR) in the radar data cube	137
4.7	Example	138
4.7.1	Simulation result	139
4.7.2	Real experiment result	150
4.8	Summary	156
5	Conclusion	159
5.1	Summary	159
5.2	Limitations	162
5.3	Possible directions for future work	162
	Appendices	164
A	The likelihood locality, Cramér-Rao bound, and computational complexity of the proposed detector	164
A.1	The likelihood locality	164

A.2	Cramér-Rao bound (CRB) for complex reflection coefficients	165
A.3	Computational complexity of the proposed detector	166
B	Original publications	169
	Bibliography	170

List of Figures

2.1	Block diagram of a conventional pulsed monostatic radar (reproduced from Figure 1.2. in [1, Chp.1]): (a) Overall system block diagram. (b) Block diagram of the signal processor in (a).	13
2.2	The geometry of radar configurations: An object (black dot) is located at $[x, y]^T$ with velocity $[\dot{x}, \dot{y}]^T$. (a) The geometry of the monostatic configuration formed by a co-located transmitter/receiver pair. (b) The bistatic configuration formed by a separated transmitter/receiver pair. (c) The multistatic configuration combined by both the monostatic and the bistatic with M separately located transmitters.	17
2.3	Geometry of a co-located transmitter/receiver pair and a single object in the monostatic channel	19
2.4	Doppler effect of a moving object with the ULA receiver: (a) Maximum Doppler shift measurement at the ULA receiver (red dots). (b) Zero Doppler shift measurement at the ULA receiver. An object (black dot) at an initial location $[x_1, y_1]^T$ moves to $[x_k, y_k]^T$ with velocity $[\dot{x}_k, \dot{y}_k]^T$. The line of sight with respect to the receiver is depicted by the solid black line.	22
2.5	Geometry of a moving object with the multistatic channel	23
2.6	Example of a pulse train (reproduced from Figure 3-1 in [2, Chp.3]): N consecutive waveforms are separated by a time interval T . The pulse waveform, $\tilde{u}(t)$, for the transmission uses a pulse duration T_p	26
2.7	Data acquisition from a ULA array receiver: The input of the pulse MF stage is the baseband signal from the front-end. The MF output is sampled by using the pulse width T_p and arranged in array index, fast time and slow time axes, respectively.	27
2.8	Spatial and temporal signal processing (reproduced from Figure 9.22. in [1, Chp.9]): There are three approaches for this purpose. One first performs Doppler filtering with N temporal samples, and then these outputs are further used for beam-forming (i.e., the pre-Doppler filtering and the post-beam-forming, respectively). The second performs first the beam-forming with L spatial samples and later the Doppler filtering with these outputs (i.e., the pre-beam-forming and the post-Doppler filtering, respectively). The last is space-time filtering that performs joint beam-forming and Doppler filtering with $L \times N$ samples. All these outputs produce the bearing-Doppler map that forms an $I \times J$ matrix.	30
2.9	Space-time data vector (reproduced from Figure 9.12. in [1, Chp.9]): Mapping of an $L \times N$ matrix at the r th range bin to an $LN \times 1$ vector as a space-time data vector.	34

2.10	Example of slowly manoeuvring objects: A helicopter consists of its body and rotor blades. The micro-Doppler shift is characterised by a rotation frequency of the rotor blades (red line), the blade length, and the number of the rotor blades.	38
2.11	Commonly used window functions defined in Table 2.3 (reproduced from Figure 7.21 in [3, Chp.7]): The solid red line is the rectangular window function, and the blue line shows the Bartlett. The solid, dashed, and dashed-dot black lines indicate the Hanning, the Hamming, and the Blackman, respectively. Each of them is plotted as a function of the continuous variable.	42
2.12	Comparison of short time Fourier transform (STFT) with different windows defined in Table 2.3:(a) STFT with the rectangular window, (b) STFT with the Bartlett, (c) STFT with the Hanning, (d) STFT with the Hamming, (e) STFT with the Blackman. All these results are obtained when a helicopter has a single rotor blade (i.e., $\tilde{L} = 1$).	43
2.13	Comparison of short time Fourier transform (STFT) and Wigner-Ville distribution (WVD): (a) STFT with the number of blades $\tilde{L} = 1$, (b) WVD with $\tilde{L} = 1$, (c) STFT with $\tilde{L} = 2$, (d) WVD with $\tilde{L} = 2$. All parameters used in this example are the wavelength $\lambda_c = 5\text{m}$, the blade length $B = 1.5\text{m}$, the Doppler shift $f_D = \frac{\Omega}{2\pi T} = 5 \times 10^3\text{Hz}$, and the PRI $T = 5 \times 10^{-5}\text{s}$	44
2.14	Relationship between the wavelength and the blade length: (a) STFT when the wavelength is larger than the blade length B : $\lambda_c < B$, (b) STFT when the wavelength is smaller than the blade length B : $\lambda_c > B$, (c) WVD when the wavelength is larger than the blade length B : $\lambda_c < B$, (d) WVD when the wavelength is larger than the blade length B : $\lambda_c < B$. All parameters are the same parameters used in Figure 2.13.	45
3.1	Problem scenario: M transmitters and a ULA receiver to detect a small object located at $[x, y]^T$ with the velocity $[\dot{x}, \dot{y}]^T$ (reproduced from Figure 2.2(c)).	56
3.2	Geometry of the problem: A ULA receiver co-located with a transmitter and the m th remote transmitter on the 2D Cartesian plane. Both polar and Cartesian coordinate variables are depicted. Each transmitter emits N pulses in a CPI. The waveforms, used here, are orthogonal.	58
3.3	Data acquisition in the m th channel reproduced from Figure 2.7 in Chapter 2: Sampled version of the received signal within a CPI as the radar data cube in the m th reflection channel. The output of the m th matched filter is sampled and arranged in array index, fast time and slow time axis. $\tilde{\mathbf{Z}}_m(r)$ is an $L \times N$ matrix, and forms an $LN \times 1$ vector as the measurement, $\mathbf{Z}_m(r)$, at the r th range bin.	60
3.4	Example of the matched filter output: The pulsed waveform has the pulse width, $T_p = 0.01\text{s}$. The corresponding output of the matched filter with this waveform is illustrated at the bottom. The highest level of this output is depicted by a red dot.	64
3.5	Block diagram of the proposed detector: (a) Inference on the object trajectory $\mathbf{X}_{1:K}$, (b) Markov model for the radar data cube measurements. T_{X_1}, \dots, T_{X_M} indicate the M transmitters.	67
3.6	Block diagram of the proposed synchronisation term estimator: The input of this estimator is the direct channel (black-dashed box) measurements, and the receiver has full knowledge of both the transmission characteristics and all the transmitter's locations as the prior knowledge. The resulting estimate (i.e., $\Delta \hat{\mathbf{t}}$) is the inputs of both, the Bayesian filtering recursions and the proposed detector.	77

3.7	Example scenario: (a) $M = 3$ transmitters (i.e., Tr_1 , Tr_2 , and Tr_3) emitting $N = 20$ pulses (solid line arrows) towards a small object (a black dot). A ULA (red dots) collects low SNR (-6dB) reflections (dashed line arrows) and direct signals (a dotted green line arrow). (b) The object's trajectory depicted with the red line. The range resolution bins resulting from sampling in time are shown by the dashed red lines. The bearing resolution bins, obtained by (2.31), are shown by the dashed blue lines. . . .	87
3.8	The proposed scheme with $M = 1$ transmitters versus the number of particles: The number of particles sets $P = 200$, $P = 400$, $P = 600$, $P = 800$, and $P = 1000$, respectively.	91
3.9	Proposed integration compared to the probability of target existence obtained by Bernoulli track-before-detect [4]: Both algorithms use the same sets of measurements. The dashed blue, the dashed cyan, the dotted green, the dashed brown, and the solid pink lines indicate SNR -1dB, -2dB, -3dB, -4dB, and -5dB, respectively. . . .	92
3.10	Detection performance comparison: The probability of detection, obtained by the proposed detector, is depicted by the solid green line, That of the Bernoulli track-before-detect is depicted by the solid black line.	93
3.11	Long time integration using the proposed scheme, the clairvoyant integrator, and the conventional coherent integrator, when $M = 3$ transmitters are used: The integrated sufficient statistics from the proposed integration averaged over 100 experiments is depicted by the solid blue line. The integrated value from the clairvoyant integrator is the dashed red line and the clairvoyant (CFAR) threshold for $P_{fa} = 10^{-6}$ (averaged for 100 experiments) is the solid magenta line. The conventional scheme is depicted by the solid black line.	95
3.12	The proposed scheme with $M = 3$ transmitters (solid blue line) versus the single channel integrations: The local channel (solid green line) integration, and the remote channel (solid brown line) integration fail to exceed the detection threshold. The clairvoyant (CFAR) threshold for $P_{fa} = 10^{-6}$ (averaged for 100 experiments) is the solid magenta line	96
3.13	The proposed scheme with $M = 3$ transmitters (solid blue line) versus the integration $M = 2$ transmitters (solid cyan line): The clairvoyant (CFAR) threshold is used in Figure 3.12.	97
3.14	Probability of detection (P_d) for the proposed scheme in comparison with the clairvoyant detector and the conventional detector: P_d for the proposed scheme (solid blue line) with $M = 3$ transmitters and P_d for the proposed scheme (solid cyan line) with $M = 2$ transmitters are compared to P_d for the clairvoyant detector (dashed red line). The probability of false alarm $P_{fa} = 10^{-6}$ compared to P_d for the clairvoyant detector (dashed red line).	98
3.15	Receiver operating characteristic (ROC) curves as a function of P_{fa} : The proposed detector with $M = 3$ transmitters (solid blue line), and, $M = 2$ transmitters (solid cyan line), respectively, are given. The solid green, the dashed brown, the dotted pink, and the dotted black lines denote the single channel integrations and the conventional coherent integration, respectively.	99
3.16	Receiver operating characteristic (ROC) curves as a function of SNR: The proposed detector with $M = 3$ transmitters (solid blue line), and $M = 2$ transmitters (solid cyan line), respectively, are given. The solid green, the dashed brown, and the dotted pink lines denote the single channel integrations, respectively.	100

3.17	Typical trajectory estimation: (a) The estimated trajectory by the proposed algorithm is depicted with the blue line. (b) Root mean square error (RMSE) of the range estimation in (a). (c) RMSE of the velocity estimation in (a). (d) RMSE of the angle of arrival estimation in (a). The dashed red lines in (b), (c), and (d) are the range resolution ($\Delta\tau = 150\text{m}$), the velocity resolution ($\Delta V = 7.5\text{m/s}$) and the bearing resolution ($\Delta\theta = 5.1^\circ$)	101
3.18	Complex reflection coefficient estimation with -6dB reflections: (a) Estimation performance of the real part of the complex reflection coefficient regarding the variance of 100 realisations by increasing the number of transmitted pulses. (b) Estimation performance of the imaginary part of (a). (c) A typical estimate of the complex reflection coefficient for the local channel by using the proposed algorithm. The blue line indicates typical estimates of the local reflection coefficient by using Algorithm 1 within Algorithm 3. The blue circle shows \pm standard deviation of 100 estimates using the proposed scheme. The blue dots show $i = 3$ iterations for finding it. The resulting estimate is compared to the ground truth value (red dot) with the \pm standard deviation of Cramér-Rao bound (CRB), i.e., $\pm\sigma_{\text{CRB}}$ (dashed red ellipse). The x axis denotes the real part of the complex reflection coefficient, and the y axis is its imaginary part. (d) A typical estimate of the complex reflection coefficient for the remote channel by using Algorithm 1 within Algorithm 3 with the same colour codes in (c).	102
3.19	Synchronised term estimation: Averaged synchronised term (solid blue line) estimated by using the proposed estimator versus the ground truth value (solid red line) with the bound the $\pm T_p$ bound (dashed black lines) of a preliminary search over the grids.	103
4.1	Sensing scenario: A radar with a UPA receiver collects reflections from a small rotary-wing aircraft's body and multiple rotating blades with the corresponding rotation frequencies (i.e., $\omega_1, \dots, \omega_M$). This aircraft is located at $[x, y, z]^T$ and has a velocity of $[\dot{x}, \dot{y}, \dot{z}]^T$ in the three-dimensional (3D) volume.	107
4.2	Radar data acquisition reproduced from Figure 2.7: Array elements are matched filtered and sampled with T_p sampling period. Samples are arranged in array index, fast time and slow time. $\mathbf{z}(t)$ and $\tilde{\mathbf{Z}}(r)$ denote the MF output and its sampled version, respectively.	110
4.3	Top view of Figure 4.1 with the m th rotor hub together with a single blade in the 2D (x, y) plane: The rotation of the rotor blade at the m th rotor hub generates an angular rotation frequency depicted by ω_m	117
4.4	Empirical resulting value of $C_{\tilde{L}}$ in (4.28): (a) $C_{\tilde{L}}(i, \mathbf{X})$ with $\tilde{i} = 0, \dots, 100$. (b) $C_{\tilde{L}}(\tilde{i}, \mathbf{X})$ with $\tilde{i} = 0, \dots, 10$. $C_{\tilde{L}}$ is converged to 0.33 at $\tilde{i} = 3$	120
4.5	Empirical resulting value of C_n with $n = 1$ in (4.27): (a) C_n with $i = -100, \dots, 100$ and $\tilde{i} = 0, \dots, 3$ (b) $C_{\tilde{L}}$ with $i = -10, \dots, 10$ and $\tilde{i} = 0, \dots, 3$. $C_n(\omega, \mathbf{X})$ is converged to 2 at $i = \pm 5$	121
4.6	Example with a UPA receiver: (a) Problem scenario. A transmitter (red triangle) co-located with a UPA receiver (red dots) emits $N = 40$ modulated pulses (solid red line). The receiver collects -3dB reflections (dashed red line) from a single UAV (black dot). (b) A typical trajectory (solid red line) of the UAV	138

4.7	Initial search for the rotation frequency (i.e., $f_r = \frac{\omega}{2\pi}$) with -3dB reflections: (a) Initial search for the rotation frequency with $N = 20$ pulses. (b) Initial search for the rotation frequency with $N = 40$ pulses. (c) Initial search for the rotation frequency with $N = 60$ pulses. (d) Initial search for the rotation frequency with $N = 80$ pulses. All solid blue lines shows the output of the initial search with the ground truth value of the rotation frequency as solid red lines.	142
4.8	Typical rotation frequency estimation via the golden section search: A typical rotation frequency (blue dot) is estimated by using Algorithm 7 within Algorithm 6 in comparison with the true value (red dot). The black crosses indicates $i_g = 8$ iterations for finding the rotation frequency in Algorithm 7	143
4.9	Rotation frequency estimation with the radar data cubes over k CPIs: (a) Typical estimate (blue solid line) of the rotation frequency using Algorithm 6. (b) Averaged estimates (blue solid line) with $\pm\sigma$ bounds (blue dashed lines) of the rotation frequency obtained by using Algorithm 6 for the 100 realisations. The red solid and dashed lines indicate the true value of the rotation frequency f_r and $\pm\Delta f_r$ bounds in conventional processing, respectively. (c) Short time Fourier transform (STFT) of the reflection coefficients estimated by the proposed scheme in Chapter 3	144
4.10	Singular value decomposition (SVD) of (c) in Figure 4.9: (a) Outputs of the first three singular values from the result of SVD. (b) Singular values of SVD.	145
4.11	Complex reflection coefficient estimation with -3dB radar data cube: (a) A typical estimate of the complex reflection coefficient for the object body by using the proposed algorithm. The blue line indicates typical estimates of the object body reflection coefficient by using Algorithm 5 within Algorithm 4. The blue circles show $i = 5$ iterations for finding it. The resulting estimate is compared to the ground truth value (red dot) with the \pm standard deviation of Cramér-Rao bound (CRB), i.e., $\pm\sigma_{\text{CRB}}$ (dashed red ellipse). The x axis denotes the real part of the complex reflection coefficient and the y axis is its imaginary part. (b) A typical estimate of the complex reflection coefficient for the rotor blades by using Algorithm 5 within Algorithm 4 with the same colour codes in (a).	145
4.12	Typical trajectory estimation: The estimated trajectory by using Algorithm 4 is depicted as the blue solid line. This output is compared to its ground truth (red solid line).	146
4.13	Root mean square error (RMSE) of the typical trajectory estimation: (a) RMSE of the range estimation obtained in Figure4.12. (b) RMSE of the velocity estimation obtained in Figure4.12. (c) RMSE of the azimuth angle estimation obtained in Figure4.12. (d) RMSE of the elevation angle estimation obtained in Figure4.12. The red dashed lines in all these figures indicate the range resolution ($\Delta R = 75\text{m}$) in (a), the velocity resolution ($\Delta V = 23.5\text{ms}^{-1}$) in (b), the azimuth resolution ($\Delta\theta = 11.81^\circ$) in (c), and the elevation resolution ($\Delta\phi = 2.93^\circ$) in (d), respectively.	147

4.14	Detection performance of the proposed detector in comparison with the clairvoyant detector and the conventional detector: (a) Long-time integration using the proposed scheme, the clairvoyant integrator, and the conventional coherent integrator. The integrated sufficient statistics from the proposed integration averaged over 100 experiments is depicted by the solid blue line with $\pm\sigma$ (blue dashed lines). The integrated value from the clairvoyant integrator is the dashed red line and the clairvoyant (CFAR) threshold for $P_{fa} = 10^{-6}$ (averaged for 100 experiments) is the solid magenta line. The conventional scheme leads to the solid black line. (b) Probability of detection (P_d) for the proposed scheme compared to those of the clairvoyant detector and the conventional detector with the same colour codes in (a).	148
4.15	Receiver operating characteristic (ROC) curves: ROC curve of the proposed detector (blue solid line) is compared to ROC curve of the conventional coherent detector (black solid line).	149
4.16	Experiment scenario: (a) Gamekeeper Thales/Aveillant radar system emits consecutive modulated pulses towards the surveillance region (light coloured region) and collects reflections from a DJI inspire 1 UAV with trajectory depicted by the solid red line. (b) UAV trajectory in the three-dimensional volume.	150
4.17	Typical rotation frequency estimation via the golden section search: (a) Initial search for the rotation frequency (i.e., $f_r = \frac{\omega}{2\pi}$). (b) Typical rotation frequency estimation via the golden section search when $k = 122$ CPIs. A typical rotation frequency (blue dot) is estimated by using Algorithm 7 within Algorithm 6 in comparison with the true value (red dot) based on the GPS ground truth. The black crosses indicates $i_g = 8$ iterations for finding the rotation frequency in Algorithm 7.	151
4.18	Rotation frequency estimation with the radar data cubes over k CPIs: (a) Short time Fourier transform (STFT) of the estimated reflection coefficients using the EM algorithm Section 3.4 (b) Typical estimate (blue solid line) of the rotation frequency using Algorithm 6. (c) Root mean square error (RMSE) of the estimated rotation frequency in (b).	152
4.19	Typical estimate of complex reflection coefficients using our estimation scheme: (a) Typical estimate of the body reflection coefficient. (b) Typical estimate of the blade hub reflection coefficient. The blue circles show $i = 4$ iterations for finding these estimates. The resulting estimates are compared to the true value (red dot) based on GPS ground truth and with the \pm standard deviation of Cramér-Rao bound (CRB), σ_{CRB} (solid red ellipse).	153
4.20	Trajectory estimation: The estimated trajectory obtained by using Algorithm 4 is depicted as the solid blue line. This output is compared to its ground truth depicted as the solid red line.	154

4.21	Root mean square error (RMSE) of the typical trajectory estimation: The trajectory estimation is obtained in Figure4.20. (a) RMSE of the range estimation. (b) RMSE of the velocity estimation. (c) RMSE of the azimuth angle estimation. (d) RMSE of the elevation angle estimation. The red dashed lines in all these figures indicate the range resolution ($\Delta R = 75\text{m}$) in (a), the velocity resolution ($\Delta V = 23.5\text{ms}^{-1}$) in (b), the azimuth resolution ($\Delta\theta = 11.81^\circ$) in (c), and the elevation resolution ($\Delta\phi = 2.93^\circ$) in (d), respectively.	157
4.22	Detection performance of the proposed detector in comparison with the conventional detector: Long-time integration using the proposed scheme, and the conventional coherent integrator. The integrated sufficient statistics from the proposed integration is depicted by the blue line. The CFAR threshold for $P_{fa} = 10^{-7}$ is the red line, and, the conventional scheme is depicted by the black line.	158

List of Tables

1.1	Comparison of FMCW radar and pulse-Doppler radar based on their applications [5–10]	4
2.1	Summary of airport surveillance radar (ASR) technical characteristics (reproduced from Table C-1 in [11])	15
2.2	Representative values and characteristics of high, medium, and low PRFs (reproduced from Table 5.9-1 in [5])	16
2.3	Commonly used window functions [3, Chp.7]	42
2.4	Characteristics of the Swerling case 0, 1, 2, 3, 4, and 5 with their fluctuation models [2, Chp.2]	50
3.1	Transmitted signal parameters	88
3.2	Computational cost	104
4.1	C_n function parameters	120
4.2	Transmitted signal parameters	140
A.1	Computational cost of the cell under test at the k th CPI	167

List of abbreviations

2D	two-dimensional
3D	three-dimensional
AMF	adaptive matched filter
AoA	angle of arrival
CFAR	constant false alarm rate
CPI	coherent processing interval
CRB	Cramér-Rao bound
CVD	cadence-velocity diagram
CW	continuous waveform
DFT	discrete Fourier transform
EM	expectation-maximisation
FMCW	frequency modulated continuous waveform
FT	Fourier transform
GLRT	generalised likelihood ratio test
GPS	global positioning system
GUI	graphical user interface
IF	intermediate frequency
KT	keystone transform
LFM	linear frequency modulated
LO	local oscillator
LVD	Lv's distribution
MF	matched filter
MIMO	multiple-input multiple-output
ML	maximum likelihood
PM	phase modulated
PRF	pulse repetition frequency
PRI	pulse repetition interval
PSD	power spectral density
RCS	radar cross section
RF	radio frequency
RMSE	root mean squared error
ROC	receiver operating curve
SMC	sequential Monte Carlo
SNR	signal to noise ratio
STFT	short-time Fourier transform
SVD	singular value decomposition
SVM	support vector machines
TBD	track-before-detect
UAV	unmanned aerial vehicle
ULA	uniform liner array
UPA	uniform planar array
WVD	Wigner-Ville distribution

Nomenclature

\otimes	Kronecker product operator
\odot	Hadamard product operator
$*$	linear convolution
$(\cdot)^*$	complex conjugate operator
$(\cdot)^H$	Hermitian operator
$(\cdot)^T$	transpose operator
$(\cdot)^{-1}$	inverse operator
$\ \cdot\ $	Euclidean norm of a vector
$ \cdot $	modulus of a scalar
$\lfloor \cdot \rfloor$	the nearest integer function
$[\cdot]_m$	the m th diagonal elements of its input matrix
$E\{\cdot\}$	expectation of a random variable or vector
$\exp\{\cdot\}$	exponential of its input argument
$\text{Im}\{\cdot\}$	imaginary part of its input complex argument
$\log\{\cdot\}$	natural logarithm of its input argument
$\text{Re}\{\cdot\}$	real part of its input complex argument
$\text{tr}\{\cdot\}$	trace of its input matrix
$\text{Var}(\cdot)$	variance of a random variable or vector
$\sim \mathcal{CN}(\cdot, \cdot, \cdot)$	complex normal distribution
$\sim \mathcal{N}(\cdot, \cdot, \cdot)$	normal distribution
$\partial(\cdot)$	partial derivative operator
$\Lambda(\cdot)$	auto-correlation of the waveform
$\Lambda_m(\cdot)$	auto-correlation of the m th waveform
$\mathbf{C}[\cdot]$	radar data cube
$d_m(\cdot)$	the m th direct channel measurement after digital beam-forming
$\mathbf{h}(\cdot, \cdot)$	space-time filter coefficients
$\mathbf{h}_s(\cdot)$	weighted vector for beam-forming
$\mathbf{h}_t(\cdot)$	vector of DFT coefficients for Doppler processing
$h(\cdot, \cdot, \cdot)$	bearing-Doppler map after the beam-forming and the Doppler processing
$J(\cdot)$	cost function of the golden section search algorithm
$J_i(\cdot)$	Bessel function of the 1st kind and i th order
$Q(\cdot)$	Q function of the EM algorithm
$\hat{Q}(\cdot)$	approximation of Q function
$\mathbf{s}(\cdot, \cdot, \cdot)$	signal model which combines the spatial and the temporal steering vectors
$\mathbf{s}_m(\cdot, \cdot)$	signal model in the m th channel
$\mathbf{s}_h(\cdot, \cdot)$	horizontal spatial steering vector in the UPA receiver

$\mathbf{s}_s(\cdot)$	spatial steering vector
$\mathbf{s}_t(\cdot)$	temporal steering vector
$\mathbf{s}_v(\cdot, \cdot)$	vertical spatial steering vector in the UPA receiver
$u(\cdot)$	pulse train
$\tilde{u}(\cdot)$	probing waveform waveform
$\tilde{u}_m(\cdot)$	probing waveform of the m th transmitter
$\mathbf{Z}_m(\cdot)$	the m th channel measurement which forms an $LN \times 1$ vector
$\tilde{\mathbf{Z}}_m(\cdot)$	the m th channel measurement which forms an $L \times N$ matrix
$\mathbf{Z}_{m,k}(\cdot)$	the m th channel measurement at the k th CPI
$Z(\cdot, \cdot, \cdot)$	measurement given range-bearing and Doppler bins
$\mathbf{z}_s(\cdot, \cdot)$	response of beam-former given range-bearing bins
$\mathbf{z}(\cdot)$	received signal at the receiver after demodulation
$\tilde{z}(\cdot)$	output of the matched filter (MF) with the probing waveform
$z_{(r,i)}(\cdot)$	one temporal sample given the r th range and the i th bearing bins
$\mathbf{0}$	vector of zeros
$\mathbf{1}$	vector of ones
$\boldsymbol{\alpha}$	vector of whole complex reflection coefficients
$\boldsymbol{\alpha}_k$	vector of complex reflection coefficients at the k th CPI
$\boldsymbol{\alpha}_{\text{true},k}$	ground true vector of complex reflection coefficients at the k th CPI
$\boldsymbol{\alpha}_k^{(i)}$	vector of complex reflection coefficients at the i th iteration of the EM algorithm
α	complex reflection coefficient
α_0	complex reflection coefficient from the object's body
α_2	complex reflection coefficient from the object's rotary-wing
α_m	complex reflection coefficient in the m th channel
$\alpha_{m,k}$	complex reflection coefficient in the m th channel at the k th CPI
$\hat{\alpha}_{m,k}$	ML estimate of the complex reflection coefficient in the m th channel or that from the m th rotor hub at the k th CPI
$\tilde{\alpha}$	complex reflection coefficient that contains the phase value of the pulse time of flight
Γ	number of range bins
Δ	time interval between two consecutive pulse train transmissions
$\Delta\theta$	bearing resolution
Δf	resolution of Doppler shift
ΔR	range resolution
$\Delta \mathbf{t}$	vector of synchronisation terms
Δt_m	synchronisation term in the m th channel
$\Delta t_{\text{true},m}$	ground true value of synchronisation term in the m th channel
$\Delta \hat{t}_m$	ML estimate of the synchronisation term in the m th channel
δ	Dirac's delta distribution
$\delta_{m,m'}$	Kronecker's delta function
ϵ	pre-defined threshold of the convergence test for the EM algorithm
$\zeta_k^{(p)}$	weight of the p th particle at the k th CPI

$\theta(X)$	angle of arrival of X
$\theta_m(X)$	bearing angle of X to the m th transmitter
λ_c	carrier wavelength
$\xi_p^{(i-1)}$	weight of the EM algorithm associated with previously found value given a set of particles
Σ	covariance matrix
Σ_m	covariance matrix of the m th channel
σ^2	noise power
σ_{CRB}^2	CRB
$\sigma_{d,m}^2$	variance of the m th direct channel
σ_t	object's radar cross section (RCS)
$\sigma_t^{(m)}$	object's RCS in the m th channel
$\tau(X)$	pulse time of flight of X
$\tau_1(X)$	pulse time of flight of the receiver to X
$\tau_m(X)$	pulse time of flight of X in the m th channel
$\tau_m^{tx}(X)$	pulse time of flight of the m th transmitter to X
$\phi(X)$	elevation angle of X to the receiver
$\Omega(X)$	angular Doppler shift of X
$\Omega_m(X)$	angular Doppler shift of X in the m th channel
ω	vector of angular rotation frequencies
ω_{true}	ground true vector of angular rotation frequencies
$\omega_k^{(j)}$	vector of angular rotation frequencies at the j th iteration of the EM algorithm
$\hat{\omega}$	ML estimates of angular rotation frequencies
ω	angular rotation frequency
ω_c	angular carrier frequency
ω_l	angular rotation frequency of the l th rotor blade
\mathbb{C}	set of all complex numbers
\mathbb{R}	set of all real numbers
\mathbb{Z}^+	set of all positive integer numbers
$\mathcal{C}(X_k)$	set of range-bearing and Doppler bins associated with the object state X_k at the time step k
$\mathcal{E}(X_k)$	set of range bins associated with the object state X_k at the k th CPI
$\mathcal{E}_m(X_k)$	set of range bins associated with the object state X_k in the m th channel at the k th CPI
$\tilde{\mathcal{E}}_m(X_k)$	set of range bins associated with the object state X_k in the m th direct channel at the k th CPI
\mathcal{T}	constant false alarm rate (CFAR) threshold
\mathcal{T}_k	CFAR threshold at the k th coherent processing interval (CPI)
B	probing waveform bandwidth or blade length
C_n	Fourier coefficient of the n th pulse
\tilde{C}_{Li}	coefficient of the Bessel function
c	speed of light

f_c	carrier frequency
G_r	receiver gain
G_t	transmitter gain
$G_t^{(m)}$	the m th transmitter gain
H_1	hypothesis that contains reflected signals from an object exists
H_0	null hypothesis that contains noise only signals
L	number of elements in the ULA receiver
\tilde{L}	number of rotor blades
L_s	system loss
M	number of transmitters or number of rotor hubs
N	number of transmitted pulses
P_d	probability of detection
P_{fa}	probability of false alarm or constant false alarm rate
P_r	received power
P_t	transmitted power
$P_t^{(m)}$	transmitted power of the m th transmitter
$R(X)$	range of X to the receiver
$R_m(X)$	range of X from the m th transmitter and to the receiver
$R_m^{tx}(X)$	range of the m th transmitter to X
T	pulse repetition interval (PRI)
T_p	probing waveform duration
\mathbf{w}	vector of weights associated with \mathbf{h}_s
X	object state
X_k	object state at the k th CPI
$X_{\text{true},k}$	ground true value of the object state at the k th CPI
$X_{1:K}$	object trajectory for K CPIs
$X_k^{(p)}$	the p th object state particle
\hat{X}_k	estimated object state at the k th CPI
$\tilde{\mathbf{Z}}(r)$	measurement at the r th range bin which forms an $L \times N$ matrix
$Z_k^{(r,i,j)}$	measurement at the r th range, the i th bearing, and j Doppler bins at the k th CPI
$\mathbf{z}_{(r,i)}$	N temporal samples given the r th range and the i th bearing bins

Chapter 1

Introduction

RADAR is an acronym for RAdio Detection And Range that consists of a transmitter and a receiver. The transmitter emits electromagnetic waves towards a surveillance region, and the receiver collects reflected versions of the transmitted waves from objects in this region [12, Chp.1]. The reflected signals vary with object-related parameters: One is the reflectivity induced by the object's surface on which the transmitted waves are reflected. The second is the time delay caused by the distance (or range) of the object to the radar. The next is the angle of arrival induced by the object's bearing angle to the radar receiver. The last is the Doppler shift caused by the object's velocity [13, Chp.9]. Signal processing with the reflected signals at the radar receiver decides on the object's presence and estimates the object-related parameters above.

Radar systems were originally developed to detect, locate and track aircraft during World War II [5, Chp.1]. The use of these systems has mainly two advantages: One provides a long detection distance in which the electromagnetic wave used in the radars can travel a longer distance than ultrasonic waves, infrared rays, and visible rays. The other gives less performance degradation of object detection and tracking due to weather changes such as fog, rain, and snow compared to the use of ultrasonic sensors and infrared light imaging sensors. Thus, since World War II, radars have played a major role for military surveillance applications such as fire control [5, Chp.4], ballistic missile defence [6], and ground-based early warning [5, Chp.8] as well as commercial applications

whose examples are weather forecast [7], air traffic control [8], and advanced driver assistance system for vehicles [9, 10].

In many radar applications, one often requires detecting and tracking manoeuvring and small objects in high noise background environmental conditions. It is challenging because such objects have a small-sized body that generates low reflected signals, and the level of them is frequently lower than that of the noise signals [14–16]. Therefore, this thesis addresses problems on this task and proposes novel approaches in order to solve them.

This chapter is organised as follows: Section 1.1 presents motivation and objectives for the detection and tracking of manoeuvring and small objects. Section 1.3 highlights contributions contained in this thesis. Section 1.4 gives the thesis outline.

1.1 Motivation and objectives

Radar systems can be categorised according to transmitting waveforms: One uses a continuous waveform (CW) for transmission. The receiver simultaneously collects the reflected signals while the transmitter is emitting the continuous waveforms. This is referred to as the CW radar [5, Chp.1]. At the initial state, the CW radar employs unmodulated continuous waveforms and only provide Doppler measurements. The distance measurement on a detected object is not available because the time reference at the receiver for measuring the time delay of the reflected signals is not applicable. The demand for this distance measurement leads to the use of a frequency-modulated continuous waveform (FMCW), which provides the time reference at the receiver to measure the time delay of the object's distance. This is referred to as the FMCW radar [5, Chp.2]. Due to the simultaneous transmission and reception, this radar often utilises separated transmission/reception antennas, which are closely located. The transmitter propagates the waveforms with relatively low power in order to prevent the leakage power from the transmission antenna to the reception antenna during the transmission. This system is hence used for short-range applications [17, Chp.1]

The other type is the pulse-Doppler radar, which employs a single antenna that propagates multiple pulsed waveforms separated by a short time interval. This interval is known as the pulse repetition interval (PRI) [2] and is divided into transmission and reception. During the transmission, the receiver is isolated from the antenna, and no signals are collected. For the reception, the receiver collects reflected signals while the transmitter stops emitting the waveforms. Consequently, the PRI is an essential factor that provides the unambiguous distance (or range) and Doppler shift of objects. For example, when the PRI is short, the maximum unambiguous range is short due to the short reception time. In contrast, the maximum unambiguous Doppler shift in the received signals is high due to the high pulse repetition frequency (PRF), which is the inverse of PRI [2, Chp.3]. As a result, the selection of PRI is a trade-off between the unambiguous range and the unambiguous Doppler shift. Regarding the separated transmission/reception intervals, the pulse-Doppler radar provides the perfect isolation of the leakage power from the transmitter to the receiver while collecting the reflected signals. Thus the pulse-Doppler radar can use the high transmission power in order to cover a long distance area [17, Chp.1]. Table 1.1 compares the detection coverage obtained by the FMCW radar and the pulse-Doppler radar, respectively, based on their applications. For example, surveillance systems using the pulse-Doppler radar provide the detection range (i.e., 200km) much longer than the use of the FMCW radar (i.e., 32km). Therefore, many surveillance systems utilise the pulse-Doppler radars instead of the FMCW radars.

The primary focus in this thesis is on the detection of manoeuvring and small object using pulse-Doppler radar systems. Regarding active sensing, the object detection at the receiver is made by testing the hypothesis that the received signal contains the reflections against the noise only signal hypothesis [1, Chp.6] [18, Chp.7]. This test uses the sampled output of the matched filter (MF) in which the front-end input is filtered with a system response matching the probing waveform [1, Chp.6]. The resulting samples correspond to resolution bins in equally divided range space. In conventional processing chains, these samples are further segmented by using beam-forming and Doppler processing.

Table 1.1: Comparison of FMCW radar and pulse-Doppler radar based on their applications [5–10]

Radar type	Application	Typical detection range
FMCW	Surveillance	20km to 32km
	Weather sensing	120km
	Altimeters	2.4km to 15.2km
	Aircraft landing and obstacle avoidance	1.5km to 6km
	Advanced driver assistance system	50m to 250m
	Level measurement	60m
	Imaging	20m to 50m
Pulse-Doppler	Surveillance	120km to 200km
	Weather sensing	115km to 468km
	Fire-control	120km
	Ballistic missile defence	3000km to 6000km
	Air traffic control	96km

These outputs correspond to resolution bins in equally divided bearing and Doppler space [2, Chp.7].

In order to detect small objects, the sufficient statistics of multiple pulse-returns (i.e., multiple measurements) need to be considered because of the low signal to noise ratio (SNR) reflected signals. This is obtained by summing the associated reflections across themselves over time. This process is referred to as the pulse integration [1, Chp.8]. Conventional methods such as coherent integration and non-coherent integration integrate reflections in the same range-bearing and Doppler bins across them over time. However, when small objects manoeuvre, the reflections follow their trajectories across the corresponding resolution bins over time. The conventional methods fail to collect evidence on the object's presence for a long time due to not considering their trajectories. On the other hand, a longer integration time provides a higher integrated value, which improves the probability of detection for a given false alarm rate.

One possible approach for this purpose is to design filters with long impulse responses, which match the multiple pulse returns along with the selection of possible range-bearing and Doppler values [19–23]. However, the number of filters required in this approach

easily becomes impractically excessive in order to increase the integration time. An alternative approach employs a dynamic programming perspective and integrates the MF outputs along a trajectory estimated simultaneously. This approach is referred to as the track-before-detect (TBD) [24, Chp.11].

Most TBD algorithms use the modulus of the MF within models, which describe the statistics of the modulus of the MF output [25] [26]. The MF output is, however, a complex value that is a sum of the reflections and noise background. Thus, the existing TBD algorithms cannot fully exploit the complex measurements. On the other hand, the detection performance can be improved by taking into account both the phase and the modulus of the data samples [27]. In principle, coherent processing achieves the best detection performance [1]. This process requires the complex reflection coefficient estimation from the MF outputs. This is challenging because the estimation of this quantity with a reasonable accuracy requires more samples than those, which can be collected at the pulse-width sampling rate in a coherent processing interval (CPI) [4].

The degree of identifying the object-related parameters can be improved by using an array antenna structure. This antenna enables one to form a narrow beam which can improve the signal-to-noise ratio (SNR) of reflected signals from a particular region due to the attenuation of reflections from the other regions produced by the beam pattern. The angle of arrival is also found by steering the beam mechanically or electronically [2, Chp.8]. Modern radar systems often employ a phased array antenna. Each element on this antenna has an amplifier cascading to a phase shifter that can form multiple narrow beams. Thus, the phased array antenna is capable of collecting uninterrupted and simultaneous signals by electronically steering multiple beams in arbitrarily selected directions [5, Chp.8] [28].

The identifiability of the object-related parameter estimation using the phased array receiver can be further improved by using geographically separated transmitter/receiver locations. When the receiver is separately located at the transmitter, this setting provides different angles in the transmission/reception of the signals and is referred to as the bistatic configuration [29, Chp.1]. When the co-located transmitter/receiver

pair together with the separately located transmitter is used, this configuration provides the spatial diversity of angles for the transmission and reception from geographically separated transmitter/receiver locations and is referred to as the multistatic configuration. This diversity enables one to improve the degree of identifiability of the object kinematics [30] and can improve the detection performance using multiple pulse returns emitted from the separately located transmitters [29, Chp.1]. These benefits can only be practically feasible if the receiver is synchronised with the separately located transmitters. This synchronisation can be done by using a physical communication line between the transmitter and the receiver. However, in practice, there are many difficulties in connecting the physical communication line. For example, a radar transmitter is located on the top of a mountain, and the corresponding receiver is located at 500km away along a mountainous region. It would be difficult to connect the physical communication line between them due to the long-distance and harsh environmental conditions. Therefore, one needs to find a possible approach to synchronise the separately located transmitter/receiver pair without connecting the physical communication line.

The other primary focus in this thesis is on the micro-Doppler signature (or shift) estimation of slowly manoeuvring and small objects. Such objects create detection difficulties in discriminating them from radar clutter due to the limitation in resolving range-bearing and Doppler estimates [31, Chp.1]. In general, objects have propulsion components. When transmitted waveforms illuminate these components, additional frequency shifts centred at the main Doppler shift are generated [32, Chp.3]. These extra shifts are referred to as the micro-Doppler signature [33, Chp.1]. This signature contains information on the specific types of propulsion components and can help to discriminate the slowly moving objects from radar clutter [34].

The micro-Doppler signature is a time-varying value: One needs to analyse this value in both time and frequency domains. A common method for this purpose is the short-time Fourier transform (STFT) [35] [36]. This process often requires a long dwell time to collect many reflections in a CPI and is performed for a given range bin after the

detection decision is made. When the pulsed transmission is used for illumination, the collection of the reflected signals in a CPI is, however, insufficient in order to provide the desired frequency resolution.

1.1.1 Objectives

This thesis mainly considers the aforementioned two difficulties and aims to develop efficient algorithms, which can detect/classify manoeuvring and small objects by incorporating the long time pulse integration and the micro-Doppler estimation in different radar configurations. In order to achieve this aim, the following objectives are considered:

1. Investigate existing TBD algorithms in different radar configurations such as the monostatic radar, the bistatic radar, and the multistatic radar.
2. Develop TBD algorithms that can perform the coherent integration in order to detect manoeuvring and small objects in all the different radar configurations where the receiver is not synchronised with the separately located transmitters.
3. Investigate existing micro-Doppler estimation algorithms for a low SNR object in the monostatic radar system.
4. Develop a joint object detection and micro-Doppler estimation algorithm for manoeuvring and small objects.

1.2 Assumptions

A radar system considered in this thesis is a ground-based security surveillance system for small aircraft detection, where multiple transmitters and a single receiver are located at different regions on the ground and observe small aircraft in the sky. Regarding this system, the following assumptions are made:

1. Small aircraft are assumed to be small rotary-wing unmanned aerial vehicles, and their body size is less than the size of a range-bearing resolution obtained by the radar system.
2. Radar clutters are not specified because all objects in the sky are not stationary and considered detectable objects.
3. Multipath interference at the receiver is not considered because the level of reflections along the radar line of sight, discussed in this thesis, is much less than that of the receiver noise.
4. Jammers are not considered in the signal model.
5. Receiver noise is modelled with a circular symmetry complex Gaussian random vector, and noise samples are statistically independent.
6. The receiver is assumed not to be synchronised with the separately located transmitters.
7. The radar system uses phased array antennas whose calibration is assumed to be completed.
8. Electromagnetic field of reflected waves is assumed to be the far field.

1.3 Contributions

This thesis contains a series of contributions that can improve the detection performance and the object-related parameter estimation of manoeuvring and small objects in high noise background. There are two main contributions highlighted in this thesis.

The first contribution is on detecting manoeuvring and small objects with phased array radars in the monostatic setting, the bistatic setting, and the multistatic radar

configuration. In all these configurations, a reliable detection scheme is proposed. This scheme can coherently integrate reflected signals within a CPI and continue the integration for an arbitrarily long time across consecutive CPIs. Unlike existing TBD algorithms, the proposed scheme is evaluated by taking a long-time likelihood ratio conditioned on a trajectory, reflection coefficients, and synchronisation terms. For finding the kinematic quantities, a Markov state-space model is used together with the Bayesian recursive filtering. The reflection coefficients are estimated by using an expectation-maximisation (EM) algorithm within the Bayesian filtering recursions. Compounded with these computations is the estimation of unknown time-reference shifts of the separated transmitters, which is necessary for coherent processing. The object detection is made by using the resulting integration value in a Neyman-Pearson test against a constant false alarm rate threshold. Parts of this work have been published.

The second work employs the coherent track-before-detect scheme in the first work and extends the micro-Doppler signature estimation for object identification/classification. This work is on the micro-Doppler signature estimation of small rotary-wing aircraft in a co-located transmitter/uniform planar array (UPA) receiver. The micro-Doppler signature of such aircraft is considered a rotation frequency of rotor blades. In this scenario, a joint object detection/micro-Doppler estimation algorithm is proposed: This algorithm can estimate both the rotation frequency of the rotor blades and the reflection coefficients of the fuselage while simultaneously tracking the aircraft. In particular, the proposed estimation scheme uses a maximum likelihood (ML) approach that finds the rotation frequency to maximise a likelihood function. In order to evaluate this ML, a joint Bayesian recursive filtering/EM approach is proposed. The estimation scheme of this work has been published, and the joint detection and estimation scheme has been published for IET Radar, Sonar and Navigation.

All the publications related to this thesis are listed in Appendix B.

1.4 Thesis outline

The rest of this thesis is organised as follows:

Chapter 2 provides the background materials which are related to the object detection and the micro-Doppler estimation with radars. It will start by introducing a brief overview of radar configurations with their advantages and disadvantages. Then, conventional processing for detection will be introduced. Next, it will present a brief introduction to time-frequency analysis methods for micro-Doppler signatures. The following section will introduce pulse integration. Finally, the concept of track-before-detect algorithms and the recent advanced in this topic will be present.

Chapter 3 is the first technical chapter that introduces the first contribution. This chapter will start by introducing a problem scenario using mathematical statements. Then, the trajectory estimation using Bayesian recursive filtering will be introduced. The next will explain the ML estimators for both the complex reflection coefficients and the synchronisation terms. Finally, the proposed detector's efficacy will be demonstrated compared to a clairvoyant detector and other schemes.

Chapter 4 is the second technical chapter that provides the second contribution. First, it will present a problem scenario with a UPA receiver and detail mathematical expressions of reflected signals from small rotary-wing aircraft. The following section will explain the trajectory estimation using Bayesian recursive filtering. Next, the proposed EM algorithm for both the complex reflection coefficient estimation and the micro-Doppler signature estimation will be introduced. Finally, the efficacy of the proposed scheme will be demonstrated compared to that of other methods.

Chapter 5 summarises the proposed approaches presented in this thesis and provides possible directions for future work.

Chapter 2

Background

2.1 Introduction

Active sensing systems with geographically distributed transmitter/receiver components promise the detection and localisation performance higher than the use of a single transmitter/receiver pair [37–41]. Such systems provide the diversity of aspect angles in which the reflections from an object are observed [42]. This diversity gives benefits to the object detection and its kinematic estimation, such as the location and the velocity. A brief overview of radar configurations and their advantages will be described in Section 2.2.

The object detection with radars involves testing the hypothesis that the received signal contains the reflected versions of transmitted waveforms from objects against the noise only hypothesis [1, Chp.4]. These reflections are characterised by the object reflectivity, the kinematic quantities, and the other relevant physical features. In conventional processing, the detection test is evaluated by a fixed set of these object-related parameter values [1, Chp.6]. This processing chain for the detection will be shown in Section 2.3.

Slowly moving objects create detection difficulties in discriminating them from radar clutters due to limitations in resolving their object-related parameters, such as range, bearing and velocity [31, Chp.1]. Such object’s reflections contain micro-Doppler signatures (or shifts) generated by their propulsion devices, such as rotating rotor

blades or jet engines. These shifts, hence, can provide information on a specific type of propulsion devices on the object [33, Chp.1]. Section 2.4 will provide a brief introduction to the estimation of micro-Doppler shifts.

For manoeuvring and small objects in high noise background, the detection is challenging because such objects generate low reflectivity, which induces low signal to noise ratio (SNR) reflections in radar measurements. In order to achieve a plausible detection performance, one needs to consider the sufficient statistics of multiple pulse returns. This sufficient statistics is found by summing the associated reflections across themselves, which is referred to as the pulse integration [1, Chp.8]. Section 2.5 will introduce the integration methods.

Conventional integration methods for detecting manoeuvring and small objects often fail to collect evidence on the object that exists within a coherent processing interval due to not taking into account their manoeuvres. In order to overcome this challenge, one approach has proposed a joint tracking and detection algorithm, which is referred to as the track-before-detect (TBD) approach [14, 43], [44, Chp.8]. Section 2.6 will introduce a brief overview of TBD along with the recent advances in this topic, and the summary of this chapter is given in Section 2.7.

2.2 Radar fundamentals

Regarding active sensing systems, a radar consists of a transmitter connected to a transmitting antenna for propagating modulated pulses separated by a PRI towards a surveillance region and a receiver connected to a receiving antenna for collecting reflected versions of the transmitted waveforms from objects in this region. Figure 2.1 illustrates the block diagram of a conventional pulsed monostatic radar system. Here, the black arrowheads indicate the signal flow between consecutive blocks. The system components are as follows:

1. Waveform generator: This component generates the desired waveform, such as a

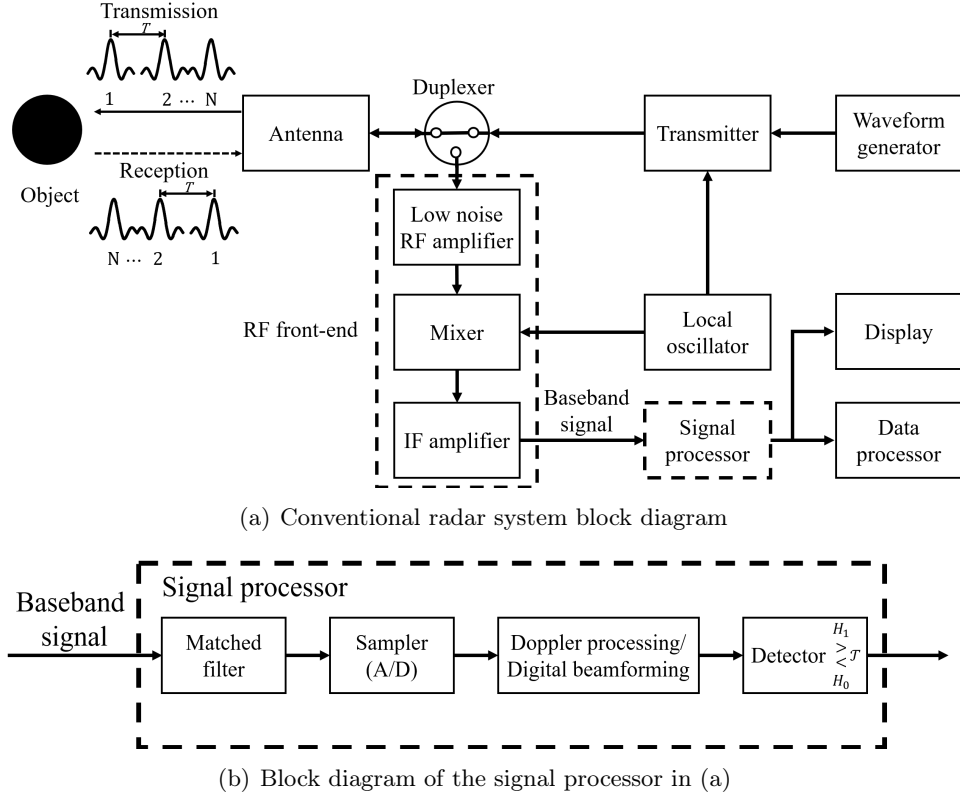


Figure 2.1: Block diagram of a conventional pulsed monostatic radar (reproduced from Figure 1.2. in [1, Chp.1]): (a) Overall system block diagram. (b) Block diagram of the signal processor in (a).

monotone waveform, a linear frequency modulated (LFM) waveform, or a phase modulated (PM) waveform.

2. **Transmitter:** This component can be a power amplifier in which the outputs of the waveform generator are further modulated with a carrier frequency supplied from a local oscillator (LO).
3. **Duplexer:** This component acts as a transmission/reception switch that the antenna is connected to the transmitter during the transmission and disconnected to the radio frequency (RF) front-end (depicted by the dashed rectangular box). For the reception, the antenna is connected to the RF front-end and disconnected to the transmitter.
4. **Antenna:** This component is the interface between the transmitter's outputs and the atmosphere by forming a radiation pattern (i.e., the beam-pattern). There

are many different types of antennas used in radar systems. For example, the common types are parabolic reflector antennas, horn antennas, and phased array antennas [2, Chp.8].

5. Low noise RF amplifier: This component is the first stage in the RF front-end and amplifies a low power signal which contains reflections (depicted by the dashed line) without significantly degrading the signal-to-noise ratio (SNR).
6. Mixer: This component creates an intermediate frequency (IF) signal by mixing (i.e., addition and subtraction) the reflected signal with the carrier frequency supplied from the LO.
7. IF amplifier: This component is the last stage in the front-end, and its output is the baseband signal obtained by amplifying the output of a low-pass filter cascading to an IF band-pass filter that filters out the mixer output [45, Chp.11].
8. Signal processor: The purpose of this component is to reject undesired signals in the front-end output and to find the object kinematics by using pulse matched filtering for finding the range, Doppler processing for estimating the velocity, and spatial filtering for finding the angle of arrival. Compounded with these computations is deciding on the presence of objects or the absence (i.e., H_1 or H_0 , respectively) using statistical models. This processing chain for the object detection is illustrated in Figure 2.1(b) and will be detailed in Section 2.3.
9. Data processor: This processing unit performs tracking, classification, and recognition of the detected objects after the object detection is made.
10. Display: This stage displays information on the detected objects and their kinematics using a graphical user interface (GUI) to radar operators.

Table 2.1 shows the summary of airport surveillance radar (ASR) technical characteristics as an example of typical radar system parameters. Here, the ASR-8,-9,

Table 2.1: Summary of airport surveillance radar (ASR) technical characteristics (reproduced from Table C-1 in [11])

Parameter	Units	ASR-8 Value	ASR-9 Value	ASR-11 Value
Detection range	km	110	110	110
Peak transmitter power	kW	1×10^3	1.32×10^3	25
Operating-frequency range	MHz	2700 to 2900	2700 to 2900	2700 to 2900
Antenna type		Parabolic reflector	Parabolic reflector	Parabolic reflector
Antenna gain	dBi	34	34	34
Antenna beam width (horizontal)	°	2.3	2.3	2.3
Antenna beam width (vertical)	°	0.3 to 30	0.3 to 30	0.3 to 30
Antenna beam-scanning rate	rpm	12.5	12.5	12.5
Transmitted pulse width	us	0.6	1.05	89
Transmitted pulse modulation		Monotone	Monotone	LFM
Transmitted pulse repetition frequency (PRF)	Hz	1014	1156	865
Local oscillator frequency	MHz	2800	2800	2800
LNA gain	dB	10	10	10
IF range	MHz	2.6 to 3.9	3.1 to 3.8	3.3 to 4.4
IF 3dB bandwidth	MHz	1.3	0.7	1.1

and -11 are the airport surveillance radar systems used in the United States and select low PRF values due to the long unambiguous range ($\leq 110\text{km}$) for the detection [46]. As explained in Chapter 1.1, the selection of PRFs is an essential factor to provide the unambiguous range/velocity and is a trade-off between the unambiguous range and the unambiguous velocity. Table 2.2 shows unambiguous ranges and unambiguous velocities obtained by the typical values of high, medium, and low PRFs.

Another important factor for the radar operation is the dwell time. This term is defined as the data acquisition interval in which the collection of reflected signals from a surveillance region is processed for the detection [47]. For example, the ASR-8,

Table 2.2: Representative values and characteristics of high, medium, and low PRFs (reproduced from Table 5.9-1 in [5])

Parameter	Units	High PRF	Medium PRF	Low PRF
PRF	kHz	100 to 300	5 to 30	0.5 to 2
Unambiguous range	km	0.5 to 1.5	5 to 30	75 to 300
Unambiguous velocity	m/s	750 to 2250	37.5 to 225	3.75 to 15

-9, and -11 in Table 2.1 employ mechanically rotating antennas, which produce the limited dwell time due to the mechanical beam-scanning rate when the transmitted waveforms illuminate an object within a processing interval. They, hence, might fail to collect sufficient measurements to be processed for the estimation of object-related parameters accurately. A uniform linear array (ULA) receiver, on the other hand, can collect uninterrupted measurements from all directions simultaneously and then filter out signals from selected directions by the digital beam-forming [48, Chp.2]. This receiver structure, therefore, improves the estimation performance of the object-related parameters with better accuracy. This accuracy can be further improved by using separately located transmitter/receiver pairs in exploiting the diversity of aspect angles in which the objects are illuminated, and the reflections are observed [42].

Figure 2.2 illustrates the geometry of different radar configurations with the ULA receiver (depicted by the red dots). Here, $\mathbf{X} = [x, y, \dot{x}, \dot{y}]^T$ in the two-dimensional (2D) Cartesian plane denotes the object kinematic state (depicted by the black dot), where $[x, y]^T$ is the location with the velocity, $[\dot{x}, \dot{y}]^T$, and T denotes the vector transpose. As briefly explained in Chapter 1.1, there are mainly three different configurations, which are the monostatic setting (depicted by the red triangle and the red dots in Figure 2.2(a)), the bistatic configuration (depicted by the blue triangle and the red dots in Figure 2.2(b)), and the multistatic setting (illustrated in Figure 2.2(c)), respectively. Here, the propagated waveforms travel from the transmitter to the object and, upon echo, back to the receiver. This path is referred to as the channel (or the medium). The channel used in this thesis is assumed to be free space. One important property of the free space is that the electromagnetic waves travel at the speed of light defined by a constant $c \approx 3 \times 10^8$ m/s. Another is that the superposition principle (i.e.,

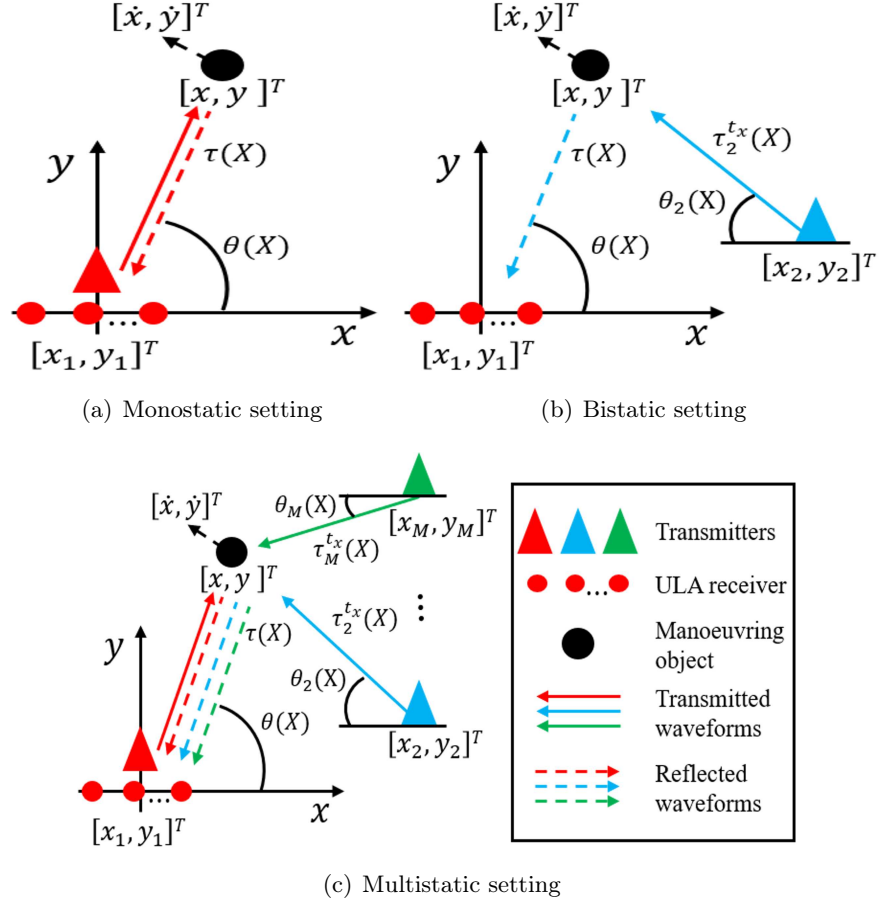


Figure 2.2: The geometry of radar configurations: An object (black dot) is located at $[x, y]^T$ with velocity $[\dot{x}, \dot{y}]^T$. (a) The geometry of the monostatic configuration formed by a co-located transmitter/receiver pair. (b) The bistatic configuration formed by a separated transmitter/receiver pair. (c) The multistatic configuration combined by both the monostatic and the bistatic with M separately located transmitters.

additivity and homogeneity) is always true. The other properties are detailed in [49, Chp.2].

Regarding the free space (or vacuum), it contains no air and atmospheric pressure. The propagation speed (or the wave speed) equals the speed of light, which is obtained by the electric permittivity, ϵ_0 , and the magnetic permeability, μ_0 , of the free space [49, Chp.2]:

$$\begin{aligned}
 c &= \frac{1}{\sqrt{\epsilon_0 \mu_0}} \\
 &= 2.9979245 \times 10^8 \\
 &\approx 3 \times 10^8 \text{ m/s}.
 \end{aligned} \tag{2.1}$$

A specific medium has its relative electric permittivity, ε_r , and its relative magnetic permeability, μ_r . The propagation speed in a specific medium is found by the ratio of the speed of light in a vacuum to the product of ε_r and μ_r :

$$v = \frac{c}{\sqrt{\varepsilon_r \mu_r}}, \quad (2.2)$$

where v denotes the propagation speed in a specific medium. For example, when a wave propagates through water, the wave speed is found by using (2.2) and is $2.249 \times 10^8 \text{m/s}$. This speed is slower than the speed of light in a vacuum. Furthermore, the ratio of the speed of light in a vacuum to its speed in a specific medium is often referred to as the refractive index [49, Chp.3]:

$$n = \frac{c}{v}, \quad (2.3)$$

where n denotes the refractive index. The refractive index of the free space is 1, and that of other mediums can be calculated by (2.3). The refractive index also indicates that a higher index value gives a slower propagation speed compared to its speed in the free space.

In practice, the channel is Earth's atmosphere, which contains air and other gases with atmospheric pressure. This atmosphere consists of layers, each of which has its own properties, such as composition, temperature and pressure. These components differ in relative electric permittivity and relative magnetic permeability [49, Chp.4]. In this thesis, it is assumed that the radar system is located on the ground and observes objects up to the troposphere, which contains 78.08% of air. The refraction index of air is $n = 1.0000027$, which is very close to that of the free space. In other words, the propagation speed in air approximates the speed of light in the free sapce [49, Chp.3]. Thus, the propagation speed in this thesis is assumed to be the speed of light in the free space. Also the free space properties hold in the rest of thesis. On the basis of the free space properties, the characteristics of reflected signals through the channel in all the different configurations in Figure 2.2 will be explored in the next section. Furthermore, regarding a signal model at a receiver, the signal model is based on the two dimantional

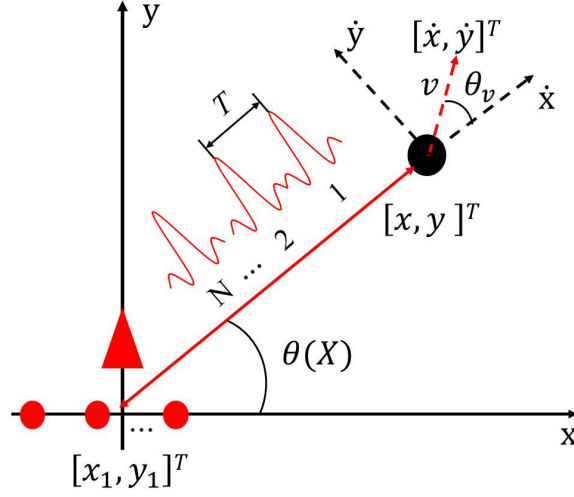


Figure 2.3: Geometry of a co-located transmitter/receiver pair and a single object in the monostatic channel

(2D) Cartesian coordinates and aims to provide the basic concept of reflected signals to be understood. More complicated models will be discussed in Chapter 3 and 4.

2.2.1 Monostatic configuration

In the monostatic channel, Figure 2.3 shows the geometry of the co-located transmitter/receiver pair and a single object. Here, the distance from the object kinematic state, \mathbf{X} , to the receiver at $[x_1, y_1]$ is the same as that from the co-located transmitter to \mathbf{X} . Let one denote this distance by $R(\mathbf{X})$. Because the transmitted waveform travels at the speed of light, c , this quantity is found as

$$R(\mathbf{X}) \triangleq \sqrt{(x_1 - x)^2 + (y_1 - y)^2} \quad (2.4)$$

$$\tau(\mathbf{X}) = 2 \times \frac{R(\mathbf{X})}{c} \quad (2.5)$$

where $\tau(\mathbf{X})$ is the time of flight for the reflected signals in the monostatic channel and the factor, 2, is used due to the two-way propagation.

Regarding the distance (or range), it can calculate the received power of the reflected signals at the receiver by using the radar range equation [50, Chp.2]. Let one denote this power by P_r . Also, consider the transmitted power denoted by P_t and the gain

denoted by G_t . The received power at the RF front-end, hence, can be found as

$$\begin{aligned} P_r &= \frac{\lambda_c^2}{(4\pi)^3} \times \frac{P_t G_t}{R^2(\mathbf{X})} \times \frac{G_r L_s}{R^2(\mathbf{X})} \times \sigma_t \\ &= \lambda_c^2 \times \frac{P_t G_t G_r L_s}{(4\pi)^3 R^4(\mathbf{X})} \times \sigma_t, \end{aligned} \quad (2.6)$$

where

- G_r denotes the receiver gain.
- L_s denotes the system loss.
- σ_t denotes the object's radar cross section (RCS) which is related to the object reflectivity.
- $\lambda_c = \frac{c}{f_c}$ is the carrier wavelength of the carrier frequency, f_c .
- $R(\mathbf{X})$ is the range of the object state, \mathbf{X} , to the receiver given in (2.4).

Here, (2.6) contains the product of the transmitted gain and the receiver gain, each of which is inversely proportional to $R(\mathbf{X})^2$ due to the two-way propagation. The received power is hence inversely proportional to $R(\mathbf{X})^4$. For the signal to noise ratio (SNR) at the receiver, the front-end signal is the superposition of all reflections from objects and noise background. In practice, the noise is random and can be characterised by its power spectral density (PSD) function in the radar operating bandwidth. Let one assume that the noise is white Gaussian thermal noise with its power, σ^2 . Now, the SNR of the reflected signals from the object state, \mathbf{X} , at the receiver can be found by dividing both sides of (2.6) with the noise power:

$$\begin{aligned} \text{SNR} &\triangleq \frac{P_r}{\sigma^2} \\ &= \lambda_c^2 \times \frac{P_t G_t G_r L_s}{(4\pi)^3 R^4(\mathbf{X})} \times \frac{\sigma_t}{\sigma^2}. \end{aligned} \quad (2.7)$$

For the detection of manoeuvring objects using radars, the object velocity is an important indicator, which can discriminate moving objects from the background, such

as trees and buildings. A moving object when illuminated by the pulse train generates an angular frequency shift in the consecutively reflected pulses (see, Figure 2.3). This is referred to as the angular Doppler shift. This quantity with the object velocity $[\dot{x}, \dot{y}]$ in the 2D Cartesian coordinates when the object recedes from the receiver can be found in [51] [52] [53]:

$$\begin{aligned}
\Omega(\mathbf{X}) &= -\frac{2\pi T}{\lambda_c} \{ \dot{x} \times (\cos \theta(\mathbf{X}) + \cos \theta(\mathbf{X})) + \dot{y} \times (\sin \theta(\mathbf{X}) + \sin \theta(\mathbf{X})) \} \quad (2.8) \\
&= -\frac{4\pi T}{\lambda_c} (\dot{x} \cos \theta(\mathbf{X}) + \dot{y} \sin \theta(\mathbf{X})) \\
&= -\frac{4\pi T}{\lambda_c} (v \cos \theta_v \cos \theta(\mathbf{X}) + v \sin \theta_v \sin \theta(\mathbf{X})) \\
&= -\frac{4\pi T}{\lambda_c} v \cos (\theta_v - \theta(\mathbf{X})), \\
v &= \sqrt{\dot{x}^2 + \dot{y}^2}, \quad \theta_v = \arctan \left(\frac{\dot{y}}{\dot{x}} \right)
\end{aligned}$$

where T denotes the PRI, and $\theta(\mathbf{X})$ denotes the angle of arrival (AoA) of the reflections from the object state, \mathbf{X} , to the receiver. This quantity is given by

$$\theta(\mathbf{X}) = \arctan \left(\frac{y_1 - y}{x_1 - x} \right), \quad (2.9)$$

where the geometry of all these variables in (2.8) and (2.9) is illustrated in Figure 2.3.

Note that the angular Doppler shift, $\Omega(\mathbf{X})$, in (2.8) varies with the object velocity and the angle of arrival. One provides its maximum value when an object travels along the line of sight (i.e., $\theta_v = 0^\circ$ and $\theta(\mathbf{X}) = 0^\circ$), whereas this value becomes zero when the object moves horizontally with respect to the receiver (i.e., $\theta_v = 90^\circ$ and $\theta(\mathbf{X}) = 0^\circ$). As a result, the monostatic system's major disadvantage is that this system cannot measure the object velocity when moving horizontally with respect to the receiver. This is illustrated in Figure 2.4.

In conventional detection processing chains, the decision on the object's presence is often made after Doppler processing. In this processing, there are mainly two methods used [1, Chp.5]: One is the notch filter that filters out signals which contain zero Doppler frequencies from the stationary background. The other uses the spectral analysis of received signals and considers non-zero Doppler frequencies in the frequency domain.

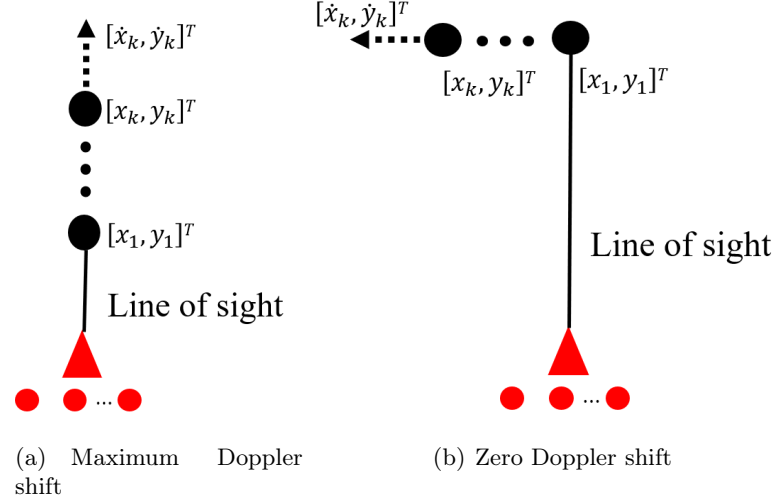


Figure 2.4: Doppler effect of a moving object with the ULA receiver: (a) Maximum Doppler shift measurement at the ULA receiver (red dots). (b) Zero Doppler shift measurement at the ULA receiver. An object (black dot) at an initial location $[x_1, y_1]^T$ moves to $[x_k, y_k]^T$ with velocity $[\dot{x}_k, \dot{y}_k]^T$. The line of sight with respect to the receiver is depicted by the solid black line.

However, when an object moves horizontally with respect to the receiver, its Doppler frequency is close to zero, and this object might be considered the stationary background. Therefore, the conventional detectors using the monostatic channel are likely to fail in detecting it.

2.2.2 Bistatic and multistatic configurations

Let this section consider the characteristics of reflected signals in the bistatic/multistatic channels. The bistatic system is comprised of a separately located transmitter/receiver pair. Unlike this system, the multistatic system consists of M transmitters and one receiver. One of these transmitters is co-located with the receiver, and the others are separately located from the receiver (see, Figure 2.2(c)). Figure 2.5 shows an example of the multistatic channel with one co-located transmitter/receiver pair and the m th separately located transmitter. This configuration involves both the monostatic (see, red dashed box) channel and the bistatic (see, green dashed box) channel. In order to avoid repetitions, this section only focuses on the multistatic channel.

The monostatic channel has the same distance from the transmitter to an object and it to the receiver, whereas the distance in the bistatic channel is different: The distance

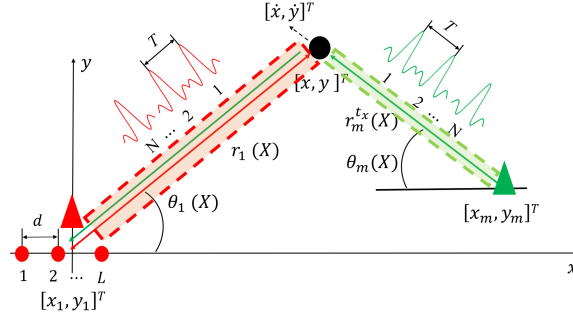


Figure 2.5: Geometry of a moving object with the multistatic channel

of the object state, \mathbf{X} , to the receiver differs from that of \mathbf{X} to the separately located transmitters. Let one denote the distance of the object state, \mathbf{X} , to the m th transmitter by $R_m^{tx}(\mathbf{X})$ for $m = 1, \dots, M$, where, $m = 1$ indicates the distance in the monostatic channel (see, Figure 2.5). This quantity for the m th channel is hence given by

$$R_m^{tx}(\mathbf{X}) \triangleq \sqrt{(x_m - x)^2 + (y_m - y)^2}, \quad m = 1, \dots, M, \quad (2.10)$$

and the distance of \mathbf{X} to the receiver is denoted by $R(\mathbf{X})$. This quantity is given in (2.4). The corresponding pulse time of flight in the m th channel is hence found as

$$\begin{aligned} \tau_m(\mathbf{X}) &= \tau_m^{tx}(\mathbf{X}) + \tau^{rx}(\mathbf{X}), \quad m = 1, \dots, M, \\ \tau_m^{tx}(\mathbf{X}) &= \frac{R_m^{tx}(\mathbf{X})}{c}, \\ \tau^{rx}(\mathbf{X}) &= \frac{R(\mathbf{X})}{c}, \end{aligned} \quad (2.11)$$

where $m > 1$ indicates the bistatic channels.

In the multistatic channel, the front-end signal is the superposition of all reflections from M different channels. Its received power is hence found as

$$P_r = \sum_{m=1}^M \frac{P_t^{(m)} G_t^{(m)} G_r L_s \sigma_t^{(m)} \lambda_c^2}{(4\pi)^3 R_m^{tx}(\mathbf{X})^2 R(\mathbf{X})^2}. \quad (2.12)$$

where $P_t^{(m)}$, $G_t^{(m)}$, and $\sigma_t^{(m)}$ denote the transmitted power, the transmitter gain, and the object's RCS, respectively, at the m th transmitter. As a result, the SNR of the

front-end signal in the multistatic channel is found as

$$\begin{aligned}\text{SNR} &= \frac{P_r}{\sigma^2} \\ &= \sum_{m=1}^M \frac{P_t^{(m)} G_t^{(m)} G_r L_s \sigma_t^{(m)} \lambda_c^2}{(4\pi)^3 R_m^{t_x^2}(\mathbf{X}) R^2(\mathbf{X})} \times \frac{1}{\sigma^2},\end{aligned}\quad (2.13)$$

where the SNR indicates a sum of M channels and is inversely proportional to $R_m^{t_x^2}(\mathbf{X}) R^2(\mathbf{X})$.

For velocity measurements in the multistatic channel, the angular Doppler shift of the object state, \mathbf{X} , in the m th channel for $m = 1, \dots, M$ when \mathbf{X} recedes from the receiver is found by using (2.8) with the bearing angle of the object to the m th transmitter. This quantity is given in [38] [51] [52] [53]:

$$\Omega_m(\mathbf{X}) = -\frac{2\pi T}{\lambda_c} \{ \dot{x} \times (\cos \theta_m(\mathbf{X}) + \cos \theta(\mathbf{X})) + \dot{y} \times (\sin \theta_m(\mathbf{X}) + \sin \theta(\mathbf{X})) \}, \quad (2.14)$$

where $\theta(\mathbf{X})$ is the AoA in (2.9), and $\theta_m(\mathbf{X})$ denotes the bearing angle of the object state, \mathbf{X} , to the m th transmitter. This quantity is given by

$$\theta_m(\mathbf{X}) = \arctan \left(\frac{y_m - y}{x_m - x} \right). \quad (2.15)$$

Note that the angular Doppler shift, $\Omega_m(\mathbf{X})$, in (2.14) varies with the AoA, $\theta(\mathbf{X})$, and the bearing angle, $\theta_m(\mathbf{X})$. For $m = 1$, $\theta_1(\mathbf{X})$ equals to $\theta(\mathbf{X})$ (i.e., $\theta_1(\mathbf{X}) = \theta(\mathbf{X})$) due to the co-located transmitter/receiver pair. $\Omega_1(\mathbf{X})$ also yields the same angular Doppler shift, $\Omega(\mathbf{X})$, in (2.8). When $m > 1$, $\Omega_m(\mathbf{X})$ differs from $\Omega(\mathbf{X})$ because $\theta_m(\mathbf{X})$ is not the same value of $\theta(\mathbf{X})$. This leads to an advantage in the velocity measurement compared to that in the monostatic channel. For example, when an object moves horizontally with respect to the receiver, the multistatic configuration enable one to find the object velocity, which cannot be found using the monostatic channel alone (see, Figure 2.4). Another advantage of the multistatic channel is that the SNR for the multistatic configuration provides a sum of M SNRs with $m = 1$ indexing monostatic channel and $m > 1$ accounting for the bistatic channels. These highly desired features can only be practically feasible if the receiver is synchronised with the separately located transmitters.

The synchronisation of the separately located transmitter/receiver pairs involves finding the differences between the receiver time reference and that of the transmitters so as to accurately map the receiver time axis onto spatial locations [29]. For example, if the time reference shift of the transmitters with respect to the receiver is known precisely, these values can be further mapped to precise spatial (bistatic) range values [29]. The ambiguity of these quantities significantly deteriorates the system performance [54]. A typical approach to estimate the transmitters' time reference shift is to use atomic clocks and/or external references, such as global positioning system (GPS) signals [55]. Such a process is tedious and requires expensive pieces of equipment to measure external references precisely. Also, this is prone to errors due to inaccuracy in locating transmitter and receiver elements [29]. A data-driven solution consisting of processing at the receiver side is preferable. Chapter 3 will consider this problem in a scenario where the ULA receiver is not synchronised with separately located transmitters, and it will introduce local processing for the estimation of a time reference shift of each transmitter using a digital beam-forming technique at the receiver side.

This section has introduced the basic elements of a radar system and discussed the advantages and disadvantages of the monostatic, bistatic, and multistatic configurations. The next section will introduce an overview of conventional detection processing chains using phased array radar receivers.

2.3 Conventional object detection in array receivers

The object detection using radars involves testing the hypothesis that the received signal contains reflections from objects against the noise only hypothesis. This test uses sampled outputs of a matched filter (MF), which filters out the front-end input with an impulse response that matches the probing waveform [1, Chp.4].

In conventional processing chains, the aforementioned test is evaluated by using a pre-specified set of kinematic parameters corresponding to the sample timings of the MF stage. In effect, these samples correspond to equally separated range values that

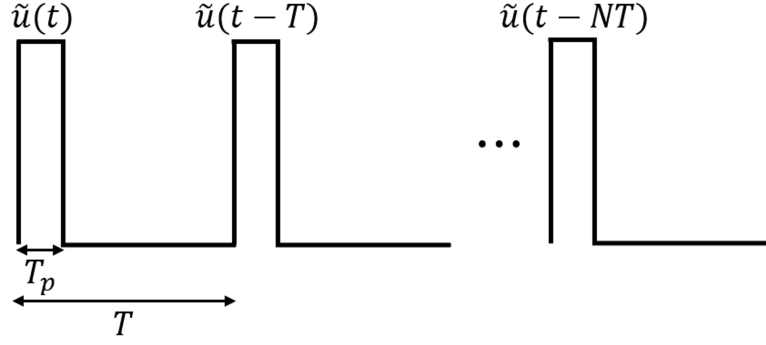


Figure 2.6: Example of a pulse train (reproduced from Figure 3-1 in [2, Chp.3]): N consecutive waveforms are separated by a time interval T . The pulse waveform, $\tilde{u}(t)$, for the transmission uses a pulse duration T_p .

partition the range space into equally divided bins. These samples are further used with conventional beam-forming and Doppler processing. These correspond to segmenting the bearing and Doppler space into resolution bins. The decision on the object's presence in each bin is made by using the hypothesis testing the corresponding processed data sample, which involves testing a likelihood ratio against a detection threshold.

The problem scenario in this section is illustrated in Figure 2.3, where the co-located transmitter(see, red triangle)/receiver(see, the red dots) pair is located in the origin of the 2D Cartesian coordinates. This transmitter emits N consecutive pulse waveforms, $\tilde{u}(t)$, separated by the PRI, T , towards a surveillance region after modulating with a common carrier that has an angular frequency of $\omega_c = 2\pi f_c$. This is given by

$$u(t) = \text{Re}\left\{ \sum_{n=0}^{N-1} \tilde{u}(t - nT) e^{j\omega_c t} \right\}, \quad (2.16)$$

where $\text{Re}\{\cdot\}$ denotes the real part of its input complex argument, and n for $n = 0, \dots, N-1$ indicates the n th pulse waveform. This waveform for the transmission uses its pulse duration denoted by T_p with its bandwidth denoted by B_w . This is illustrated in Figure 2.6.

In the surveillance region, a single object at the kinematic state, \mathbf{X} , is illuminated by the transmitted waveforms defined in (2.16). The receiver co-located with the transmitter utilises the ULA antenna, which has L elements spaced by half of the carrier wavelength. Each array element collects the reflected signals, each of which is the superposition of the reflections from an object and noise background. The object reflectivity is assumed to

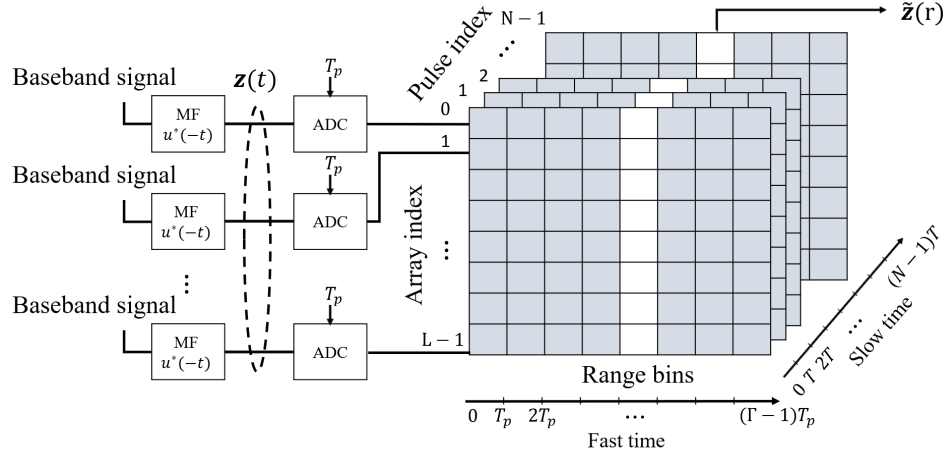


Figure 2.7: Data acquisition from a ULA array receiver: The input of the pulse MF stage is the baseband signal from the front-end. The MF output is sampled by using the pulse width T_p and arranged in array index, fast time and slow time axes, respectively.

remain coherent (i.e., unchanged) during the collection of N pulses. This time interval is known as the coherent processing interval (CPI).

Let one detail the reflected signals from \mathbf{X} . For narrowband, the reflections collected at the array elements are characterised by a spatial steering vector as a function of θ [48, Chp.2]:

$$\mathbf{s}_s(\theta) = \left[1, e^{-j\omega_c \frac{d}{c} \sin \theta}, \dots, e^{-j\omega_c (L-1) \frac{d}{c} \sin \theta} \right]^T, \quad (2.17)$$

where $d = \lambda_c/2$ is the separation between the array elements selected as half of the carrier wavelength. Substituting this quantity together with $c = \lambda_c \times f_c$ in (2.17) leads to

$$\mathbf{s}_s(\theta) = \left[1, e^{-j\pi \sin \theta}, \dots, e^{-j(L-1)\pi \sin \theta} \right]^T, \quad (2.18)$$

where $\mathbf{s}_s \in \mathbb{C}^{L \times 1}$ is an $L \times 1$ vector.

The superposition of N reflections after demodulation at the receiver together with (2.18) when the single object is in the surveillance region is found as

$$\mathbf{z}(t) = \mathbf{s}_s(\theta(\mathbf{X})) \sum_{n=0}^{N-1} \alpha e^{jn\Omega(\mathbf{X})} e^{-j\omega_c \tau(\mathbf{X})} \times \tilde{u}(t - \tau(\mathbf{X}) - nT), \quad (2.19)$$

where α is a complex coefficient modelling the reflectivity. Here, $\theta(\mathbf{X})$ is the AoA given in (2.9). $\tau(\mathbf{X})$ and $\Omega(\mathbf{X})$ are the time of flight given in (2.5) and the Doppler shift given in (2.8), respectively.

The reflections in the received signal are searched by convolving the input with inverted versions of the probing waveforms. This filtering is referred to as the matched filtering (MF) [13]. For the array processing, each of L array elements cascades to each of L matched filters. The outputs of the MFs for the array elements are then sampled with a period that is equal to the pulse duration of T_p . This is found as

$$\begin{aligned}\tilde{\mathbf{z}}(t) &\triangleq \mathbf{z}(t) * \tilde{u}(-t) \\ &= \alpha \mathbf{s}_s(\theta(\mathbf{X})) \sum_{n=0}^{N-1} e^{jn\Omega(\mathbf{X})} e^{-j\omega_c\tau(\mathbf{X})} \times \Lambda(t - \tau(\mathbf{X}) - nT).\end{aligned}\quad (2.20)$$

where $*$ denotes convolution and $\Lambda(\cdot)$ is the auto-correlation of the waveform given by

$$\Lambda(t) = \int_0^{T_p} \tilde{u}(t') \tilde{u}^*(t' - t) dt'. \quad (2.21)$$

Now, these samples uniformly divide the PRI of T into Γ samples with T_p interval (i.e., $T = \Gamma \times T_p$), where $\Gamma \in \mathbb{Z}^+$ is the positive integer number. $\Gamma \times N$ samples of this discrete-time vector sequence is given by

$$\tilde{\mathbf{z}}(\gamma T_p) = [\tilde{\mathbf{z}}_0(\gamma T_p), \tilde{\mathbf{z}}_1(\gamma T_p), \dots, \tilde{\mathbf{z}}_n(\gamma T_p), \dots, \tilde{\mathbf{z}}_{N-1}(\gamma T_p)], \quad \gamma = 0, \dots, \Gamma - 1, \quad (2.22)$$

and the discrete-time vector for the n th pulse when the object is located in the γ th sample is given by

$$\begin{aligned}\tilde{\mathbf{z}}_n[\gamma] &\triangleq \tilde{\mathbf{z}}_n(\gamma T_p) \\ &= \alpha e^{-j\omega_c\tau(\mathbf{X})} \times \mathbf{s}_s(\theta(\mathbf{X})) \times e^{jn\Omega(\mathbf{X})} \Lambda(\gamma T_p - \tau(\mathbf{X}) - nT),\end{aligned}\quad (2.23)$$

where the resulting output is an $L \times 1$ vector.

Next, the vector sequence in (2.22) is arranged as a cube by folding the two dimensional data array in lengths of Γ samples. The n th layer of the resulting cube corresponds to the samples collected between L array elements and Γ outputs of MF when the n th pulse is reflected:

$$\mathbf{C}_n \triangleq [\tilde{\mathbf{z}}_n[0], \tilde{\mathbf{z}}_n[1], \dots, \tilde{\mathbf{z}}_n[\Gamma - 1]],$$

and the cube that captures N reflected pulses is given by

$$\mathbf{C} = [\mathbf{C}_0, \mathbf{C}_1, \dots, \mathbf{C}_{N-1}]^T. \quad (2.24)$$

This processing chain is illustrated in Figure 2.7 together with the cube, \mathbf{C} , which is also known as the radar data cube [1]. The axes of this cube are array index, slow-time, and fast-time, respectively. The fast-time axis consists of Γ samples of the MF filter output, each of which is associated with a time delay of the reflected signal. These time delays correspond to the time of flights which can easily be converted to range (or distance) values using (2.5). The corresponding resolution is given in [2, Chp.3]:

$$\Delta R = \frac{c}{2} \times T_p, \quad (2.25)$$

$$T_p = \Delta R \times \frac{2}{c}. \quad (2.26)$$

Each range bin (or range sample) consists of L spatial samples collected from the array elements along the array index axis and N Doppler samples (or temporal samples), which indicate N pulse returns separated by the PRI of T along the slow-time axis. As a result, N measurements when the object state, \mathbf{X} , is located at the r th range bin are a slice along the slow time axis, which is given by

$$\begin{aligned} \tilde{\mathbf{Z}}(r) &\triangleq [\tilde{\mathbf{z}}_0[r], \tilde{\mathbf{z}}_1[\Gamma + r], \dots, \tilde{\mathbf{z}}_{N-1}[(N-1)\Gamma + r]] \\ &= \alpha e^{-j\omega_c \tau(\mathbf{X})} \mathbf{s}_s(\theta(\mathbf{X})) \mathbf{s}_t^T(\Omega(\mathbf{X})) \times \Lambda(rT_p - \tau(\mathbf{X})), \end{aligned} \quad (2.27)$$

and the term $\mathbf{s}_t \in \mathbb{C}^{N \times 1}$ is referred to as the temporal steering vector [56] given by

$$\mathbf{s}_t(\Omega') \triangleq [1, e^{j\Omega'}, \dots, e^{j(N-1)\Omega'}]^T. \quad (2.28)$$

Note that $\tilde{\mathbf{Z}}(r)$ in (2.27) form an $L \times N$ matrix, which is used to further map the bearing and Doppler spaces by using spatial and temporal filtering (i.e., beam-forming and Doppler processing), respectively. For this purpose, there are three different sequences to be processed [1, Chp.9] [57, Chp.3]: One first performs the Doppler processing with N temporal samples at each spatial sample, and then the beam-forming with these outputs is performed. Another is that the beam-forming with L spatial samples at each

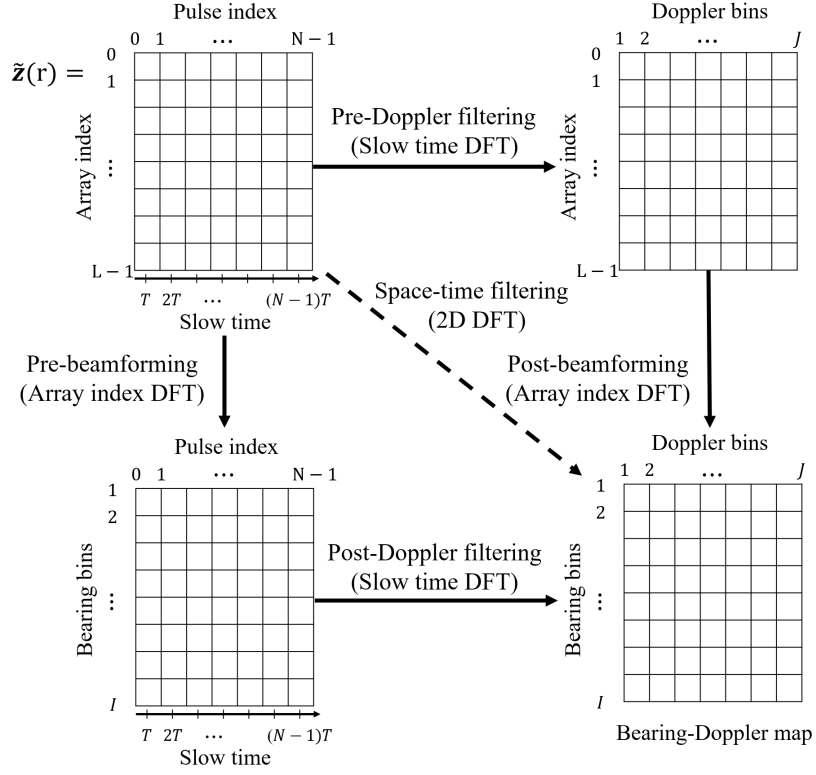


Figure 2.8: Spatial and temporal signal processing (reproduced from Figure 9.22. in [1, Chp.9]): There are three approaches for this purpose. One first performs Doppler filtering with N temporal samples, and then these outputs are further used for beam-forming (i.e., the pre-Doppler filtering and the post-beam-forming, respectively). The second performs first the beam-forming with L spatial samples and later the Doppler filtering with these outputs (i.e., the pre-beam-forming and the post-Doppler filtering, respectively). The last is space-time filtering that performs joint beam-forming and Doppler filtering with $L \times N$ samples. All these outputs produce the bearing-Doppler map that forms an $I \times J$ matrix.

temporal sample is performed, and then the Doppler processing with these outputs is processed. The other uses a space-time filter, which performs joint beam-forming and Doppler processing with $L \times N$ samples. The outputs of all these sequences correspond to the bearing-Doppler map at each range bin. These processing chains are illustrated in Figure 2.8. The remaining parts of this section will introduce the beam-forming in Section 2.3.1 and then the Doppler processing in Section 2.3.2. The conventional space-time filtering will be detailed in Section 2.3.3. Then, the object detection process will be introduced in Section 2.3.4.

2.3.1 Beam-forming

This subsection considers the digital beam-forming with L spatial samples from the array elements. The aim of this technique provides identifiability concerning AoAs of the reflected signals at the receiver [1, Chp.9]. In a sensing context, these AoAs correspond to the bearing angles of objects. Conventional beam-forming is a non-adaptive method and implemented by using a weighted sum of the array element measurements (i.e., L spatial samples) given a bearing angle [48, Chp.2]. Let one denote these weights by a vector of \mathbf{h}_s as a function of the bearing angle, θ . This quantity is given in Equation 9.5 [1, Chp.9]:

$$\mathbf{h}_s(\theta) = \mathbf{w} \odot \mathbf{s}_s^*(\theta), \quad (2.29)$$

where $\mathbf{w} \triangleq [w_0, \dots, w_{L-1}]^T$ denotes weights, $\mathbf{s}_s^* \in \mathbb{C}^{L \times 1}$ is the conjugate of the spatial steering vector in (2.18), and \odot denotes the Hadamard product operator.

The AoA of the reflected signal from the object state, \mathbf{X} , is searched by matching θ to $\theta(X)$ using (2.29) over the bearing space. This space is equally divided into I resolution bins with a interval, $\Delta\theta$. This is known as the bearing bins [48]. This interval (i.e., resolution) can be calculated by the half-power beamwidth (or 3dB beamwidth). This quantity is given in Table 2.2 [48, Chp.2] and approximates to

$$\Delta\theta \approx 2 \times \arcsin \frac{\sqrt{2} \times \lambda_c}{\pi \times L \times d}. \quad (2.30)$$

When $d = \frac{\lambda_c}{2}$, the bearing resolution in (2.30) becomes

$$\begin{aligned} \Delta\theta &\approx 2 \times \arcsin \frac{\sqrt{2} \times \lambda_c \times 2}{\pi \times L \times \lambda_c} \\ &\approx 2 \times \arcsin \frac{0.89}{L}. \end{aligned} \quad (2.31)$$

As a result, the the beam-forming response with $\tilde{\mathbf{Z}}(r)$ in (2.27) at the receiver steered to $i \times \Delta\theta$ over I bearing bins is given by

$$\mathbf{z}_s(r, i) \triangleq \mathbf{h}_s^T(i\Delta\theta) \times \tilde{\mathbf{Z}}(r), \quad i = 1, \dots, I. \quad (2.32)$$

These outputs are I bearing samples along the slow-time axis given the r th range bin.

This is illustrated in the bottom left plot in Figure 2.8. For example, when all of weights in (2.29) are equal to 1 (i.e., $\mathbf{w} = [1, \dots, 1]^T$), the measurement at the i th bearing bin and the r th range bin that contain the reflections from \mathbf{X} is found as

$$\begin{aligned} \mathbf{z}_s(r, i) = & \frac{\sin\{L\frac{\pi}{2}(\sin(i\Delta\theta) - \sin\theta(\mathbf{X}))\}}{\sin\{\frac{\pi}{2}(\sin(i\Delta\theta) - \sin\theta(\mathbf{X}))\}} \\ & \times e^{j(L-1)\pi(\sin(i\Delta\theta) - \sin\theta(\mathbf{X}))} \\ & \times \alpha e^{-j\omega_c\tau(\mathbf{X})} \mathbf{s}_t(\Omega(\mathbf{X}))^T \times \Lambda(rT_p - \tau(\mathbf{X})). \end{aligned} \quad (2.33)$$

Note that $\mathbf{z}_s(r, i) \in \mathbb{C}^{1 \times N}$ in (2.33) provides N temporal samples (i.e., the slow-time samples) and gives the peak value when $i\Delta\theta$ is matched to $\theta(X)$ (i.e., $i\Delta\theta = \theta(X)$). The next section will introduce the Doppler processing with these samples.

2.3.2 Doppler processing

The Doppler processing aims to filter out signals at the receiver front-end concerning the velocity induced by the reflector/source. This processing uses the reflected versions of multiple pulses illuminated in the surveillance region. These reflections contain frequency shifted versions of the transmitted waveforms by the reflector velocity. The estimation of this quantity, for example, enables one to discriminate moving objects from stationary objects.

The spectral analysis of the slow-time samples at each range bin uses the discrete Fourier transform (DFT) to find a frequency domain representation of the slow-time samples [1, Chp.5] [2, Chp.7]. This can be done by using a temporal steering vector. Let one denote a DFT coefficient vector by \mathbf{h}_t as a function of the Doppler frequency, f . This vector is given by

$$\mathbf{h}_t(f) = \mathbf{s}_t^*(2\pi fT), \quad (2.34)$$

where $\mathbf{s}_t^* \in \mathbb{C}^{N \times 1}$ is the conjugate of the temporal steering vector in (2.28).

The Doppler shift of the reflected signal from the object state, \mathbf{X} , is searched using (2.34) over the Doppler space. This space is equally divided into J resolution bins known as

the Doppler bins [1, Chp.5]. The resolution of these bins with N temporal samples is determined by

$$\Delta f = \frac{1}{N \times T}. \quad (2.35)$$

Given the r th range bin, the Doppler response of $\mathbf{z}_s(r, i)$ in (2.32) using (2.34) over I bearing bins and J Doppler bins is found as

$$h(r, i, j) = \mathbf{z}_s(r, i) \mathbf{h}_t(j \Delta f) \quad i = 1, \dots, I \text{ and } j = 1, \dots, J. \quad (2.36)$$

These outputs form an $I \times J$ bearing-Doppler map converted from the $L \times N$ samples at the r th range bin and correspond to resolution bins equally spaced by the bearing resolution $\Delta \theta$ given in (2.30) and the Doppler resolution Δf given in (2.35). This is illustrated in the bottom right plot in Figure 2.8. As a result, the measurement at the r th range bin, the i th bearing bin, and the j th Doppler bin that contains the reflection from \mathbf{X} is given by

$$\begin{aligned} h(r, i, j) = & \frac{\sin\{L \frac{\pi}{2} (\sin(i \Delta \theta) - \sin \theta(\mathbf{X}))\}}{\sin\{\frac{\pi}{2} (\sin(i \Delta \theta) - \sin \theta(\mathbf{X}))\}} \times e^{\{j \pi (L-1) (\sin i \Delta \theta - \sin \theta(\mathbf{X}))\}} \\ & \times \frac{\sin\{N (2 \pi j \Delta f - \Omega(\mathbf{X})) \frac{T}{2}\}}{\sin\{(2 \pi j \Delta f - \Omega(\mathbf{X})) \frac{T}{2}\}} \times e^{\{-j \frac{(N-1)}{2} (2 \pi j \Delta f - \Omega(\mathbf{X})) T\}} \\ & \times \alpha e^{-j \omega_c \tau(\mathbf{X})} \times \Lambda(r T_p - \tau(\mathbf{X})), \end{aligned} \quad (2.37)$$

where the first line indicates the bearing sample at the i th bearing bin, the second line shows the Doppler sample at the j th Doppler bin, and the last represents the range sample at the r th range bin.

2.3.3 Space-time filtering

This subsection considers the space-time filtering with the radar data cube. This filtering is joint beam-forming and Doppler processing with $L \times N$ data samples at each range bin. For this purpose, it stacks the columns of $\tilde{\mathbf{Z}}(r)$ in (2.27) and form an $LN \times 1$ data vector. Let one denote this vector by $\mathbf{Z}(r)$, which is found as

$$\mathbf{Z}(r) = \alpha e^{-j \omega_c \tau(\mathbf{X})} \mathbf{s}_s(\theta(\mathbf{X})) \otimes \mathbf{s}_t(\Omega(\mathbf{X})) \times \Lambda(r T_p - \tau(\mathbf{X})). \quad (2.38)$$

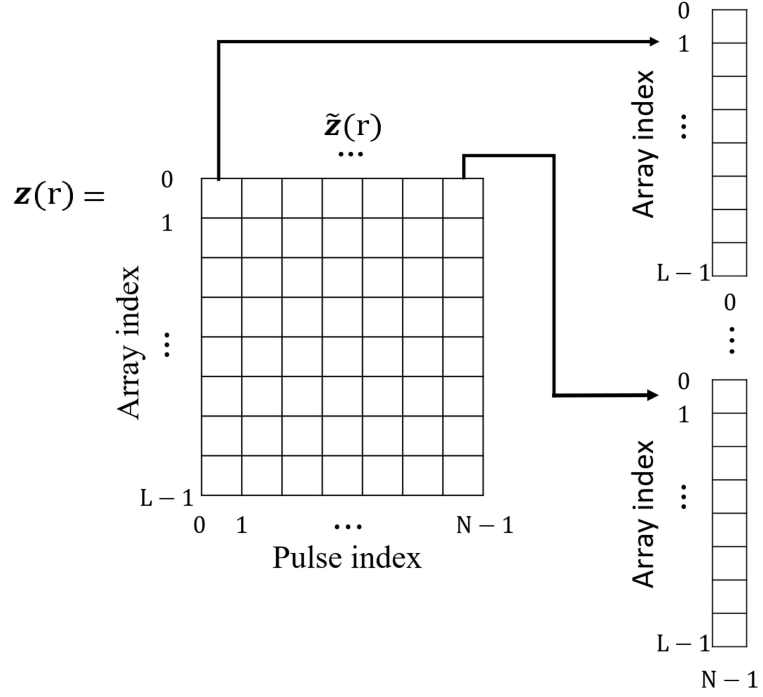


Figure 2.9: Space-time data vector (reproduced from Figure 9.12. in [1, Chp.9]): Mapping of an $L \times N$ matrix at the r th range bin to an $LN \times 1$ vector as a space-time data vector.

where \otimes denotes the Kronecker product operator. This vector at the r th range bin is illustrated in Figure 2.9.

The conventional space-time filtering can be done by combining the weighted vector of the beamforming and the vector of the DFT coefficients for the Doppler processing [1, Chp.9]. This quantity is found as

$$\mathbf{h}(\theta, f) \triangleq \mathbf{h}_s(\theta) \otimes \mathbf{h}_t(f), \quad (2.39)$$

where $\mathbf{h}_s(\cdot)$ is the weighted vector of the beamforming given in (2.29), and $\mathbf{h}_t(\cdot)$ is the vector of the DFT coefficients given in (2.34).

Given the r th range bin, the space-time filtering response with (2.38) is obtained by multiplying $\mathbf{h}(\cdot)$ in (2.39) and $\mathbf{Z}(r)$ over I bearing bins and J Doppler bins. These outputs provide a bearing-Doppler map, which is equivalent to the map obtained by using h in (2.37):

$$\mathbf{h}(i\Delta\theta, j\Delta f)^T \times \mathbf{Z}(r) = h(r, i, j), \quad i = 1, \dots, I \text{ and } j = 1, \dots, J, \quad (2.40)$$

where $\Delta\theta$ is the bearing resolution given in (2.30), and, Δf is the Doppler resolution given in (2.35). The next section will show the object detection using (2.40).

2.3.4 Object detection

The object detection performs a hypothesis test based on two hypotheses. These hypotheses are found by using the modulus of (2.40): One is the hypothesis that contains a single reflection from an object state, \mathbf{X} . The other is the null hypothesis that contains a noise only signal. These are defined with (2.40):

$$Z(r, i, j) = \begin{cases} |h(r, i, j)| + n(r, i, j) & , H_1 \text{ holds,} \\ n(r, i, j) & , H_0 \text{ holds,} \end{cases} \quad (2.41)$$

where H_1 denotes the hypothesis that an object exists, H_0 is the null the hypothesis, and $n(r, i, j)$ is the noise background modelled with a circular symmetry Gaussian random value $n(r, i, j) \sim \mathcal{N}(\cdot; 0, \sigma^2)$ of zero mean and variance σ^2 . Here, this test is assumed that a single object is located at a range bin. The matched filter output, however, takes more range bins than one range bin due to the auto-correlation. Also, this test only uses the modulus value, which is the magnitude of a reflected signal without its phase component. This implies that the hypothesis test using the modulus value might lose information on the phase component.

A conventional detector uses a likelihood ratio test against a threshold in the Neyman-Pearson sense [18, Chp.3] [1, Chp.6]. The decision on the object's presence is made at each resolution bin. This processing requires to perform $\Gamma \times I \times J$ hypothesis tests in order to detect an object. The detector at the (r, i, j) th bin hence takes the form:

$$L(r, i, j) \underset{H_0}{\overset{H_1}{\gtrless}} \mathcal{T}, \quad (2.42)$$

where \mathcal{T} denotes the detect threshold for selecting one of the two hypotheses. The likelihood ratio on the left hand side of (2.42) is found as

$$L(r, i, j) = \frac{l(Z(r, i, j)|H = H_1)}{l(Z(r, i, j)|H = H_0)}. \quad (2.43)$$

The numerator term in (2.43) can easily be found using the distribution of the noise in the signal model in (2.41):

$$l(Z(r, i, j)|H = H_1) = \mathcal{N}(Z(r, i, j); |h(r, i, j)|, \sigma^2), \quad (2.44)$$

and the denominator regarding the noise only hypothesis is found as

$$l(Z(r, i, j)|H = H_0) = \mathcal{N}(Z(r, i, j); 0, \sigma^2). \quad (2.45)$$

Therefore, the likelihood ratio after substituting (2.44) and (2.45) into (2.43) is found as

$$\begin{aligned} L(r, i, j) &\triangleq \frac{\mathcal{N}(Z(r, i, j); |h(r, i, j)|, \sigma^2)}{\mathcal{N}(Z(r, i, j); 0, \sigma^2)} \\ &= \exp \left\{ \frac{2}{\sigma^2} |h(r, i, j)| Z(r, i, j) \right\} \\ &\quad \times \exp \left\{ -\frac{2}{\sigma^2} |h(r, i, j)|^2 \right\}. \end{aligned} \quad (2.46)$$

The conventional detector often uses a log-likelihood ratio [18, Chp.13] that takes the natural logarithm of (2.42):

$$\log L(r, i, j) \underset{H_0}{\overset{H_1}{\geq}} \log \mathcal{T} \quad (2.47)$$

$$\log L(r, i, j) = \frac{2}{\sigma^2} |h(r, i, j)| Z(r, i, j) - \frac{2}{\sigma^2} |h(r, i, j)|^2 \quad (2.48)$$

As a result, the decision on the object's presence when the object is located in the (r, i, j) th bin is found as

$$|h(r, i, j)| Z(r, i, j) \underset{H_0}{\overset{H_1}{\geq}} \frac{\log \mathcal{T} \times \sigma^2}{2} + |h(r, i, j)|^2. \quad (2.49)$$

An alternative is the hypothesis test that directly uses the space-time data vector given in (2.38) without preprocessing for the digital beam-forming and Doppler processing. For convenience regarding the notation in the rest of this section, let one combine the spatial vector and the temporal steering vector as a function of the bearing angle, θ ,

and the angular Doppler shift, Ω , given the r th range bin:

$$\mathbf{s}(r, \theta, \Omega) \triangleq \mathbf{s}_s(\theta) \otimes \mathbf{s}_t(\Omega) \times \Lambda(rT_p - \tau) \quad (2.50)$$

where $\mathbf{s}_s(\cdot)$ is the spatial steering vector in (2.18), and $\mathbf{s}_t(\cdot)$ is the temporal steering vector in (2.28). As a result, the measurement in (2.38) with the noise background for the hypothesis that an object exists and the null hypothesis is found as

$$\mathbf{Z}(r) = \begin{cases} \tilde{\alpha} \mathbf{s}(r, \theta, \Omega) + \mathbf{n}(r) & , H_1 \text{ holds,} \\ \mathbf{n}(r) & , H_0 \text{ holds,} \end{cases} \quad (2.51)$$

where

$$\tilde{\alpha} \triangleq \alpha e^{-j\omega_c \tau}$$

is the complex reflection coefficient that contains the phase value of the pulse time of flight, and $\mathbf{n}(r) \sim \mathcal{CN}(\cdot; \mathbf{0}, \Sigma)$ models a circular symmetry complex Gaussian random vector with zero mean and covariance Σ .

Given (r, θ, Ω) , the most-well known detector that uses the inverse covariance is the adaptive matched filter (AMF) detector given in [58]:

$$\frac{|\mathbf{s}^H(r, \theta, \Omega) \hat{\Sigma}^{-1} \mathbf{Z}(r)|^2}{\mathbf{s}^H(r, \theta, \Omega) \hat{\Sigma}^{-1} \mathbf{s}(r, \theta, \Omega)} \underset{H_0}{\overset{H_1}{\gtrless}} \mathcal{T}. \quad (2.52)$$

where

$$\hat{\Sigma} = \mathbb{E}\{\mathbf{Z}(r) \mathbf{Z}^H(r) | H = H_0\}$$

is the estimate of the covariance, Σ , using the noise only signals, $\mathbb{E}\{\cdot\}$ denotes the expectation, and $(\cdot)^H$ is the Hermitian of its argument. In [59], the generalised likelihood ratio test (GLRT) detector is also found as

$$\frac{|\mathbf{s}^H(r, \theta, \Omega) \hat{\Sigma}^{-1} \mathbf{Z}(r)|^2}{\mathbf{s}^H(r, \theta, \Omega) \hat{\Sigma}^{-1} \mathbf{s}(r, \theta, \Omega) \{1 + \mathbf{s}^H(r, \theta, \Omega) \hat{\Sigma}^{-1} \mathbf{Z}(r)\}} \underset{H_0}{\overset{H_1}{\gtrless}} \mathcal{T}. \quad (2.53)$$

Note that the GLRT detector in (2.53) compared to the AMF detector in (2.52) has an additional term in the denominator because this detector includes both the reflected signals and the noise only signals when estimating the covariance. In contrast, the

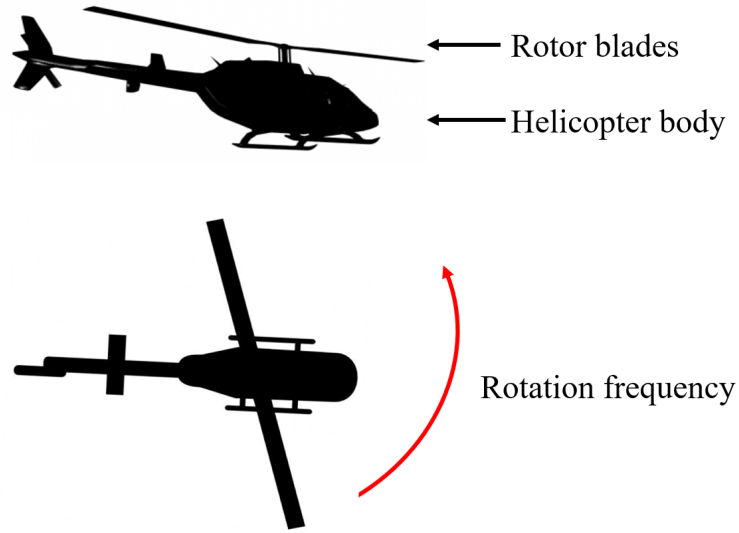


Figure 2.10: Example of slowly manoeuvring objects: A helicopter consists of its body and rotor blades. The micro-Doppler shift is characterised by a rotation frequency of the rotor blades (red line), the blade length, and the number of the rotor blades.

AMF detector uses the noise only signals for finding the covariance. When θ and Ω are unknown, these detectors need to estimate them. The typical approach for this purpose is to use a pre-specified set of kinematic parameters corresponding to the sample timings of the MF stage as discussed in Section 2.3.1 and Section 2.3.2. Another important factor for the detection test is a selection of the detection threshold, \mathcal{T} , because this value affects a constant false alarm rate for the detection. The selection of the detection threshold in the case of the multistatic channel will be explained in Chapter 3.

The low velocity of moving objects generates a small Doppler shift close to zero. The aforementioned detectors fail to discriminate them from the stationary background due to the limited Doppler resolution. The next section will introduce an additional signal feature that can help to discriminate these objects from the stationary background.

2.4 Micro-Doppler signatures

In general, moving objects have their propulsion components to move, such as rotor blade based engines and jet aircraft engines [32, Chp.3]. A moving object when illuminated by transmitted waveforms induces a frequency shift due to its velocity. The reflections when the transmitted waveform illuminates its propulsion component contain an additional

frequency shift centred at the main Doppler shift. This extra shift is referred to as the micro-Doppler shift [33, Chp.1]. The micro-Doppler shift differs from different types of propulsion components and enables one to classify them [34]. For example, jet aircraft engines' micro-Doppler shifts are characterised by sinusoid harmonic signals with a combination of different fundamental frequencies. These shifts differ from those collected from rotor blade based engines [60]. [33, Chp.2] is also shown that the micro-Doppler measurements from human gaits differ from horse walking. Therefore, Information on micro-Doppler measurements allows one to discriminate slowly moving objects from the stationary background.

This section focuses on the micro-Doppler shifts (or signatures) of slowly manoeuvring objects. One type of such objects is a helicopter with a rotor blade based engine with several rotor blades, which can hover and fly at low velocity. This is illustrated in Figure 2.10. The helicopter's micro-Doppler shift is characterised by the rotation frequency of rotor blades, the blade length, and the number of the rotor blades [61–63]. The front-end signal reflected from the helicopter is the superposition of all reflections from both the helicopter's body and its rotor blades. Owing to the superposition of the full reflections in the received signal, one needs to separate the rotor blade reflections from them in order to analyse the micro-Doppler shift. One possible approach is to transmit waveforms with high bandwidth and sampling the MF outputs with a high sampling rate. This leads to high-resolution range bins, each containing the reflections from different parts of the object. This is referred to as the high-resolution range profile [31, Chp.3].

The radar system considered in this section uses the same radar introduced in Section 2.3. Suppose that the ULA receiver collects N reflected pulses from \tilde{L} rotor blades of the helicopter. Each of them has the blade length denoted by B . When these blades are rotating with an angular frequency, ω , the rotating blades induce micro-Doppler shifts. The quantity for the l th rotating blade is hence given in [33, Chp.3] [62]:

$$\mu_D^{(l)}(t) = \frac{4\pi}{\lambda_c} \times B \times \sin\left(\omega t + \frac{2\pi(l-1)}{\tilde{L}}\right), \quad l = 1, \dots, \tilde{L}, \quad (2.54)$$

where the micro-Doppler shift indicates that it varies with $\sin(\omega t)$ over time and is a time-varying parameter. And, the signal model using (2.27) that captures the micro-Doppler shifts in (2.54) for \tilde{L} rotor blades and N reflected pulses is given by

$$\begin{aligned} \tilde{\mathbf{Z}}(r) = \mathbf{s}_s(\theta(\mathbf{X})) \times & \left(\mathbf{s}_t(\Omega(\mathbf{X})) \odot \begin{bmatrix} \sum_{l=1}^{\tilde{L}} B \times \text{sinc}\{\mu_D^{(l)}(0)\} \times e^{j\omega_l(0)} \\ \sum_{l=1}^{\tilde{L}} B \times \text{sinc}\{\mu_D^{(l)}(T)\} \times e^{j\omega_l(T)} \\ \vdots \\ \sum_{l=1}^{\tilde{L}} B \times \text{sinc}\{\mu_D^{(l)}((N-1)T)\} \times e^{j\omega_l(N-1)T} \end{bmatrix} \right)^T \\ & \times \alpha e^{-j\omega_c \tau(\mathbf{X})} \Lambda(rT_p - \tau(\mathbf{X})), \end{aligned} \quad (2.55)$$

where $\mathbf{X} = [x, y, \dot{x}, \dot{y}]$ denotes the helicopter state associated with $\theta(\mathbf{X})$, $\Omega(\mathbf{X})$ and $\tau(\mathbf{X})$ given in (2.4), (2.9), and (2.8), respectively, and \odot denotes the Hadamard (i.e., element-by-element) product operator. Here, \mathbf{s}_s is given in (2.18), and $\text{sinc}\{x\} = \frac{\sin(x)}{x}$ denotes the sinc function. After the beam-forming is applied using \mathbf{h}_s in (2.29), the resulting expression is given by

$$\mathbf{z}_s(r, i) = \mathbf{h}_s^T(i\Delta\theta) \tilde{\mathbf{Z}}(r) \quad (2.56)$$

where the output of $\mathbf{z}_s(r, i) \in \mathbb{C}^{1 \times N}$ has N temporal samples given the r th range bin and the i th bearing bin. For convenience regarding the notation in the rest of this section, let one denote N temporal samples in (2.56) by $\mathbf{z}_{(r,i)}$, which is given by

$$\mathbf{z}_{(r,i)} = [z_{(r,i)}(0), z_{(r,i)}(1), \dots, z_{(r,i)}(n), \dots, z_{(r,i)}(N-1)]. \quad (2.57)$$

When $rT_p = \tau(\mathbf{X})$ and $i\Delta\theta = \theta(\mathbf{X})$, the n th temporal sample from the MF output in (2.55) through (2.56) and (2.57) is found as

$$z_{(r,i)}(n) = L \times \tilde{\alpha} e^{jn\Omega(X)} \times \sum_{l=1}^{\tilde{L}} B \times \text{sinc}\{\mu_D^{(l)}(nT)\} \times e^{j\omega_l(nT)}, \quad (2.58)$$

where L is the total number of the array elements in the ULA, and $\tilde{\alpha}$ is the complex reflection coefficient given in (2.51). Here, the mathematical expression only emphasises reflected signals on the micro-Doppler shifts. The full details of the radar data cube, which contains the entire reflected signals from different parts of an object and noise background, will be considered in Chapter 4.

As discussed in Section 2.3.2, the temporal samples are analysed by using Doppler processing. This is done by using the DFT. This method only provides frequency information on the reflected signals and does not fit for the analysis of micro-Doppler shifts because they are time-varying samples collected in a CPI. In order to analyse the time-varying samples, one considers the time-frequency analysis, which provides both time and frequency information on the reflected signals. A common method for this purpose is the short-time Fourier transform (STFT) [64, Chp.8], which assumes that signals contain constant frequencies in a short-time interval. In this interval, the Fourier transform is performed without the effect of frequency variation. The STFT of (2.57) is found as

$$\text{STFT}(\tau, f) = \sum_{n=0}^{N-1} z_{(r,i)}(n)w(n - \tau)e^{-j2\pi f \frac{n}{N}}, \quad (2.59)$$

where τ and f denote time and frequency of the STFT, $z_{(r,i)}(n)$ is the n th temporal sample given in (2.58), w denotes a window function used to divide $\mathbf{z}_{(r,i)}$ into equally uniformed time intervals, and N is the number of temporal samples (i.e., N pulses).

The purpose of window functions for STFT is to truncate a continuing signal into segments with the window length. This also suppresses Gibbs' phenomenon that produces oscillatory behaviour of the signal at the truncated point [3, Chp.2] as well as the side-lobe in the frequency domain [3, Chp.7]. The level of the side-lobe suppression depends on the coefficients of the window function. Commonly used window functions are listed in Table 2.3, where the window length is denoted by N_t . These functions are symmetric and plotted as a function of the continuous variable. These are illustrated in Figure 2.11.

Figure 2.12 illustrates an example of STFT results with the use of different window functions defined in Table 2.3 and Figure 2.11. In this example, the parameters for transmission set $N = 1024$ transmitted pulses with the carrier wavelength, $\lambda_c = 6 \times 10^{-2}\text{m}$, and the PRI, $T = 5 \times 10^{-5}\text{s}$. A ULA receiver with $L = 10$ array elements collects reflections from a single rotor of the helicopter: The number of blades sets $\tilde{L} = 1$ blade with its length $B = 1.5\text{m}$ (see, Figure 2.10). The main Doppler shift

Table 2.3: Commonly used window functions [3, Chp.7]

Name	Window functions
Rectangular	$w(n) = \begin{cases} 1, & 0 \leq n \leq N_t \\ 0, & \text{otherwise} \end{cases}$
Bartlett(triangular)	$w(n) = \begin{cases} \frac{2 \times n}{N_t}, & 0 \leq n \leq \frac{N_t}{2} \\ 2 - \frac{2 \times n}{N_t}, & \frac{N_t}{2} \leq n \leq N_t \\ 0, & \text{otherwise} \end{cases}$
Hanning	$w(n) = \begin{cases} 0.5 - 0.5 \cos(\frac{2\pi \times n}{N_t}), & 0 \leq n \leq N_t \\ 0, & \text{otherwise} \end{cases}$
Hamming	$w(n) = \begin{cases} 0.54 - 0.46 \cos(\frac{2\pi \times n}{N_t}), & 0 \leq n \leq N_t \\ 0, & \text{otherwise} \end{cases}$
Blackman	$w(n) = \begin{cases} 0.42 - 0.5 \cos(\frac{2\pi \times n}{N_t}) + 0.08 \cos(\frac{4\pi \times n}{N_t}), & 0 \leq n \leq N_t \\ 0, & \text{otherwise} \end{cases}$

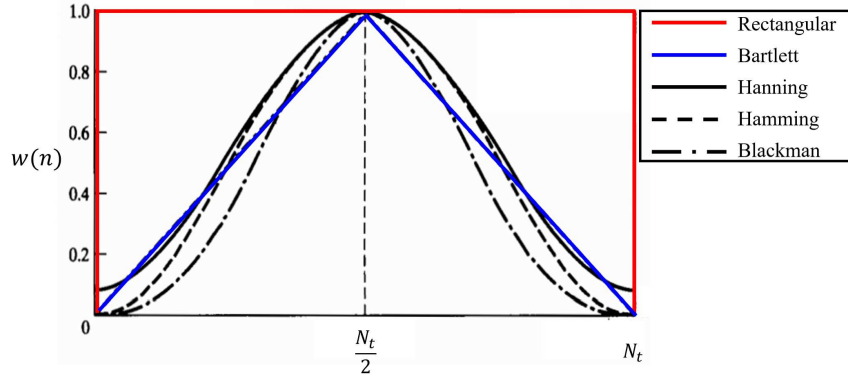


Figure 2.11: Commonly used window functions defined in Table 2.3 (reproduced from Figure 7.21 in [3, Chp.7]): The solid red line is the rectangular window function, and the blue line shows the Bartlett. The solid, dashed, and dashed-dot black lines indicate the Hanning, the Hamming, and the Blackman, respectively. Each of them is plotted as a function of the continuous variable.

sets $f_D = \frac{\Omega}{2\pi} = 5 \times 10^3 \text{ Hz}$ which is induced by the helicopter velocity. After sampling outputs of the MF stage in (2.55) and matching the bearing angle to the AoA in (2.56), the STFT in (2.59) uses these samples, each of which is given in (2.57). The window length in this STFT sets $N_t = 128$, which provides the time-interval $\Delta\tau = 6.4 \times 10^{-3} \text{ s}$ in a CPI = $51.2 \times 10^{-3} \text{ s}$. In Figure 2.12, (a), (b), (c), (d), and (e) are obtained by the rectangular, the Bartlett, the Hanning, the Hamming, and the Blackman, respectively, as the window functions. Here, the main Doppler shift is depicted by the yellow line. The frequency changes in the frequency domain (i.e., the y axis) form a sinusoidal signal in the CPI (i.e., the x axis) as depicted by yellow colour. This can indicate that the number of rotor blades is the same number of sinusoidal signals. The rotation frequency

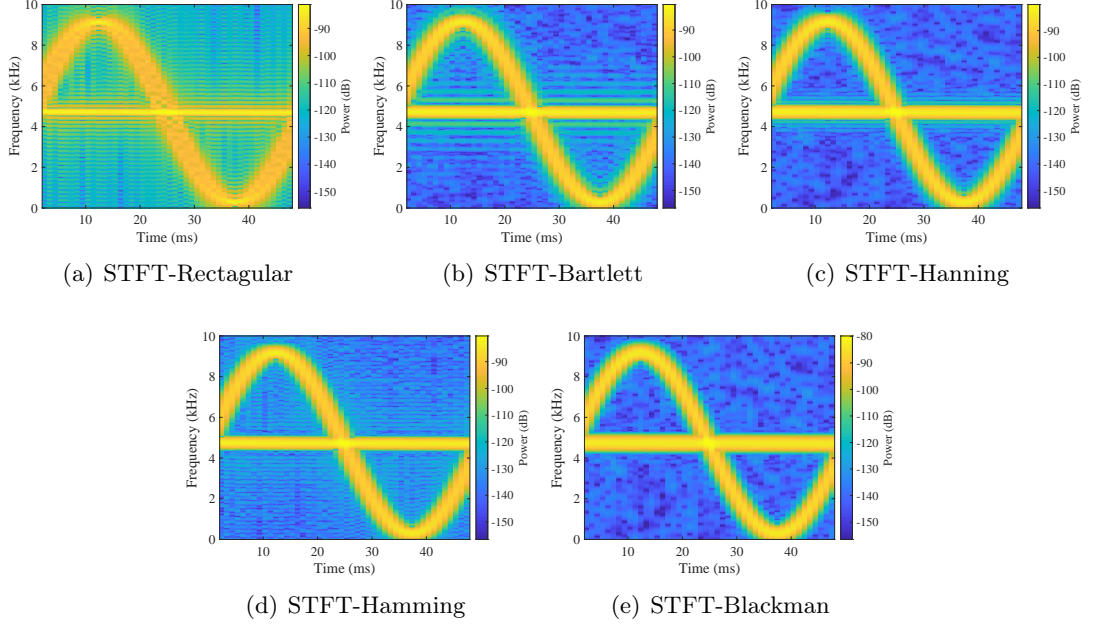


Figure 2.12: Comparison of short time Fourier transform (STFT) with different windows defined in Table 2.3: (a) STFT with the rectangular window, (b) STFT with the Bartlett, (c) STFT with the Hanning, (d) STFT with the Hamming, (e) STFT with the Blackman. All these results are obtained when a helicopter has a single rotor blade (i.e., $\tilde{L} = 1$).

and the blade length can be found by using the inverse period and the amplitude of the sinusoidal signal, respectively, (see, for example [33, Chp.2]).

For side-lobe suppression, the background colour of the STFT shows the level of the side-lobe signals. Here, the Hanning and the Blackman perform better suppression than the others (see, (c) and (e) in Figure 2.12). For time and frequency resolutions, the vertical thickness of the sinusoidal signal shows the frequency resolution. Its horizontal thickness indicates the time resolution. Overall, the Hanning window provides the resolution and the side-lobe suppression better than the others. Note that the length of the window function in (2.59) indicates the time interval in which frequency components are found. Hence, the selection of this window length is a trade-off between time and frequency resolutions [64, Chp.2]. In order to obtain the acceptable resolution in the frequency domain, the STFT often requires the collection of many temporal samples in a CPI.

An alternative, which provides a better frequency resolution than that in STFT, is a quadratic time-frequency representation. This is referred to as the Wigner-Ville

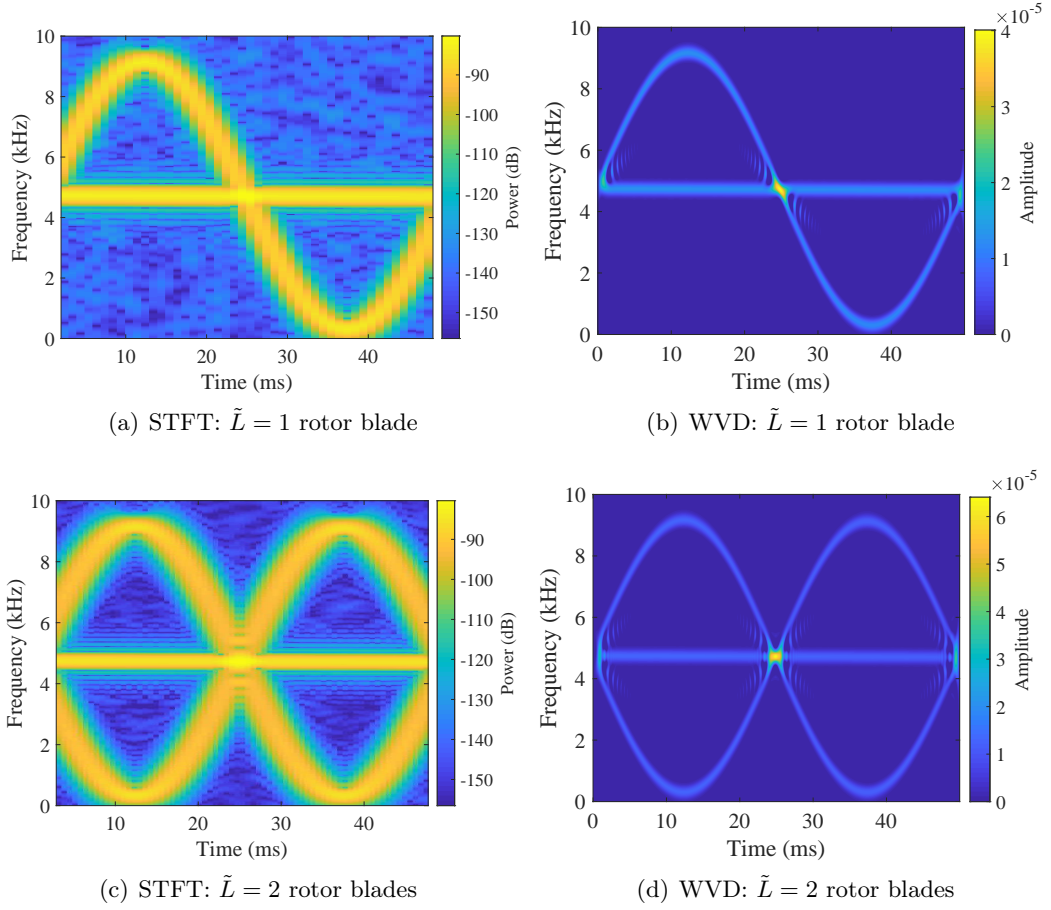


Figure 2.13: Comparison of short time Fourier transform (STFT) and Wigner-Ville distribution (WVD): (a) STFT with the number of blades $\tilde{L} = 1$, (b) WVD with $\tilde{L} = 1$, (c) STFT with $\tilde{L} = 2$, (d) WVD with $\tilde{L} = 2$. All parameters used in this example are the wavelength $\lambda_c = 5\text{m}$, the blade length $B = 1.5\text{m}$, the Doppler shift $f_D = \frac{\Omega}{2\pi T} = 5 \times 10^3\text{Hz}$, and the PRI $T = 5 \times 10^{-5}\text{s}$.

distribution (WVD) [34]:

$$\text{WVD}(n, f) = \sum_{\tau=-N}^N z_{(r,i)} \left(n + \frac{\tau}{2} \right) z_{(r,i)}^* \left(n - \frac{\tau}{2} \right) e^{-j2\pi f \frac{\tau}{N}}, \quad (2.60)$$

where the WVD performs auto-correlation of the temporal samples given in (2.57). One disadvantage of this method has cross-terms, which deteriorate the degree of identifiability of frequency components in the time-frequency analysis when the samples combine more than two different signals.

Figure 2.13 illustrates an example of the WVD in (2.60) compared to the STFT in (2.59). In this example, the same parameters are used in Figure 2.12 and the Hanning window is selected for the STFT in Figure 2.13(a). The WVD using (2.60) with the same samples

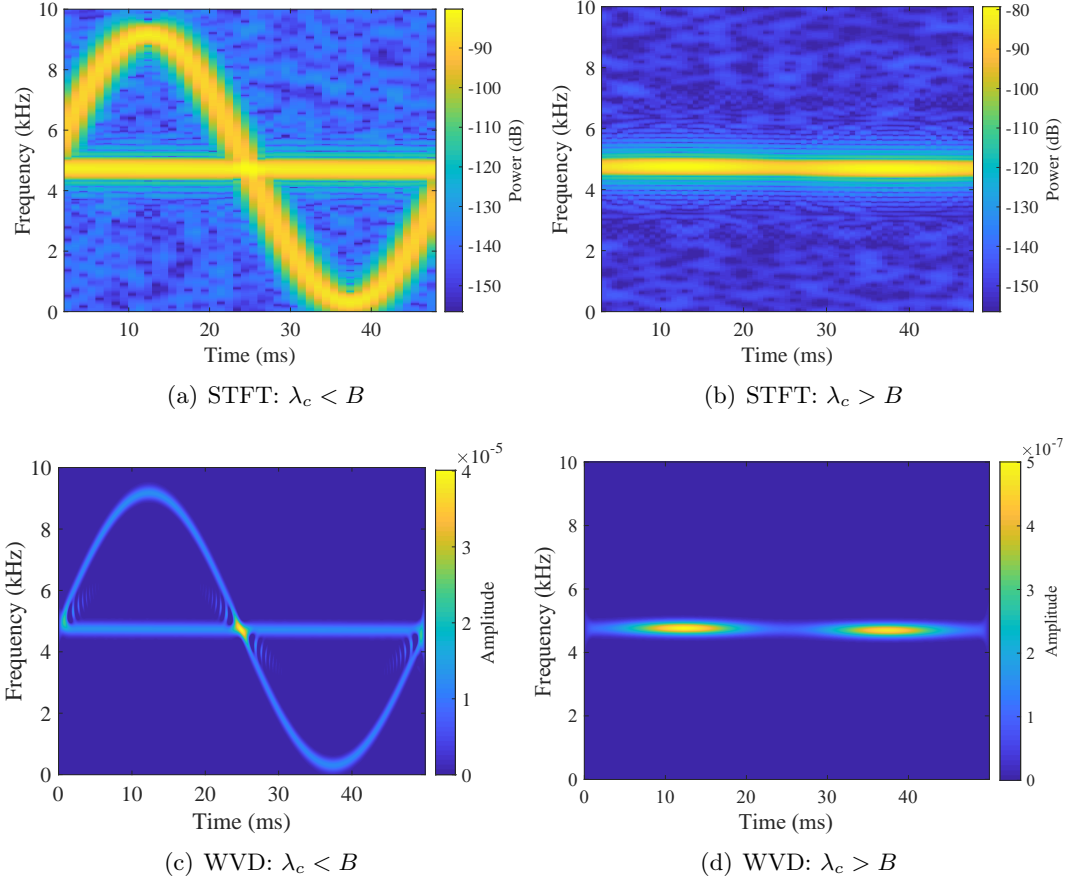


Figure 2.14: Relationship between the wavelength and the blade length: (a) STFT when the wavelength is larger than the blade length B : $\lambda_c < B$, (b) STFT when the wavelength is smaller than the blade length B : $\lambda_c > B$, (c) WVD when the wavelength is larger than the blade length B : $\lambda_c < B$, (d) WVD when the wavelength is larger than the blade length B : $\lambda_c < B$. All parameters are the same parameters used in Figure 2.13.

used in the STFT is illustrated in Figure 2.13(b). This resulting plot shows the same sinusoidal signal depicted by the cyan line, where this line is much narrower than that in the STFT. In Figure 2.13(c) and (d), the outputs of the STFT and the WVD present two sinusoidal signals, which imply that $\tilde{L} = 2$ rotor blades are rotating.

Another important factor is the relation between the wavelength, λ_c , and the blade length, B . Figure 2.14 illustrates this relation. When $\lambda_c > B$, one can find the rotation frequency, the blade length, and the number of the blades regarding the output of the STFT as discussed above and illustrated in Figure 2.14(a). When $\lambda_c < B$, the STFT is unable to find these parameters due to small unresolvable difference between the Doppler shift and the micro-Doppler signature (see, Figure 2.14(b)). In the case of the

WVD used, the parameters mentioned above can be found in the WVD when $\lambda_c > B$, whereas they cannot be found when $\lambda_c < B$ (see, Figure 2.14(c) and (d), respectively). Chapter 4 will consider this scenario in which the carrier wavelength is longer than the rotor blade length and will introduce the solution to the micro-Doppler signature estimation in this scenario.

Current literature on this study has focused on estimating micro-Doppler signatures from small rotor based unmanned aerial vehicle (UAV) systems [65]. This is challenging because small UAVs generate low reflectivity, and their reflected signals are the superposition of all reflections from the entire UAV. In [66], it is shown that the reflected signal model of a small UAV explains a sum of its different parts' reflections, and the commercial UAVs' micro-Doppler signatures are analysed using this model. For the classification of commercial UAVs, [35] proposes an algorithm, which extracts micro-Doppler signatures from the STFT output by using support vector machine (SVM) and then classifies different UAVs and birds. Another algorithm uses singular value decomposition (SVD) to extract micro-Doppler signatures from the STFT output [36] and classifies loaded/unloaded UAVs by using a naive Bayes classifier. In [67], convolutional neural network (CNN) is used to extract micro-Doppler signatures of small UAVs from an image used in both STFT and cadence-velocity diagram (CVD). These algorithms involve the time-frequency analysis that often requires a long dwell time in order to collect many reflections in a CPI. However, when the pulsed transmission is used for illumination, the collection of reflections in a CPI is insufficient in order to provide the desired frequency resolution. Also, the aforementioned algorithms can be processed after the detection decision is made.

The detection of such objects often requires more reflected signals than those collected in a CPI. In order to achieve a plausible detection performance, one considers the sufficient statistics of multiple measurements found by summing the associated reflections across themselves, which is referred to as the pulse integration [1, Chp.8]. The next section will introduce the pulse integration.

2.5 Pulse integration

As discussed in 2.3, the radar data cube after the MF stage is a complex number. After the beam-forming and the Doppler processing with this cube, the output is also a complex number. Conventional integration methods are mainly categorised into non-coherent integration and coherent integration [1, Chp.6]: The first is found by summing the modulus of the complex samples of the MF stage at the same range-bearing and Doppler bins across time. The latter is obtained by taking the modulus of the sum of the complex samples at the same bins over time. This is known as the coherent processing [2, Chp.2] [1, Chp.6]. In [68], it is shown that the integrated gain using the coherent integration is always higher than that using the non-coherent.

In the case of a manoeuvring and small object, the reflection follows its trajectory across the corresponding resolution bins over time. The conventional methods might fail to collect all evidence on the object's presence for a long time due to not considering its manoeuvres. In principle, a longer integration time provides a higher probability of detection for a given false alarm rate. In order to achieve the long time integration for manoeuvring objects, one needs to be considered range-bearing and Doppler migration in which the reflections move across their resolution bins during the integration time. In the current literature on this topic, keystone transform (KT) is used for matching multiple-pulse returns with all possible range values in order to reduce the range migration effect [19, 21, 23]. The keystone transform is a filter that matches the object's kinematic parameters (i.e., range and velocity) with measurements collected during a time window and reduce the migration effect within this time window. [22] uses KT and Lv's distribution (LVD) in order to reduce the range and Doppler migration effect. In [20], radon-fractional Fourier transform is proposed to moderate the range and Doppler migration effect. These algorithms are filters with long impulse responses that match the multiple-pulse returns along with a selection of possible range and Doppler values. These are, however, impractical because the number of filters required quickly becomes computationally excessive with increasing integration time.

An alternative is to employ a dynamic programming perspective that uses a regular probing pulse MF to integrate its outputs along a trajectory estimated simultaneously. This approach is referred to as the track-before-detect (TBD) [24, Chp.11] [26, 43, 69]. The next section will introduce a basic concept of TBD along with the recent advances in this topic.

2.6 Track-before-detect

As explained in Section 2.3, conventional detectors use two hypotheses that form a likelihood ratio and test this ratio against a threshold at each resolution bin. Unlike these detectors, track-before-detect (TBD) is a joint detection and tracking algorithm that estimates the object-related parameters with measurements before the detection decision is made and then makes the decision on the object's presence by evaluating a probability of the object existence using the estimated parameters [24, Chp.11].

Typically TBD is a batch algorithm implemented by using Hough transform [70], maximum likelihood estimation [71, 72], or dynamic programming [14, 15, 73]. These algorithms are only used for moving objects with a constant velocity, which makes the linear movements. In the recent literature of this topic, many algorithms use Bayesian recursive filtering because this framework enables one to use stochastic dynamic equations that represent manoeuvring objects. Also, this filtering can implement an online algorithm that does not require to store and process multiple scans of measurements [43, 69, 74–76].

In details, the Bayesian TBD uses a Markov state space model [24, Chp.1] and performs Bayesian recursive filtering, which consists of prediction and update stage [77]. Suppose the distribution of the state variable, \mathbf{X}_{k-1} , at the time step $k-1$ is available, and this distribution is based on all the measurements collected up to $k-1$. In order to update this prior at the time step k , the prediction density is given in Equation (11.10) [24,

Chp.11]:

$$\begin{aligned}
p(\mathbf{X}_k, E_k = 1 | \mathbf{Z}_{k-1}) &= \int p(\mathbf{X}_k, E_k = 1 | \mathbf{X}_{k-1}, E_{k-1} = 1, \mathbf{Z}_{k-1}) \\
&\quad \times p(\mathbf{X}_{k-1}, E_{k-1} = 1 | \mathbf{Z}_{k-1}) d\mathbf{X}_{k-1} \\
&\quad + \int p(\mathbf{X}_k, E_k = 1 | \mathbf{X}_{k-1}, E_{k-1} = 0, \mathbf{Z}_{k-1}) \\
&\quad \times p(\mathbf{X}_{k-1}, E_{k-1} = 0 | \mathbf{Z}_{k-1}) d\mathbf{X}_{k-1}
\end{aligned} \tag{2.61}$$

where $\mathbf{X}_k = [x_k, y_k, \dot{x}_k, \dot{y}_k, I_k]^T$ denotes the object's kinematic state which consists of the location $[x_k, y_k]$, the velocity $[\dot{x}_k, \dot{y}_k]$, and the intensity I_k , respectively, at the time step k , and $E_k \in \{0, 1\}$ indicates the object's presence when $E_k = 1$ and the object's absence when $E_k = 0$. Here, the intensity is defined as the reflected energy that indicates the square of modulus of (2.37). The first term inside the integral of (2.61) is the Markov transition. The update stage of this filtering is found by using the product of this prediction density and the measurement likelihood given in Equation (11.13) [24, Chp.11]:

$$p(\mathbf{X}_k, E_k = 1 | \mathbf{Z}_k) = \frac{l(\mathbf{Z}_k | \mathbf{X}_k, E_k = 1) \times p(\mathbf{X}_k, E_k = 1 | \mathbf{Z}_{k-1})}{p(\mathbf{Z}_k | \mathbf{Z}_{k-1})}, \tag{2.62}$$

where the first term in the right hand side is the measurement likelihood, and the second term is the prediction density given in (2.61).

In the Bayesian TBD, the key factor is the measurement likelihood in (2.62). Most TBD algorithms use the modulus of the MF within models, which describe the statistics of the modulus of the MF output. For example, the measurement likelihood in (2.62) is expressed in Equation (11.14) [24, Chp.11]:

$$l(\mathbf{Z}_k | \mathbf{X}_k, E_k) = \begin{cases} \prod_{r=1}^{\Gamma} \prod_{i=1}^I \prod_{j=1}^J p_{s+n} \left(Z_k^{(r,i,j)} | \mathbf{X}_k \right) & , E_k = 1 \text{ holds,} \\ \prod_{r=1}^{\Gamma} \prod_{i=1}^I \prod_{j=1}^J p_n \left(Z_k^{(r,i,j)} \right) & , E_k = 0 \text{ holds.} \end{cases} \tag{2.63}$$

Here, $p_{s+n}(\cdot)$ is the probability density function that contains the reflection at the r th range bin, the i th bearing bin, and the j th Doppler bin, and, models

$$p_{s+n} \left(Z_k^{(r,i,j)} | \mathbf{X}_k \right) \sim \mathcal{N} \left(Z_k^{(r,i,j)}; |h_k(r, i, j)|, \sigma^2 \right),$$

Table 2.4: Characteristics of the Swerling case 0, 1, 2, 3, 4, and 5 with their fluctuation models [2, Chp.2]

RCS model	Swerling case	Model	Notation
Non-fluctuation	Case 0/ 5	$A \exp(j\theta_A)$	<ul style="list-style-type: none"> • A: Amplitude • θ_A: Phase.
Fluctuation	Case 1/ 2	$P(\sigma_t) = \frac{1}{\sigma_0} \exp\left(-\frac{\sigma_t}{\sigma_0}\right)$	<ul style="list-style-type: none"> • σ_t: RCS of the target. • σ_0: Mean of RCS over all target fluctuations.
	Case 3/ 4	$P(\sigma_t) = \frac{4}{\sigma_0^2} \exp\left(-\frac{2\sigma_t}{\sigma_0}\right)$	

where $h_k(\cdot)$ is the range-bearing and Doppler map obtained by MF outputs in (2.37) as explained in Section 2.3, $|\cdot|$ denotes the modulus of its input argument, and σ^2 is the variance given in (2.7). The probability density function of $p_n(\cdot)$ in (2.63) contains the noise only signal and models

$$p_n\left(Z_k^{(r,i,j)}\right) \sim \mathcal{N}\left(Z_k^{(r,i,j)}; 0, \sigma^2\right).$$

In [76], the measurement likelihood is parametrised on the object state, \mathbf{X}_k , and the complex reflection coefficient and evaluated by marginalising the complex reflection coefficient out. This marginal likelihood with the measurements in (2.51) can be found as

$$l(|\mathbf{Z}_k|^2|\mathbf{X}_k) = \int_0^\infty l(|\mathbf{Z}_k|^2|\mathbf{X}_k, \tilde{\alpha}) \times p(\tilde{\alpha}) d\tilde{\alpha} \quad (2.64)$$

where \mathbf{Z}_k is given in (2.51), and $p(\tilde{\alpha})$ is a prior of the complex reflection coefficient. This prior often uses Swerling fluctuation models that represent probability distribution of the reflection coefficient based on the radar-cross-section (RCS) [1, Chp.6] [2, Chp.2].

Table 2.4 shows the characteristics of Swerling models, which are categorised into two different models: One is the non-fluctuation model in which an object when illuminated by the transmitted waveform generates constant scatters for all CPIs. This model is shown in Case 0/ 5. The other is the fluctuation models, which are divided into 4 cases.

Case 1 is assumed that scatters reflected from an object are random and all equally weighted. These scatters within a CPI are correlated but uncorrelated from one CPI to another. Case 2 is assumed that the scatters are uncorrelated from one reflected pulse to another, and the object's aspect angle changes rapidly. The model of these cases is shown in Case 1/ 2. Next, Case 3 and 4 are assumed that an object consists of one dominant reflector and several sub-reflectors. In Case 3, the scatters within a CPI are correlated but uncorrelated from one CPI to another, whereas the scatters are uncorrelated from one pulse to another in Case 4. These models are shown in Case 3/ 4.

Some other TBD algorithms employ likelihood ratios instead of using the measurement likelihood. For example, [25, 43, 74, 78, 79] use a likelihood ratio:

$$L(\mathbf{Z}_k|\mathbf{X}_k) \propto \prod_{r \in \mathcal{C}(\mathbf{X}_k)} \prod_{i \in \mathcal{C}(\mathbf{X}_k)} \prod_{j \in \mathcal{C}(\mathbf{X}_k)} \frac{p_{s+n} \left(Z_k^{(r,i,j)} | \mathbf{X}_k \right)}{p_n \left(Z_k^{(r,i,j)} \right)} \quad (2.65)$$

where $\mathcal{C}(\mathbf{X}_k)$ denotes a set of range-bearing and Doppler bins associated with the object state, \mathbf{X}_k , at the time step k .

In the recent literature on this topic, [80] proposes the modified particle filter that uses the range-Doppler map obtained from preprocessing. The use of this map leads to a simple calculation of particle weights for the update stage and can detect low SNR target in the range-Doppler map domain with lower computational complexity. Another is that [81] proposes multi-frame track-before-detect (MF-TBD), which, first, employs a low detection threshold to detect target candidates, and then MF-TBD is applied for further tracking based on particle filtering. In [69], a novel particle filter for multiple target tracking with track-before-detect measurement models is proposed: This approach employs the dimensional reduction technique into the proposed particle filtering in order to reduce the computation effort for the multiple-target case. Moreover, in [82], the multi-mode-multi-target TBD (MM-MM-TBD) algorithm is proposed: This algorithm can estimate the probabilities of all possible combinations of target existence scenarios and then obtain the joint multi-target posterior probability density function in a recursive Bayesian framework with a heuristic decision-directed based approach.

All these algorithms are developed based on the sequential Monte carol method known as the particle filtering [77].

An alternative approach is that [83] proposes a novel Greedy algorithm-based TBD for weak target detection and tracking in order to solve problems on the computational burden and the complex threshold determination, which are produced by typical dynamic programming TBD algorithms. This proposed scheme, first, conducts the detection with a low threshold to eliminate noise cells and then employs detection processing based on the Greedy algorithm to determine whether the target exists or not. Another one is that dynamic-programming based track-before-detect (DP-TBD) for radar systems with a high clutter environmental condition. In this algorithm, the log-likelihood ratio (LLR) is used to evaluate pulse integration for low SNR target detection [84].

For other approaches, [85] employs a Bernoulli filter TBD algorithm based on a random finite set (RFS) for target detection and tracking handling real radar measurements collected from a multiple-input multiple-output radar system in a high clutter environmental condition. The likelihood used in this algorithm is evaluated using the Rayleigh distribution for the null hypothesis and the Rician distribution for the target-present hypothesis. The RFS represents a random (spatial) point pattern on a radar screen in which the points are random and unordered as treat random variables. Regarding this concept, [86] proposes an online path planning algorithm with joint detection and tracking for UAVs. This algorithm employs a partially observable Markov decision process with a random finite set track-before-detect (TBD) multi-object filter. [87] proposes a Bernoulli track-before-detect filter together with a signal model that captures the target amplitude fluctuation model and improves performance in detecting a small object and estimating its kinematic parameters.

As discussed in Section 2.3, the sample that corresponds to the actual object kinematic state is a complex value that is a sum of the reflection coefficient and noise background [13]. It is emphasised that the models used for the modulus of the MF output in the aforementioned algorithms are averaged and cannot hence fully exploit

information on the actual object kinematic state captured by the measurements. In [27], it is shown that the detection performance of using the modulus of data samples can be further improved by taking into account the phase of the data samples in addition to the modulus.

The best achievable detection performance is obtained by coherent processing [1], in which one needs to estimate the complex reflection coefficient from the complex samples of the MF outputs, and then the pulse integration is performed by injecting this estimate into a complex likelihood. This corresponds to a non-averaged model in which the reflection coefficient is a random variable that remains the same during a coherent processing interval (CPI) and is changed randomly between consecutive CPIs [13]. This is challenging partly because the estimation of this quantity with a reasonable accuracy requires more samples than those which can collect at the pulse-width sampling rate in a CPI [4]. For example, in [88], coherent processing together with the pulse integration within a CPI is performed with a very high sampling rate. This sampling rate yields a large number of samples in the pulse interval.

2.7 Summary

This chapter has provided the background materials on radar systems, explained the monostatic configuration and the bistatic/multistatic setting, respectively, and the conventional signal processing techniques. Section 2.2 first gave the overview of radar systems with the aforementioned configurations and explained their advantages and disadvantages. Section 2.3 explained the conventional processing chains for object detection and introduced the mathematical notation for the signal model. With this signal model, the matched filtering, the Doppler processing, and the digital beam-forming were explained for the conventional processing chains. Section 2.4 introduced the time-frequency analysis techniques for the micro-Doppler signatures of rotary-wing aircraft. Then, Section 2.5 introduced the pulse integration methods with the current literature on this topic. Finally, the track-before-detect with the current

literature on this topic was discussed in Section 2.6. The next chapter will introduce simultaneously tracking and long-time integration for the detection of manoeuvring and small objects as the solution of the aforementioned problems and the first contribution in this thesis.

Chapter 3

Detection via simultaneous trajectory estimation and long time integration

3.1 Introduction

This chapter is the first technical chapter that provides the first contribution. The radar system considered in this chapter consists of multiple transmitters and a single ULA receiver, which form the multistatic configuration, as discussed in Section 2.2.2. In particular, Figure 3.1 illustrates the system structure, where the multiple transmitters use mutually orthogonal waveforms and are separately located. The receiver, co-located with one of these transmitters, has the full knowledge of their transmission characteristics except for their time references of transmission. This receiver also steers beams to the locations of the separately located transmitters directly. This path forms a direct channel between the receiver and the separately located transmitter. The front-end signal at the receive elements is the superposition of noise, signals from the direct channels, and reflections from objects.

In this setting, a coherent processing scheme to detect manoeuvring and small objects is proposed using the coherent pulse integration based on the TBD framework. The main differences compared to existing TBD algorithms [25, 43, 69, 72, 76, 82, 89] are i) the evaluation of a complex likelihood ratio conditioned on object-related parameters,

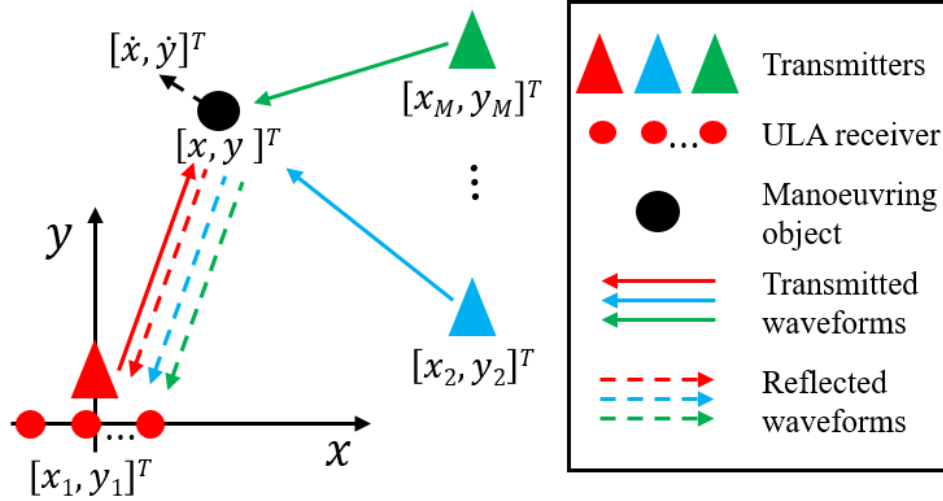


Figure 3.1: Problem scenario: M transmitters and a ULA receiver to detect a small object located at $[x, y]^T$ with the velocity $[\dot{x}, \dot{y}]^T$ (reproduced from Figure 2.2(c)).

complex reflection coefficients, and synchronisation terms based on Bayesian recursive filtering in order to achieve the coherent processing and ii) the detection test, which uses the coherent integration obtained by the resulting values of the complex likelihood ratios for an arbitrarily long time instead of the use of the probability of target existence used in the existing TBD algorithms.

Central to the proposed approach is a Markov state-space model in which the object state consists of location and velocity variables as the object-related parameters. The measurement model in this state-space model involves the radar ambiguity function. Here, the sequential Monte Carlo method is considered to estimate the state parameters for realising Bayesian recursive filtering. In this filtering, the update of the state needs to evaluate a likelihood, which uses the measurement model and captures the complex reflection coefficient as the additional parameter. This reflection coefficient needs to be estimated within the Bayesian filtering recursions in order to achieve coherent processing (or coherent integration). There are many parameter estimation approaches such as a minimum variance unbiased estimator (MVU), a maximum likelihood (ML) estimator, and a least square (LS) approach [90]. Within the filtering recursions, one plausible approach is the ML estimation due to the known noise distribution together with the measurement model. For example, one approach, proposed in [88, 91], is the ML estimate of the reflection coefficient at each sample (or particle) of the state

parameter generated from the prediction stage (for example, Section 2.6). The resulting ML estimates are uniformly distributed and produce the average of them as the final estimate. The accuracy of this estimate might not be enough to perform the coherent processing. The proposed ML estimator in this chapter, on the other hand, uses an expectation-maximisation algorithm that captures the state samples together with their corresponding weights and leads to a more accurate estimate. It is also shown that this scheme is an empirical Bayesian method [92] for realising the update stage of the filtering. The estimation of unknown time references in the bistatic channel is also used with this proposed approach, thereby relaxing the commonly used assumption that the local receiver is synchronised with the separately located transmitters.

For the detection processing, a Neyman-Pearson test, evaluated based on this Markov model, is used instead of the probability of target existence. Equivalently, the integrated value, obtained by using the coherent processing, is tested against a constant false alarm rate (CFAR) threshold. Therefore, the resulting algorithm enables one to collect the entire evidence of the object's presence at the receiver by i) performing coherent integration in both monostatic and bistatic channels within a coherent processing interval (CPI), ii) non-coherently integrating across different (non-coherent) channels (i.e., local monostatic and remote bistatic channels), and iii) continuing integration for an arbitrarily long interval that contains many CPIs.

This chapter is organised as follows: Section 3.2 details the mathematical statement of the problem in Figure 3.1. Section 3.3 discusses the trajectory estimation with the array measurements and details the aforementioned empirical Bayes approach. Section 3.4 first introduces the proposed EM algorithm for the ML estimates of the complex reflection coefficients. Then, the ML estimator of the synchronisation term is discussed. Section 3.5 specifies the proposed detection scheme together with the combination of these estimators. Then, the proposed algorithm's efficacy is demonstrated and compared to a clairvoyant detector and other techniques in Section 3.6. Finally, the summary of the proposed detection scheme is in Section 3.7.

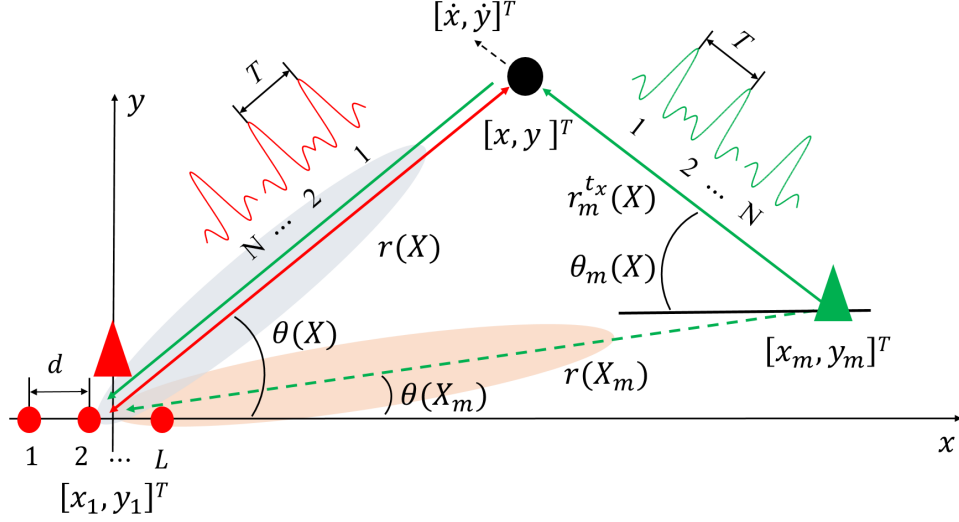


Figure 3.2: Geometry of the problem: A ULA receiver co-located with a transmitter and the m th remote transmitter on the 2D Cartesian plane. Both polar and Cartesian coordinate variables are depicted. Each transmitter emits N pulses in a CPI. The waveforms, used here, are orthogonal.

3.2 Problem statement

Let this section consider the geometry of the problem scenario as illustrated in Figure 3.1 and detail the array signal at the receiver. Figure 3.2 illustrates the geometry of $M = 2$ transmitters and a single ULA receiver as an example. Here, M transmitters use mutually orthogonal waveforms of the pulse duration, T_p , and the bandwidth, B_w . At the m th transmitter, N consecutive pulse waveforms, \tilde{u}_m , are emitted with a PRI of T and an unknown time reference of Δt_m . This waveform after modulating with an angular frequency of $\omega_c = 2\pi f_c$ is therefore given by

$$u_m(t) = \text{Re} \left\{ \sum_{n=0}^{N-1} \tilde{u}_m(t - nT - \Delta t_m) e^{j\omega_c t} \right\}. \quad (3.1)$$

Here, reflectors in the scene are assumed to remain coherent (i.e., the object reflectivity in each channel remain constant) during this overall NT seconds. This period is known as the CPI. These transmission characteristics are fully known at the receiver except for the time reference shift (i.e., Δt_m) of the separately located transmitters concerning the receiver clock for the m th channel. This time reference is designated as a synchronisation term for the rest of this chapter.

The use of such orthogonal transmit waveforms underlies the vision of multiple-input multiple-output (MIMO) radars [37, 38], a particular configuration of which is hence the system considered here. Design of orthogonal sets for MIMO sensing was investigated with various objectives such as the maximisation of diversity [93] and waveform identifiability [94]. In this chapter, a narrowband regime is considered, where frequency division multiplexing can be used to achieve orthogonality in practice.

The ULA receiver (see, red dots in Figure 3.2) has L elements spaced by half of the carrier wavelength (i.e., λ_c) and directly steers beams to locations of the separately located transmitters with the prior knowledge of their locations. Here, there are two categories of channels defined: One is a reflection channel in which transmitted waveforms travel from the transmitter to reflectors and upon echo back to the receiver as defined in Section 2.2. In the reflection channels (see, blue shaded ellipse), each element at the receiver collects the superposition of noise background and reflected signals originating from the local (monostatic) transmitter and the remote (bistatic) transmitters. The other is a direct channel in which the transmitted waveforms directly travel from the transmitter to the receiver. In the direct channels (see, red shaded ellipse), the transmitted waveforms are collected directly. The front-end signal at the receive elements is hence the superposition of noise, signals from the direct channels, and reflections in the reflection channels.

3.2.1 Spatio-temporal signal model in reflection channels

As explained in Section 2.3, the processing chain for the m th reflection channel begins with demodulation followed by matched filtering with the m th probing waveform which completely suppresses the contributions of the other channels owing to the orthogonality of the waveforms used. The output of the m th matched filter is then sampled with a period that is equal to the pulse duration of T_p . A total of Γ samples are collected for each of the N pulse at each of the L elements. The resulting data form a radar data cube (see, Figure 3.3). For the r th range bin, it stacks the columns of the data cube and forms an $LN \times 1$ data vector. When a single object exists in the surveillance region, this data vector is a function of the synchronisation term, Δt_m , and the kinematic state, \mathbf{X} . This

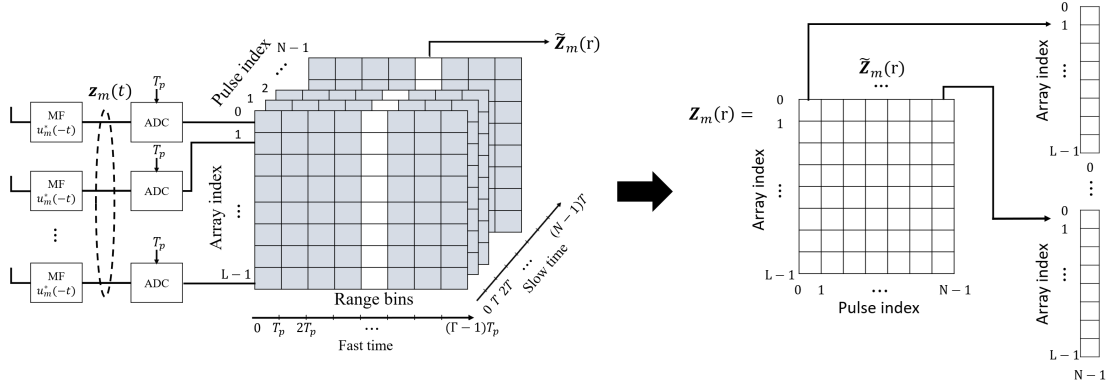


Figure 3.3: Data acquisition in the m th channel reproduced from Figure 2.7 in Chapter 2: Sampled version of the received signal within a CPI as the radar data cube in the m th reflection channel. The output of the m th matched filter is sampled and arranged in array index, fast time and slow time axis. $\tilde{\mathbf{Z}}_m(r)$ is an $L \times N$ matrix, and forms an $LN \times 1$ vector as the measurement, $\mathbf{Z}_m(r)$, at the r th range bin.

case is denoted by H_1 . Otherwise, the case when an object is absent in the surveillance region is denoted by H_0 :

$$\mathbf{Z}_m(r) = \begin{cases} \alpha_m \mathbf{s}_m(r, \mathbf{X}, \Delta t_m) + \mathbf{n}_m(r) & , H_1 \text{ holds,} \\ \mathbf{n}_m(r) & , H_0 \text{ holds,} \end{cases} \quad (3.2)$$

where \mathbf{s}_m is the reflected signal model that will be detailed later in this section, α_m is the complex reflection coefficient in the m th reflection channel, and $\mathbf{X} = [x, y, \dot{x}, \dot{y}]^T$ is the kinematic state of the reflector (i.e., its location of $[x, y]^T$ and its velocity of $[\dot{x}, \dot{y}]^T$). The noise background is modelled with a circular symmetry complex Gaussian random vector with zero mean and covariance Σ_m (see, (2.51)).

The reflected signal model in (3.2) is given by

$$\begin{aligned} \mathbf{s}_m(r, \mathbf{X}, \Delta t_m) &\triangleq s(\Delta t_m) \mathbf{s}_s(\theta(\mathbf{X})) \otimes \mathbf{s}_t(\tau_m(\mathbf{X}), \Omega_m(\mathbf{X})) \\ &\quad \times \Lambda_m(rT_p - \tau_m(\mathbf{X}) - \Delta t_m) \end{aligned} \quad (3.3)$$

$$s(\Delta t_m) \triangleq e^{-j\omega_c \Delta t_m} \quad (3.4)$$

$$\mathbf{s}_t(\tau_m, \Omega_m) \triangleq e^{-j\omega_c \tau_m} \times [1, e^{j\Omega_m}, \dots, e^{j(N-1)\Omega_m}]^T, \quad (3.5)$$

where $\theta(\mathbf{X})$, $\tau_m(\mathbf{X})$, and $\Omega_m(\mathbf{X})$ are the angle of arrival (AoA) in (2.9), the time-of-flight (ToF) in (2.11), and the angular Doppler shift in (2.14), respectively, associated with \mathbf{X}

(see, Figure 3.2), and $\Lambda_m(\cdot)$ is the auto-correlation of the m th waveform (see, (2.21)). Here, \mathbf{s}_s is the spatial steering vector in (2.18), and \mathbf{s}_t is the temporal steering vector, parametrised on $\tau_m(\mathbf{X})$ and $\Omega_m(\mathbf{X})$. This is the modified version of (2.28).

3.2.2 Spatio-temporal signal model in direct channels

The direct path signal in the m th direct channel can easily be modelled using the spatial and temporal steering vectors, respectively, in (3.3). The state of the m th transmitter is given by $\mathbf{X}_m^{(t_x)} = [x_m, y_m, 0, 0]^T$. The corresponding time-of-flight is $\tau(\mathbf{X}_m^{(t_x)})$ given in (2.11). The angle of arrival is denoted by $\theta_m(\mathbf{X}_m^{(t_x)})$, which is computed using (2.15). Unlike the reflection channel, the unknown reflectivity is replaced with a known pulse energy term. This quantity can be obtained by the product of the pulse duration, T_p , and the received power from the m th transmitter:

$$E_m = P_r^{(m)} \times T_p. \quad (3.6)$$

where E_m denotes the pulse energy, and $P_r^{(m)}$ is the received power. This received power can be calculated by using the system parameters such as the transmitted power, $P_t^{(m)}$, the transmitter gain, $G_t^{(m)}$, and the distance from the m th transmitter to the receiver [95]:

$$\begin{aligned} P_r^{(m)} &= \frac{P_t^{(m)} G_t^{(m)}}{4\pi R(\mathbf{X}_m^{(t_x)})} \times A_e K_a \\ &= \frac{P_t^{(m)} G_t^{(m)}}{4\pi R^2(\mathbf{X}_m^{(t_x)})} \times \frac{G_a \lambda_c^2}{4\pi K_a} K_a \\ &= \frac{P_t^{(m)} G_t^{(m)}}{4\pi R^2(\mathbf{X}_m^{(t_x)})} \times \frac{G_a \lambda_c^2}{4\pi}, \end{aligned} \quad (3.7)$$

where $A_e = \frac{G_a \lambda_c^2}{4\pi K_a}$ is the receiver antenna's effective area, and K_a is the efficiency of the antenna.

As explained in this section above, the receiver is assumed to have all these parameter values as the prior knowledge. Regarding this prior knowledge, the receiver has the known pulse energy, E_m , in the m th direct channel. The direct channel measurement

vector at the r th range bin obtained by sampling the m th matched filter output in a CPI is hence given by

$$\begin{aligned}
 \mathbf{Z}_m(r) &= \sqrt{E_m} \tilde{\mathbf{s}}_m(r, \mathbf{X}_m^{(t_x)}) + \mathbf{n}_m(r), \\
 \tilde{\mathbf{s}}_m(r, \mathbf{X}_m^{(t_x)}) &\triangleq s(\Delta t_m) \mathbf{s}_s(\theta(\mathbf{X}_m^{(t_x)})) \otimes \mathbf{s}_t\left(\frac{\tau(\mathbf{X}_m^{(t_x)})}{2}, \Omega(\mathbf{X}_m^{(t_x)}) = 0\right) \\
 &\quad \times \Lambda_m\left(rT_p - \frac{\tau(\mathbf{X}_m^{(t_x)})}{2} - \Delta t_m\right) \\
 &= s(\Delta t_m) s\left(\frac{\tau(\mathbf{X}_m^{(t_x)})}{2}\right) \times \mathbf{s}_s(\theta(\mathbf{X}_m^{(t_x)})) \otimes \mathbf{1} \\
 &\quad \times \Lambda_m\left(rT_p - \frac{\tau(\mathbf{X}_m^{(t_x)})}{2} - \Delta t_m\right).
 \end{aligned} \tag{3.8}$$

Here, $\theta(\mathbf{X}_m^{(t_x)})$ is the AoA from the m th transmitter given in (2.9). $\frac{\tau(\mathbf{X}_m^{(t_x)})}{2}$ is the ToF between the transmitter and the receiver using (2.5), where the factor, $\frac{1}{2}$, indicates one-way propagation. $\tilde{\mathbf{s}}_m$ is the noise free signal model associated with $\theta(\mathbf{X}_m^{(t_x)})$ and $\frac{\tau(\mathbf{X}_m^{(t_x)})}{2}$ of the transmitter state, $\mathbf{X}_m^{(t_x)}$, and $\mathbf{1}$ is an $N \times 1$ all ones vector.

Note that $\tilde{\mathbf{s}}_m$ differs from \mathbf{s}_m in (3.3): The latter uses the bistatic ToF in both the temporal steering vector and the waveform auto-correlation delay, whereas, the former uses direct path ToF. Because the transmitters are of zero Doppler frequency, the temporal steering vector reduces to an all ones vector scaled with $s\left(\frac{\tau(\mathbf{X}_m^{(t_x)})}{2}\right)$.

3.2.3 Problem definition

Here, it would like to perform a hypothesis test based on the measurement model in (3.2). These measurements are complex numbers, and it is interested in the evaluation of the sufficient statistics for the two hypotheses with them. Detection/processing using complex measurements is often referred to as the coherent detection/processing, and conventionally the input is the same resolution bin over multiple-pulse returns [1]. Therefore, in order for this operation to maintain coherence, the target position should not be changing over time.

In order to extend coherent processing to the case of manoeuvring objects and remote transmitters, the mathematical statement of the problem is considered as the evaluation of a likelihood-ratio i) using complex versions of measurements (as opposed to, for example, using only their modulus in Section 2.6) for all M reflection channels and ii) for a time window of K CPIs given an object trajectory,

$$\mathbf{X}_{1:K} \triangleq \{\mathbf{X}_k\}_{k=1}^K,$$

where $\mathbf{X}_k = [x_k, y_k, \dot{x}_k, \dot{y}_k]^T$ is the kinematic state of an object at the k th CPI. This likelihood ratio will then be tested against a threshold in a Neyman-Pearson sense [18, Chp.3]. The detector considered this section hence takes the form:

$$L(\mathbf{Z}_{1,1:K}, \dots, \mathbf{Z}_{m,1:K}, \dots, \mathbf{Z}_{M,1:K} | \mathbf{X}_{1:K}, \boldsymbol{\alpha}, \Delta \mathbf{t}) \underset{H_0}{\overset{H_1}{\gtrless}} \mathcal{T}, \quad (3.9)$$

where

$$\mathbf{Z}_{m,1:K} \triangleq \{\mathbf{Z}_{m,1}, \dots, \mathbf{Z}_{m,k}, \dots, \mathbf{Z}_{m,K}\}$$

is a set of the measurements collected in the m th reflection channel over $k = 1, \dots, K$ CPIs, and

$$\mathbf{Z}_{m,k} = [\mathbf{Z}_{m,k}(0), \dots, \mathbf{Z}_{m,k}(\Gamma - 1)]$$

is the measurement of the m th reflection channel at the k th CPI, whose size is an $LN \times \Gamma$ matrix (see, Figure 2.9). Here, $\boldsymbol{\alpha}$ and $\Delta \mathbf{t}$ are sets of reflection coefficients and synchronisation terms across all the reflection channels, respectively. They are defined by

$$\begin{aligned} \boldsymbol{\alpha} &\triangleq \{\boldsymbol{\alpha}_1, \dots, \boldsymbol{\alpha}_k, \dots, \boldsymbol{\alpha}_K\}, \\ \boldsymbol{\alpha}_k &\triangleq \{\alpha_{1,k}, \dots, \alpha_{M,k}\}, \quad k = 1, \dots, K, \\ \Delta \mathbf{t} &\triangleq \{\Delta t_1, \Delta t_2, \dots, \Delta t_M\}. \end{aligned}$$

In order to carry out the test in (3.9), the trajectory, $\mathbf{X}_{1:K}$, needs to be estimated. This is also referred to as tracking and is the subject of Section 3.3 along with the estimation of $\boldsymbol{\alpha}$. Algorithmic strategies for estimating the synchronisation term, $\Delta \mathbf{t}$, are introduced

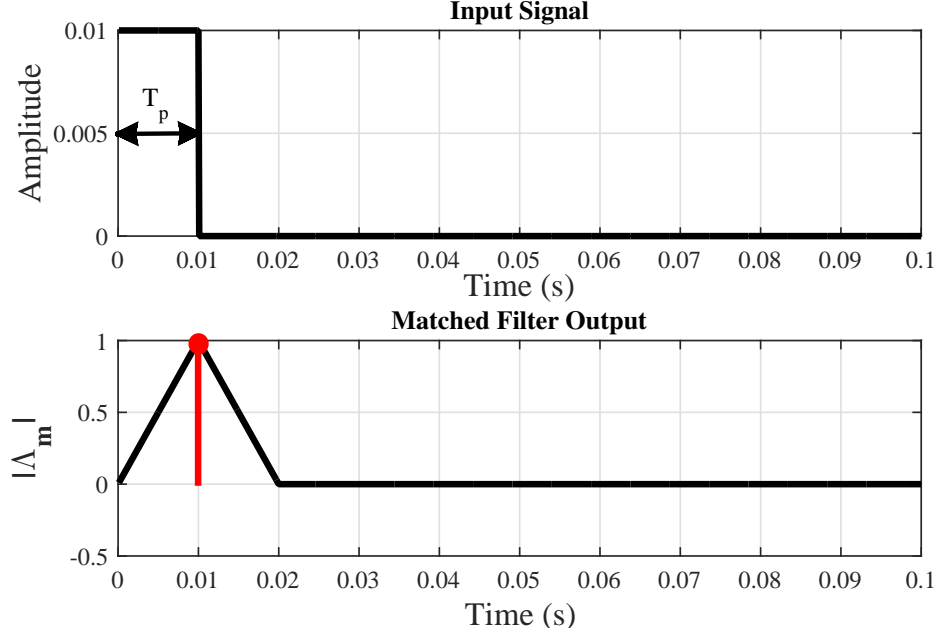


Figure 3.4: Example of the matched filter output: The pulsed waveform has the pulse width, $T_p = 0.01$ s. The corresponding output of the matched filter with this waveform is illustrated at the bottom. The highest level of this output is depicted by a red dot.

in Section 3.4. These results are combined in Section 3.5, and the threshold selection is detailed in order to evaluate the detection test in (3.9).

3.2.4 Sufficient statistics for the likelihood ratio

The likelihood ratio on the left hand side of (3.9) factorises over measurement likelihood ratios for K CPIs as the noise samples between consecutive CPIs are independent. Each time term also factorises over M channel likelihood ratios as the related parameters are independent. When a single object is in the surveillance region, this forms:

$$L = \prod_{k=1}^K \prod_{m=1}^M \frac{l(\mathbf{Z}_{m,k} | \mathbf{X}_k, \alpha_{m,k}, \Delta t_m, H = H_1)}{l(\mathbf{Z}_{m,k} | \mathbf{X}_k, \Delta t_m, H = H_0)}. \quad (3.10)$$

These measurements satisfy a locality property: The number of range bins, associated with \mathbf{X}_k , are limited by the support of the auto-correlation, which is of duration $2T_p$.

These bins are defined:

$$\mathcal{E}_m(\mathbf{X}_k) = \begin{cases} \{r_{m,k}, r_{m,k} + 1\}, & r_{m,k}T_p < \tau_m(\mathbf{X}_k) + \Delta t_m \\ \{r_{m,k}\}, & r_{m,k}T_p = \tau_m(\mathbf{X}_k) + \Delta t_m, \\ \{r_{m,k} - 1, r_{m,k}\}, & r_{m,k}T_p > \tau_m(\mathbf{X}_k) + \Delta t_m \end{cases} \quad (3.11)$$

where

$$r_{m,k} \triangleq \left\lfloor \frac{\tau_m(\mathbf{X}_k) + \Delta t_m}{T_p} \right\rfloor, \quad (3.12)$$

with $\lfloor \cdot \rfloor$ denoting the nearest integer function, and $\tau_m(\mathbf{X}_k) + \Delta t_m$ gives the time of flight in the m th reflection channel associated with the object state, \mathbf{X}_k . Figure 3.4 gives an example of the matched filter output with a single pulsed waveform. This waveform has the pulse width, $T_p = 0.01$ s. Thus, the sampling time at the ADC state is T_p . Here, the output of the auto-correlation at the matched filter is occupied with two range bins, and its highest level is centred of them in this example. In practice, the highest level might not be centred, and the range bins in (3.11) are considered in that case. Here, the range bin, $r_{m,k}$, has the highest signal-to-noise ratio (in the m th reflection channel) given Λ_m as the time auto-correlation function typically vanishes towards tails (see, the red dot in Figure 3.4).

As a result, the likelihood ratio in (3.10) further decomposes into factors over range bins using (3.11):

$$L = \prod_{k=1}^K \prod_{m=1}^M \prod_{r \in \mathcal{E}_m(\mathbf{X}_k)} \frac{l(\mathbf{Z}_{m,k}(r) | \mathbf{X}_k, \alpha_{m,k}, \Delta t_m, H = H_1)}{l(\mathbf{Z}_{m,k}(r) | H = H_0)}. \quad (3.13)$$

The numerator terms in (3.13) can easily be found using the distribution of the noise in the signal model in (3.2):

$$l(\mathbf{Z}_{m,k}(r) | \mathbf{X}_k, \alpha_{m,k}, \Delta t_m, H = H_1) = \mathcal{CN}(\mathbf{Z}_{m,k}(r); \mathbf{s}_{m,k}(r, \mathbf{X}_k, \Delta t_m), \Sigma_m). \quad (3.14)$$

The denominator in (3.13) regarding the noise only hypothesis is nothing but the noise density evaluated at $\mathbf{Z}_{m,k}(r)$. Therefore, the instantaneous likelihood ratio in (3.13)

after substituting from (3.14) and the noise distribution is found as

$$\begin{aligned}
 L(\mathbf{Z}_{m,k}(r)|\mathbf{X}_k, \alpha_{m,k}, \Delta t_m) &\triangleq \frac{\mathcal{CN}(\mathbf{Z}_{m,k}(r); \alpha_{m,k} \mathbf{s}_m(r, \mathbf{X}_k, \Delta t_m), \Sigma_m)}{\mathcal{CN}(\mathbf{Z}_{m,k}(r_{m,k}); \mathbf{0}, \Sigma_m)} \\
 &= \exp \left\{ 2\text{Re} \left\{ \alpha_{m,k}^* \mathbf{s}_m^H(r, \mathbf{X}_k, \Delta t_m) \Sigma_m^{-1} \mathbf{Z}_{m,k}(r) \right\} \right\} \\
 &\quad \times \exp \left\{ - |\alpha_{m,k}|^2 \mathbf{s}_m^H(r, \mathbf{X}_k, \Delta t_m) \Sigma_m^{-1} \mathbf{s}_m(r, \mathbf{X}_k, \Delta t_m) \right\},
 \end{aligned} \tag{3.15}$$

where $()^*$ and $|\cdot|$ denote the complex conjugate and the modulus of a complex variable, respectively.

The likelihood ratio evaluation given in (3.15) is advantageous: Only a linear operation needs to be performed on the measurements: This operation is in the form of a whitening transform with the inverse noise covariance followed by an inner product with the signal model. Because the signal model involves the spatial steering vector in (3.3), this inner product effectively performs beam-forming on the measurements filtering out contributions of other objects at the same range. This operation also involves the Doppler processing with the temporal steering vector (3.5) which extracts the velocity component.

3.3 Simultaneous tracking and reflection coefficient estimation

In the previous section, the detector defined in (3.9) needs to perform tracking object kinematics over K CPIs (i.e., $\mathbf{X}_{1:K}$) and the estimation of the other parameters (i.e., $\boldsymbol{\alpha}$ and $\Delta \mathbf{t}$) in order to evaluate the likelihood ratio in (3.13). Figure 3.5 shows the block diagram of the proposed scheme. This scheme is on-line processing when the receiver collects all radar data cubes from M reflection channels at the k th CPI as the processing input.

Let this section consider the trajectory estimation using coherent pulse returns during a CPI (i.e., the radar data cubes). An object trajectory over K CPIs is modelled as

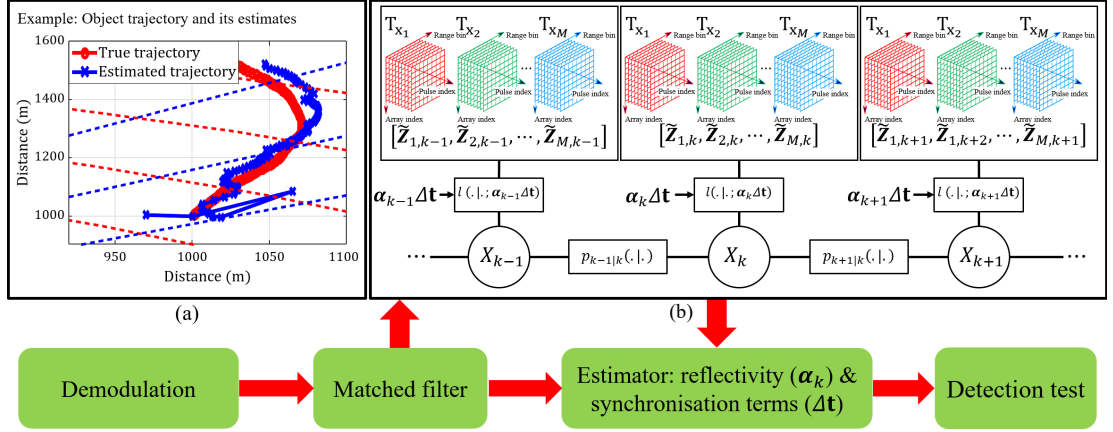


Figure 3.5: Block diagram of the proposed detector: (a) Inference on the object trajectory $\mathbf{X}_{1:K}$, (b) Markov model for the radar data cube measurements. T_{X_1}, \dots, T_{X_M} indicate the M transmitters.

random vector sequences generated by a Markov state space model [24]:

$$\mathbf{X}_{1:K} \sim p(\mathbf{X}_1) \prod_{k=2}^K p(\mathbf{X}_k | \mathbf{X}_{k-1}), \quad (3.16)$$

where the Markov transition density is selected as

$$p(\mathbf{X}_k | \mathbf{X}_{k-1}) = \mathcal{N}(\mathbf{X}_k; \mathbf{F}\mathbf{X}_{k-1}, \mathbf{Q})$$

$$\mathbf{F} = \begin{bmatrix} 1 & 0 & \Delta & 0 \\ 0 & 1 & 0 & \Delta \\ 0 & 0 & 1 & 0 \\ 0 & 0 & 0 & 1 \end{bmatrix}, \quad (3.17)$$

where Δ is the time interval between two consecutive pulse train transmissions (or, the illumination period), \mathbf{F} models constant velocity motion, and \mathbf{Q} is the covariance matrix specifying the level of the process noise modelling unknown manoeuvres [96, Chp.6]. For example, a variance of σ_v^2 in each direction of the velocity is modelled with

$$\mathbf{Q} = \sigma_v^2 \times \begin{bmatrix} \frac{\Delta^3}{3} & 0 & \frac{\Delta^2}{2} & 0 \\ 0 & \frac{\Delta^3}{3} & 0 & \frac{\Delta^2}{2} \\ \frac{\Delta^2}{2} & 0 & \Delta & 0 \\ 0 & \frac{\Delta^2}{2} & 0 & \Delta \end{bmatrix}. \quad (3.18)$$

As explained in (3.17), the constant velocity motion model is selected, which does

not have an acceleration term as the input parameter needs to be estimated. There are various motion (or dynamic) models that introduce target manoeuvres based on the acceleration term in tracking frameworks, such as a constant acceleration motion model [96, Chp.6], a constant acceleration turn rate motion model [97], and a Brownian motion model that contains unknown acceleration rates as Brownian dynamics (see, for example, [98]). These motion models can be applied to (3.17) in order to improve tracking performance. However, the primary problem considered in this chapter is the detection problem defined in Section 3.2.3, and the detection performance will be measured in the same setup used in [4] for the comparison in Section 3.6. For this reason, the constant velocity motion model holds in the rest of this chapter.

The initial distribution, $p(\mathbf{X}_1)$, is selected as a uniform distribution over the range-bearing interval for the detection test due to no prior knowledge of the object kinematics. This interval often corresponds to the radar specific resolution bin. Let this denote the corresponding bounded set in the state-space by \mathcal{B} , and a uniform distribution on \mathcal{B} by $U_{\mathcal{B}}$:

$$p(\mathbf{X}_1) = U_{\mathcal{B}}(\mathbf{X}_1). \quad (3.19)$$

Sequential estimation of $\mathbf{X}_{1:K}$ is performed by using Bayesian recursive filtering [24] as explained in Section 2.6. Suppose the distribution of the state variable at the time step $k - 1$ is given based on all the measurements collected up to this time step:

$$p(\mathbf{X}_{k-1}|\mathbf{Z}_{1:k-1}).$$

In order to update this prior information with the measurement at the k th CPI, the Chapman-Kolmogorov equation is, first, realised, and then the prediction density is found as

$$p(\mathbf{X}_k|\mathbf{Z}_{1:k-1}) = \int_{\mathbf{X}_{k-1}} p(\mathbf{X}_k|\mathbf{X}_{k-1})p(\mathbf{X}_{k-1}|\mathbf{Z}_{1:k-1})d\mathbf{X}_{k-1}, \quad (3.20)$$

where the first term inside the integral is the Markov transition given by (3.17).

The update stage of the proposed filtering starts with the product of the measurement

likelihood and a prior density for all the unknowns. This density is found as

$$p(\mathbf{X}_k, \boldsymbol{\alpha}_k, \Delta \mathbf{t} | \mathbf{Z}_{1:k}) \propto l(\mathbf{Z}_k | \mathbf{X}_k, \boldsymbol{\alpha}_k, \Delta \mathbf{t}, \mathbf{Z}_{1:k-1}) p(\boldsymbol{\alpha}_k, \Delta \mathbf{t}, \mathbf{X}_k | \mathbf{Z}_{1:k-1}). \quad (3.21)$$

Here, the measurement likelihood is independent of the previous measurements collected up to $k - 1$ CPIs as discussed in Section 3.2.4:

$$l(\mathbf{Z}_k | \mathbf{X}_k, \boldsymbol{\alpha}_k, \Delta \mathbf{t}, \mathbf{Z}_{1:k-1}) = l(\mathbf{Z}_k | \mathbf{X}_k, \boldsymbol{\alpha}_k, \Delta \mathbf{t})$$

This likelihood is given by the product of the numerator terms in the likelihood ratio in (3.13) over the object's range bins and M reflection channels for the time step k :

$$l(\mathbf{Z}_k | \mathbf{X}_k, \boldsymbol{\alpha}_k, \Delta \mathbf{t}) \propto \prod_{m=1}^M \prod_{r \in \mathcal{E}_m(\mathbf{X}_k)} l(\mathbf{Z}_{m,k}(r) | \mathbf{X}_k, \alpha_{m,k}, \Delta t_m, H = H_1), \quad (3.22)$$

and is easily computed by evaluating complex Gaussian densities as discussed in Section 3.2.4.

The second term on the right-hand side of (3.21) is rewritten by using the chain rule of probabilities:

$$p(\boldsymbol{\alpha}_k, \Delta \mathbf{t}, \mathbf{X}_k | \mathbf{Z}_{1:k-1}) = p(\boldsymbol{\alpha}_k, \Delta \mathbf{t} | \mathbf{X}_k, \mathbf{Z}_{1:k-1}) p(\mathbf{X}_k | \mathbf{Z}_{1:k-1}), \quad (3.23)$$

where $p(\boldsymbol{\alpha}_k, \Delta \mathbf{t} | \mathbf{X}_k, \mathbf{Z}_{1:k-1})$ is a prior density for the reflection coefficient and the synchronisation term, conditioned on \mathbf{X}_k and $\mathbf{Z}_{1:k-1}$. Here, this prior density is unknown: One reasonable approach of this selection is to use a non-informative prior such as Jeffrey's prior [99, Chp.5]. This is useful when it leads to tractable computations in (3.21) (see, for example, [100]). In the problem setting considered in this section, however, Jeffrey's priors for the reflection coefficients and the synchronisation terms are constant and do not help in finding a tractable form in (3.21).

In order to tackle this challenge, an empirical Bayes approach [92] is proposed: (3.21) is, first, rewritten by using the chain rule of probabilities. This quantity is found as

$$p(\mathbf{X}_k, \boldsymbol{\alpha}_k, \Delta \mathbf{t} | \mathbf{Z}_{1:k}) = p(\mathbf{X}_k | \mathbf{Z}_{1:k}, \boldsymbol{\alpha}_k, \Delta \mathbf{t}) p(\boldsymbol{\alpha}_k, \Delta \mathbf{t} | \mathbf{Z}_{1:k}), \quad (3.24)$$

and the proposed posterior density in order to update the prediction density in (3.17)

is found by marginalising out $\boldsymbol{\alpha}$ and $\Delta\mathbf{t}$:

$$p(\mathbf{X}_k|\mathbf{Z}_{1:k}) = \int \int_{\boldsymbol{\alpha}_k \Delta\mathbf{t}} p(\mathbf{X}_k|\mathbf{Z}_{1:k}, \boldsymbol{\alpha}_k, \Delta\mathbf{t}) p(\boldsymbol{\alpha}_k, \Delta\mathbf{t}|\mathbf{Z}_{1:k}) d\boldsymbol{\alpha}_k d\Delta\mathbf{t}. \quad (3.25)$$

Here, the reflection coefficients and the synchronisation terms act as model parameters to be selected, and the second term inside the integration is similar to a prior for them. Because this prior is conditioned on the measurements, more probability mass should be concentrating at the maximum likelihood (ML) estimates of these values. Let this density be selected:

$$\begin{aligned} p(\boldsymbol{\alpha}_k, \Delta\mathbf{t}|\mathbf{Z}_{1:k}) &= p(\boldsymbol{\alpha}_k|\mathbf{Z}_{1:k}) p(\Delta\mathbf{t}|\mathbf{Z}_{1:k}) \\ p(\boldsymbol{\alpha}_k|\mathbf{Z}_{1:k}) &\leftarrow \delta_{\hat{\boldsymbol{\alpha}}_k}(\boldsymbol{\alpha}_k) \\ p(\Delta\mathbf{t}|\mathbf{Z}_{1:k}) &\leftarrow \delta_{\hat{\Delta\mathbf{t}}}(\Delta\mathbf{t}), \end{aligned} \quad (3.26)$$

where \leftarrow denotes assignment and δ is Dirac's delta distribution. In other words, the model densities given the measurements are selected as a Dirac's delta distribution concentrated in the vicinity of their ML estimates, $\hat{\boldsymbol{\alpha}}_k$ and $\hat{\Delta\mathbf{t}}$, respectively.

After substituting from the empirical priors in (3.26) into (3.25), one obtains the empirical Bayes update within the proposed filtering (see, Figure 3.5) :

$$p(\mathbf{X}_k|\mathbf{Z}_{1:k}) \propto l(\mathbf{Z}_k|\mathbf{X}_k, \hat{\boldsymbol{\alpha}}_k, \hat{\Delta\mathbf{t}}) p(\mathbf{X}_k|\mathbf{Z}_{1:k-1}), \quad (3.27)$$

where \propto denotes approximate proportionality.

Note that the approximation accuracy is better when these ML estimates are obtained using informative likelihoods (as quantified by their Fisher information) and equivalently have small Cramér-Rao bounds (CRBs). When these ML estimates are reasonably accurate, the empirical Bayes update is an accurate approximation in comparison to the otherwise intractable filtering update equations. This approach is also ensured by the use of an array receiver. The details of ML estimates of $\boldsymbol{\alpha}$ and $\Delta\mathbf{t}$ will be discussed in Section 3.4. For the remaining part of this section, it is assumed that these estimates are given.

For realising the recursive filtering equations, a sequential Monte Carlo (SMC) approach known as the particle filter [77] is employed. In particular, a bootstrap filtering approach is used for estimating the object trajectory: The prediction stage at the time step $k = 1$ is realised by forming a regular grid of P points over \mathcal{B} representing samples generated from the initial state distribution in (3.19). These points constitute an equally weighted set of particles. For $k > 1$, the weighted samples (or, particles) representing the state posterior in the previous step will be found. Let this set denote

$$\left\{ \mathbf{X}_{k-1}^{(p)}, \zeta_{k-1}^{(p)} \right\}_{p=1}^P,$$

where $\zeta_{k-1}^{(p)}$ is the weight of the p th sample. The prediction stage is then realised by sampling from the Markov transition:

$$\mathbf{X}_{k|k-1}^{(p)} \sim p(\cdot | \mathbf{X}_{k-1}^{(p)}), \quad p = 1, \dots, P. \quad (3.28)$$

The weights of these samples in the particle set $\{\mathbf{X}_{k|k-1}^{(p)}, \zeta_{k|k-1}^{(p)}\}$ is given by

$$\zeta_{k|k-1}^{(p)} = \zeta_{k-1}^{(p)}, \quad (3.29)$$

in order for this set to represent the prediction density in (3.20).

In the update stage, the same sample set is used to represent the state posterior in (3.27):

$$\mathbf{X}_k^{(p)} \leftarrow \mathbf{X}_{k|k-1}^{(p)} \quad p = 1, \dots, P, \quad (3.30)$$

where \leftarrow denotes assignment. The weights of these samples need to be adjusted using the measurement likelihood (as per the importance sampling principle [101]):

$$\begin{aligned} \zeta_k^{(p)} &= \frac{\tilde{\zeta}_k^{(p)}}{\sum_{p'=1}^P \tilde{\zeta}_k^{(p')}}, \\ \tilde{\zeta}_k^{(p)} &= \zeta_{k|k-1}^{(p)} l(\mathbf{Z}_k | \mathbf{X}_k = \mathbf{X}_k^{(p)}, \hat{\boldsymbol{\alpha}}_k, \Delta \hat{\mathbf{t}}), \end{aligned} \quad (3.31)$$

After finding the normalised weights in (3.31), the degeneracy of the weighted particles is tested by finding the number of effective particles:

$$N_{eff} = \frac{1}{\sum_{p=1}^P \left(\zeta_k^{(p)} \right)^2} \quad (3.32)$$

and comparing it with a threshold, \mathcal{T}_{eff} . When $N_{eff} < \mathcal{T}_{eff}$, re-sampling and post-regularised steps (see, for example, [102, Chp.12]) are performed in order to avoid degeneracy phenomenon, in which after a few recursions, all-but-one of particles might have negligible weighted values and sample impoverishment, which is a loss of diversity among particles due to the small number of very high weighted particles [77]. The output of these steps is a new set of equally weighted samples:

$$\{\zeta_k^{(p)} \leftarrow 1/P, \mathbf{X}_k^{(p)} \leftarrow \tilde{\mathbf{X}}_k^{(p)}\}_{p=1}^P.$$

Here,

$$\zeta_k^{(p)} \leftarrow 1/P \quad (3.33)$$

is the output of the re-sampling, and $\tilde{\mathbf{X}}^{(p)}$ is the output of the post-regularised step, which is found in [102, Chp.12]:

$$\tilde{\mathbf{X}}_k^{(p)} = \mathbf{X}_{k|k-1}^{(p)} + h\mathbf{I}_{n_x}\boldsymbol{\varepsilon}_x^{(p)}, \quad (3.34)$$

where $h = A_K P^{-\frac{1}{n_x+4}}$ and $A_K = (\frac{4}{(n_x+2)})$ denote the bandwidth of a kernel and its coefficient, respectively, from Equation (12.2.7) in [102, Chp.12], and $n_x = 4$ is the dimension of \mathbf{X}_k . Here, $\boldsymbol{\varepsilon}_x^{(p)}$ is an $n_x \times 1$ vector and denotes the regularisation samples generated from the Gaussian kernel with zero mean and covariance \mathbf{I}_{n_x} in this filtering:

$$\boldsymbol{\varepsilon}_x^{(p)} \sim \mathcal{N}(\cdot; \mathbf{0}, \mathbf{I}_{n_x}),$$

where \mathbf{I}_{n_x} is the $n_x \times n_x$ identity matrix. Using the proposed particle filter, the object state, \mathbf{X}_k , at the k th CPI is estimated by using the empirical weighted average:

$$\hat{\mathbf{X}}_k = \sum_{p=1}^P \zeta_k^{(p)} \mathbf{X}_{k|k-1}^{(p)}, \quad (3.35)$$

where $\hat{\mathbf{X}}_k$ denotes the estimated object state, \mathbf{X}_k .

A remarkable feature of the processing scheme driven by the Bayesian recursions above is that no fixed selections of the spatio-temporal steering vectors are used. The evaluation of the likelihood in the update stage in (3.31) specifies the steering vectors through (3.3) and (3.14) as a function of the state value, $\mathbf{X}_k^{(p)}$. Because $\mathbf{X}_k^{(p)}$ is generated

Algorithm 1 Particle EM algorithm for estimation of the reflection coefficients

```

1: Input:  $\alpha^{(0)}, \epsilon$  ▷ Initial guess and termination threshold
2: Input:  $\{\zeta_{k|k-1}^{(p)} X_{k|k-1}^{(p)}\}_{p=1}^P$  ▷ Particles from  $p(X_k|\mathbf{Z}_{1:k-1})$ 
3:  $i \leftarrow 1, \alpha^{(1)} \leftarrow \infty$  ▷ Initialisation for the iterations
4: while  $\|\alpha^{(i)} - \alpha^{(i-1)}\| > \epsilon$  do ▷ Test convergence
5:   Find  $\hat{Q}(\alpha_k, \alpha_k^{(i-1)})$  in (3.44) using (3.42), (3.43) ▷ E step
6:   Find  $\alpha^{(i)} \leftarrow \{\hat{\alpha}_{m,k}\}_{m=1}^M$  using (3.45), (3.43) ▷ M step
7:    $i \leftarrow i + 1$ 
8: end while
9: Return  $\hat{\alpha}_k \leftarrow \alpha^{(i)}$ 
    
```

by sequential processing of the data cubes over CPIs, the resulting set of spatio-temporal steering vectors adapt to the measurements. This is in stark contrast with conventional processing chains in which the bearing and Doppler space is sampled with equal size steps leading to a fixed set of steering vectors and corresponding resolution bins. Thus, a super-resolution effect is achieved when finding the object locations. This will be demonstrated in Section 3.6.

3.4 Maximum Likelihood estimation of unknown parameters

Let this section consider ML estimators for the reflection coefficients, α_k , and the synchronisation terms, $\Delta \mathbf{t}$. Section 3.4.1 discusses the ML estimator for the reflection coefficients that proposes an iterative EM algorithm at each step of the recursive filtering as explained in Section 3.3. Then, Section 3.4.2 introduces the ML synchronisation term estimator used with the direct channel measurements in (3.8). These estimates are substituted into both the update stage of the filtering and the likelihood ratio in order to evaluate them (see, Figure 3.5).

3.4.1 ML estimation of the reflection coefficients

The reflection coefficient associated with an object at state, \mathbf{X}_k , is unknown constant during a CPI and varies across consecutive CPIs due to the change of the effective reflective surface (i.e., the object's aspect angle). This might be due to the object

changing its location (hence, changing the strength of the reflected signal) and/or its orientation of reflections. In order to estimate this term, a ML estimator is considered, which finds the most likely value that maximises the likelihood defined in (3.22). Here, there are two unknown terms (i.e., the object state, \mathbf{X}_k , and synchronisation term, $\Delta \mathbf{t}$). The latter term will be found by the direct channel measurements in (3.8) and will be discussed in the next section. It is hence assumed that the synchronisation term, $\Delta \hat{\mathbf{t}}$, is given in this section, and \mathbf{X}_k is treated as unobserved data (or latent variable). Due to this latent variable, the ML estimator, proposed here, uses an EM approach, which offers an iterative solution in which the lower bounds of the logarithm of (3.22) can iteratively be maximised so that the difference between the lower and the actual value leads to zero when the optimal α_k equals the ML estimate [103]. Thus, EM iterations are given for $i = 1, 2, \dots$ by solving the problem:

$$\alpha_k^{(i)} = \arg \max_{\alpha_k} Q(\alpha_k, \alpha_k^{(i-1)}), \quad (3.36)$$

where Q is the function, which needs to be maximised for given $\alpha_k^{(i-1)}$ and $\Delta \hat{\mathbf{t}}$, and is defined:

$$\begin{aligned} Q(\alpha_k, \alpha_k^{(i-1)}) &\triangleq \mathbb{E}\{\log p(\mathbf{X}_k, \mathbf{Z}_k | \alpha_k, \Delta \mathbf{t} = \Delta \hat{\mathbf{t}}) | \mathbf{Z}_k, \alpha_k^{(i-1)}, \Delta \mathbf{t} = \Delta \hat{\mathbf{t}}\} \quad (3.37) \\ &= \int_{\mathbf{X}_k} \log p(\mathbf{X}_k, \mathbf{Z}_k | \alpha_k, \Delta \hat{\mathbf{t}}) \times p(\mathbf{X}_k | \mathbf{Z}_k, \alpha_k^{(i-1)}, \Delta \hat{\mathbf{t}}) d\mathbf{X}_k. \end{aligned}$$

Note that \mathbf{Z}_k is the current measurement at the k th CPI, and \mathbf{X}_k is unknown and treated as the unobserved data in Q .

As discussed in Section 3.2.4, it is assumed that all the unknown variables in the conditional likelihood are independent because one has no influences on the change of the others. Regarding this assumption, the first term inside the integral of (3.37) is given by using Bayes' rule:

$$\begin{aligned} \log p(\mathbf{X}_k, \mathbf{Z}_k | \alpha_k, \Delta \hat{\mathbf{t}}) &= \log\{l(\mathbf{Z}_k | \mathbf{X}_k, \alpha_k, \Delta \hat{\mathbf{t}}) \times p(\mathbf{X}_k | \alpha_k, \Delta \hat{\mathbf{t}})\} \\ &= \log l(\mathbf{Z}_k | \mathbf{X}_k, \alpha_k, \Delta \hat{\mathbf{t}}) + \log p(\mathbf{X}_k), \end{aligned} \quad (3.38)$$

where $\log p(\mathbf{X}_k)$ is not dependent on α_k . The second term inside the integral of (3.37)

can also be expressed using Bayes' rule:

$$p(\mathbf{X}_k | \mathbf{Z}_k, \boldsymbol{\alpha}_k^{(i-1)}, \Delta \hat{\mathbf{t}}) \propto l(\mathbf{Z}_k | \mathbf{X}_k, \boldsymbol{\alpha}_k^{(i-1)}, \Delta \hat{\mathbf{t}}) \times p(\mathbf{X}_k | \boldsymbol{\alpha}_k^{(i-1)}, \Delta \hat{\mathbf{t}}). \quad (3.39)$$

Here, $\boldsymbol{\alpha}_k^{(i-1)}$ and $\Delta \hat{\mathbf{t}}$ are given, and $p(\mathbf{X}_k | \cdot)$ is a prior density and selected as the prediction density in (3.20) because this prediction density is already defined in (3.20) and is realised in (3.28). \mathbf{X}_k is also independent to the other variables:

$$p(\mathbf{X}_k | \boldsymbol{\alpha}_k^{(i-1)}, \Delta \hat{\mathbf{t}}) \leftarrow p(\mathbf{X}_k | \mathbf{Z}_{1:k-1}). \quad (3.40)$$

As result, the Q in (3.37) is rewritten using (3.38) (3.39) and (3.40):

$$Q(\boldsymbol{\alpha}_k, \boldsymbol{\alpha}_k^{(i-1)}) \propto \int_{\mathbf{X}_k} \log l(\mathbf{Z}_k | \mathbf{X}_k, \boldsymbol{\alpha}_k, \Delta \hat{\mathbf{t}}) \times l(\mathbf{Z}_k | \mathbf{X}_k, \boldsymbol{\alpha}_k^{(i-1)}, \Delta \hat{\mathbf{t}}) \times p(\mathbf{X}_k | \mathbf{Z}_{1:k-1}) d\mathbf{X}_k. \quad (3.41)$$

Now, it focus on the computation of the expectation in (3.41) and its maximisation. The samples, generated in the prediction stage in (3.28) and (3.29), lead to an importance sampling estimate of the expectation. This is a novel approach that realises the ML estimate of $\boldsymbol{\alpha}_k$ and the update density in (3.27) within the Bayesian recursions. Given $\left\{ \mathbf{X}_{k|k-1}^{(p)}, \zeta_{k|k-1}^{(p)} \right\}_{p=1}^P$, this importance sampling estimate is given by

$$\hat{Q}(\boldsymbol{\alpha}_k, \boldsymbol{\alpha}_k^{(i-1)}) \propto \sum_{p=1}^P \xi_p^{(i-1)} \log l(\mathbf{Z}_k | \mathbf{X}_k = \mathbf{X}_{k|k-1}^{(p)}, \boldsymbol{\alpha}_k, \Delta \hat{\mathbf{t}}), \quad (3.42)$$

$$\xi_p^{(i-1)} = \frac{l(\mathbf{Z}_k | \mathbf{X}_k = \mathbf{X}_{k|k-1}^{(p)}, \boldsymbol{\alpha}_k^{(i-1)}, \Delta \hat{\mathbf{t}}) \zeta_{k|k-1}^{(p)}}{\sum_{p'=1}^P l(\mathbf{Z}_k | \mathbf{X}_k = \mathbf{X}_{k|k-1}^{(p')}, \boldsymbol{\alpha}_k^{(i-1)}, \Delta \hat{\mathbf{t}}) \zeta_{k|k-1}^{(p')}}, \quad (3.43)$$

where \hat{Q} denotes the estimate of the term proportional to the Q in (3.41). This proposed approximation is new and a sum of terms quadratic in $\boldsymbol{\alpha}_k$. This can easily be seen by substituting from (3.14) and (3.22) to (3.42). The resulting expression is given by

$$\begin{aligned} \hat{Q}(\boldsymbol{\alpha}_k, \boldsymbol{\alpha}_k^{(i-1)}) &= \sum_{p=1}^P \sum_{m=1}^M \sum_{r \in \mathcal{E}_m(\mathbf{X}_{k|k-1}^{(p)})} \xi_p^{(i-1)} \\ &\times \left(-\log(\pi^{LN} \det(\Sigma_m)) - \mathbf{Z}_{m,k}^H(r) \Sigma_m^{-1} \mathbf{Z}_{m,k}(r) \right. \\ &+ 2 \operatorname{Re}\{\alpha_{m,k}^* \mathbf{s}_m^H(r, \mathbf{X}_{k|k-1}^{(p)}, \Delta \hat{\mathbf{t}}_m) \Sigma_m^{-1} \mathbf{Z}_{m,k}(r)\} \\ &\left. - |\alpha_{m,k}|^2 \mathbf{s}_m^H(r, \mathbf{X}_{k|k-1}^{(p)}, \Delta \hat{\mathbf{t}}_m) \Sigma_m^{-1} \mathbf{s}_m(r, \mathbf{X}_{k|k-1}^{(p)}, \Delta \hat{\mathbf{t}}_m) \right) \end{aligned} \quad (3.44)$$

After taking the first order partial derivative of (3.44) with respect to $\alpha_{m,k}$ and setting it to zero, the ML estimate of the m th reflection channel is found in closed form:

$$\hat{\alpha}_{m,k} = \frac{\sum_{p=1}^P \sum_{r \in \mathcal{E}_m(\mathbf{X}_{k|k-1}^{(p)})} \xi_p^{(i-1)} \mathbf{s}_m^H(r, \mathbf{X}_{k|k-1}^{(p)}, \Delta \hat{t}_m) \Sigma_m^{-1} \mathbf{Z}_{m,k}(r)}{\sum_{p=1}^P \sum_{r \in \mathcal{E}_m(\mathbf{X}_{k|k-1}^{(p)})} \xi_p^{(i-1)} \mathbf{s}_m^H(r, \mathbf{X}_{k|k-1}^{(p)}, \Delta \hat{t}_m) \Sigma_m^{-1} \mathbf{s}_m(r, \mathbf{X}_{k|k-1}^{(p)}, \Delta \hat{t}_m)}. \quad (3.45)$$

Here, the ML estimate, obtained by the proposed EM approach within the Bayesian filtering recursions, contains the set of weighted particles, which completely defers from that of existing EM algorithms, in which equally weighted samples in evaluating the Monte Carol integration are used for the expectation (see, for example [104, 105]).

The ML estimator in (3.45) takes the inner product of the “whitened” measurements with the signal model \mathbf{s}_m given in (3.3) for each state particle, $\mathbf{X}_{k|k-1}^{(p)}$. This operation effectively performs digital beam-forming towards the particle state in which an object is located in a surveillance region. The conventional beam-forming, however, needs to scan all the surveillance region with a regular grid (i.e., angular resolution, $\Delta\theta$) in order to find the angle of arrival as discussed in Section 2.3.1. This operation also matches its approach speed through its Doppler frequency encoded in \mathbf{s}_m . As a result, the estimator will not be rejecting interference from other objects unless they appear very close to the state value in terms of the achievable spatial and Doppler resolution.

After finding $\hat{\boldsymbol{\alpha}}_k^{(i)} = \{\hat{\alpha}_{m,k}^{(i)}\}_{m=1}^M$ for M reflection coefficients using (3.45), convergence is tested by comparing the norm of the difference between parameter configurations, which is found in consecutive iterations with a threshold. In other words, the EM iterations are terminated at i when

$$\| \boldsymbol{\alpha}_k^{(i)} - \boldsymbol{\alpha}_k^{(i-1)} \| < \epsilon,$$

where $\|\cdot\|$ denotes the complex Euclidean norm. A pseudo-code of these steps are given in Algorithm 1.

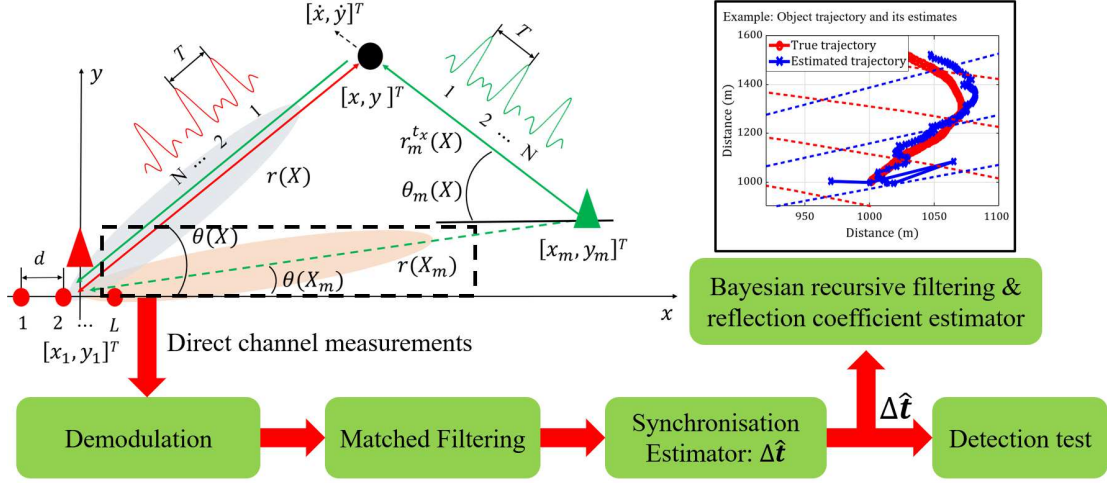


Figure 3.6: Block diagram of the proposed synchronisation term estimator: The input of this estimator is the direct channel (black-dashed box) measurements, and the receiver has full knowledge of both the transmission characteristics and all the transmitter's locations as the prior knowledge. The resulting estimate (i.e., $\Delta \hat{t}$) is the inputs of both, the Bayesian filtering recursions and the proposed detector.

3.4.2 Synchronisation of the local processor with remote transmitters

Let this section consider the ML estimation of the unknown synchronisation term, Δt_m , parametrising the time origin shift between the local receiver and the m th separately located transmitter. Figure 3.6 shows the overall processing sequences of the synchronisation term estimator using the block diagram: The proposed approach exploits, in fact, the data cube for the m th remote (or bistatic) channel that contains direct path signals (depicted by the dashed black box) from the separately located transmitter. This collection can be done by simultaneously diverting multiple (digital) beams towards both the transmitter spatial states and the object spatial state for other processing tasks on the data cube. For example, the latter, which is related to the estimation of an object's trajectory and reflection coefficients, is not the same regions of the transmitter spatial states. Here, it is assumed that the receiver has full knowledge of both the transmission characteristics defined in (3.1) and the system characteristics in (3.7) as well as all the transmitter's locations, $\mathbf{X}^{(tx)} = \{\mathbf{X}_m^{(tx)}\}_{m=1}^M$, as the prior knowledge. The input of this estimator is the m th radar data cube that contains the direct path signal in (3.8).

When reflectors are present, the superposition of this signal and reflections from different spatio-temporal states is collected. In order to recover the direct path signal (see, the black-dashed box), this uses a spatio-temporal steering vector that is matched to $\tilde{\mathbf{s}}_m$ in (3.8). This steering vector for the m th direct channel with the known location of the m th transmitter, $\mathbf{X}_m^{(t_x)}$, is given by

$$\begin{aligned}\mathbf{h}(\mathbf{X}_m^{(t_x)}) &\triangleq \mathbf{s}_s(\theta(\mathbf{X}_m^{(t_x)})) \otimes \mathbf{s}_t\left(\frac{\tau(\mathbf{X}_m^{(t_x)})}{2}, \Omega_m(\mathbf{X}_m^{(t_x)}) = 0\right), \\ &= s\left(\frac{\tau(\mathbf{X}_m^{(t_x)})}{2}\right) \times \mathbf{s}_s(\theta(\mathbf{X}_m^{(t_x)})) \otimes \mathbf{1},\end{aligned}\quad (3.46)$$

where $\theta(\mathbf{X}_m^{(t_x)})$ is the AoA from the m th transmitter given in (2.9), $\frac{\tau(\mathbf{X}_m^{(t_x)})}{2}$ is the ToF in one-way propagation between the transmitter and the receiver using (2.5), and $\mathbf{1}$ is an $N \times 1$ all ones vector. All these values for M direct channels are known at the receiver.

Note that this filter is nothing but a (scaled) beam-forming vector diverting a beam towards $\theta(\mathbf{X}_m^{(t_x)})$ and maps the $LN \times 1$ measurement vector, $\mathbf{Z}_m(r)$, to a single complex value given by

$$\begin{aligned}d_m(r) &\triangleq \mathbf{h}(\mathbf{X}_m^{(t_x)})^H \mathbf{Z}_m(r) \\ &= LN\sqrt{E_m}s(\Delta t_m)\Lambda_m\left(rT_p - \frac{\tau(\mathbf{X}_m^{(t_x)})}{2} - \Delta t_m\right) + n_m(r).\end{aligned}\quad (3.47)$$

Here, E_m is the received energy, which can be calculated by using (3.6) and (3.7) with the known system parameters, and the noise term is the inner product of the beam-forming vector and the complex Gaussian measurement noise in (3.2):

$$n_m(r) = \mathbf{h}(\mathbf{X}_m^{(t_x)})^H \mathbf{n}_m(r)$$

which itself is a random variable with a complex Gaussian distribution of mean zero and variance:

$$\sigma_{d,m}^2 = \mathbf{h}^H(\mathbf{X}_m^{(t_x)})\Sigma_m\mathbf{h}(\mathbf{X}_m^{(t_x)}).$$

As a result, the likelihood to be maximised is

$$l(d_m(0), \dots, d_m(\Gamma-1)|\Delta t_m) = \prod_{r=0}^{\Gamma-1} \mathcal{CN}(d_m(r); \mu_{d,m}(\Delta t_m), \sigma_{d,m}^2) \quad (3.48)$$

where the expected value of the complex Gaussian distributions as a function of Δt_m is given by

$$\mu_{d,m}(\Delta t_m) = \sqrt{E_m} L N \exp(-j\omega_c \Delta t_m) \times \Lambda_m \left(r T_p - \frac{\tau(\mathbf{X}_m^{(t_x)})}{2} - \Delta t_m \right). \quad (3.49)$$

Note that only those range bins for which the argument of Λ_m falls within $(0, 2T_p)$ contribute to the maximisation. Otherwise, the corresponding distribution is the same with that for the noise term. These range bins are hence given by

$$\tilde{\mathcal{E}}_m(\Delta t_m) = \begin{cases} \{r_m, r_m + 1\} & r_m T_p < \frac{\tau(\mathbf{X}_m^{(t_x)})}{2} + \Delta t_m \\ \{r_m\} & r_m T_p = \frac{\tau(\mathbf{X}_m^{(t_x)})}{2} + \Delta t_m \\ \{r_m, r_m - 1\} & r_m T_p > \frac{\tau(\mathbf{X}_m^{(t_x)})}{2} + \Delta t_m \end{cases}. \quad (3.50)$$

Here

$$r_m = \left\lfloor \frac{\tau(\mathbf{X}_m^{(t_x)})}{2 \times T_p} + \frac{\Delta t_m}{T_p} \right\rfloor,$$

where this range bin is different to (3.12) due to one-way propagation and contains the same synchronisation term with (3.12). Thus, the ML estimator that takes into account k data cubes at time k , which starts from the first one up to, is given by

$$\begin{aligned} \Delta \hat{t}_m &= \arg \max_{\Delta t_m} J_k(\Delta t_m) \\ J_k(\Delta t_m) &= \log \prod_{k'=1}^k \prod_{r \in \tilde{\mathcal{E}}_m(\Delta t_m)} \mathcal{CN}(d_{m,k'}(r); \mu_{d,m}(\Delta t_m), \sigma_{d,m}^2) \\ &\propto \sum_{k'=1}^k \sum_{r \in \tilde{\mathcal{E}}_m(\Delta t_m)} (d_{m,k'}(r) - \mu_{d,m}(\Delta t_m))^* \times (d_{m,k'}(r) - \mu_{d,m}(\Delta t_m)), \end{aligned} \quad (3.51)$$

where $k' = 1, \dots, k$ indicates the k' th CPI up to the k th CPI.

Note that the relation between Δt and the objective function, J_k , is a concave relation on the average (and as k increases, asymptotically). However, (3.49) does not yield a closed-form solution and render gradient-free iterative methods such as one-dimensional line search techniques [106] as better alternatives. These algorithms require only evaluation of (3.51) and iteratively reduce an initially selected interval of uncertainty. For this reason, the proposed estimator uses the golden section search algorithm [106]

Algorithm 2 Maximum likelihood estimation of Δt_m via golden section line search: The initial interval of uncertainty is selected as $[\Delta \hat{t}_0 - T_p, \Delta \hat{t}_0 + T_p]$ as detailed in Section 3.4.2.

```

1: Input:  $[\Delta t_1, \Delta t_2]$ ,  $\epsilon = \frac{T_p}{10}$   $\triangleright$  Initial interval of uncertainty and termination threshold
2:  $\alpha \leftarrow 0.618$ 
3:  $\Delta \tilde{t}_1 \leftarrow \Delta t_1 + (1 - \alpha)(\Delta t_2 - \Delta t_1)$   $\triangleright$  Evaluation point 1
4:  $\Delta \tilde{t}_2 \leftarrow \Delta t_1 + \alpha(\Delta t_2 - \Delta t_1)$   $\triangleright$  Evaluation point 2
5: Compute  $J_k(\Delta \tilde{t}_1)$  and  $J_k(\Delta \tilde{t}_2)$  using (3.51), (3.49), (3.47)
6: while  $|\Delta t_2 - \Delta t_1| > \epsilon$  do  $\triangleright$  Until  $\epsilon$  accuracy is reached
7:     if  $J_k(\Delta \tilde{t}_1) > J_k(\Delta \tilde{t}_2)$  then
8:          $\Delta t_2 \leftarrow \Delta \tilde{t}_2$   $\triangleright$  New interval:  $[\Delta t_1, \Delta \tilde{t}_2]$ 
9:          $\Delta \tilde{t}_2 \leftarrow \Delta \tilde{t}_1$ ,  $J_k(\Delta \tilde{t}_2) \leftarrow J_k(\Delta \tilde{t}_1)$   $\triangleright$  Assignments
10:         $\Delta t_1 \leftarrow \Delta t_1 + (1 - \alpha)(\Delta t_2 - \Delta t_1)$ 
11:        Compute  $J_k(\Delta \tilde{t}_1)$  using (3.51), (3.49), (3.47)  $\triangleright$  New evaluation
12:    else
13:         $\Delta t_1 \leftarrow \Delta \tilde{t}_1$   $\triangleright$  New interval:  $[\Delta \tilde{t}_1, \Delta t_2]$ 
14:         $\Delta \tilde{t}_1 \leftarrow \Delta \tilde{t}_2$ ,  $J_k(\Delta \tilde{t}_1) \leftarrow J_k(\Delta \tilde{t}_2)$   $\triangleright$  Assignments
15:         $\Delta \tilde{t}_2 \leftarrow \Delta t_1 + \alpha(\Delta t_2 - \Delta t_1)$ 
16:        Compute  $J_k(\Delta \tilde{t}_2)$  using (3.51), (3.49), (3.47)  $\triangleright$  New evaluation
17:    end if
18: end while
19: if  $J_k(\Delta \tilde{t}_1) > J_k(\Delta \tilde{t}_2)$  then
20:     Return  $\Delta \hat{t}_m = \Delta t_1$ 
21: else
22:     Return  $\Delta \hat{t}_m = \Delta t_2$ 
23: end if
    
```

and selects the initial interval for Δt_m based on a preliminary search over the grid of values, $\Delta t_m \in \{0, T_p, 2T_p, \dots, (\Gamma - 1)T_p\}$, which yields a rough estimate. Let this term denote $\Delta \hat{t}_0$, which produces

$$\hat{r}_m = \left\lfloor \frac{\tau(\mathbf{X}_m^{(t_x)})}{2 \times T_p} + \frac{\Delta \hat{t}_0}{T_p} \right\rfloor.$$

The initial interval of uncertainty is selected as $[\Delta \hat{t}_0 - T_p, \Delta \hat{t}_0 + T_p]$. The golden section search reduces the width of this interval exponentially to a ratio of $(0.618)^{\nu-1}$ after ν iterations [106]. Therefore, in eight iterations, this width reduces below one tenth of a pulse duration (i.e., $\frac{T_p}{10}$). A termination threshold in this golden section search algorithm is hence selected as this value ($\epsilon = \frac{T_p}{10}$). This search algorithm is detailed in Algorithm 2.

3.5 Long time integration for detection

Let this section consider the evaluation of the statistical test given in (3.9). The sufficient statistics of this test is given in (3.13)–(3.15) of Section 3.2.4. Here, the results from Sections 3.3 and 3.4 are, first, combined into a single algorithm. Then, Section 3.5.1 provides explicit formulae for finding the threshold as a function of the selected constant false alarm rate, P_{fa} , and integration time k .

In order to evaluate the likelihood ratio in (3.13), $\Delta\hat{\mathbf{t}}$ is, first, estimated using Algorithm 2 for all direct channels. Given this quantity, the target trajectory, $\hat{X}_{1:k}$, is sequentially estimated using Section 3.3. At the prediction stage of the Bayesian filtering recursions for $k = 1, \dots, K$ CPIs, the EM iterations in Algorithm 1 over $k = 1, \dots, K$ produces $\hat{\alpha}_k$. As such, the integration of instantaneous likelihood ratios in (3.15), which is evaluated by given the aforementioned estimates into the test value in (3.13), is carried out recursively. For this purpose, let one define the logarithm of the test value at k :

$$\begin{aligned} \log L_k &\triangleq \sum_{k'=1}^k \sum_{m=1}^M \sum_{r \in \mathcal{E}_m(\hat{\mathbf{X}}_k)} \log L(\mathbf{Z}_{m,k'}(r) | \hat{\mathbf{X}}_{k'}, \hat{\alpha}_{m,k'}, \Delta\hat{t}_m) \\ &= \log L_{k-1} + L(\mathbf{Z}_k(\hat{\mathbf{X}}_k) | \hat{\mathbf{X}}_k, \hat{\alpha}_k, \Delta\hat{\mathbf{t}}), \end{aligned} \quad (3.52)$$

and the second term on the right-hand side of the second line is defined using M reflection channels and the range bins associated with $\hat{\mathbf{X}}_k$ in (3.11):

$$\begin{aligned} L(\mathbf{Z}_k(\hat{\mathbf{X}}_k) | \hat{\mathbf{X}}_k, \hat{\alpha}_k, \Delta\hat{\mathbf{t}}) &\triangleq \sum_{m=1}^M \sum_{r \in \mathcal{E}_m(\hat{\mathbf{X}}_k)} \log L(\mathbf{Z}_{m,k}(r) | \hat{\mathbf{X}}_k, \hat{\alpha}_{m,k}, \Delta\hat{t}_m) \\ &= \sum_{m=1}^M \sum_{r \in \mathcal{E}_m(\hat{\mathbf{X}}_k)} \left(2\text{Re}\{\hat{\alpha}_{m,k}^* \mathbf{s}_m^H(r, \hat{\mathbf{X}}_k, \Delta\hat{t}_m) \Sigma_m^{-1} \mathbf{Z}_{m,k}(r)\} \right. \\ &\quad \left. - |\hat{\alpha}_{m,k}|^2 \mathbf{s}_m^H(r, \hat{\mathbf{X}}_k, \Delta\hat{t}_m) \Sigma_m^{-1} \mathbf{s}_m(r, \hat{\mathbf{X}}_k, \Delta\hat{t}_m) \right). \end{aligned} \quad (3.53)$$

Note that, (3.53) is the contribution of the measurements at time k into the integration in (3.52). The proposed processing performs coherent integration of $\mathcal{E}_m(\hat{\mathbf{X}}_k) \times L \times N$ samples during a CPI in each reflection channel. The integration is non-coherent across

Algorithm 3 The proposed simultaneous tracking and long time integration algorithm

```

1: Input: Data cubes  $\mathbf{Z}_{m,k}$  for channels  $m = 1, \dots, M$ , time steps  $k = 1, \dots, K$   $\triangleright$ 
   see (3.2)
2: Input: Detection threshold  $\mathcal{T}_K$ 
3: Initialisation: Generate particles in the cell under test  $\{\mathbf{X}_1^{(p)}, \zeta_1^{(p)}\}_{p=1}^P$   $\triangleright$  see (3.19)
4: Initialisation:  $\log L_0 \leftarrow 0$ 
5: for  $k = 1, \dots, K$  do
6:   if  $k \geq 2$  then  $\triangleright$  Prediction stage
7:     Generate  $\{\mathbf{X}_{k|k-1}^p, \zeta_{k|k-1}^p\}_{p=1}^P$   $\triangleright$  see (3.28), (3.29)
8:   end if
9:   Find  $\Delta \hat{\mathbf{t}}$  using Algorithm 2 for  $m = 2, \dots, M$   $\triangleright$  see Section 3.4.2
10:  Find  $\hat{\boldsymbol{\alpha}}_k$  using the EM iterations in Algorithm 1
11:  Update  $\{\mathbf{X}_k^{(p)}, \zeta_k^{(p)}\}_{p=1}^P$  using (3.30), (3.31)  $\triangleright$  Update stage
12:  Estimate  $\hat{\mathbf{X}}_k$  using (3.35)
13:  Compute  $L(\mathbf{Z}_k(\hat{\mathbf{X}}_k) | \hat{\mathbf{X}}_k, \hat{\boldsymbol{\alpha}}_k, \Delta \hat{\mathbf{t}})$  using (3.53)
14:   $\log L_k = \log L_{k-1} + L(\mathbf{Z}_k(\hat{\mathbf{X}}_k) | \hat{\mathbf{X}}_k, \hat{\boldsymbol{\alpha}}_k, \Delta \hat{\mathbf{t}})$   $\triangleright$  Integration step, see (3.52)
15: end for
16: if  $\log L_K > \log \mathcal{T}_K$  then  $\triangleright$  The detection test in (3.54)
17:   Return  $H_1$ 
18: else
19:   Return  $H_0$ 
20: end if
    
```

the channels as well as consecutive CPIs. The key is that the object trajectory is taken into account when performing all these simultaneously.

The object detection is hence performed by comparing the output of the aforementioned log-likelihood ratio to a detection threshold:

$$\log L_K \underset{H_0}{\overset{H_1}{\geq}} \log \mathcal{T}_K, \quad (3.54)$$

where $\log \mathcal{T}_K$ is the detection threshold for a given constant false alarm rate (CFAR) for K steps of integration. The next section details the computation of this threshold value. A pseudo-code of the overall process is given in Algorithm 3.

3.5.1 Constant false alarm rate threshold for the detection test

In the hypothesis test in (3.54) it is highly desirable to select the threshold, \mathcal{T}_K , that yields a selected constant false alarm rate (CFAR), P_{fa} . For the calculation of \mathcal{T}_K as a

function of P_{fa} , let one consider the distribution of the likelihood ratio given in (3.13) under the $H = H_0$ hypothesis for the measurement in (3.2). The logarithm of this likelihood ratio after substituting from (3.15) into (3.13) is given by

$$\begin{aligned}\eta_K &\triangleq \log L_K \\ &= \sum_{k=1}^K \sum_{m=1}^M \sum_{r \in \mathcal{E}_m(\mathbf{X}_k)} \eta_{m,k,r}\end{aligned}\quad (3.55)$$

where the terms inside the summations are given by

$$\begin{aligned}\eta_{m,k,r} &= 2\text{Re}\{\mathbf{s}_{m,k,r}^H \Sigma_m^{-1} \mathbf{Z}_{m,k}(r)\} - \mathbf{s}_{m,k,r}^H \Sigma_m^{-1} \mathbf{s}_{m,k,r} \\ \mathbf{s}_{m,k,r} &= \alpha_{m,k} \mathbf{s}_m(r, \mathbf{X}_k, \Delta t_m).\end{aligned}\quad (3.56)$$

The distribution of the real variable, $\eta_{m,k,r}$, is a Gaussian when the signal model, $\mathbf{s}_{m,k,r}$, is known and the measurements, $\mathbf{Z}_{m,k}(r)$, are generated from a complex Gaussian [18, Chp.13] (i.e., $\eta_{m,k,r} \sim \mathcal{N}(\cdot; \mu_{m,k,r}, \sigma_{m,k,r}^2)$) with the moments given by

$$\begin{aligned}\mu_{m,k,r} &= -\mathbf{s}_{m,k,r}^H \Sigma_m^{-1} \mathbf{s}_{m,k,r}, \\ \sigma_{m,k,r}^2 &= 2\mathbf{s}_{m,k,r}^H \Sigma_m^{-1} \mathbf{s}_{m,k,r}.\end{aligned}$$

Owing to the independence of the noise samples, η_K is also Gaussian for the case, i.e., $\eta_K \sim \mathcal{N}(\cdot; \mu_K, \sigma_K^2)$, with the moments given by

$$\mu_K = \sum_{k=1}^K \sum_{m=1}^M \sum_{r \in \mathcal{E}_m(X_k)} \mu_{m,k,r} \quad (3.57)$$

$$\sigma_K^2 = \sum_{k=1}^K \sum_{m=1}^M \sum_{r \in \mathcal{E}_m(X_k)} \sigma_{m,k,r}^2. \quad (3.58)$$

Therefore, the probability of false alarm, P_{fa} , is related to the test variable, η_K , in (3.55)

and the threshold, \mathcal{T}_K , through

$$\begin{aligned} P_{fa} &= Pr\{\eta_K > \log \mathcal{T}_K | H = H_0\} \\ &= \int_{\log \mathcal{T}_K}^{+\infty} \mathcal{N}(\eta'_K; \mu_K, \sigma_K^2) d\eta'_K \\ &= Q\left(\frac{\log \mathcal{T}_K - \mu_K}{\sigma_K}\right) \end{aligned}$$

where $Q(\cdot)$ denotes the tail probability function of the standard normal distribution [18].

As a result, the threshold, \mathcal{T}_K , given P_{fa} for K steps of integration is found as

$$\mathcal{T}_K = \exp\left(Q^{-1}(P_{fa})\sigma_K + \mu_K\right). \quad (3.59)$$

Similarly, the probability of detection, P_d , is related to the integrated value, $\log L_k$, in (3.52) and the threshold, \mathcal{T}_K , through

$$\begin{aligned} P_d &= Pr\{\log L_k > \log \mathcal{T}_K | H = H_1\} \\ &= Q\left(\frac{\log \mathcal{T}_K - \log L_k}{\sigma_K}\right). \end{aligned} \quad (3.60)$$

The relation between P_d and P_{fa} can also be found after substituting (3.59) into (3.60):

$$\begin{aligned} P_d &= Q\left(\frac{Q^{-1}(P_{fa})\sigma_K + \mu_K - \log L_k}{\sigma_K}\right) \\ &= Q\left(Q^{-1}(P_{fa}) + \frac{\mu_K - \log L_k}{\sigma_K}\right). \end{aligned} \quad (3.61)$$

As a summary, the CFAR threshold for the proposed integration scheme is calculated using (3.56)–(3.59) given the true values of the reflection coefficients and the object trajectory specifying (3.56). This clairvoyant threshold is used in Section 3.6 for comparing Algorithm 3 with the clairvoyant integrator and a conventional alternative.

3.5.2 Signal to noise ratio (SNR) in the radar data cube

This subsection provides explicit formulae for the signal to noise ratio (SNR) of the m th channel radar data cube in (3.2). In the problem setting in this chapter, it is assumed that all parameters are independent because regarding the signal model of the m th

reflection channel, which contains the object kinematic (i.e., \mathbf{X}), the reflection coefficient (i.e., α_m), and the synchronisation term (i.e., Δt_m), the change of one parameter produces no influences on the change of the others. Another assumption is that the reflection coefficient varies with the radar cross section (RCS) and the orientation of the object's aspect angle. With these assumptions, SNR at the k th CPI for the m th channel is found as a function of the object state, \mathbf{X}_k , at the r th range bin:

$$\begin{aligned} \text{SNR}_{m,k}(r, \mathbf{X}_k) &\triangleq \frac{\mathbb{E}\{(\alpha_{m,k}\mathbf{s}_m(r, \mathbf{X}_k, \Delta t_m))^T (\alpha_{m,k}\mathbf{s}_m(r, \mathbf{X}_k, \Delta t_m))\}}{\mathbb{E}\{\mathbf{n}_m(r)^T \mathbf{n}_m(r)\}} \\ &= \frac{\mathbb{E}\{\alpha_{m,k}^* \alpha_{m,k}\} \mathbb{E}\{\mathbf{s}_m^T(r, \mathbf{X}_k, \Delta t_m) \mathbf{s}_m(r, \mathbf{X}_k, \Delta t_m)\}}{\text{tr}\{\Sigma_m\}}, \end{aligned} \quad (3.62)$$

where $\alpha_{m,k} \triangleq \text{Re}\{\alpha_{m,k}\} + j\text{Im}\{\alpha_{m,k}\}$ is the complex reflection coefficient of the m th channel which is comprised of a real part, $\text{Re}\{.\}$, and an imaginary part, $\text{Im}\{.\}$, and $\mathbf{s}_m \in \mathbb{C}^{LN \times 1}$ is the signal model associated with the object state, \mathbf{X}_k , as given in (3.2). Here, $\text{tr}\{\Sigma_m\}$ denotes the trace of Σ_m , $\mathbf{n}_m \sim \mathcal{CN}(.; \mathbf{0}, \Sigma_m)$ models the noise background of the m th channel and is a complex random variable with zero mean and covariance of Σ_m as discussed in Section 3.2.1.

The SNR associated with the object state, \mathbf{X}_k , over the range bins is considered: Due to the auto-correlation function, Λ_m , in (3.3), the second term in the numerator of (3.62) yields

$$\mathbb{E}\left\{ \sum_{r \in \mathcal{E}_m(\mathbf{X}_k)} \mathbf{s}_m^T(r, \mathbf{X}_k, \Delta t_m) \mathbf{s}_m(r, \mathbf{X}_k, \Delta t_m) \right\} = LN \times \Lambda_m(\mathcal{E}_m(\mathbf{X}_k)) \quad (3.63)$$

$$\begin{aligned} \Lambda_m(\mathcal{E}_m(\mathbf{X}_k)) &\triangleq \sum_{r \in \mathcal{E}_m(\mathbf{X}_k)} \Lambda_m^*(rT_p - \tau_m(\mathbf{X}_k) - \Delta t_m) \\ &\quad \times \Lambda_m(rT_p - \tau_m(\mathbf{X}_k) - \Delta t_m), \end{aligned} \quad (3.64)$$

where L indicates the number of array elements, and N is the number of transmitted pulses in a CPI. Thus, the SNR for the radar data cube at the k th CPI for the m th channel through (3.62)–(3.64) is given by

$$\text{SNR}_{m,k} = \frac{LN \Lambda_m(\mathcal{E}_m(\mathbf{X}_k)) \mathbb{E}\{\alpha_{m,k}^* \alpha_{m,k}\}}{\text{tr}\{\Sigma_m\}} \quad (3.65)$$

$$\text{SNR}_{\text{dB}}^{m,k} = 10 \log_{10}(\text{SNR}_{m,k}), \quad (3.66)$$

where $\text{SNR}_{\text{dB}}^{m,k}$ denotes $\text{SNR}_{m,k}$ in decibels (dB). As a result, the SNR for an integrated value of all radar data cubes up to k CPIs for M reflection channels is found by using the sum of all the M reflection channel SNRs:

$$\text{SNR}_k = \sum_{k'=1}^k \sum_{m=1}^M \text{SNR}_{m,k'}. \quad (3.67)$$

Now, it is shown that the expectation of the long time likelihood ratio for the detection test equals to that of the SNR in (3.67). The test value at the k th CPI for detection, $\log L_k$, in (3.52) is found by using the sum of instantaneous likelihood ratios up to time k . The instantaneous likelihood ratio in (3.53) at time k is easily factorised to the m th reflection channel instantaneous likelihood ratio:

$$\begin{aligned} L_m(\mathbf{Z}_k(\mathbf{X}_k)|\mathbf{X}_k, \boldsymbol{\alpha}_k, \Delta t_m) &\triangleq \sum_{r \in \mathcal{E}_m(\mathbf{X}_k)} \log L(\mathbf{Z}_{m,k}(r)|\mathbf{X}_k, \alpha_{m,k}, \Delta t_m) \\ &= \sum_{r \in \mathcal{E}_m(\mathbf{X}_k)} \left(2\text{Re}\{\alpha_{m,k}^* \mathbf{s}_m^H(r, \mathbf{X}_k, \Delta t_m) \Sigma_m^{-1} \mathbf{Z}_{m,k}(r)\} \right. \\ &\quad \left. - |\alpha_{m,k}|^2 \mathbf{s}_m^H(r, \mathbf{X}_k, \Delta t_m) \Sigma_m^{-1} \mathbf{s}_m(r, \mathbf{X}_k, \Delta t_m) \right). \end{aligned} \quad (3.68)$$

Then, the expectation of this likelihood ratio is given by

$$\begin{aligned} \mathbb{E}\{L_m(\mathbf{Z}_k(\mathbf{X}_k)|\mathbf{X}_k, \boldsymbol{\alpha}_k, \Delta t_m)\} &= \sum_{r \in \mathcal{E}_m(\mathbf{X}_k)} \left(2\text{Re}\{\alpha_{m,k}^* \mathbf{s}_m^H(r, \mathbf{X}_k, \Delta t_m) \Sigma_m^{-1} \mathbb{E}\{\mathbf{Z}_{m,k}(r)\}\} \right. \\ &\quad \left. - |\alpha_{m,k}|^2 \mathbf{s}_m^H(r, \mathbf{X}_k, \Delta t_m) \Sigma_m^{-1} \mathbf{s}_m(r, \mathbf{X}_k, \Delta t_m) \right). \end{aligned} \quad (3.69)$$

From the radar data cube in (3.2), when $H = H_1$ hypothesis holds, the expectation of $\mathbf{Z}_{m,k}(r)$ is given by

$$\mathbb{E}\{\mathbf{Z}_{m,k}(r)\} = \alpha_{m,k} \mathbf{s}_m(r, \mathbf{X}_k, \Delta t_m). \quad (3.70)$$

After substituting (3.70) into (3.69), the resulting expression is found as

$$\begin{aligned} \mathbb{E}\{L_m(\mathbf{Z}_k(\mathbf{X}_k)|\mathbf{X}_k, \boldsymbol{\alpha}_k, \Delta t_m)\} &= \sum_{r \in \mathcal{E}_m(\mathbf{X}_k)} |\alpha_{m,k}|^2 \mathbf{s}_m^H(r, \mathbf{X}_k, \Delta t_m) \Sigma_m^{-1} \mathbf{s}_m(r, \mathbf{X}_k, \Delta t_m) \\ &= \sum_{r \in \mathcal{E}_m(\mathbf{X}_k)} \text{SNR}_{m,k}(r, \mathbf{X}_k). \end{aligned} \quad (3.71)$$

As a result, the expectation of the m th instantaneous likelihood in (3.71) for the r th

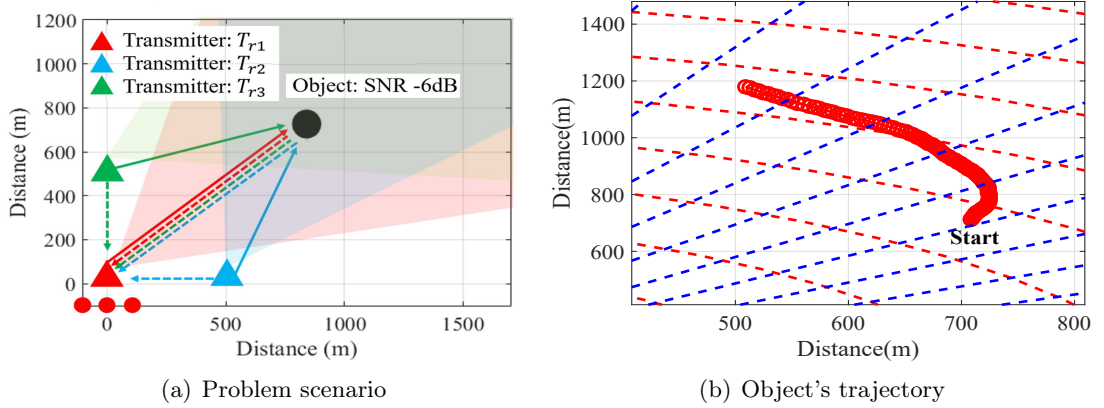


Figure 3.7: Example scenario: (a) $M = 3$ transmitters (i.e., Tr_1 , Tr_2 , and Tr_3) emitting $N = 20$ pulses (solid line arrows) towards a small object (a black dot). A ULA (red dots) collects low SNR (-6dB) reflections (dashed line arrows) and direct signals (a dotted green line arrow). (b) The object's trajectory depicted with the red line. The range resolution bins resulting from sampling in time are shown by the dashed red lines. The bearing resolution bins, obtained by (2.31), are shown by the dashed blue lines.

range bin is equivalent to $SNR_{m,k}(r, \mathbf{X}_k)$ in (3.62). Therefore, the integrated value of $\log L_k$ in (3.52) is equivalent to the estimate of SNR_k in (3.67).

3.6 Example

This section demonstrates the proposed algorithm through an example and compares its efficacy to other techniques. A scenario is considered that a ULA (red dots) receiver co-located with a transmitter (red triangle) is at the origin of the 2D Cartesian plane. The other two separated transmitters (green and cyan triangles) are located at $[0m, 500m]$ and $[500m, 0m]$, respectively (see. Figure 3.7(a)). In this setting, $M = 3$ transmitters emit $N = 20$ linear frequency modulated (i.e., up-chirp) waveforms towards a surveillance region (shaded region in Figure 3.7(a)) and repeats this illumination pattern every 0.1s. In this region, there is a small object (black dot) with an initial state, $\mathbf{X}_0 = [700m, 700m, 10m/s, 50m/s]$, moving along an unknown trajectory (see, Figure 3.7(b)). This trajectory is generated from the object dynamic model following (3.17). The ULA receiver with $L = 20$ elements collects reflections (dashed line arrows) in accordance with the signal model in (3.2) from the local (dashed red line arrow) and the remote (dashed green/cyan line arrows) channels. Superposition in the remote

Table 3.1: Transmitted signal parameters

Parameter	Value
Carrier frequency, i.e., f_c	10 GHz
Probing waveform bandwidth, i.e., B	1 MHz
Probing waveform duration, i.e., T_p	1.0 μ s
Pulse repetition interval (PRI), i.e., T	100 μ s
Number of range bins, i.e., Γ	100
Number of pulses, i.e., N	20
Number of elements in the ULA, i.e., L	20
Length of the coherent processing interval (CPI)	2 ms
Illumination period (Δ in (3.17))	0.1 s
Number of transmitters, i.e., M	3

channels is the direct probing transmission from the separately located transmitters. The parameter configuration of these transmissions is shown in Table 3.1.

In this example, when the separately located transmitters are close to the receiver, the performance of synchronisation term estimates will be improved due to the high SNR of direct channels when no objects are located at the line of sight from the transmitters. In practice, objects might be located at the line of sight from the separately located transmitters, but not be at the locations of the transmitters. In this case, the proposed estimator for the synchronisation terms can resolve $\Delta \mathbf{t}$ estimation by the filtering in (3.46) with the prior knowledge of all the transmitter locations, and the receiver can detect the objects. When objects are located at the separately located transmitters and are slowly moving, the receiver cannot detect them because the receiver treats them as the locations of the transmitters. In this case, the receiver requires spatial filtering (i.e., digital beam-forming) by using planar array antennas in order to separate objects from the transmitters. This filtering with a uniform planar array receiver will be discussed in Chapter 4. For the rest of this section, it is assumed that the regions for the direct channels (see, the dashed lines between the receiver and the separately located transmitters in Figure 3.7(a)) are not included in the surveillance region (see, shaded regions).

This experiment simulates 100 independent sets of trajectories, which produce 100 sets of array measurements: When the $H = H_1$ hypothesis holds, the array measurements at the k th CPI are associated with the object state, \mathbf{X}_k , and the reflection coefficient, $\alpha_{m,k}$. These quantities are generated from a complex Gaussian by using

$$\begin{aligned} \mathbf{Z}_{m,k}(r) &\sim \mathcal{CN}(\cdot; \alpha_m \mathbf{s}_m(r, \mathbf{X}_k, \Delta t_m), \Sigma_m), \\ m &= 1, \dots, M, \quad r \in \mathcal{E}(\mathbf{X}_k), \end{aligned} \quad (3.72)$$

where m indicates the m th reflection channel, $\mathcal{E}(\mathbf{X}_k)$ is the set of the range bins associated with \mathbf{X}_k in (3.11). Otherwise, the measurements are generated from

$$\begin{aligned} \mathbf{Z}_{m,k}(r) &\sim \mathcal{CN}(\cdot; \mathbf{0}, \Sigma_m), \\ m &= 1, \dots, M, \quad r \in \Gamma \setminus \mathcal{E}(\mathbf{X}_k), \end{aligned} \quad (3.73)$$

where Γ is the length of range bins given in Table 3.1.

Each direct signal from the separately located transmitter is received with additive noise using (3.8) with the SNR of 0dB. The common time reference shift, Δt , between the separately located transmitters and the receiver is selected randomly in the range of $0 < \Delta t < \text{PRI}$, and this value is used for all experiments.

Algorithm 3 uses 100 CPIs and spans 10 s. Each CPI corresponds to one radar data cube (see, Figure 3.3). The performance of the proposed scheme in this scenario is compared with the following detectors:

1. The clairvoyant detector: This detector uses the ground truth values of the unknown parameters (i.e., the object trajectory, reflection coefficient, and the synchronisation term) when evaluating the logarithm of the likelihood ratio test in (3.13). In other words, this test substitutes the true values of these unknowns in (3.52) and leads to

$$\log L_k \underset{H_0}{\overset{H_1}{\geq}} \log \mathcal{J}_k \quad (3.74)$$

$$\log L_k = \log L_{k-1} + L(\mathbf{Z}_k(\mathbf{X}_{\text{true},k}) | \mathbf{X}_{\text{true},k}, \boldsymbol{\alpha}_{\text{true},k}, \Delta \mathbf{t}_{\text{true}}), \quad (3.75)$$

where $\mathbf{X}_{\text{true},k}$, $\boldsymbol{\alpha}_{\text{true},k}$, and Δt_{true} are the true values of \mathbf{X}_k , $\boldsymbol{\alpha}_k$, and Δt , respectively. The CFAR threshold, $\log \mathcal{T}_k$, for this detector is found with $P_{fa} = 10^{-6}$ using (3.56)–(3.59) as discussed in Section 3.5.1.

Note that the clairvoyant detector is the optimal detector [18, Chp.13]. The k integrated value of $\log L_k$ with the ground truth values provides the maximum achievable value for the detection test. Therefore, this integrated value is used as the performance upper bound when comparing the efficacy of the proposed integration approach in this section.

2. Conventional coherent detector: This detector processes the measurements after mapping them over a grid of bearing and Doppler bins. These bins correspond to resolution cells, which are found for the example system as follows: The bearing resolution is found as $\Delta\theta = 5.1^\circ$ using (2.31). The range resolution is found as $\Delta R = 150\text{m}$ using (2.25). The velocity resolution of the conventional processing is found as $\Delta V = 7.5\text{m/s}$ using $\Delta V = \frac{\lambda_c}{2NT}$ (or, equivalently, the Doppler resolution $\Delta\omega = 4\pi f_c \frac{\Delta V}{c} T$ as $\pi/10 \text{ rad s}^{-1}$).

The conventional coherent detector over a grid of bearing and Doppler bins is found in [18, Chp.13], and this detector with the signal model in (3.3) with given Δt is given by

$$T_K(r, X(i, j)) = \sum_{k=1}^K \sum_{m=1}^M \text{Re}\{\mathbf{s}_m(r, \mathbf{X}(i, j), \Delta t) \Sigma_m^{-1} \mathbf{Z}_{m,k}(r)\} \underset{H_0}{\overset{H_1}{\gtrless}} \log \mathcal{T}_k. \quad (3.76)$$

Here, $\mathbf{X}(i, j)$ denotes a location (i.e., range and bearing) and velocity associated with the i th bearing bin and the j th Doppler for the r th range bin. This detector integrates the mapped complex values for the same “cell under test” across time without taking into account object manoeuvres [18, Chp.13] [1]. This detector is compared to the proposed detector.

For the selection of the number of particles, the proposed algorithm is initiated with $P = 200$, $P = 400$, $P = 600$, $P = 800$, and $P = 1000$ particles, respectively, and

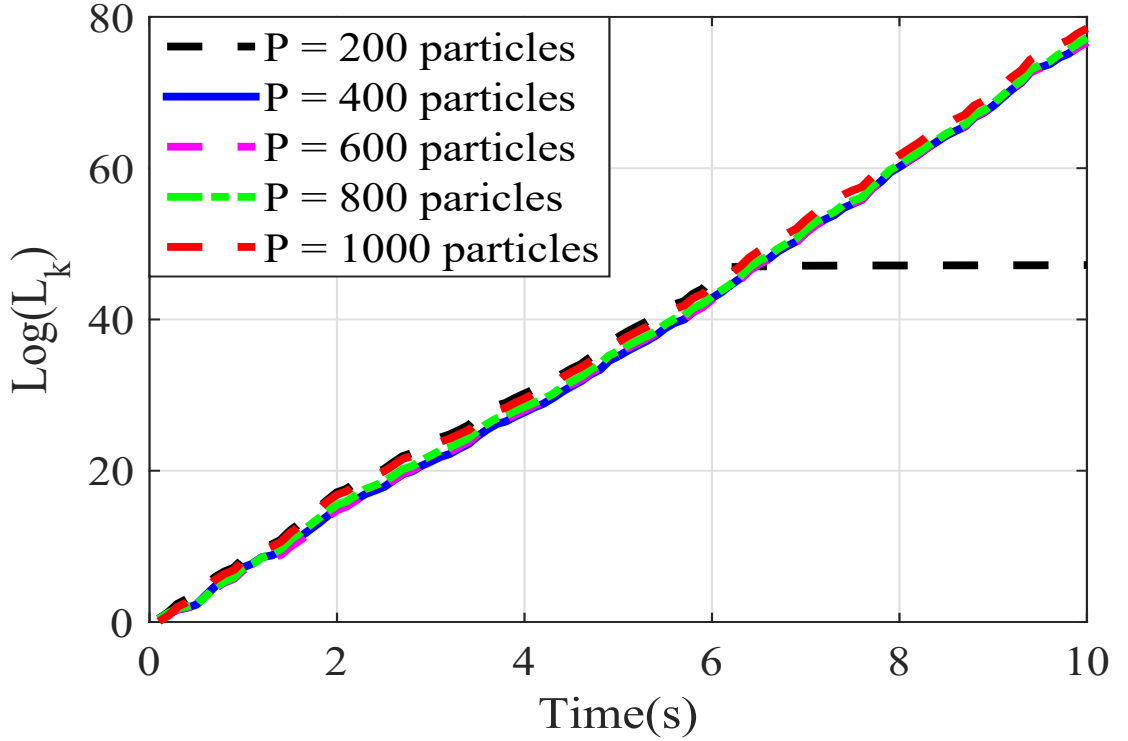


Figure 3.8: The proposed scheme with $M = 1$ transmitters versus the number of particles: The number of particles sets $P = 200$, $P = 400$, $P = 600$, $P = 800$, and $P = 1000$, respectively.

performs Algorithm 3 with the only local channel measurements, whose SNR sets -3dB . This quantity is found by using $\text{SNR}_{\text{dB}}^{m,k}$ in (3.66). Figure 3.8 illustrates the resulting integrated value using $P = 200$, $P = 400$, $P = 600$, $P = 800$, and $P = 1000$ particles, respectively. Here, the algorithm with $P = 200$ particles fails to continue the integration (i.e., dashed black line). Regarding these results, the number of particles sets $P = 400$ for the rest of the experiments. These particles are initialised as an 20×20 uniform grid over a bounded region of location and velocity vectors such that the locations span the “cell under test”. Note that because all the steering vectors during processing are selected by the Bayesian recursive filtering, there are no fixed bearing or velocity resolution cells for the proposed approach unlike the conventional detector. As the Bayesian filtering and trajectory estimation steps iterate, these particles evolve to converge to the true state of the object simultaneously giving rise to the integrated value in (3.52).

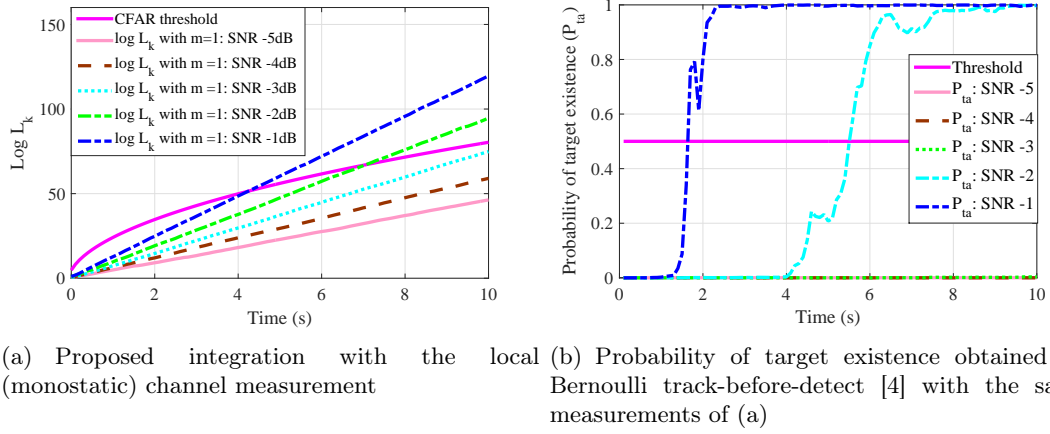


Figure 3.9: Proposed integration compared to the probability of target existence obtained by Bernoulli track-before-detect [4]: Both algorithms use the same sets of measurements. The dashed blue, the dashed cyan, the dotted green, the dashed brown, and the solid pink lines indicate SNR -1dB , -2dB , -3dB , -4dB , and -5dB , respectively.

3.6.1 Detection test via long time integration

This section, first, discusses the detection via long time integration with only local channel measurements (i.e., $M = 1$). Then, this results are compared to the probability of target existence obtained by Bernoulli track-before-detect [4]. It is assumed that this Bernoulli track-before-detect has the full knowledge of the reflection coefficients as the known parameter. Next, the benefit of multiple transmitters (i.e., $M > 1$) is demonstrated.

Long time integration versus probability of target existence for $M = 1$ transmitter

Let one compare the proposed long time integration using $M = 1$ reflection channel with a probability of target existence. This is because the existing TBD algorithms commonly use the probability of target existence for the detection instead of the integration scheme. Here, the proposed integration is the key difference compared to the existing TBDs.

In order to measure the integration performance, Algorithm 3 uses the different SNRs of array measurements in the range of -20dB to -1dB to provide the proposed long time integration. Then, this resulting integration is compared to the probability of

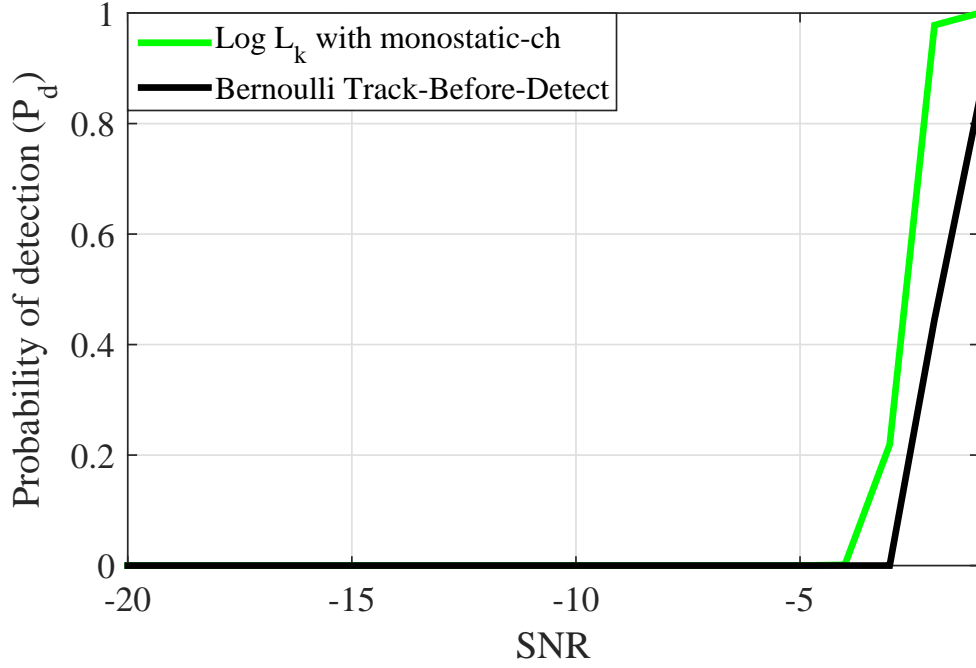


Figure 3.10: Detection performance comparison: The probability of detection, obtained by the proposed detector, is depicted by the solid green line, That of the Bernoulli track-before-detect is depicted by the solid black line.

target existence (i.e., equivalent to (2.62) in Section 2.6) obtained by the Bernoulli track-before-detect [4] with the same measurements used in Algorithm 3. These results obtained by using the array measurements in the range of -5dB to -1dB are illustrated in Figure 3.9. Here, the clairvoyant CFAR detection threshold for $P_{fa} = 10^{-6}$ is depicted as the solid magenta line in Figure 3.9(a). The predefined threshold for the probability of target existence sets 0.5 and is depicted as the solid magenta line in Figure 3.9(b).

As discussed in Section 3.5, the integrated value is a function of time. The proposed integration continues integrating measurements over many CPIs for all the cases (see, Figure 3.9(a)). The detection is made by comparing these integration values against the clairvoyant CFAR threshold. The last two integrated values (i.e., SNR -1dB and -2dB) exceed this threshold after $t = 4\text{s}$ (dashed blue line) and $t = 7\text{s}$ (dashed green line). In the other hand, the probabilities of target existence for SNR -1dB and -2dB measurements only produce high values and exceed the threshold after $t = 1.8\text{s}$ (dashed blue line) and $t = 5.7\text{s}$ (dashed cyan line) as illustrated in Figure 3.9(b). It is emphasised that the probability of target existence is not equivalent to that of detection.

As discussed in Section 3.5.1, the probability of detection for the proposed detector is defined in (3.60). The probability of detection for the Bernoulli track-before-detect is obtained by using

$$P_d = \frac{\text{The number of trials that exceeds the threshold}}{\text{The total number of trials}},$$

where the number of trials that exceeds the threshold counts the probability of target existence that exceeds the threshold at each CPI, and the total number of trials is 100 CPIs in this case. Figure 3.10 illustrates the probabilities of detection with the expected SNR for measurements in the range of -20dB to -1dB . Here, it is clearly shown that the proposed detector (solid green line) provides the higher probability of detection than that of the Bernoulli track-before-detect (solid black line).

Long time integration for $M > 1$ transmitters

Let one consider the proposed long time integration with $M = 3$ transmitters and demonstrate the benefits of multiple transmitters used for the detection. For this purpose, Algorithm 3 is repeated with 100 scenario realisations. The performance of the resulting long time integration is compared with that of the clairvoyant and conventional detectors. Here, the Bernoulli track-before-detect is not considered because, as discussed above, its detection performance is lower than that of the proposed detector when $M = 1$ transmitter is used (see, Figure 3.10). In order to demonstrate the benefits of multiple transmitters used, the clairvoyant CFAR detection threshold used in Figure 3.9(a) is used for the rest of experiments, and the expected SNR for the m th channel measurement in a CPI sets -6dB .

In Figure 3.11, the clairvoyant integrator sets an upper bound for the integrated sufficient statistics, the average of which is depicted by the dashed red line. Long time integration accuracy of the proposed algorithm is coupled to the trajectory estimation performance through the EM iterations for finding the reflection coefficients (i.e., Algorithm 1). As shown in Figure 3.11, the integration performance obtained by the proposed scheme produces an integrated value, which is very close to the clairvoyant

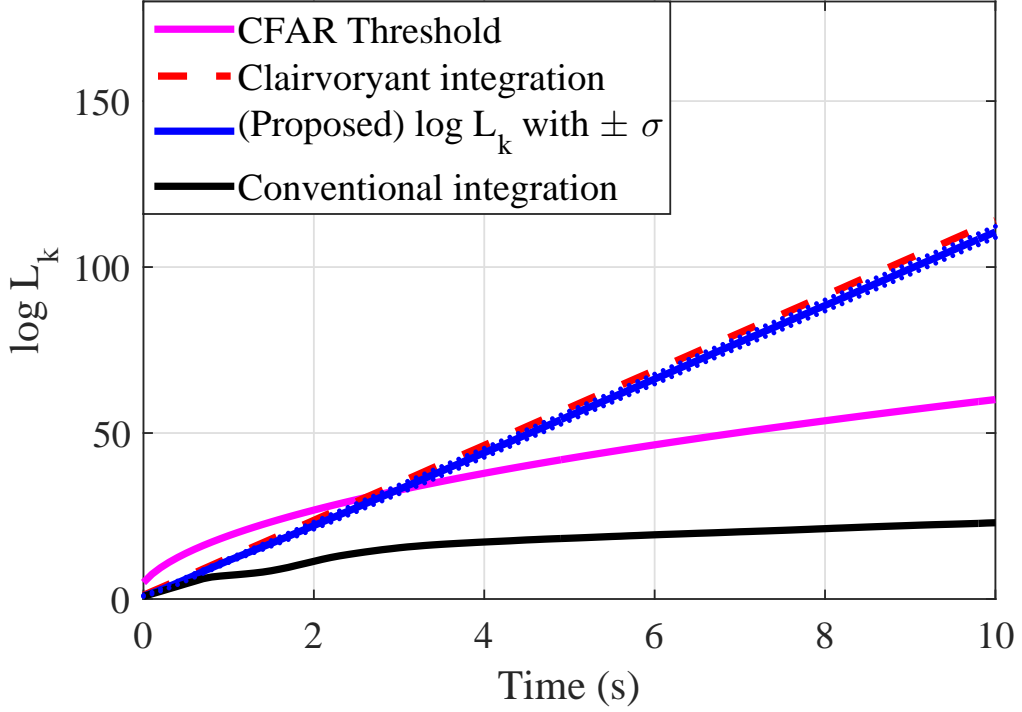


Figure 3.11: Long time integration using the proposed scheme, the clairvoyant integrator, and the conventional coherent integrator, when $M = 3$ transmitters are used: The integrated sufficient statistics from the proposed integration averaged over 100 experiments is depicted by the solid blue line. The integrated value from the clairvoyant integrator is the dashed red line and the clairvoyant (CFAR) threshold for $P_{fa} = 10^{-6}$ (averaged for 100 experiments) is the solid magenta line. The conventional scheme is depicted by the solid black line.

detector bound (solid blue line rendering the average with $\pm\sigma$ bounds shown with dotted blue lines). Here, the proposed integration reaches to 110.6 at $t = 10$ s, which is relatively close to 114 achieved by the clairvoyant integration. This indicates that the loss in integration performance due to the estimation errors of the target trajectory and reflection coefficients is very small. The conventional scheme fails to continue the integration after the object leaves at the initial cell under test. This is because the conventional integration does not take into account the object movement and integrates the received energy across the same resolution bins over time. This integration is shown with the solid black line in Figure 3.11. For the detection, the proposed scheme exceeds the CFAR threshold and enables one to decide on the object existence hypothesis ($H = H_1$) at $t = 3$ s whereas the conventional scheme stays in the region for the noise only signal hypothesis ($H = H_0$).

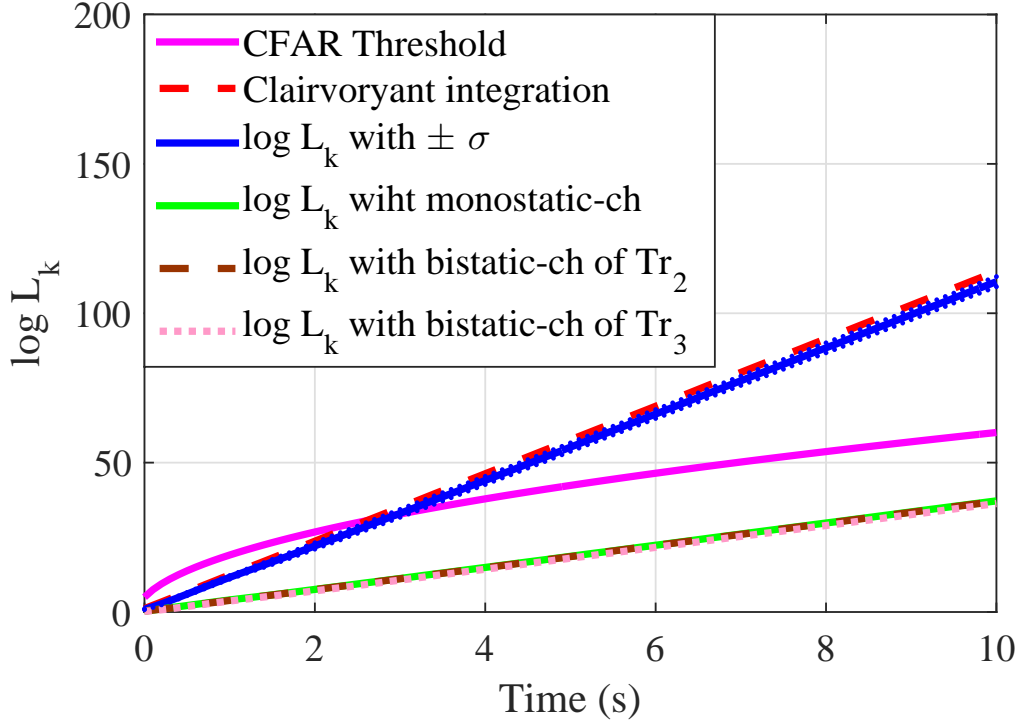


Figure 3.12: The proposed scheme with $M = 3$ transmitters (solid blue line) versus the single channel integrations: The local channel (solid green line) integration, and the remote channel (solid brown line) integration fail to exceed the detection threshold. The clairvoyant (CFAR) threshold for $P_{fa} = 10^{-6}$ (averaged for 100 experiments) is the solid magenta line

Figure 3.12 illustrates the benefit of the multi-channel integration compared to the single-channel integration. The results are averaged over 100 experiments. All these integrations (see, the multi-channel integration using $M = 3$ reflection channels depicted by the solid blue line, the single-channel integration using the local channel depicted by the solid green line, and the single-channel integration using the remote channel depicted by the dashed brown line (or the dotted pink line)) increase over time. However, the single integration fails to exceed the CFAR threshold by itself. Also, Figure 3.13 illustrates the proposed integration with $M = 2$ reflection channels (solid cyan line) in comparison with the previous integration for $M = 3$ reflection channels (solid blue line). The integrated value using $M = 2$ reflection channels exceeds the CFAR threshold at $t = 6.3$ s which is the much slow detection time in comparison to the required time for $M = 3$ reflection case ($t = 3$ s). These results reveal the advantage of using more transmitters.

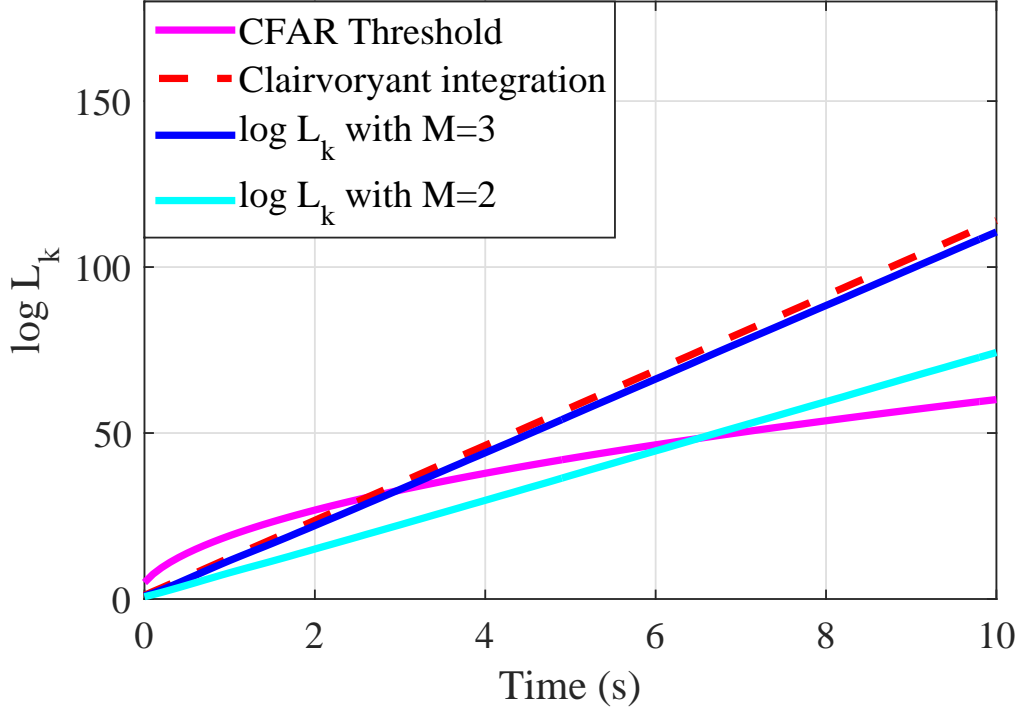


Figure 3.13: The proposed scheme with $M = 3$ transmitters (solid blue line) versus the integration $M = 2$ transmitters (solid cyan line): The clairvoyant (CFAR) threshold is used in Figure 3.12.

Now, consider the probability of detection, P_d , as a function of the integration time. This is illustrated in Figure 3.14. Here, the P_d of the clairvoyant detector (dashed red line) sets the upper performance bound. The P_d of the proposed scheme for $M = 3$ reflection channels is drawn by the solid blue line in Figure 3.14. This quantity increases with time and reaches $P_d = 1$ at $t = 5$ s, which is relatively close to the $P_d = 1$ at $t = 4.5$ s of the clairvoyant detector. The P_d of the proposed scheme for $M = 2$ reflection channels (solid cyan line) increases with time and reaches $P_d = 0.97$ at $t = 10$ s, which enables one to detect the object after $t = 6.6$ s. The P_d s of the local channel (solid green line) and the remote channel integrations (brown and pink lines) stay in the vicinity of zeros and indicate that they fail to detect the object in an overwhelming majority of the experiments.

Next, consider the probability of detection P_d as a function of different false alarm (P_{fa}) values in the range of $P_{fa} = 10^{-15}$ to $P_{fa} = 10^0$. This is referred to as the receiver operating characteristic (ROC) curve [18, Chp.3] and is defined in (3.61). For ROC

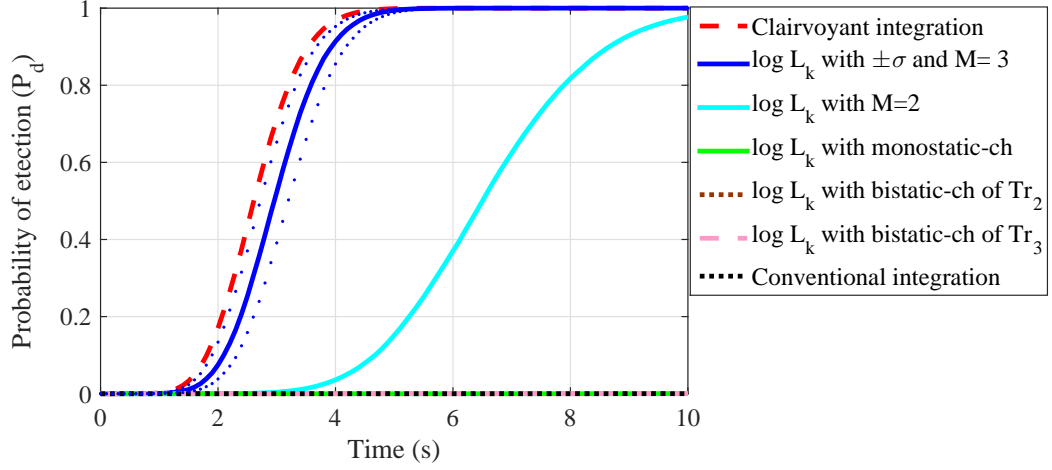


Figure 3.14: Probability of detection (P_d) for the proposed scheme in comparison with the clairvoyant detector and the conventional detector: P_d for the proposed scheme (solid blue line) with $M = 3$ transmitters and P_d for the proposed scheme (solid cyan line) with $M = 2$ transmitters are compared to P_d for the clairvoyant detector (dashed red line). The probability of false alarm $P_{fa} = 10^{-6}$ compared to P_d for the clairvoyant detector (dashed red line).

calculation, the resulting integrated values at $t = 10$ s are used because P_d is a function of integration time (see, Figure 3.12). Figure 3.15 illustrates the ROC curves obtained by using Algorithm 3 for $M = 3$ reflection channels, $M = 2$ reflection channels, the local channel, and the remote channels, respectively, as well as the ROC of the conventional coherent detector (dotted black line). The ROC of the proposed integration for $M = 3$ reflection channels (solid blue line) provides $P_d = 1$ after $P_{fa} = 10^{-15}$, whereas the integration value for $M = 2$ reflection channels (solid cyan line) yields $P_d = 1$ after $P_{fa} = 10^{-5}$. Furthermore, the single channel integration (solid green, dotted brown, and dashed pink lines) enables one to have $P_d = 1$ after a small false alarm rate of $P_{fa} = 10^{-2}$. The conventional coherent integration, however, provides $P_d = 1$ after $P_{fa} = 10^0$.

The ROCs in Figure 3.15 can present the probability of detection P_d as a function of different SNR values in the range of $\text{SNR} = -20\text{dB}$ to $\text{SNR} = -1\text{dB}$. For this ROC calculation, the resulting integrated values at $t = 10$ s are used. Figure 3.16 illustrates the ROC curves obtained by using Algorithm 3 for $M = 3$ reflection channels, $M = 2$ reflection channels, and the single channel. The ROC of the proposed integration for $M = 3$ reflection channels (solid blue line) provides $P_d = 1$ after $\text{SNR} = -6\text{dB}$, whereas

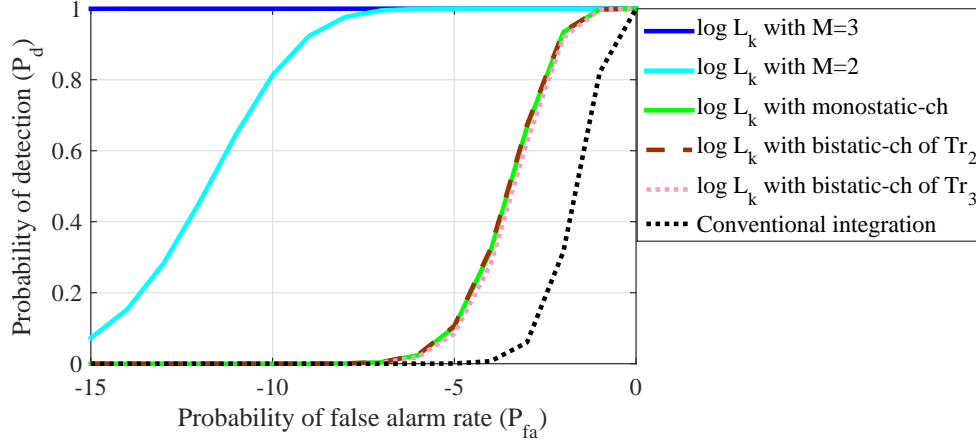


Figure 3.15: Receiver operating characteristic (ROC) curves as a function of P_{fa} : The proposed detector with $M = 3$ transmitters (solid blue line), and, $M = 2$ transmitters (solid cyan line), respectively, are given. The solid green, the dashed brown, the dotted pink, and the dotted black lines denote the single channel integrations and the conventional coherent integration, respectively.

the integration value for $M = 2$ reflection channels (solid cyan line) yields $P_d = 1$ after $\text{SNR} = -4\text{dB}$. Furthermore, the single channel integration (solid green, dotted brown, and dashed pink lines) enables one to have $P_d = 0.98$ after $\text{SNR} = -2\text{dB}$.

3.6.2 Performance in estimating the unknowns

This subsection demonstrates the inner workings of Algorithm 3. In particular, consider the estimation accuracy of the object trajectory, the reflection coefficient, and the synchronisation term within Algorithm 3. Here, the estimation performance is based on $M = 2$ transmitters used in order to avoid repetitions.

Figure 3.17(a) illustrates the typical trajectory (red line), which would lead to resolution bin migrations in conventional processing. The trajectory estimate output by the proposed algorithm is depicted by the blue line along the resolution bins (dashed lines) of a conventional detector. Figure 3.17(b) shows the root mean squared error (RMSE) of the corresponding range estimate in comparison with the range resolution of $\Delta\tau$ (dashed red line). Note that the error reduces to 20% of the range resolution after 2.3 s. Figure 3.17(c) presents the RMSE of the velocity component of the trajectory estimate

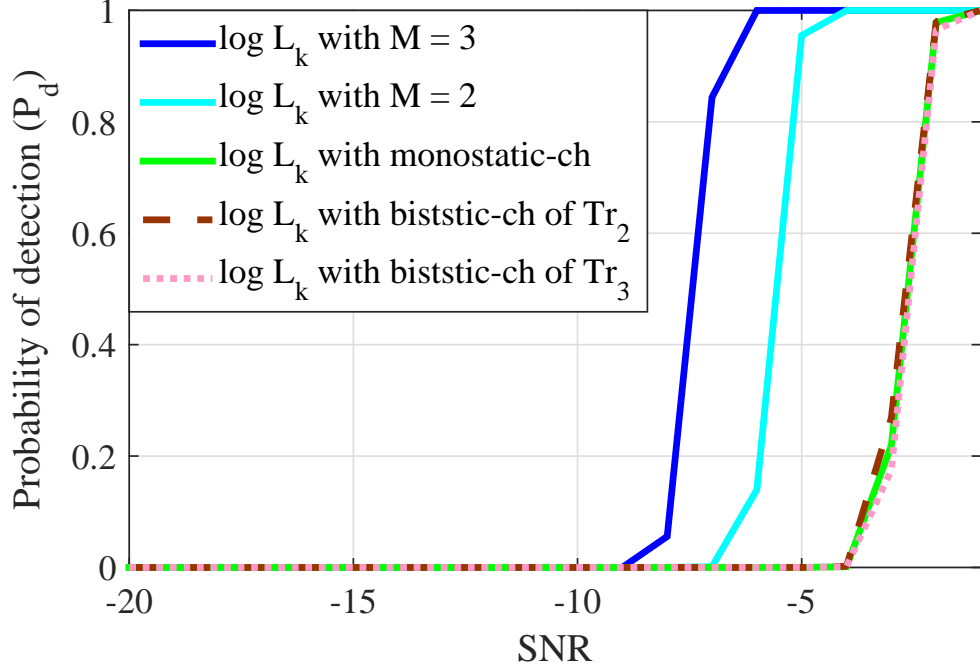


Figure 3.16: Receiver operating characteristic (ROC) curves as a function of SNR: The proposed detector with $M = 3$ transmitters (solid blue line), and $M = 2$ transmitters (solid cyan line), respectively, are given. The solid green, the dashed brown, and the dotted pink lines denote the single channel integrations, respectively.

in Figure 3.17(a). This estimation error is below the velocity resolution of ΔV (dashed red line), where the error between 6 s and 10 s shows a relatively large value due to the object's manoeuvres. Figure 3.17(d) illustrates the RMSE of the bearing component of the trajectory estimate in Figure 3.17(a). Here, the estimation error is a very small compared to the bearing resolution of $\Delta\theta$ (dashed red line). Note that the resolution bins of the system provides only a coarse view of the trajectory whereas the proposed algorithm yields a super-resolution effect.

Now, consider the estimation performance in finding the complex reflection coefficient in the radar data cube. Before this, let one consider the estimation performance given true values of all unknowns except for the complex reflection coefficient. For this purpose, Algorithm 1 is used with given the true values of the object state and the synchronisation term. The number of transmitted pulses also increases in the range of 1 to 30 and generates 100 measurements for each case in order to justify the number of pulses that are required to estimate the complex reflection coefficients in fine accuracy.

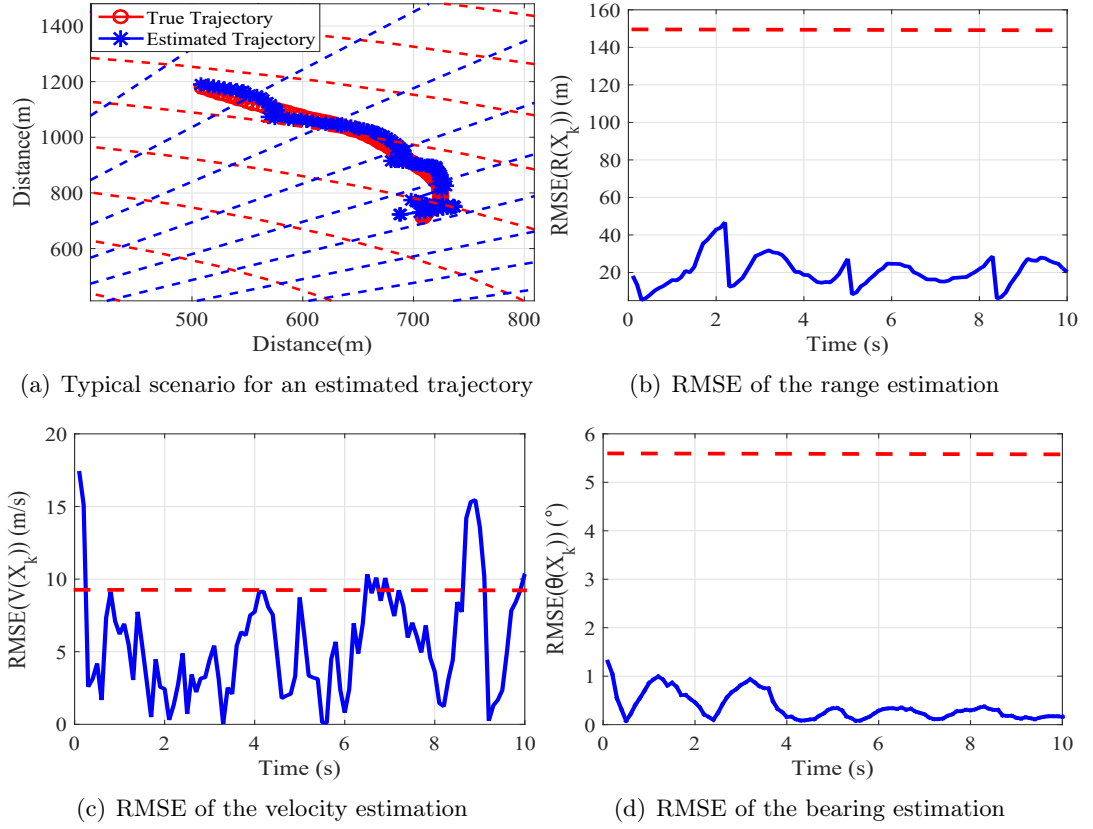


Figure 3.17: Typical trajectory estimation: (a) The estimated trajectory by the proposed algorithm is depicted with the blue line. (b) Root mean square error (RMSE) of the range estimation in (a). (c) RMSE of the velocity estimation in (a). (d) RMSE of the angle of arrival estimation in (a). The dashed red lines in (b), (c), and (d) are the range resolution ($\Delta\tau = 150\text{m}$), the velocity resolution ($\Delta V = 7.5\text{m/s}$) and the bearing resolution ($\Delta\theta = 5.1^\circ$)

Given the true values, Algorithm 1 estimates the complex reflection coefficient for 100 realisations at each scenario and obtains its variance. This value is compared to CRB in Appendix A.2. Figure 3.18(a) and (b) show the real part variance and the imaginary part variance of the estimated reflection coefficient obtained when the number of pulses increases. The variance of the proposed estimator is very close to the CRB after 15 pulses used. This also implies that the proposed estimator is unbiased in this case.

Next, Algorithm 1 is used within Algorithm 3 for 100 scenario realisations. Figure 3.18(c) and (d) show typical estimates of the complex reflection coefficients for the typical steps of Algorithm 1, where the x axis indicates the real part of the complex reflection coefficient, and the y axis shows its imaginary part. The resulting estimates are compared with their ground truth values. Also, the \pm standard deviation of Cramér-Rao bound (CRB), $\pm\sigma_{\text{CRB}}$, (see, CRB in Appendix A.2) are given for

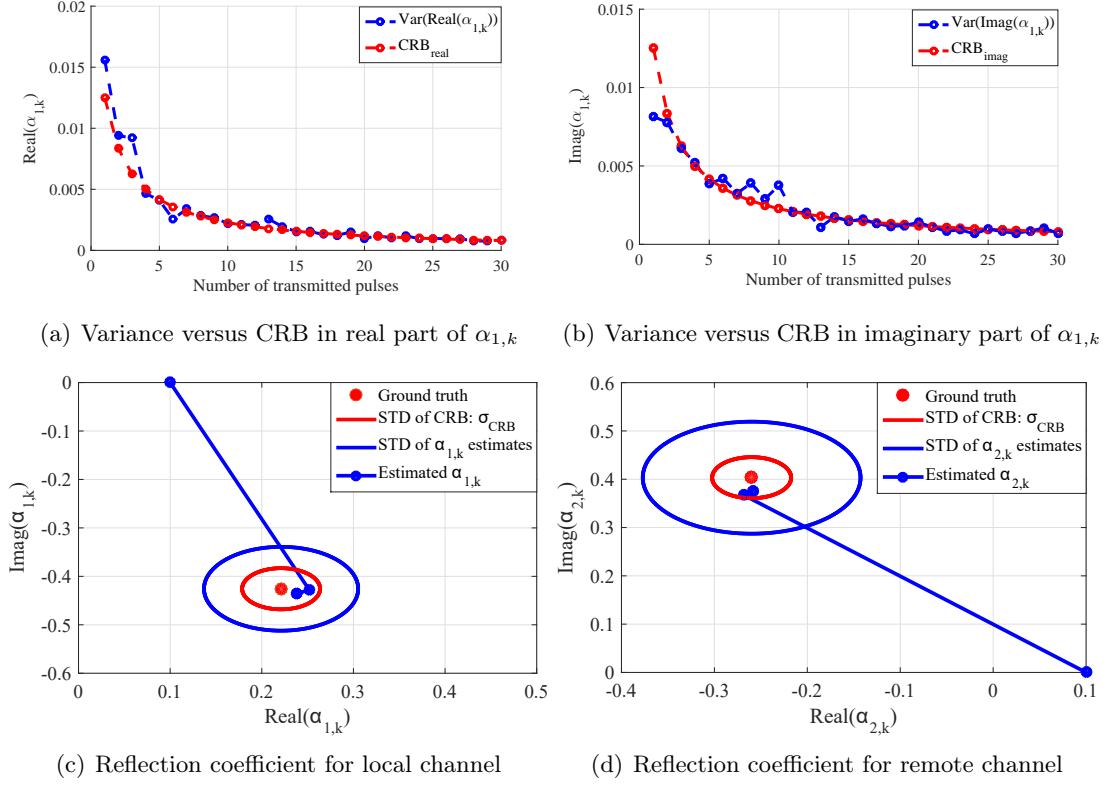


Figure 3.18: Complex reflection coefficient estimation with -6dB reflections: (a) Estimation performance of the real part of the complex reflection coefficient regarding the variance of 100 realisations by increasing the number of transmitted pulses. (b) Estimation performance of the imaginary part of (a). (c) A typical estimate of the complex reflection coefficient for the local channel by using the proposed algorithm. The blue line indicates typical estimates of the local reflection coefficient by using Algorithm 1 within Algorithm 3. The blue circle shows \pm standard deviation of 100 estimates using the proposed scheme. The blue dots show $i = 3$ iterations for finding it. The resulting estimate is compared to the ground truth value (red dot) with the \pm standard deviation of Cramér-Rao bound (CRB), i.e., $\pm\sigma_{\text{CRB}}$ (dashed red ellipse). The x axis denotes the real part of the complex reflection coefficient, and the y axis is its imaginary part. (d) A typical estimate of the complex reflection coefficient for the remote channel by using Algorithm 1 within Algorithm 3 with the same colour codes in (c).

comparison. In Figure 3.18(c), the estimated reflection coefficient (blue line) for the local channel stays within $\pm\sigma_{\text{CRB}}$ (solid red ellipse) after only a few iterations (blue dots), where the blue dots indicate the number of i iterations for finding the reflection coefficient in Algorithm 1. The resulting estimate is close to its ground truth value (red dot). For the remote channel, Figure 3.18(d) presents the typical estimate of the remote complex reflection coefficient. The resulting estimate for the remote channel (solid blue line) stays within $\pm\sigma_{\text{CRB}}$ (solid red ellipse), and is reasonably close to the ground truth value (red dot). It also provides \pm standard deviations (solid blue circle) obtained by the 100 realisations of both the real part and imaginary part of the complex reflection

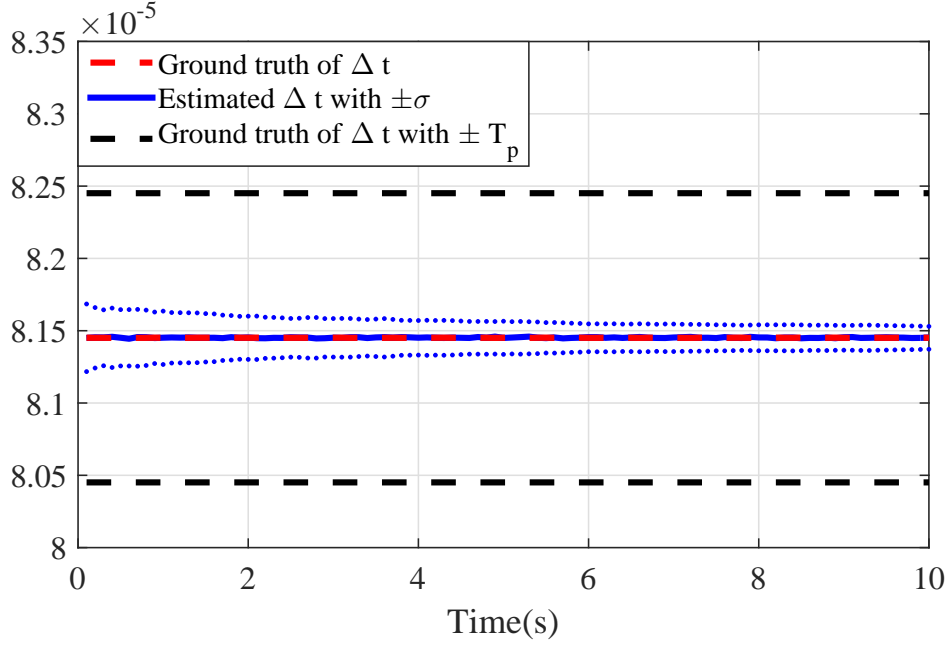


Figure 3.19: Synchronised term estimation: Averaged synchronised term (solid blue line) estimated by using the proposed estimator versus the ground truth value (solid red line) with the bound the $\pm T_p$ bound (dashed black lines) of a preliminary search over the grids.

coefficient estimates, respectively. These values are larger than the CRB due to the estimation errors of both the object state and the synchronisation term.

Let one consider the estimation of the time shift, Δt , in the remote channel. For this purpose, Algorithm 2 within Algorithm 3 is used for the 100 realisations. Figure 3.19 presents the averaged estimates (solid blue line) with $\pm\sigma$ bounds (dotted blue lines). These resulting values are compared with the true value of Δt (red solid line). Also, the $\pm T_p$ bounds (dashed black lines) are given for comparison. It is seen that the estimation error stays within a small fraction of the total pulse width T_p .

The benefits of the proposed scheme come with some additive cost of computations compared to the conventional scheme. The computational complexity of the proposed detector for the cell under test for K CPIs is $\mathcal{O}(PN_I)$, whereas the conventional coherent detector requires $\mathcal{O}(K)$. Here, P indicates the number of particles, and N_I denotes the number of iterations for the EM algorithm in Algorithm 1. This is detailed in Appendix A.3. Table 3.2 shows the processing time (average time for 100 measurements) measured from the proposed detector using Algorithm 3 when the

Table 3.2: Computational cost

Time	Proposed detector: $\mathcal{O}(PN_I)$	Conventional detector: $\mathcal{O}(K)$
Processing time ($K = 100$ CPIs)	2980s for $P = 400$ 4463s for $P = 600$ 5982s for $P = 800$	8.6s
Processing time for each CPI ($K = 1$ CPI)	29.89s for $P = 400$ 44.59s for $P = 600$ 58.44s for $P = 800$	0.083s

number of particles used are $P = 400$, $P = 600$, and $P = 800$, respectively. It is also shown that the processing time is obtained by the conventional detector using (3.76). The computer used for these measurements has i7 6500U CPU without a graphics processing unit (GPU). Here, it is clearly shown that the conventional detector takes 8.6s, whereas the proposed detector takes the much longer processing time (i.e., 2980s for $P = 400$, 4463s for $P = 600$, and 5982s for $P = 800$) required.

3.7 Summary

This chapter has proposed the detection algorithm that performs the most efficient statistical test in order to detect manoeuvring and low SNR objects with an arbitrarily long time window of measurements in the multistatic configuration. This test is carried out by simultaneous trajectory estimation and long time integration. This approach has the capability of collecting the entire evidence on the object's presence at the receiver by i) coherently integrating both the monostatic channel and the bistatic channel within a CPI, ii) performing non-coherent integration across different channels, and iii) continuing integration for an arbitrarily long interval that contains many CPIs. It is also demonstrated that the proposed approach can provide the integration that is close to the best achievable by the clairvoyant integrator. As a result, this approach enables one to detect manoeuvring and very low SNR objects, which cannot be detected by using other techniques.

For slowly manoeuvring objects such as hovering drones, the proposed detector might

not detect such objects because it cannot discriminate them from stationary objects. There are additional signal features, which can be explored in improving detection performance. In general, manoeuvring objects have propulsion devices, for example, rotating wheels or rotating rotor blades. Such devices generate additional frequency modulation around the main Doppler shift. This is referred to as the micro-Doppler shift, which provides information on the characterisation of objects. Chapter 4 will introduce an algorithm, which can estimate micro-Doppler shifts from rotary-wing aircraft such as unmanned aerial vehicles (UAVs) or drones before the detection decision is made.

Chapter 4

Joint micro-Doppler signature estimation and track-before-detect in an array receiver

4.1 Introduction

This chapter considers the micro-Doppler signature estimation in order to identify/classify objects detected. This is important regarding the detection of small objects to discriminate objects of interest from natural objects. The objects of interest in this chapter consider small rotary-wing aircraft such as drones or unmanned aerial vehicles (UAVs). Such aircraft consist of a less than 1m^2 sized fuselage and multiple rotor blades (see, for example, the specifications of commercial UAVs in [35]). Unlike fixed-wing aircraft, these rotary-wing aircraft can hover above ground with very low speed and can easily be masked by/confused with background objects such as birds, trees, or buildings. Thus, the detection needs to discriminate these aircraft from the radar clutter by using information on specific signal features they admit. Reflections from these aircraft, when illuminated by consecutive radio-frequency (RF) waveforms, are characterised by the object reflectivity, location, and velocity. In particular, the radial component of the velocity induces a frequency shift which is known as the Doppler. The rotating and/or moving components manifest themselves as additional frequency shifts centred at the Doppler frequency and constitute a micro-Doppler signature. For example, rotary-wing aircraft induce a line spectra of micro-Doppler shifts. These shifts

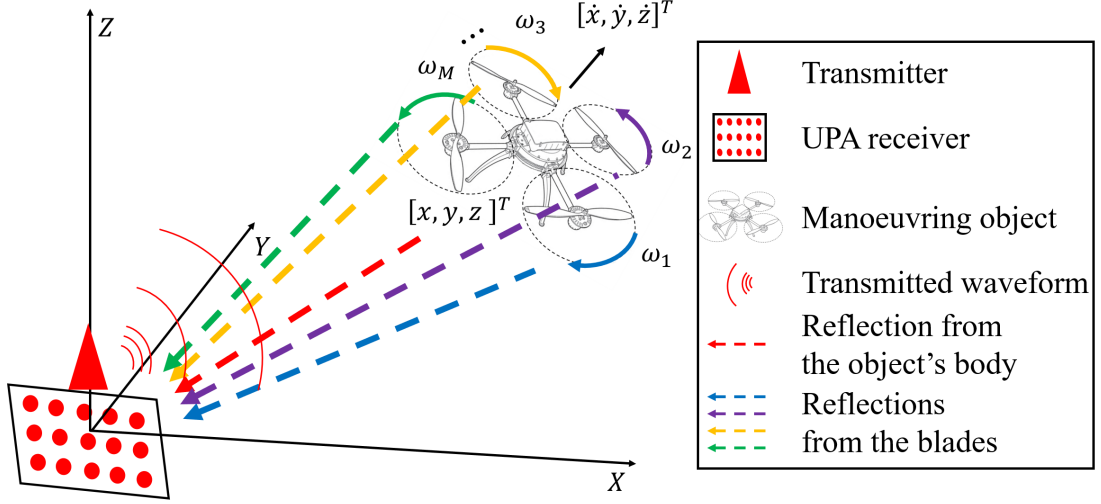


Figure 4.1: Sensing scenario: A radar with a UPA receiver collects reflections from a small rotary-wing aircraft's body and multiple rotating blades with the corresponding rotation frequencies (i.e., $\omega_1, \dots, \omega_M$). This aircraft is located at $[x, y, z]^T$ and has a velocity of $[\dot{x}, \dot{y}, \dot{z}]^T$ in the tree-dimensional (3D) volume.

are specified by the rotation frequency, the number of rotating blades, and the blade lengths as discussed in Section 2.4.

In this chapter, a problem scenario is motivated from demands for preventing drone-misuse (or drone-attack) resulting from the abuse of civilian drones or military UAVs (see, for example, [107, 108]). A radar system is also motivated by a recently developed staring radar that can continuously observe the three-dimensional (3D) volume of a surveillance region based on reflections through the monostatic channel [109]. In simulation, the system parameters of this radar are used to perform an algorithm which is developed in this chapter. The radar system considered here is a monostatic radar with a uniform planar array (UPA) receiver in order to observe drones in the (3D) volume. This receiver structure has mainly two advantages compared to the uniform linear array (ULA) receiver used in Chapter 3: i) The combination of vertical and horizontal elements in the array allows the receiver to separate/filtering out reflections from the ground clutter using the digital beam-forming techniques. ii) This combination enables the receiver to estimate azimuth and elevation angles of drones. The front-end signals at the array elements are the superposition of all the reflections from the entire drone and noise background. This is illustrated in Figure 4.1.

In this problem setting, the coherent track-before-detect scheme, proposed in Chapter 3, is employed/extended to estimate micro-Doppler signatures for object identification/classification. It is assumed that the number of rotor hubs and rotor blades is known. This estimation is only concerned with the monostatic channel measurement and measures its performance. In particular, the proposed estimation scheme uses a maximum likelihood (ML) approach that finds the rotation rate of rotor blades (i.e., rotation frequency) to maximise a likelihood function conditioned on the object kinematics, the rotation frequency, and the reflection coefficient. In order to solve this ML problem that involves latent variables such as the object kinematics and the reflection coefficient, a joint Bayesian recursive filtering and expectation-maximisation (EM) approach is proposed. The measurement model in this filtering captures the radar ambiguity function parametrised on the reflection coefficient together with the rotation frequency as the micro-Doppler signature of interest. These parameters are found by the proposed (EM) algorithm within the Bayesian recursive filtering. Here, the detection scheme is the same used in Section 3.5 of Chapter 3: It first evaluates the long time likelihood ratio as the pulse integration. This value is used in a Neyman-Person test against a constant false alarm rate (CFAR) threshold. Therefore, this chapter mainly focuses on the micro-Doppler signature estimation only.

This chapter is organised as follows: Section 4.2 details the problem scenario, and Section 4.3 introduces the mathematical expression of reflections from small rotary-wing aircraft at the array receiver. Section 4.4 explains the trajectory estimation with the radar data cube and details the empirical Bayes update within the Bayesian recursive filtering. Section 4.5 proposes an EM algorithm, which estimates the rotation frequency and the reflection coefficient. Section 4.6 combines this estimation approach together with the detection scheme explained in Chapter 3. Section 4.7 demonstrates the efficacy of the proposed scheme through an example in comparison to other techniques, and Section 4.8 summarises the proposed scheme.

4.2 Problem statement

Let this section detail the problem scenario as illustrated in Figure 4.1. A radar with a UPA receiver utilises the pulse waveform used in Section 2.3 (i.e., $\tilde{u}(t)$ in (2.16)). This waveform is characterised by a pulse duration of T_p and a bandwidth of B_w to modulate a carrier with an angular frequency of ω_c . In a coherent processing interval (CPI), the radar transmitter emits N consecutive waveforms separated by a pulse repetition interval (PRI) of T . The UPA consists of N_v vertical and N_h horizontal elements, which are spaced with a distance that selects half of the carrier wavelength, λ_c . In this scenario, the reflector of interest is a small rotary-wing aircraft such as a drone. Typically, a drone has M rotor hubs with \tilde{L} blades at each hub. These rotating components when illuminated by the transmitted waveforms induce a micro-Doppler signature on the reflections. Each array element in the UPA receiver collects the superposition of noise, background reflections, and the reflections from both the aircraft's body and blades as the front-end input.

4.2.1 Received signal model and baseband processing

The front-end processing chain begins with demodulation followed by matched filtering (MF) with the probing waveform, $\tilde{u}(t)$, without loss of generality. This processing chain is illustrated in Figure 4.2. Let one consider an object (or drone) at the state, $\mathbf{X} = [x, y, z, \dot{x}, \dot{y}, \dot{z}]^T$, where the first three variables are the coordinates of the position, and the last three variables are the coordinates of the velocity, respectively. The reflections from this object is modelled by a complex reflection coefficient, α_0 , that signifies reflections from the body, a second coefficient, α_1 , that is associated with the superposition of existing rotor hubs, and ω denoting the rotation frequency of the blades at the hubs (see, Figure 4.1). The (vector valued) MF stage output, in this setting, is

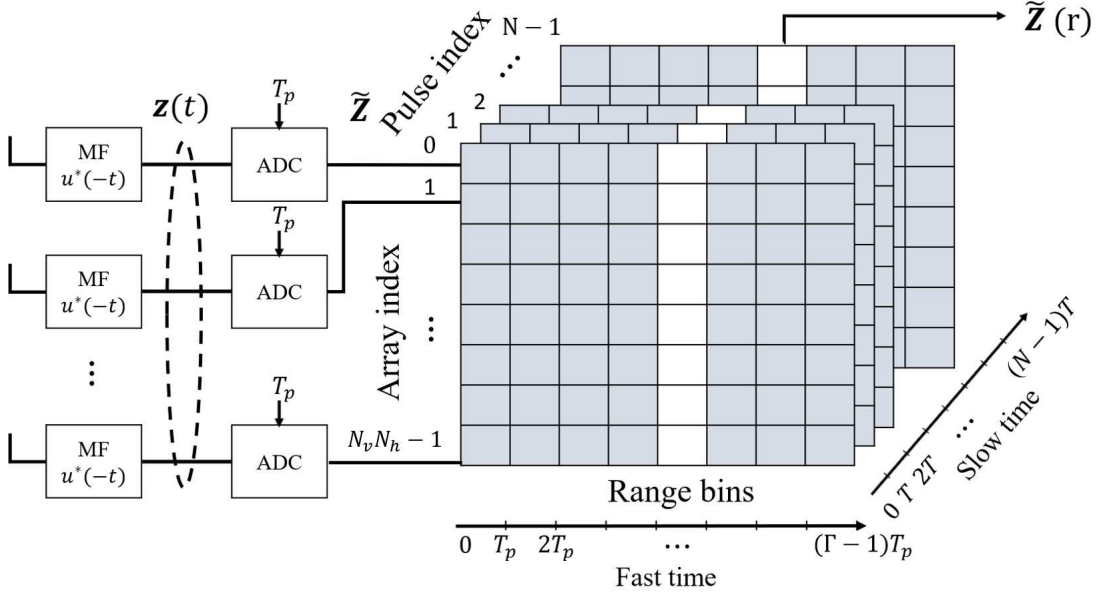


Figure 4.2: Radar data acquisition reproduced from Figure 2.7: Array elements are matched filtered and sampled with T_p sampling period. Samples are arranged in array index, fast time and slow time. $\mathbf{z}(t)$ and $\tilde{\mathbf{Z}}(r)$ denote the MF output and its sampled version, respectively.

modelled by

$$\begin{aligned}
 \mathbf{z}(t) = & \mathbf{s}_s(\phi(\mathbf{X}), \theta(\mathbf{X})) e^{-j\omega_c \tau(\mathbf{X})} \\
 & \times \left(\alpha_0 \sum_{n=0}^{N-1} e^{j\Omega(\mathbf{X})nT} \times \Lambda(t - \tau(\mathbf{X}) - nT) \right. \\
 & \left. + \alpha_1 \sum_{n=0}^{N-1} e^{j\Omega(\mathbf{X})nT} C_n(\omega, \mathbf{X}) \times \Lambda(t - \tau(\mathbf{X}) - nT) \right) + \boldsymbol{\eta}(t),
 \end{aligned} \tag{4.1}$$

where $\boldsymbol{\eta}$ is the nuisance terms at the filter output, and $\Lambda(\cdot)$ is the auto-correlation function of the probing waveform, $\tilde{u}(t)$, which is given in (2.21).

In this output of the matched filter, $\tau(\mathbf{X}) = \frac{R(\mathbf{X})}{2}$ is the pulse time of flight in (2.5), where $R(\mathbf{X})$ is the radial distance of \mathbf{X} to the receiver:

$$R(X) = \sqrt{x^2 + y^2 + z^2}, \tag{4.2}$$

and the velocity of \mathbf{X} induces the angular Doppler shift in (4.1), which contains the

elevation and the azimuth of \mathbf{X} , and is given by

$$\Omega(\mathbf{X}) = -\frac{4\pi}{\lambda_c} V(\mathbf{X}), \quad (4.3)$$

$$V(\mathbf{X}) = \left(\dot{x} \times \cos \phi(\mathbf{X}) \cos \theta(\mathbf{X}) + \dot{y} \times \cos \phi(\mathbf{X}) \sin \theta(\mathbf{X}) + \dot{z} \times \sin \phi(\mathbf{X}) \right), \quad (4.4)$$

where $\phi(\mathbf{X})$ and $\theta(\mathbf{X})$ are the elevation and the azimuth, respectively:

$$\begin{aligned} \phi(\mathbf{X}) &= \arctan \left(\frac{z}{\sqrt{x^2 + y^2}} \right), \\ \theta(\mathbf{X}) &= \arctan \left(\frac{y}{x} \right). \end{aligned} \quad (4.5)$$

Now, C_n in (4.1) captures the micro-Doppler modulations induced by the rotating components and is the main different term in comparison with the MF output in (2.20).

This term is given by

$$C_n(\omega, \mathbf{X}) \triangleq \sum_{i=-\infty}^{+\infty} \sum_{\tilde{i}=0}^{+\infty} e^{j \times \tilde{L} i \times \omega \times n T} \frac{2(-1)^{\tilde{L} i} \tilde{L}}{\frac{4\pi}{\lambda_c} \cos(\phi(\mathbf{X}))} \times J_{\tilde{L} i + 2\tilde{i} + 1} \left(B \frac{4\pi}{\lambda_c} \cos(\phi(\mathbf{X})) \right), \quad (4.6)$$

where \tilde{L} is the number of blades, B is the blade length, and J_i is the Bessel function [110] of the 1st kind and i th order. Section 4.3.1 will introduce explicit formulae for this derivation. Note that \mathbf{s}_s in (4.1) is the spatial steering vector characterised by the combination of vertical and horizontal spatial steering vectors [48, Chp.3], which differs from the spatial steering vector in (2.18): With the common distance, d , between two consecutive array elements, the vertical steering vector with N_v vertical elements is given by

$$\mathbf{s}_v(\phi, \theta) = \left[1, e^{-j\omega_c \frac{d}{c} \cos \phi \sin \theta}, \dots, e^{-j\omega_c (N_v - 1) \frac{d}{c} \cos \phi \sin \theta} \right]^T,$$

and the horizontal spatial steering vector with N_h horizontal elements is given by

$$\mathbf{s}_h(\phi, \theta) = \left[1, e^{-j\omega_c \frac{d}{c} \cos \phi \cos \theta}, \dots, e^{-j\omega_c (N_h - 1) \frac{d}{c} \cos \phi \cos \theta} \right]^T,$$

where d is selected as half of the carrier wavelength (i.e., $d = \frac{\lambda_c}{2}$). The spatial steering vector, \mathbf{s}_s , is hence given by

$$\mathbf{s}_s(\phi, \theta) = \mathbf{s}_v(\phi, \theta) \otimes \mathbf{s}_h(\phi, \theta), \quad (4.7)$$

where the size of $\mathbf{s}_s \in \mathbb{C}^{N_v N_h \times 1}$ is an $N_v N_h \times 1$ vector.

As discussed Section 2.3 and 3.2, in the baseband processing chain, the MF output is sampled with the pulse duration of T_p . The resulting output consists of Γ samples collected for each of the N pulses at each of the $N_v N_h$ array elements. These samples are arranged and form an $N_v N_h \times N \times \Gamma$ cube known as the radar data cube (see, $\tilde{\mathbf{Z}}$ as the sampled version of the MF output in Figure 4.2). Here, the axes of this data cube are the array index from 0 to $N_v N_h - 1$, the pulse index from 0 to $N - 1$, and the range index from 0 to $\Gamma - 1$, respectively. In the range axis (i.e., the fast time axis), each sample is associated with a time delay of the reflected signal and can easily be converted to range values. In the pulse axis (i.e., the slow time axis), N samples separated by a PRI of T are indexed. These complex valued samples embody both a main Doppler shift and micro-Doppler shifts due to rotating components in their phase. Thus, the superposition of all reflectors in the r th range bin is captured in the column stack of the radar data cube that forms an $N_v N_h N \times 1$ data vector:

$$\mathbf{Z}(r) = \begin{cases} \mathbf{H}(r, \mathbf{X}, \omega) \boldsymbol{\alpha} + \mathbf{n}(r) & , H_1 \text{ holds,} \\ \mathbf{n}(r) & , H_0 \text{ holds,} \end{cases} \quad (4.8)$$

where $H = H_1$ denotes the case in which an object exists at \mathbf{X} with a complex reflection coefficient vector,

$$\boldsymbol{\alpha} \triangleq [\alpha_0, \alpha_1]^T, \quad (4.9)$$

and rotating rate with the angular frequency, ω . The matrix valued function $\mathbf{H} \in \mathbb{C}^{N_v N_h N \times 2}$ will be introduced in Section 4.3.2. Here, $H = H_0$ denotes the nuisance-only hypothesis with \mathbf{n} modelling sampler output due to the nuisance term $\boldsymbol{\eta}$ in (4.1). This term is the superposition of the background and the receiver noise. In this chapter, \mathbf{n} is a circularly symmetric complex Gaussian random vector with zero mean and covariance σ given in (2.51).

Note that it is possible to accommodate structured noise with a non-zero mean in (4.8) and use sample estimators to learn these parameters from data in the absence of objects of interest, in practice. Further elaboration on these aspects remains as future work.

4.2.2 Problem definition

This chapter aims to algorithmically perform a statistical test that takes into account multiple consecutive data cubes collected over a time window spanning K CPIs: This processing is equivalent to long time integration with coherent integration within a CPI and non-coherent integration across CPIs. This facilitates the detection of faint/small objects. Let these radar data cubes denote:

$$\begin{aligned}\mathbf{Z}_{1:K} &\triangleq \{\mathbf{Z}_1, \dots, \mathbf{Z}_k, \dots, \mathbf{Z}_K\}, \\ \mathbf{Z}_k &\triangleq [Z_k(0), \dots, Z_k(\Gamma - 1)],\end{aligned}\tag{4.10}$$

where \mathbf{Z}_k is an $N_v N_h N \times \Gamma$ matrix, which is the rearranged version of the radar data cube based on (4.8) at the k th CPI. Here,

$$\boldsymbol{\alpha}_{1:K} \triangleq \{\boldsymbol{\alpha}_1, \dots, \boldsymbol{\alpha}_K\}$$

is also denoted as a set of the complex reflection coefficient vectors over K CPIs.

Detection with unknown trajectory and Doppler signature

Let one consider a composite hypothesis test with a set of unknowns. The hypothesis variable, H , takes the value, H_1 , for modelling an object which at time step $k = 1$ has its kinematic state from a set, \mathcal{B} , which captures, for example, the volume under test and admissible velocity values. Typically, \mathcal{B} is a bounded set and might be selected as the Cartesian product of a cubical grid cell in the surveillance volume (i.e., an l_1 ball in the surveillance region) and an l_2 ball in \mathbb{C}^3 centred at the origin.

Let \mathbf{X}_k denote the object kinematic state at the time step k . This time step is equivalent to the k th CPI. The object trajectory associated with $H = H_1$ is thus represented by

$$\mathbf{X}_{1:K} \triangleq \{\mathbf{X}_1, \dots, \mathbf{X}_K\},$$

where $\mathbf{X}_1 \in \mathcal{B}$. The reflections at the k th CPI are captured by $\boldsymbol{\alpha}_k$ and remain the same

within this CPI. The (angular) rotation frequency, ω , of the rotor blades is also assumed to be constant during the K CPIs of concern.

This chapter addresses two sets of problems under a single framework that are detailed in the rest of this chapter. The first set is the estimation of the state trajectory, $\mathbf{X}_{1:K}$, the reflection coefficients, $\boldsymbol{\alpha}_{1:K}$, and the rotation angular frequency, ω , given K radar data cubes, $\mathbf{Z}_{1:K}$, and a region under test, \mathcal{B} . This estimation is a core difference in comparison to Chapter 3.

The second set is the problem on the evaluation of sufficient statistics for the likelihood ratio:

$$L(\mathbf{Z}_{1:K}|\hat{\mathbf{X}}_{1:K}, \hat{\boldsymbol{\alpha}}_{1:K}, \hat{\omega}) \triangleq \frac{l(\mathbf{Z}_{1:K}|\hat{\mathbf{X}}_{1:K}, \hat{\boldsymbol{\alpha}}_{1:K}, \hat{\omega}, H = H_1)}{l(\mathbf{Z}_{1:K}|H = H_0)}, \quad (4.11)$$

where $\hat{\mathbf{X}}_{1:K}$, $\hat{\boldsymbol{\alpha}}_{1:K}$, and $\hat{\omega}$ are the estimates of $\mathbf{X}_{1:K}$, $\boldsymbol{\alpha}_{1:K}$, and ω , respectively, and H_0 is the null hypothesis. The computation of a constant false alarm (CFAR) decision threshold, \mathcal{T}_K , followed by the Neyman-Pearson test [18, Chp.3] is hence given by

$$L(\mathbf{Z}_{1:K}|\hat{\mathbf{X}}_{1:K}, \hat{\boldsymbol{\alpha}}_{1:K}, \hat{\omega}) \underset{H_0}{\overset{H_1}{\geq}} \mathcal{T}_K. \quad (4.12)$$

for the detection of a small object in \mathcal{B} .

4.2.3 Sufficient statistics of the likelihood functions

Let one focus on the likelihood functions underlying the estimation and detection problems stated in Section 4.2.2 following the signal model in (4.8) under the two hypotheses. Here, the same assumptions in Section 3.2.4 hold: The likelihood ratio in (4.11) factorises over measurement likelihood ratios for individual data cubes over K CPIs as the noise samples and the parameters for different CPIs are independent, respectively. The measurement likelihood is also decomposed by using a locality property that satisfies the number of range bins associated with \mathbf{X}_k . These bins are limited by the support of duration $2T_p$ due to the output of auto-correlation at the MF

stage (see, for example, Figure 3.4). This set of the range bins is defined:

$$\mathcal{E}(\mathbf{X}_k) = \begin{cases} \{r, r+1\}, & rT_p < \tau(\mathbf{X}_k) \\ \{r\}, & rT_p = \tau(\mathbf{X}_k) \\ \{r-1, r\}, & r_k T_p > \tau(\mathbf{X}_k) \end{cases}, \quad r \triangleq \left\lfloor \frac{\tau(\mathbf{X}_k)}{T_p} \right\rfloor, \quad (4.13)$$

where $\lfloor \cdot \rfloor$ denotes the nearest integer function, and $\tau(\mathbf{X}_k)$ is the pulse time of flight in (4.2). The numerator term in (4.11) is the measurement likelihood when $H = H_1$ holds. The locality of the measurements $\mathbf{Z}_k(r) \in \mathcal{E}(\mathbf{X}_k)$ to \mathbf{X}_k at the k th CPI is given by

$$l(\mathbf{Z}_k | \mathbf{X}_k, \boldsymbol{\alpha}_k, \omega, H = H_1) = \prod_{r \in \mathcal{E}(\mathbf{X}_k)} l(\mathbf{Z}_k(r) | \mathbf{X}_k, \boldsymbol{\alpha}_k, \omega, H = H_1) \prod_{r' \in \bar{\mathcal{E}}(\mathbf{X}_k)} p(\mathbf{Z}_k(r')), \quad (4.14)$$

where $\bar{\mathcal{E}}(\mathbf{X}_k) \triangleq \{1, 2, \dots, \Gamma\} \setminus \mathcal{E}(\mathbf{X}_k)$ denotes the complement of \mathcal{E} in the set of range bins. Similarly, the denominator term in (4.11) is the likelihood for the null hypothesis for K CPI. The locality of the measurements at the k th CPI factorises as

$$l(\mathbf{Z}_k | H = H_0) = \prod_{r \in \mathcal{E}(\mathbf{X}_k)} l(\mathbf{Z}_k(r) | H = H_0) \prod_{r' \in \bar{\mathcal{E}}(\mathbf{X}_k)} p(\mathbf{Z}_k(r')), \quad (4.15)$$

Thus, the likelihood ratio in (4.11) with the set of range bins in (4.12) over K CPIs is found as

$$L(\mathbf{Z}_{1:K} | \mathbf{X}_{1:K}, \boldsymbol{\alpha}_{1:K}, \omega) \propto \prod_{k=1}^K \prod_{r \in \mathcal{E}(\mathbf{X}_k)} L(\mathbf{Z}_k(r) | \mathbf{X}_k, \boldsymbol{\alpha}_k, \omega), \quad (4.16)$$

where the likelihood ratio on the right hand side denotes the instantaneous ratio given the r th range bin:

$$L(\mathbf{Z}_k(r) | \mathbf{X}_k, \boldsymbol{\alpha}_k, \omega) \triangleq \frac{l(\mathbf{Z}_k(r) | \mathbf{X}_k, \boldsymbol{\alpha}_k, \omega, H = H_1)}{l(\mathbf{Z}_k(r) | H = H_0)}. \quad (4.17)$$

As discussed Section 3.2.4, the numerator term in (4.17) is the measurement likelihood when $H = H_1$ holds. This can easily be found using the distribution of the noise in (4.8), and the denominator corresponding to the null hypothesis when $H = H_0$ holds is the

noise density. The instantaneous likelihood ratio in (4.17) is hence found as

$$\begin{aligned}
 L(\mathbf{Z}_k(r)|\mathbf{X}_k, \boldsymbol{\alpha}_k, \omega) &= \frac{\mathcal{CN}(\mathbf{Z}_k(r); \mathbf{H}(r, \mathbf{X}_k, \omega)\boldsymbol{\alpha}_k, \Sigma)}{\mathcal{CN}(\mathbf{Z}_k(r); \mathbf{0}, \Sigma)} \\
 &= e^{2\text{Re}\{(\mathbf{H}(r, \mathbf{X}_k, \omega)\boldsymbol{\alpha}_k)^H \Sigma^{-1} \mathbf{Z}_k(r)\}} \\
 &\quad \times e^{-(\mathbf{H}(r, \mathbf{X}_k, \omega)\boldsymbol{\alpha}_k)^H \Sigma^{-1} \mathbf{H}(r, \mathbf{X}_k, \omega)\boldsymbol{\alpha}_k}. \tag{4.18}
 \end{aligned}$$

Note that ω in (4.16) is associated with both the trajectory, $\mathbf{X}_{1:K}$, and the complex reflection coefficients, $\boldsymbol{\alpha}_{1:K}$, as unknowns for K CPIs. In order to perform the hypothesis test in (4.12) through the evaluation of (4.16)–(4.18), ω needs to be estimated along with the estimation of both $\mathbf{X}_{1:K}$ and $\boldsymbol{\alpha}_{1:K}$.

4.3 Spatio-temporal signal model components

This section first explicitly shows the derivation of the micro-Doppler model $C_n(\omega, \mathbf{X})$ in (4.6). Then, it specifies the sampled signal model, $\mathbf{H} \in \mathbb{C}^{N_v N_h N \times 2}$, in (4.8).

4.3.1 MF Output due to rotating blades: The micro-Doppler model

Let one consider the geometry of reflected signals from rotating blades in Figure 4.1 and detail the superposition of them. Figure 4.3 illustrates the top view of a single rotating component with the rotation axis in the z -direction and the UPA placed on the $x - z$ plane. Here, the radial distance of the centre (i.e., \mathbf{X}) to the m th rotor hub denotes d_m . The distance of the m th rotor hub to the receiver is hence found by using the law of cosines:

$$R_m(\mathbf{X}) = \sqrt{R^2(\mathbf{X}) + d_m^2 - 2R(\mathbf{X})d_m \cos(\theta_m)}, \tag{4.19}$$

where $R(\mathbf{X})$ is the radial distance of the object to the receiver given in (4.2), and θ_m denotes an angle between the $R(\mathbf{X})$ and the m th rotor hubs, which assumes to be known.

found using (4.21):

$$\mu_D^{(m,n)}(\mathbf{X}, \Theta_l) = -\frac{4\pi}{\lambda_c} B' \cos(\phi(X)) \sin\left(\omega_m nT + \frac{2\pi(l-1)}{\tilde{L}}\right), \quad (4.22)$$

where $\mu_D^{(m,n)}(\mathbf{X}, \Theta_l)$ denotes the micro-Doppler shift induced by the l th rotating blade on the m th hub for the n th received pulse. In comparison to the micro-Doppler shift of (2.54) in Section 2.4, (4.22) contains the cosine term of the elevation angle of \mathbf{X} .

Note that, in this problem setting, the reflector of interest is a small drone. Because of the small sized body, the radial distance of $R(\mathbf{X})$ in (4.2) is very close to that of $R_m(X)$ in (4.19) due to $d_m \ll R(X)$. In other words, the corresponding time of flight is very close to that of $R_m(X)$ (i.e., $\tau(X) \approx \tau_m(X)$). The front-end input hence approximates to the superposition of the reflections with the same times of flight from both the aircraft body and its rotating blades.

After the demodulation and MF, the MF output of the array reflections from the m th rotor hub associated with the $\tilde{L} > 1$ rotating blades is found by using (4.22) and a Bessel series [110]:

$$\begin{aligned} \tilde{\mathbf{s}}_m^{(r)}(t) &\triangleq \tilde{\alpha}_m \mathbf{s}_s(\phi(\mathbf{X}), \theta(\mathbf{X})) e^{-j\omega_c \tau(\mathbf{X})} \sum_{n=0}^{N-1} e^{j\Omega(\mathbf{X})nT} \\ &\quad \times \sum_{l=1}^{\tilde{L}} e^{j\mu_D^{(m,n)}(\mathbf{X}, \Theta_l)} \times \Lambda(t - \tau(\mathbf{X}) - nT) \\ &= \tilde{\alpha}_m \mathbf{s}_s(\phi(\mathbf{X}), \theta(\mathbf{X})) e^{-j\omega_c \tau(\mathbf{X})} \sum_{n=0}^{N-1} e^{jn\Omega(\mathbf{X})} \\ &\quad \times \sum_{i=-\infty}^{+\infty} J_i\left(-\frac{4\pi}{\lambda_c} B' \cos(\phi(\mathbf{X}))\right) e^{j \times i \omega_m nT} \\ &\quad \times \sum_{l=1}^{\tilde{L}} e^{j \times i \frac{2\pi(l-1)}{\tilde{L}}} \Lambda(t - \tau(\mathbf{X}) - nT) \end{aligned} \quad (4.23)$$

where $\tilde{\alpha}_m$ is the reflection coefficient associated with \tilde{L} rotating blades of the m th hub, and J_i is the Bessel function of the 1st kind and i th order in (4.6). Here, the reason for the use of the Bessel function combines all influences on the micro-Doppler modulations of individual rotating blades and provides a single function that contains

the micro-Doppler components and acts as the Fourier coefficient for them. This will be shown through the derivation for the rest of this section.

It is emphasized that (4.23) is the reflection from the unit reflector patch, B' , along the blade length, B . In order to obtain the micro-Doppler shift along the total blade length, B , (4.23) needs to take the integral over the total blade length:

$$\mathbf{s}_m^{(r)}(t) \triangleq \int_{B'=0}^{B'=B} \tilde{\mathbf{s}}_m^{(r)}(t) dB',$$

and the resulting expression obtained by using the integral of Bessel series [110, Chp.3] is found as

$$\begin{aligned} \mathbf{s}_m^{(r)}(t) &= \tilde{\alpha}_m \mathbf{s}_s(\phi(\mathbf{X}), \theta(\mathbf{X})) e^{-j\omega_c \tau(\mathbf{X})} \sum_{n=0}^{N-1} e^{jn\Omega(\mathbf{X})} \\ &\times \sum_{i=-\infty}^{+\infty} \sum_{\tilde{i}=0}^{+\infty} \frac{2(-1)^{\tilde{L}i}}{\frac{4\pi}{\lambda_c} \cos(\phi(\mathbf{X}))} J_{\tilde{L}i+2\tilde{i}+1} \left(B \frac{4\pi}{\lambda_c} \cos(\phi(\mathbf{X})) \right) \\ &\times e^{j \times i \omega_m n T} \sum_{l=1}^{\tilde{L}} e^{j \times i \frac{2\pi(l-1)}{\tilde{L}}} \Lambda(t - \tau(\mathbf{X}) - nT). \end{aligned} \quad (4.24)$$

Here, the summation term on the last line of (4.24) is the sum of roots of unity given by

$$\sum_{l=1}^{\tilde{L}} e^{j \times i \frac{2\pi(l-1)}{\tilde{L}}} = \begin{cases} 0 & \text{if } i \neq 0, \pm\tilde{L}, \pm 2\tilde{L}, \dots \\ \tilde{L} & \text{if } i = 0, \pm\tilde{L}, \pm 2\tilde{L}, \dots \end{cases}. \quad (4.25)$$

After substituting (4.25) into the micro-Doppler reflection in (4.24), one obtains

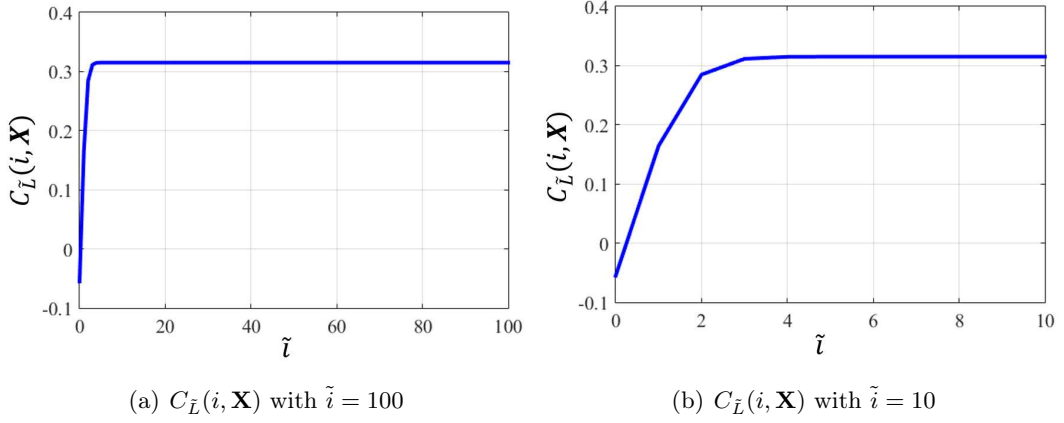
$$\mathbf{s}_m^{(r)}(t) = \tilde{\alpha}_m \mathbf{s}_s(\phi(\mathbf{X}), \theta(\mathbf{X})) e^{-j\omega_c \tau(\mathbf{X})} \sum_{n=0}^{N-1} e^{j\Omega(\mathbf{X})nT} \times C_n(\omega_m, \mathbf{X}) \Lambda(t - \tau(\mathbf{X}) - nT), \quad (4.26)$$

where C_n is a function of the m th rotation frequency and \mathbf{X} capturing the summation over all the Bessel functions in (4.24) and is given in (4.6).

Let one consider the computation of (4.6). This function has two infinite summation terms, which are not straightforward to be evaluated. Here, this function is divided into inner and outer summation. The outer summation that contains the inner summation

Table 4.1: C_n function parameters

Parameter	Value
Wavelength, i.e., λ_c	0.3 m
Pulse repetition interval (PRI), i.e., T	133 μ s
Number of rotor blades, i.e., \tilde{L}	2
Elevation angle, i.e., $\phi(\mathbf{X})$	0
Rotation frequency, i.e., ω	$2\pi \times 68$ Hz
Blade length, i.e., B	0.16 m


Figure 4.4: Empirical resulting value of $C_{\tilde{L}}$ in (4.28): (a) $C_{\tilde{L}}(i, \mathbf{X})$ with $\tilde{i} = 0, \dots, 100$. (b) $C_{\tilde{L}}(i, \mathbf{X})$ with $\tilde{i} = 0, \dots, 10$. $C_{\tilde{L}}$ is converged to 0.33 at $\tilde{i} = 3$.

is given by:

$$C_n(\omega, \mathbf{X}) \triangleq \sum_{i=-\infty}^{+\infty} C_{\tilde{L}}(i, \mathbf{X}) \times e^{j \times \tilde{L} i \times \omega \times n T}, \quad (4.27)$$

where $C_{\tilde{L}}$ is the inner summation and is given by

$$C_{\tilde{L}}(i, \mathbf{X}) \triangleq \sum_{\tilde{i}=0}^{+\infty} \frac{2(-1)^{\tilde{L}\tilde{i}}}{\frac{4\pi}{\lambda_c} \cos(\phi(\mathbf{X}))} \times J_{\tilde{L}i+2\tilde{i}+1} \left(B \frac{4\pi}{\lambda_c} \cos(\phi(\mathbf{X})) \right) \quad (4.28)$$

Regarding (4.28) and (4.27), Figure 4.4 illustrates empirical resulting values of the inner summation in (4.28). The parameters used in this experiment is listed in Table 4.1. Here, Figure 4.4(a) shows the empirical resulting value of (4.28) in the range of $\tilde{i} = 0, \dots, 100$, and Figure 4.4(b) illustrates its resulting value for $\tilde{i} = 0, \dots, 10$, respectively. As shown in Figure 4.4, $C_{\tilde{L}}$ is converged to 0.33 at $\tilde{i} = 3$ in both cases. Similarly,

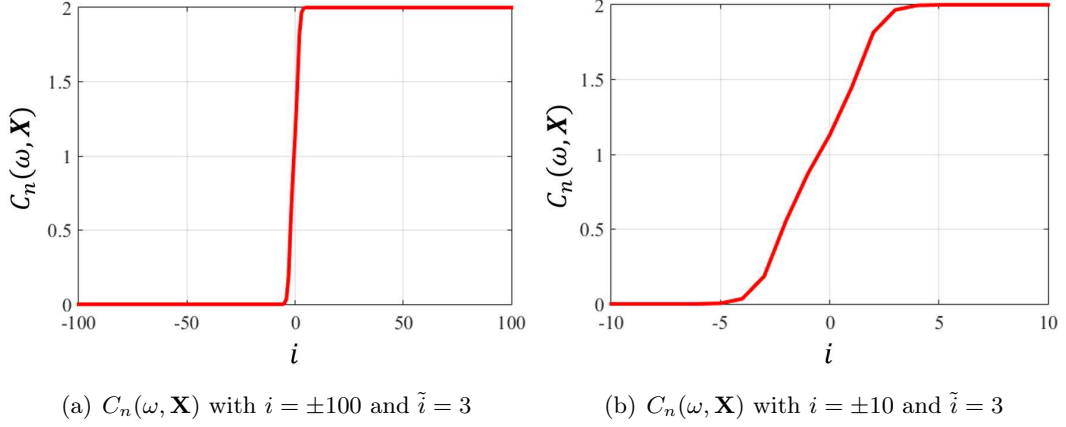


Figure 4.5: Empirical resulting value of C_n with $n = 1$ in (4.27): (a) C_n with $i = -100, \dots, 100$ and $\tilde{i} = 0, \dots, 3$ (b) C_n with $i = -10, \dots, 10$ and $\tilde{i} = 0, \dots, 3$. $C_n(\omega, \mathbf{X})$ is converged to 2 at $i = \pm 5$.

Figure 4.5 presents empirical resulting values of (4.27) with the same parameter values used in Figure 4.4. The inner summation term sets the range of $\tilde{i} = 0, \dots, 3$ due to its convergence. Figure 4.5(a) and (b) show the resulting values in the range of $i = -100, \dots, 100$ and of $i = -10, \dots, 10$, respectively. Both values are converged to 2 at $i = 5$. Regarding these experiments, it is concluded that the computation of C_n requires the minimum range of $\tilde{i} = 0, \dots, 3$ for the inner summation and of $i = -5, \dots, 5$ for the outer summation, respectively, in order to find this coefficient. For the rest of this chapter, these summation terms set $\tilde{i} = 0, \dots, 3$ and $i = -5, \dots, 5$ to compute C_n for each of N pulses in a CPI.

In the case of $M > 1$ rotor hubs, rotation frequencies of blades on separately located rotor hubs are very close during flight. There are experimental results on the power spectrum of radar measurements on a commercial quad-rotor drone when flying. These results show harmonics of a single fundamental frequency as the rotating blades (see, for example, [112]). In other words, all the (angular) rotation frequencies of rotating blades at M rotor hubs can be represented with one degree of freedom:

$$\omega_m \approx \omega, \quad m = 1, \dots, M.$$

As a result, the MF output of reflections from all rotating blades at M rotor hubs, each

of which considers the same position and velocity of the aircraft's body, becomes

$$\mathbf{s}^{(r)}(t) = \boldsymbol{\alpha}_1 \mathbf{s}_s(\phi(\mathbf{X}), \theta(\mathbf{X})) e^{-j\omega_c \tau(\mathbf{X})} \sum_{n=0}^{N-1} e^{j\Omega(\mathbf{X})nT} \times C_n(\omega, \mathbf{X}) \Lambda(t - \tau(\mathbf{X}) - nT), \quad (4.29)$$

where

$$\boldsymbol{\alpha}_1 \triangleq \sum_{m=1}^M \tilde{\alpha}_m$$

is the sum of M reflection coefficients that captures the reflectivity of the hubs as well as the reflectivity of the blades. It is straightforward to identify this term in the matched filter output model in (4.1). It is also emphasised that this resulting expression is a new mathematical expression for small drones.

4.3.2 Measurement model

This subsection provides explicit formulae for the measurement model in (4.8) starting from the radar data cube. As explained in Section 4.2.1, $\tilde{\mathbf{Z}}$ is the radar data cube that contains $N_v N_h \times N \times \Gamma$ data samples from the array index, the pulse index, and the range index, respectively, as illustrated in Figure 4.2. Before specifying $\tilde{\mathbf{Z}}$, let one denote a temporal matrix by $\mathbf{s}_t(\mathbf{X}, \Omega, \omega) \in \mathbb{C}^{N \times 2}$ that captures the micro-Doppler components in (4.27) induced by the (angular) rotation frequency, ω , when the receiver collects the N pulses:

$$\mathbf{s}_t(\mathbf{X}, \Omega, \omega) \triangleq e^{-j\omega_c \tau(\mathbf{X})} \times \begin{bmatrix} 1 & C_0(\omega, \mathbf{X}) \\ \vdots & \vdots \\ e^{j\Omega(N-1)T} & C_{N-1}(\omega, \mathbf{X}) e^{j\Omega(N-1)T} \end{bmatrix}. \quad (4.30)$$

For the r th range bin, $N_v N_h \times N$ array measurements are hence a slice along the pulse index. This is given by

$$\begin{aligned} \tilde{\mathbf{Z}}(r) &= \mathbf{s}_s(\phi(\mathbf{X}), \theta(\mathbf{X})) \times \{\mathbf{s}_t(\mathbf{X}, \Omega(\mathbf{X}), \omega) \times \boldsymbol{\alpha}\}^T \times \Lambda(rT_p - \tau(\mathbf{X})) \\ &\quad + \mathbf{s}_s(\phi(\mathbf{X}), \theta(\mathbf{X})) \times \tilde{\mathbf{n}}^T(r), \end{aligned} \quad (4.31)$$

$$\tilde{\mathbf{n}}(r) \triangleq [\boldsymbol{\eta}(rT_p), \boldsymbol{\eta}(rT_p + T), \dots, \boldsymbol{\eta}(rT_p + (N-1)T)]^T, \quad (4.32)$$

where $\tilde{\mathbf{n}}$ is the sampler output due to the nuisance term, $\boldsymbol{\eta}$, in (4.1) and is the superposition of the background and the receiver noise.

As explained in Section 4.2.1, it stacks columns of $\tilde{\mathbf{Z}}(r)$ and forms an $N_v N_h N \times 1$ data vector. As a result, $\mathbf{H} \in \mathbb{C}^{N_v N_h N \times 2}$ in (4.8) is identified and is a function of the object kinematic state, \mathbf{X} , and the (angular) rotation frequency, ω :

$$\mathbf{H}(r, \mathbf{X}, \omega) \triangleq \mathbf{s}_s(\phi(\mathbf{X}), \theta(\mathbf{X})) \otimes \mathbf{s}_t(\mathbf{X}, \Omega(\mathbf{X}), \omega) \times \Lambda(rT_p - \tau(\mathbf{X})), \quad (4.33)$$

where \otimes denotes the Kronecker product operator.

4.4 Trajectory estimation with Bayesian filtering of the radar data cubes

Let this section consider tracking $\mathbf{X}_{1:K}$ with the radar data cubes collected for the time window K . As discussed in Section 3.3 a Markov state-space model [24, Chp.3] is used and models $\mathbf{X}_{1:K}$ as a sequence of kinematic states in (3.16). The initial distribution is selected as the uniform distribution in (3.19) due to no prior knowledge of the position and the velocity of the reflector at an initial state. This uniform distribution uses a bounded set, \mathcal{B} , of the range-angle (i.e., the position) and the Doppler (i.e., the velocity) intervals, which often correspond to radar specific resolution bins. The Markov transition density in this section is selected as

$$p(\mathbf{X}_k | \mathbf{X}_{k-1}) = \mathcal{N}(\mathbf{X}_k; \mathbf{F}\mathbf{X}_{k-1}, \mathbf{Q}), \quad (4.34)$$

where \mathbf{F} models constant velocity motion with the time interval of Δ between two consecutive pulse train transmissions (or the illumination period) given by

$$\mathbf{F} = \begin{bmatrix} 1 & 0 & 0 & \Delta & 0 & 0 \\ 0 & 1 & 0 & 0 & \Delta & 0 \\ 0 & 0 & 1 & 0 & 0 & \Delta \\ 0 & 0 & 0 & 1 & 0 & 0 \\ 0 & 0 & 0 & 0 & 1 & 0 \\ 0 & 0 & 0 & 0 & 0 & 1 \end{bmatrix}, \quad (4.35)$$

and \mathbf{Q} is the covariance matrix specifying the level of the process noise modelling unknown manoeuvres. For example, a variance of σ_v^2 in each direction of the velocity vector is modelled with

$$\mathbf{Q} = \sigma_v^2 \times \begin{bmatrix} \frac{\Delta^3}{3} & 0 & 0 & \frac{\Delta^2}{2} & 0 & 0 \\ 0 & \frac{\Delta^3}{3} & 0 & 0 & \frac{\Delta^2}{2} & 0 \\ 0 & 0 & \frac{\Delta^3}{3} & 0 & 0 & \frac{\Delta^2}{2} \\ \frac{\Delta^2}{2} & 0 & 0 & \Delta & 0 & 0 \\ 0 & \frac{\Delta^2}{2} & 0 & 0 & \Delta & 0 \\ 0 & 0 & \frac{\Delta^2}{2} & 0 & 0 & \Delta \end{bmatrix}. \quad (4.36)$$

Sequential estimate, \mathbf{X}_k , uses the measurement likelihood of the signal model, which is found using (4.8) for $H = H_1$, and using (4.14):

$$l(\mathbf{Z}_k | \mathbf{X}_k, \boldsymbol{\alpha}_k, \omega) \propto \prod_{r \in \mathcal{E}(\mathbf{X}_k)} l(\mathbf{Z}_k(r) | \mathbf{X}_k, \boldsymbol{\alpha}_k, \omega, H = H_1). \quad (4.37)$$

In particular, a bootstrap filtering approach is used for this purpose: For the prediction stage at time step $k = 1$, a regular grid of P samples (or particles) over \mathcal{B} is generated from the initial state distribution in (3.19). These samples constitute an equally weight set denoted by

$$\left\{ \mathbf{X}_1^{(p)}, \zeta_1^{(p)} \leftarrow \frac{1}{P} \right\}_{p=1}^P.$$

For time step $k > 1$, suppose that a set of weighted particles is available, represents the

state posterior in the previous step and denote this set by

$$\left\{ X_{k-1}^{(p)}, \zeta_{k-1}^{(p)} \right\}_{p=1}^P.$$

The prediction stage with this set is realised by using the Markov transition in (4.34):

$$\mathbf{X}_{k|k-1}^{(p)} \sim p(\cdot | \mathbf{X}_{k-1}^{(p)}), \quad p = 1, \dots, P. \quad (4.38)$$

The corresponding weights are used as the previous weights:

$$\zeta_{k|k-1}^{(p)} \leftarrow \zeta_{k-1}^{(p)}. \quad (4.39)$$

Now, the prediction stage obtains a new set of P samples (or particles):

$$\left\{ \mathbf{X}_{k|k-1}^{(p)}, \zeta_{k|k-1}^{(p)} \right\}_{p=1}^P. \quad (4.40)$$

As explained in Section 3.3, for the update stage, P state variables are used as the state variables from the prediction stage:

$$\mathbf{X}_k^{(p)} \leftarrow \mathbf{X}_{k|k-1}^{(p)}, \quad p = 1, \dots, P. \quad (4.41)$$

The corresponding weights are updated by using the measurement likelihood in (4.37) together with the given (hypothesised) reflection coefficients, $\boldsymbol{\alpha}_k$, and the rotation frequency, ω :

$$\zeta_k^{(p)} = \frac{\tilde{\zeta}_k^{(p)}}{\sum_{p'=1}^P \tilde{\zeta}_k^{(p')}}, \quad (4.42)$$

$$\tilde{\zeta}_k^{(p)} = \zeta_{k|k-1}^{(p)} l(\mathbf{Z}_k | \mathbf{X}_k^{(p)}, \boldsymbol{\alpha}_k, \omega). \quad (4.43)$$

After finding the normalised weights $\zeta_k^{(p)}$ in (4.42), the degeneracy is tested using (3.32) to find the number of the effective particles and comparing this value to a pre-defined threshold of \mathcal{T}_{eff} . When $N_{eff} < \mathcal{T}_{eff}$, perform the re-sampling using (3.33) and the post-regularised step using (3.34), which provides a new set of the particles. Afterwards, continue filtering with this new set of equally weighted particles.

After the degeneracy test, the re-sampling, and the post-regularised step, the object

state at the k th CPI is estimated by using the weighted average:

$$\hat{X}_k = \sum_{p=1}^P \zeta_k^{(p)} X_k^{(p)}. \quad (4.44)$$

where \hat{X}_k denotes the estimated object state X_k .

4.5 Maximum likelihood estimation of the micro-Doppler shift and the reflectivity

The previous section details a particle filter for generating weighted samples from filtering distributions that facilitate the estimation of the state variable. Let this section consider estimating ω and $\alpha_{1:K}$ in order to evaluate the hypothesis test in (4.12) through (4.14)–(4.18).

In the signal model derived from Section 4.3.1, ω is a frequency shift characterising micro-Doppler signature captured by $C_n(\mathbf{X}, \omega)$ in (4.6). In the literature, micro-Doppler signatures (or shifts) are often found by using time-frequency analysis (TFA) techniques after the detection processing is completed (see, for example, [113, 114]). These techniques often require long dwell times to collect sufficient data samples in a CPI so that the TFA can achieve a favourable frequency resolution. In the case of manoeuvring and small reflectors, these conditions cannot be easily achieved due to the low reflectivity, which delivers difficulties in detecting such objects in the first place, and the manoeuvres, which limit the length of a CPI and the number of reflections collected during this interval.

Unlike the TFA approaches, the proposed scheme is interested in evaluating the sufficient statistics of ω using the radar data cubes collected during the time window of K CPIs. Each data cube is the complex number and parametrised on the reflector kinematic state, the complex reflection coefficients, and the (angular) rotation frequency (see, (4.31)). As discussed in Section 3.4.1, an expectation-maximisation (EM) algorithm is proposed due to latent variables such as $\mathbf{X}_{1:K}$ and $\alpha_{1:K}$. It is emphasised that even though the

proposed scheme is the same used in Section 3.4.1, the problem setting here differ from that in Section 3.4.1: The previously proposed EM just solved the estimation problem of α_k considering the likelihood that takes the measurements collected at time step k (, equivalently the k th CPI) and has no considerations for previous measurements due to the change of the reflectivity from one CPI to another. The problem here, on the other hand, considers all the measurements during the time window of K CPIs in the range of $k = 1, \dots, K$ in order to estimate ω , and the number of latent variables in the proposed EM have two variables as unknowns. For the problem at hand, the EM iterations to solve the optimisation problem for $j = 1, 2, \dots$ is given by

$$\omega^{(j)} = \arg \max_{\omega} Q \left(\omega, \omega^{(j-1)} \right), \quad (4.45)$$

and

$$\begin{aligned} Q \left(\omega, \omega^{(j-1)} \right) &\triangleq \mathbb{E} \left\{ \log p(\mathbf{X}_{1:K}, \alpha_{1:K}, \mathbf{Z}_{1:K} | \omega); \mathbf{Z}_{1:K}, \omega^{(j-1)} \right\} \\ &= \int \int_{\mathbf{X}_{1:K} \alpha_{1:K}} \log p(\mathbf{X}_{1:K}, \alpha_{1:K}, \mathbf{Z}_{1:K} | \omega) \\ &\quad \times p(\mathbf{X}_{1:K}, \alpha_{1:K} | \mathbf{Z}_{1:K}, \omega^{(j-1)}) d\mathbf{X}_{1:K} d\alpha_{1:K} \end{aligned} \quad (4.46)$$

where $\mathbb{E}\{\cdot\}$ is the expectation, and the density underlying the expectation above is conditioned on $\mathbf{Z}_{1:K}$ and the previously found value, $\omega^{(j-1)}$.

The first term inside the integral of (4.46) is expressed by using the Bayes' rule and the chain rule of probabilities:

$$\begin{aligned} &\log p(\mathbf{X}_{1:K}, \alpha_{1:K}, \mathbf{Z}_{1:K} | \omega) \\ &= \log \{ l(\mathbf{Z}_{1:K} | \mathbf{X}_{1:K}, \alpha_{1:K}, \omega) \times p(\mathbf{X}_{1:K} | \alpha_{1:K}, \omega) \times p(\alpha_{1:K} | \omega) \} \\ &= \log l(\mathbf{Z}_{1:K} | \mathbf{X}_{1:K}, \alpha_{1:K}, \omega) + \log p(\mathbf{X}_{1:K} | \alpha_{1:K}, \omega) + \log p(\alpha_{1:K} | \omega). \end{aligned} \quad (4.47)$$

As discussed in Section 4.2.3, it is assumed that all variables, which the likelihood is conditioned on, are independent because one parameter has no influences on the change of the other parameters. In other words, $\mathbf{X}_{1:K}$ and $\alpha_{1:K}$ are not affected by ω . Here, another assumption holds as the conditional independence of the measurement variable,

\mathbf{Z}_k at time k given \mathbf{X}_k , $\boldsymbol{\alpha}_k$, and ω . Regarding these assumptions, (4.47) is rewritten by

$$\begin{aligned} & \log p(\mathbf{X}_{1:K}, \boldsymbol{\alpha}_{1:K}, \mathbf{Z}_{1:K} | \omega) \\ &= \sum_{k=1}^K \log l(\mathbf{Z}_k | \boldsymbol{\alpha}_k, \mathbf{X}_k, \omega) + \log p(\mathbf{X}_{1:K}) + \log p(\boldsymbol{\alpha}_{1:K}). \end{aligned} \quad (4.48)$$

The second term inside the integral of (4.46) also expands using the chain rule of probabilities with the conditional independence:

$$p(\mathbf{X}_{1:K}, \boldsymbol{\alpha}_{1:K} | \mathbf{Z}_{1:K}, \omega^{(j-1)}) = \prod_{k=1}^K p(\mathbf{X}_k, \boldsymbol{\alpha}_k | \mathbf{Z}_{1:K}, \omega^{(j-1)}). \quad (4.49)$$

As a result, the EM objective (i.e., Q function) in (4.46) through (4.47)–(4.49) is rewritten by

$$\begin{aligned} Q(\omega, \omega^{(j-1)}) &= \int_{\mathbf{X}_{1:K}} \int_{\boldsymbol{\alpha}_{1:K}} \sum_{k=1}^K \log l(\mathbf{Z}_k | \boldsymbol{\alpha}_k, \mathbf{X}_k, \omega) \prod_{k=1}^K p(\mathbf{X}_k, \boldsymbol{\alpha}_k | \mathbf{Z}_{1:K}, \omega^{(j-1)}) d\mathbf{X}_{1:K} d\boldsymbol{\alpha}_{1:K} \\ &+ \int_{\mathbf{X}_{1:K}} \int_{\boldsymbol{\alpha}_{1:K}} \log p(\mathbf{X}_{1:K}) \prod_{k=1}^K p(\mathbf{X}_k, \boldsymbol{\alpha}_k | \mathbf{Z}_{1:K}, \omega^{(j-1)}) d\mathbf{X}_{1:K} d\boldsymbol{\alpha}_{1:K} \\ &+ \int_{\mathbf{X}_{1:K}} \int_{\boldsymbol{\alpha}_{1:K}} \log p(\boldsymbol{\alpha}_{1:K}) \prod_{k=1}^K p(\mathbf{X}_k, \boldsymbol{\alpha}_k | \mathbf{Z}_{1:K}, \omega^{(j-1)}) d\mathbf{X}_{1:K} d\boldsymbol{\alpha}_{1:K} \\ &\propto \sum_{k=1}^K \int_{\mathbf{X}_k} \int_{\boldsymbol{\alpha}_k} \log l(\mathbf{Z}_k | \boldsymbol{\alpha}_k, \mathbf{X}_k, \omega) p(\mathbf{X}_k, \boldsymbol{\alpha}_k | \mathbf{Z}_{1:K}, \omega^{(j-1)}) d\mathbf{X}_k d\boldsymbol{\alpha}_k. \end{aligned} \quad (4.50)$$

Here, the second and third lines are not dependent on ω as explained through (4.47) and (4.48). Thus, the Q function is only considered with the likelihood term that is conditioned on \mathbf{X}_k , $\boldsymbol{\alpha}_k$, and ω . Also, the Q function is proportional to the last line in (4.50). Furthermore, the evaluation of (4.50) involves smoothing [115] over K radar data cubes (i.e., $\mathbf{Z}_{1:k}$). The smoothing differs from the filtering: The filtering in Bayesian framework computes (or finds) the distribution of variables based on sequence of observations. On the other hand, the smoothing requires all observations up to time K and computes the distribution of variables based on these observations. This, hence, needs to have more computation effort than the use of sequential filtering. In order to facilitate the sequential filtering, the smoothing density in (4.50) is replaced with the

filtering density, and the correspondence is given by

$$\tilde{Q}_K(\omega, \omega^{(j-1)}) \triangleq \sum_{k=1}^K \int \int_{\mathbf{X}_k \alpha_k} \log l(\mathbf{Z}_k | \mathbf{X}_k, \alpha_k, \omega) p(\mathbf{X}_k, \alpha_k | \mathbf{Z}_{1:k}, \omega^{(j-1)}) d\mathbf{X}_k d\alpha_k, \quad (4.51)$$

where the right hand side is an approximation to the right hand side in the last line of (4.50). This objective can make a recursive form, which is given by

$$\tilde{Q}_k(\omega, \omega^{(j-1)}) = \tilde{Q}_{k-1}(\omega, \omega^{(j-1)}) + \tilde{R}_k(\omega, \omega^{(j-1)}), \quad (4.52)$$

for $k = 1, \dots, K$ with the initial $\tilde{Q}_0 = 0$, and

$$\tilde{R}_k(\omega, \omega^{(j-1)}) \triangleq \int \int_{\mathbf{X}_k \alpha_k} \log l(\mathbf{Z}_k | \mathbf{X}_k, \alpha_k, \omega) p(\mathbf{X}_k, \alpha_k | \mathbf{Z}_{1:k}, \omega^{(j-1)}) d\mathbf{X}_k d\alpha_k, \quad (4.53)$$

The filtering density as discussed above is the second term inside the integral of (4.53) and is still complex to be evaluated. This density involves both the state variable and the complex reflection coefficients. This term further decomposes using the chain rule of probabilities:

$$p(\mathbf{X}_k, \alpha_k | \mathbf{Z}_{1:k}, \omega^{(j-1)}) = p(\mathbf{X}_k | \alpha_k, \mathbf{Z}_{1:k}, \omega^{(j-1)}) \times p(\alpha_k | \mathbf{Z}_{1:k}, \omega^{(j-1)}) \quad (4.54)$$

Here, the first term on the right hand side is the filtering density on the kinematic state, \mathbf{X}_k , at time k conditioned on the radar data cubes collected up to k CPIs and the signal model parameters. Computation of this density can be viewed as track-before-detect as discussed in Chapter 3. The second term in (4.54) is the density of the complex reflection coefficients conditioned on the measurements, $\mathbf{Z}_{1:k}$, and the rotation frequency, ω . Note that it is desirable to use a sufficiently flat (or non-informative) prior for these reflection coefficients. Here, the conditioning on the measurements places more probability mass in the posterior concentrated in the vicinity of the ML estimate of α_k given $\omega^{(j-1)}$. Thus, the following approximation to this density is considered:

$$p(\alpha_k | \mathbf{Z}_{1:k}, \omega^{(j-1)}) \leftarrow \delta_{\hat{\alpha}_k(\omega^{(j-1)})}(\alpha_k), \quad (4.55)$$

$$\hat{\alpha}_k(\omega^{(j-1)}) = \arg \max_{\alpha_k} l(\mathbf{Z}_{1:k} | \alpha_k, \omega^{(j-1)}), \quad (4.56)$$

where δ is Dirac's delta distribution, and \leftarrow denotes assignment that the distribution

on the left hand side is asserted to be the Dirac's delta on the right hand side. Here, the ML estimate of $\boldsymbol{\alpha}_k$ is dependent on $\omega^{(j-1)}$ and becomes a function of $\omega^{(j-1)}$. This is an instance of empirical Bayes as discussed in Section 3.3.

As a result, after substituting (4.54) and (4.55) from time step 1 to k into (4.53), this leads to the objective function component at the time step k :

$$\begin{aligned} \tilde{R}_k \left(\omega, \omega^{(j-1)} \right) &\approx \int_{\mathbf{X}_k} \log l \left(\mathbf{Z}_k | \mathbf{X}_k, \hat{\boldsymbol{\alpha}}_k \left(\omega^{(j-1)} \right), \omega \right) \\ &\quad \times p \left(\mathbf{X}_k | \mathbf{Z}_{1:k}, \hat{\boldsymbol{\alpha}}_k \left(\omega^{(j-1)} \right), \omega^{(j-1)} \right) d\mathbf{X}_k. \end{aligned} \quad (4.57)$$

Let one focus on the evaluation of (4.57). For this purpose, the Monte Carlo integration [101] is used with a set of particles representing the filtering distribution with the density $p \left(\mathbf{X}_k | \mathbf{Z}_{1:k}, \hat{\boldsymbol{\alpha}}_k \left(\omega^{(j-1)} \right), \omega^{(j-1)} \right)$. This set is obtained/computed through (4.40)–(4.43) using the steps detailed in Section 4.4. Thus, a Monte Carlo approximation to (4.57) with the set of $\left\{ \mathbf{X}_k^{(p)}, \zeta_k^{(p)} \right\}_{p=1}^P$ is given by

$$\hat{R}_k \left(\omega, \omega^{(j-1)} \right) \approx \sum_{p=1}^P \zeta_k^{(p)} \times \log l \left(\mathbf{Z}_k | \mathbf{X}_k = \mathbf{X}_k^{(p)}, \hat{\boldsymbol{\alpha}}_k \left(\omega^{(j-1)} \right), \omega \right) \quad (4.58)$$

Thus, (4.52) approximates:

$$\hat{Q}_k \left(\omega, \omega^{(j-1)} \right) \approx \hat{Q}_{k-1} + \hat{R}_k \left(\omega, \omega^{(j-1)} \right), \quad (4.59)$$

$$\hat{Q}_{k-1} \approx \sum_{k=1}^{k-1} \hat{R}_k \left(\omega, \omega^{(j-1)} \right), \quad (4.60)$$

and (4.51) approximates:

$$\hat{Q}_{k=K} \left(\omega, \omega^{(j-1)} \right) \approx \sum_{k=1}^{k=K} \hat{R}_k \left(\omega, \omega^{(j-1)} \right), \quad (4.61)$$

The formula above facilitates the gradient-free methods such as one-dimensional line search techniques to solve the maximisation problem in (4.45). As discussed in Section 3.4.2, the golden section search algorithm that iteratively finds ω maximising the Monte Carlo approximation to the EM objective in (4.50) evaluated through (4.51)–(4.60). This evaluation relies on being able to solve the second nested

ML problem that involves the estimation of the reflection coefficients in (4.56). This problem differs from that of Chapter 3. In the next section, the explicit formulae for solving (4.56) and extend the coherent track-before-detect algorithm in Chapter 3 together with the signal model in Section 4.3 that captures the micro-Doppler shift term.

4.5.1 ML estimation for the reflection coefficients

Let this subsection consider the ML estimation problem in (4.56). The empirical Bayes approximation asserted from 1 to k estimates the reflection coefficients at all time steps and is conditioned on the filtering density in (4.58). This operation leads to the sequence of $\alpha_{k'}$ estimation for $k' = 1, \dots, k$ time steps. This approach requires another EM iterations inside the above EM algorithm in order to find $\hat{\omega}$. Here, for the sake of simplicity in notion, the dependence of the reflection coefficient estimates to the micro-Doppler shift (i.e., $\hat{\alpha}_{k'}(\omega^{(j-1)})$) is not used for the rest of this section. Thus, EM iterations to estimate $\alpha_{k'}$ are given for $i = 1, 2, \dots$ by solving the problem:

$$\alpha_{k'}^{(i)} = \arg \max_{\alpha_{k'}} S_{\omega^{(j-1)}}(\alpha_{k'}, \alpha_{k'}^{(i-1)}), \quad (4.62)$$

where

$$\begin{aligned} S_{\omega^{(j-1)}}(\alpha_{k'}, \alpha_{k'}^{(i-1)}) &\triangleq \mathbb{E}\{\log p(\mathbf{X}_{k'}, \mathbf{Z}_{k'} | \alpha_{k'}, \omega^{(j-1)}) | \mathbf{Z}_{k'}, \alpha_{k'}^{(i-1)}, \omega^{(j-1)}\} \\ &= \int_{\mathbf{X}_{k'}} \log p(\mathbf{X}_{k'}, \mathbf{Z}_{k'} | \alpha_{k'}, \omega^{(j-1)}) \times p(\mathbf{X}_{k'} | \mathbf{Z}_{k'}, \alpha_{k'}^{(i-1)}, \omega^{(j-1)}) d\mathbf{X}_{k'}. \\ &\propto \int_{\mathbf{X}_{k'}} \log l(\mathbf{Z}_{k'} | \mathbf{X}_{k'}, \alpha_{k'}, \omega) \times p(\mathbf{X}_{k'} | \mathbf{Z}_{k'}, \alpha_{k'}^{(i-1)}, \omega^{(j-1)}) d\mathbf{X}_{k'}. \end{aligned} \quad (4.63)$$

Note that as discussed in Section 3.4.1, this objective is obtained by using the same steps through (3.37)–(3.41). The second term inside the integral in (4.64) is the prior density for the object state, $\mathbf{X}_{k'}$, conditioned on the reflection coefficient estimates given value at $(i-1)$ and the fixed micro-Doppler shift, $\omega^{(j-1)}$. The density can also be expressed using Bayes' rule:

$$p(\mathbf{X}_{k'} | \mathbf{Z}_{k'}, \alpha_{k'}^{(i-1)}, \omega^{(j-1)}) \propto l(\mathbf{Z}_{k'} | \mathbf{X}_{k'}, \alpha_{k'}^{(i-1)}, \omega^{(j-1)}) \times p(\mathbf{X}_{k'} | \alpha_{k'}^{(i-1)}, \omega^{(j-1)}). \quad (4.65)$$

Here, $\alpha_{k'}^{(i-1)}$ and $\omega^{(j-1)}$ are given. $p(\mathbf{X}_{k'}|\cdot)$ is a prior density, where $\mathbf{X}_{k'}$ is independent to the other variables and is selected as the prediction density which is already defined in Section 4.4:

$$p(\mathbf{X}_{k'}|\alpha_{k'}^{(i-1)}, \omega^{(j-1)}) \leftarrow p(\mathbf{X}_{k'}|\mathbf{Z}_{1:k'-1}), \quad (4.66)$$

Thus, the Monte Carlo approximation to (4.63) is readily available when the sequence of problems until $k' - 1$ have been solved to obtain $\hat{\alpha}_{1:k'}$, and a particle set that represents the prediction density is generated.

When $k' = k$, $\hat{\alpha}_{1:k-1}$ have been estimated for a hypothesised micro-Doppler shift value of ω , and the set of $\{\mathbf{X}_{k|k-1}^{(p)}, \zeta_{k|k-1}^{(p)}\}$ has been obtained using the steps through (4.38)–(4.40) detailed in Section 4.4. Then, the MC approximation is given by

$$\hat{S}_\omega(\alpha_k, \alpha_k^{(i-1)}) \propto \sum_{p=1}^P \xi_k^{(p,i-1)} \log l(\mathbf{Z}_k|\mathbf{X}_k = \mathbf{X}_{k|k-1}^{(p)}, \alpha_k, \omega), \quad (4.67)$$

$$\xi_k^{(p,i-1)} = \frac{l(\mathbf{Z}_k|\mathbf{X}_k = \mathbf{X}_{k|k-1}^{(p)}, \alpha_k^{(i-1)}, \omega) \zeta_{k|k-1}^{(p)}}{\sum_{p'=1}^P l(\mathbf{Z}_k|\mathbf{X}_k = \mathbf{X}_{k|k-1}^{(p')}, \alpha_k^{(i-1)}, \omega) \zeta_{k|k-1}^{(p')}}, \quad (4.68)$$

For solving (4.62), it takes the first order partial derivative of (4.67) with respect to α_k . The resulting expression is given by

$$\begin{aligned} \frac{\partial \hat{S}_\omega(\alpha_k, \alpha_k^{(i-1)})}{\partial \alpha_k} &= \left[\frac{\frac{\partial \hat{S}_\omega(\alpha_k, \alpha_k^{(i-1)})}{\partial \alpha_{0,k}}}{\frac{\partial \hat{S}_\omega(\alpha_k, \alpha_k^{(i-1)})}{\partial \alpha_{1,k}}} \right] \\ &= \sum_{p=1}^P \sum_{r \in \mathcal{E}(\mathbf{X}_{k|k-1}^{(p)})} \xi_k^{(p,i-1)} \left\{ 2\mathbf{H}^H(r, \mathbf{X}_{k|k-1}^{(p)}, \omega) \Sigma^{-1} \mathbf{Z}_k(r) \right. \\ &\quad \left. - 2\mathbf{H}^H(r, \mathbf{X}_{k|k-1}^{(p)}, \omega) \Sigma^{-1} \mathbf{H}(r, \mathbf{X}_{k|k-1}^{(p)}, \omega) \right\}, \end{aligned} \quad (4.69)$$

where $\xi_k^{(p,i-1)}$ is given in (4.68). After setting this expression to zero, the ML estimate of the reflection coefficients at the k th CPI is found as a closed-form

Algorithm 4 Particle filtering and EM iterations for the estimation of reflection coefficients

- 1: Input: $\mathbf{Z}_{1:K}$ ▷ Radar data cubes for K CPIs
 - 2: Input: ω ▷ A micro-Doppler shift value
 - 3: Input: $\hat{\alpha}_0 \leftarrow \infty$
 - 4: **for** $k = 1, \dots, K$ **do** ▷ Particle filtering and EM
 - 5: Find $\{\mathbf{X}_{k|k-1}^{(p)}, \zeta_{k|k-1}^{(p)}\}_{p=1}^P$ through (4.38)–(4.40) with ω and $\hat{\alpha}_{1:k-1}$ ▷ Prediction stage in Section 4.4
 - 6: Find $\hat{\alpha}_k$ using Algorithm 5 with $\{\mathbf{X}_{k|k-1}^{(p)}, \zeta_{k|k-1}^{(p)}\}_{p=1}^P$ and ω ▷ Reflection coefficient estimation in Section 4.5.1
 - 7: Find $\{\mathbf{X}_k^{(p)}, \zeta_k^{(p)}\}_{p=1}^P$ through (4.41)–(4.43) with $\{\mathbf{X}_{k|k-1}^{(p)}, \zeta_{k|k-1}^{(p)}\}_{p=1}^P$, ω , and $\hat{\alpha}_k$ ▷ Update stage in Section 4.4
 - 8: **end for**
 - 9: Return $\hat{\alpha}_{1:K}$ and $\{\mathbf{X}_{1:K}^{(p)}, \zeta_{1:K}^{(p)}\}_{p=1}^P$
-

solution for given $\alpha_k^{(i-1)}$:

$$\begin{aligned}
 \alpha_k^{(i)} = & \left\{ \sum_{p=1}^P \sum_{r \in \mathcal{E}(\mathbf{x}_{k|k-1}^{(p)})} \xi_k^{(p,i-1)} \mathbf{H}^H(r, \mathbf{x}_{k|k-1}^{(p)}, \omega) \Sigma^{-1} \mathbf{H}(r, \mathbf{x}_{k|k-1}^{(p)}, \omega) \right\}^{-1} \\
 & \times \sum_{p=1}^P \sum_{r \in \mathcal{E}(\mathbf{x}_{k|k-1}^{(p)})} \xi_k^{(p,i-1)} \mathbf{H}^H(r, \mathbf{x}_{k|k-1}^{(p)}, \omega) \Sigma^{-1} \mathbf{Z}_k(r). \quad (4.70)
 \end{aligned}$$

Note that the ML estimator in (4.70) takes the inner product of the measurements with the signal model, \mathbf{H} , in (4.33) given the angular rotation frequency, ω . This operation effectively performs the digital beam-forming towards the reflector position encoded in the state, $\mathbf{x}_{k|k-1}^{(p)}$, by substituting P state variable particles into the signal model \mathbf{H} . In contrast, other beam-forming techniques require to find the reflector position by scanning all the surveillance region. The proposed estimator also simultaneously matches the Doppler frequency encoded in the signal model, \mathbf{H} , with its true value by using these P state particles. Therefore, this estimator will be rejecting interference with other objects, unless their state values are very close to the target state value in the achievable spatial and Doppler bandwidths.

The discussion above specifies Algorithm 4 and 5. The EM iterations are called during the iterations of particle filtering which was detailed in Section 4.4. These steps are given in Algorithm 4 for a hypothesised micro-Doppler shift of ω . The EM iterations are called at Step 6 and captured in Algorithm 5. Remind that these estimates are

Algorithm 5 Particle EM algorithm for the estimation of the reflection coefficients

- | | |
|---|---|
| 1: Input: ω | ▷ The hypothesised micro-Doppler shift |
| 2: Input: $\alpha_k^{(0)}$ and ϵ | ▷ Initial value and termination threshold |
| 3: Input: $\{\mathbf{X}_{k k-1}^{(p)}, \zeta_{k k-1}^{(p)}\}$ | ▷ Prediction stage in Section 4.4 |
| 4: Input: $i \leftarrow 0$ | ▷ Initialisation for the EM iterations |
| 5: repeat | |
| 6: $i \leftarrow i + 1$ | |
| 7: Find weights $\{\zeta_k^{(p,i-1)}\}_{p=1}^P$ using (4.68) with $\alpha_k^{(i-1)}$ and ω | ▷ E – step |
| 8: Find $\alpha_k^{(i)}$ using (4.70) | ▷ M – step |
| 9: until $\ \alpha_k^{(i)} - \alpha_k^{(i-1)}\ < \epsilon$ | ▷ Test convergence |
| 10: Return $\hat{\alpha}_k \leftarrow \alpha_k^{(i)}$ | |
-

substituted into the EM objective (4.58) and (4.60) when finding the ML estimate of the micro-Doppler shift, $\hat{\omega}$.

4.5.2 ML estimation for the angular rotation frequencies

The EM iterations in (4.45) with the Monte Carlo approximation through (4.58) - (4.61) lead to the particle EM algorithm for the ML estimation of ω . These steps are given in Algorithm 6 and 7. An initial value, $\omega^{(0)}$, is improved in terms of likelihoods in the iterations Algorithm 6 in which the complex reflection coefficients are estimated in Step 7 using the numerical procedures introduced in Section 4.5.1 and in Algorithm 5. Then, these estimates and the particles generated during their estimation is used in Algorithm 6 to find the micro-Doppler shift that maximises the Monte Carlo approximation to the expectation of concern given in (4.58) and (4.61). In particular, the golden section search algorithm is used. This algorithm only requires the evaluation of and iteratively reduces an initially selected interval of uncertainty as discussed in Section 3.4.2.

In order to improve convergence properties, the initial value of ω is searched by an initial search processing, and Algorithm 6 takes this value as $\omega^{(0)}$. For this search, it uses only \mathbf{Z}_1 and directly evaluate the logarithm of the likelihood conditioned on the reflection coefficients estimated using Algorithm 4 and 5. Then, the maximising value is selected as the initial point, $\omega^{(0)}$, in Algorithm 6. The initial search is specified over a uniform grid of values in the range of minimum and maximum angular rotation frequencies. This minimum value is selected by using 25% of the maximum possible angular rotation

Algorithm 6 EM iterations for the estimation of ω together with $\alpha_{1:K}$ and $\mathbf{X}_{1:K}$

```

1: Input:  $\omega^{(0)}$  ▷ Initial value
2: Input:  $\epsilon_\omega$  ▷ Termination threshold
3: Input:  $\mathbf{Z}_{1:K}$  ▷ Radar data cubes for  $K$  CPIs
4: Input:  $j \leftarrow 0$  ▷ Initialisation for the EM iterations
5: repeat
6:    $j \leftarrow j + 1$ 
7:   Find  $\hat{\alpha}_{1:K}(\omega^{(j-1)})$  and  $\{\mathbf{X}_{1:K}^{(p)}, \zeta_{1:K}^{(p)}\}_{p=1}^P$  by using Algorithm 5 within Algorithm 4 with
      $\omega \leftarrow \omega^{(j-1)}$ 
8:   Find  $\omega^*$  that maximises  $Q_K(\omega, \omega^{(j-1)})$  by using Algorithm 7 ▷ EM – step
9:    $\omega^{(j)} \leftarrow \omega^*$ 
10: until  $\|\omega^{(j)} - \omega^{(j-1)}\| < \epsilon_\omega$  ▷ Test convergence
11: Find  $\hat{\alpha}_{1:K}(\omega^{(j)})$  and  $\{\mathbf{X}_{1:K}^{(p)}, \zeta_{1:K}^{(p)}\}_{p=1}^P$  by using Algorithm 5 within Algorithm 4 with
      $\omega \leftarrow \omega^{(j)}$ 
12: Find  $\hat{\mathbf{X}}_{1:K}$  using  $\{\mathbf{X}_{1:K}^{(p)}, \zeta_{1:K}^{(p)}\}_{p=1}^P$  by using (4.44) for  $k = 1, \dots, K$ 
13: Return  $\hat{\omega} \leftarrow \omega^{(j)}$ ,  $\hat{\alpha}_{1:K} \leftarrow \hat{\alpha}_{1:K}(\omega^{(j)})$ , and  $\hat{\mathbf{X}}_{1:K}$ 
    
```

frequency (see, for example, [66]), and the total number of angular frequencies uniformly separated by using a pre-defined resolution, $\Delta\omega$, is determined by

$$N_{max} \triangleq \left\lfloor \frac{\omega_{max} - \omega_{min}}{\Delta\omega} \right\rfloor, \quad (4.71)$$

where ω_{min} and ω_{max} denote minimum and maximum angular rotation frequencies, receptively, and $\lfloor \cdot \rfloor$ denotes the nearest integer function.

4.6 Detection via long time integration using the proposed estimator

The proposed estimators above enable one to evaluate the statistical hypothesis test through (4.11) and (4.14)–(4.18). This test realises the sum of the instantaneous likelihood ratios along an object's trajectory, $\mathbf{X}_{1:K}$, thereby long-time integrating their reflections. As discussed in Section 3.5, this test is following steps through (3.52)–(3.54).

After using Algorithm 4 and 5 within Algorithm 6 and 7, the resulting estimates obtain $\hat{\omega}$, $\hat{\alpha}_{1:K}$ and $\hat{\mathbf{X}}_{1:K}$. With these estimates, the logarithm of the likelihood ratio in (4.16)

Algorithm 7 Maximisation step of EM algorithm via golden section line search as detailed in Section 4.5.2.

```

1: Input: Radar data cubes  $\mathbf{Z}_{k'}$  for  $k' = 1, 2, \dots, k$  CPIs ▷ see (4.8)
2: Input:  $\{X_{k'|k'-1}^{(p)}, \zeta_{k'|k'-1}^p\}_{p=1}^P$  for  $k' = 1, 2, \dots, k$  CPIs ▷ see Section 4.4
3: Input:  $\omega_k^{(j-1)}$  ▷ Previously found values using the EM algorithm
4: Input:  $\Delta\omega$  ▷ Initial interval of uncertainty
5: Input:  $\epsilon_g$  ▷ Termination threshold
6:  $\omega_1 \leftarrow \omega_k^{(j-1)} - \Delta\omega$ 
7:  $\omega_2 \leftarrow \omega_k^{(j-1)} + \Delta\omega$ 
8:  $\alpha_g \leftarrow 0.618$  ▷ Golden ratio
9:  $\tilde{\omega}_1 \leftarrow \omega_1 + (1 - \alpha_g)(\omega_2 - \omega_1)$  ▷ Evaluation point 1
10:  $\tilde{\omega}_2 \leftarrow \omega_1 + \alpha_g(\omega_2 - \omega_1)$  ▷ Evaluation point 2
11: Compute  $\hat{Q}_k(\tilde{\omega}_1, \omega_k^{(j-1)})$  and  $\hat{Q}_k(\tilde{\omega}_2, \omega_k^{(j-1)})$  ▷ see (4.58) and (4.61)
12:  $Q_1 \leftarrow \hat{Q}_k(\tilde{\omega}_1, \omega_k^{(j-1)})$ ,  $Q_2 \leftarrow \hat{Q}_k(\tilde{\omega}_2, \omega_k^{(j-1)})$ 
13: while  $|\omega_2 - \omega_1| > \epsilon$  do ▷ Until  $\epsilon$  accuracy is reached
14:   if  $Q_1 > Q_2$  then
15:      $\omega_2 \leftarrow \tilde{\omega}_2$  ▷ New interval:  $[\omega_1, \tilde{\omega}_2]$ 
16:      $\tilde{\omega}_2 \leftarrow \tilde{\omega}_1$ ,  $Q_2 \leftarrow Q_1$  ▷ Assignments
17:      $\tilde{\omega}_1 \leftarrow \omega_1 + (1 - \alpha_g)(\omega_2 - \omega_1)$ 
18:     Compute  $\hat{Q}_k(\tilde{\omega}_1, \omega_k^{(j-1)})$ ,  $Q_1 \leftarrow \hat{Q}_k(\tilde{\omega}_1, \omega_k^{(j-1)})$  ▷ New evaluation
19:   else
20:      $\omega_1 \leftarrow \tilde{\omega}_1$  ▷ New interval:  $[\tilde{\omega}_1, \omega_2]$ 
21:      $\tilde{\omega}_1 \leftarrow \tilde{\omega}_2$ ,  $Q_1 \leftarrow Q_2$  ▷ Assignments
22:      $\tilde{\omega}_2 \leftarrow \omega_1 + \alpha_g(\omega_2 - \omega_1)$ 
23:     Compute  $\hat{Q}_k(\tilde{\omega}_2, \omega_k^{(j-1)})$ ,  $Q_2 \leftarrow \hat{Q}_k(\tilde{\omega}_2, \omega_k^{(j-1)})$  ▷ New evaluation
24:   end if
25: end while
26: if  $Q_1 > Q_2$  then
27:   Return  $\omega_k^{(j)} \leftarrow \tilde{\omega}_1$ 
28: else
29:   Return  $\omega_k^{(j)} \leftarrow \tilde{\omega}_2$ 
30: end if
    
```

is evaluated:

$$\log L_K \triangleq \sum_{k=1}^K \log L_k \quad (4.72)$$

$$\begin{aligned}
 \log L_k &\triangleq \sum_{r \in \mathcal{E}(\hat{\mathbf{X}}_k)} \log L(\mathbf{Z}_k(r) | \hat{\mathbf{X}}_k, \hat{\boldsymbol{\alpha}}_k, \hat{\omega}) \\
 &= \sum_{r \in \mathcal{E}(\hat{\mathbf{X}}_k)} \left(2\text{Re} \left\{ \left(\mathbf{H}(r, \hat{\mathbf{X}}_k, \hat{\omega}_k) \hat{\boldsymbol{\alpha}}_k \right)^H \Sigma^{-1} \mathbf{Z}_k(r) \right\} \right. \\
 &\quad \left. - \left(\mathbf{H}(r, \hat{\mathbf{X}}_k, \hat{\omega}_k) \hat{\boldsymbol{\alpha}}_k \right)^H \Sigma^{-1} \mathbf{H}(r, \hat{\mathbf{X}}_k, \hat{\omega}_k) \hat{\boldsymbol{\alpha}}_k \right).
 \end{aligned} \quad (4.73)$$

Here, (4.73) is the logarithm of the instantaneous likelihood ratio and admits the interpretation of being the contribution of the radar data cube at time k into the integration in (4.72). Note that this summation corresponds to the coherent integration

of $\mathcal{E}(\hat{X}_k) \times N_h \times N_v \times N$ samples at the MF output during a CPI and non-coherent integration across consecutive CPIs. The decision on the object's presence is thus made by comparing the output of (4.72) to a detection threshold:

$$\log L_K \underset{H_0}{\overset{H_1}{\geq}} \log \mathcal{T}_K. \quad (4.74)$$

where $\log \mathcal{T}_K$ is the detection threshold for a given constant false alarm rate (CFAR) for K steps of integration. The selection of this threshold value is discussed in Section 3.5.1, and can be found using (3.59) for a single transmitter case. The next section defines a signal to noise ratio (SNR) for the radar data cubes to be used later in the demonstration of the proposed scheme in Section 4.7.

4.6.1 Signal to noise ratio (SNR) in the radar data cube

Let this subsection provide explicit formulae for the signal to noise ratio (SNR) of the radar data cube in (4.8). The steps to find this SNR is following steps through (3.62)–(3.66) and, all the same assumptions in Section 3.5.2 hold to find the SNR. Thus, the SNR at the k th CPI is found as a function of the object state \mathbf{X}_k at the r th range bin:

$$\begin{aligned} \text{SNR}_k(r, \mathbf{X}_k) &\triangleq \frac{\mathbb{E}\{(\mathbf{H}(r, \mathbf{X}_k, \omega)\boldsymbol{\alpha}_k)^T (\mathbf{H}(r, \mathbf{X}_k, \omega)\boldsymbol{\alpha}_k)\}}{\mathbb{E}\{\mathbf{n}(r)^T \mathbf{n}(r)\}} \\ &= \frac{\mathbb{E}\{\boldsymbol{\alpha}_k^T \mathbf{H}(r, \mathbf{X}_k, \omega)^T \mathbf{H}(r, \mathbf{X}_k, \omega) \boldsymbol{\alpha}_k\}}{\text{tr}\{\Sigma\}}, \end{aligned} \quad (4.75)$$

where $\boldsymbol{\alpha}_k \in \mathbb{C}^{2 \times 1}$ is a vector of the reflection coefficients, $\mathbf{H} \in \mathbb{C}^{N_h N_v N \times 2}$ is the signal model associated with the range bin r and the reflector state, \mathbf{X}_k , as given in (4.33), and $\text{tr}\{\Sigma\}$ denotes the trace of Σ . Here, $\mathbf{n} \sim \mathcal{CN}(\cdot; \mathbf{0}, \Sigma)$ models the noise background and is a complex random variable with zero mean and covariance of Σ as discussed in Section 4.2.

Now, consider the SNR associated with the reflector state, \mathbf{X}_k , over the range bins in

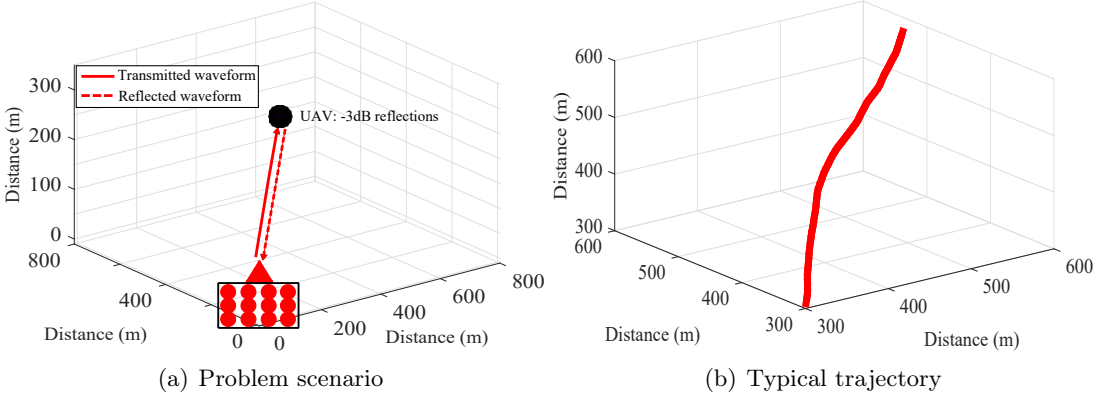


Figure 4.6: Example with a UPA receiver: (a) Problem scenario. A transmitter (red triangle) co-located with a UPA receiver (red dots) emits $N = 40$ modulated pulses (solid red line). The receiver collects -3dB reflections (dashed red line) from a single UAV (black dot). (b) A typical trajectory (solid red line) of the UAV

which, due to the auto-correlation output Λ in (4.33), the nominator of (4.75) yields

$$\begin{aligned} & \mathbb{E}\left\{\boldsymbol{\alpha}_k^T \mathbf{H}(r, \mathbf{X}_k, \omega)^T \mathbf{H}(r, \mathbf{X}_k, \omega) \boldsymbol{\alpha}_k\right\} \\ &= N_h N_v N \times 2 \times \Lambda(\mathcal{E}(\mathbf{X}_k)) \mathbb{E}\{\boldsymbol{\alpha}_k^T \boldsymbol{\alpha}_k\} \end{aligned} \quad (4.76)$$

$$\Lambda(\mathcal{E}(\mathbf{X}_k)) \triangleq \sum_{r \in \mathcal{E}(\mathbf{X}_k)} \Lambda^*(r T_p - \tau(\mathbf{X}_k)) \times \Lambda(r T_p - \tau(\mathbf{X}_k)), \quad (4.77)$$

where $N_h N_v$ indicates the number of array elements, and N is the number of transmitted pulses in a CPI. Thus, the SNR for the radar data cube at the k th CPI through (4.75)–(4.77) is given by

$$\text{SNR}_k = \frac{2 N_h N_v N \Lambda(\mathcal{E}(\mathbf{X}_k)) \mathbb{E}\{\boldsymbol{\alpha}_k^T \boldsymbol{\alpha}_k\}}{\text{tr}\{\Sigma\}} \quad (4.78)$$

$$\text{SNR}_{dB}^k = 10 \log_{10} (\text{SNR}_k), \quad (4.79)$$

where SNR_{dB}^k denotes SNR_k in the decibels (dB).

4.7 Example

This section demonstrates the efficacy of the proposed approach in comparison with other techniques through two examples: Section 4.7.1 uses simulated data to demonstrate the proposed scheme. Section 4.7.2 demonstrates the proposed approach with real measurements collected from a Thales/Aveillant Gamekeeper system [109, 112].

For the system parameters, both sections use common system parameters, which follows the system parameters used in the Thales/Aveillant Gamekeeper system [109] except for modulation schemes.

4.7.1 Simulation result

This subsection considers a scenario in which a transmitter (red triangle) co-located with a UPA receiver (red dots) is located at the origin of the 3D volume and emits $N = 40$ linear frequency modulated (i.e., up-chirp) waveforms (solid red line) towards a surveillance region. This illumination pattern is repeated with a time interval of 0.1s. This scenario is illustrated in Figure 4.6(a).

In the surveillance region, there is a small rotary-wing aircraft (black dot), which consists of $M = 1$ rotor hub with $\tilde{L} = 2$ rotor blades. The blade length is $B = 0.16\text{m}$, which is shorter than the carrier wavelength $\lambda_c = 0.25\text{m}$. This complicates micro-Doppler feature extraction using common techniques such as the Short Time Fourier Transform (STFT) analysis, which is explained later, in this section. This UAV with an initial state of $\mathbf{X}_0 = [300\text{m}, 300\text{m}, 300\text{m}, 50\text{m/s}, 50\text{m/s}, 50\text{m/s}]$ flies along an unknown trajectory (solid red line) generated from the object dynamic model in (4.35) as illustrated in Figure 4.6(b).

The UPA receiver is comprised of $N_v = 16$ vertical elements and $N_h = 4$ horizontal elements in the array and collects measurements in accordance with the signal model defined in (4.8). The front-end signals at the receiver are the superposition of background noise, reflections from the object's body and the rotor blades. The parameters used in the aforementioned transmissions are listed in Table 4.2. In this setting, the rotation frequency, i.e., $f_r \triangleq \frac{\omega}{2\pi}$, is selected randomly in the range of $f_{min} \leq f_r \leq f_{max}$ and is used for all experiments. Here, it sets $f_{max} = 233\text{ Hz}$ (see, [66]), which is the maximum possible rotation frequency, and $f_{min} = 58.25\text{ Hz}$ obtained by 25% of f_{max} denotes the minimum rotation frequency.

Table 4.2: Transmitted signal parameters

Parameter	Value
Carrier frequency, i.e., f_c	1.2 GHz
Probing waveform bandwidth, i.e., B_w	1 MHz
Probing waveform duration, i.e., T_p	1 μ s
Pulse repetition interval (PRI), i.e., T	133 μ s
Number of range bins, i.e., Γ	200
Number of pulses, i.e., N	40
Number of vertical elements in the UPA, i.e., N_v	16
Number of horizontal elements in the UPA, i.e., N_h	4
Length of the coherent processing interval (CPI)	5.32 ms
Illumination period (Δ in (4.35))	0.1 s
Number of rotor hubs, i.e., M	1
Number of rotor blades, i.e., \tilde{L}	2
Blade length, i.e., B	0.16 m

For experiments, 100 independent sets of the object trajectories and array measurements are generated: When $H = H_1$ hypothesis holds, the array measurement at the k th CPI associated with the reflector state, \mathbf{X}_k , the complex reflection coefficients, $\boldsymbol{\alpha}_k$, and the angular rotation frequency, ω , is generated from a complex Gaussian using

$$\mathbf{Z}_k(r) \sim \mathcal{CN}(\cdot; \mathbf{H}(r, \mathbf{X}_k, \omega) \boldsymbol{\alpha}_k, \Sigma), \quad r \in \mathcal{E}(\mathbf{X}_k), \quad (4.80)$$

where $\boldsymbol{\alpha}_k = [\alpha_{0,k}, \alpha_{1,k}]^T$ is a vector of the complex reflection coefficients, and $\mathcal{E}(\mathbf{X}_k)$ is a set of range bins associated with \mathbf{X}_k given in (4.13). Otherwise, the measurement is generated from

$$\mathbf{Z}_k(r) \sim \mathcal{CN}(\cdot; \mathbf{0}, \Sigma), \quad r \in \Gamma \setminus \mathcal{E}(\mathbf{X}_k), \quad (4.81)$$

where Γ is the length of range bins given in Table 4.2. The expected SNR of the measurement at the k th CPI is -3 dB. This quantity is found by using SNR_{dB}^k in (4.79).

After mapping the array measurements over a grid of angle bins and Doppler bins, these bins correspond to resolution cells which are calculated by using the parameters used in the transmissions of the example system (see, Table 4.2): The angle consists of an azimuth angle and an elevation angle. The azimuth resolution is found as $\Delta\theta = 11.81^\circ$ using (2.30) with N_h . The elevation resolution is found as $\Delta\phi = 2.93^\circ$ using (2.30)

with N_v (see, Section 2.3.1). The range resolution, corresponding to the sample version of the MF output, is found as $\Delta R = 75\text{m}$ using (2.25). The velocity resolution of the conventional processing is found as $\Delta V = 23.5\text{ms}^{-1}$ using $\Delta V = \frac{\lambda_c}{2NT}$ (or, equivalently, the Doppler resolution of $\Delta\Omega = 0.05\pi\text{rads}^{-1}$ using $\Delta\Omega = 2\pi\frac{2\Delta V}{\lambda_c}T$).

Algorithm 4 is used for $K = 50$ CPIs which spans 5 s. Each CPI indicates an array measurement collected in a CPI as a radar data cube. This algorithm is initiated with $P = 400$ particles such that a 20×20 uniform grid over a bounded region of known initial location and velocity vectors in each resolution cell. These particles evolve to converge to the true state of the object by simultaneously estimating the reflection coefficients and the rotation frequency as the particle filtering iteratively estimates the object trajectory.

Performance in estimating unknowns

Here, it demonstrates the inner workings of the proposed algorithm in which the estimation accuracy of the object trajectory, the complex reflection coefficients, and the rotation frequency is compared to the conventional processing. In order to initiate Algorithm 6, it selects the initial guess as one that maximises the likelihood for the first radar data cube only over a grid of rotation frequencies. The likelihood evaluation follows the estimation of \mathbf{X}_1 and $\boldsymbol{\alpha}_1$ using Algorithms 4 and 5 with the points in the ω grid over the range of f_{min} and f_{max} uniformly divided by $\Delta f = 10\text{Hz}$. Figure 4.7 illustrates outputs of the initial searches given $N = 20$, $N = 40$, $N = 60$, and $N = 80$ transmitted pulses in a CPI, where the true value of the rotation frequency is depicted by the red lines, and the blue lines indicate the outputs of $Q_{k=1}$ in (4.61). It is shown that the peak values obtained by the preliminary search become narrower when increasing N pulses, and the relation between the objective function, $Q_{k=1}$, and $\omega = 2\pi f_r$ is a concave when ω is close to the true value.

Now, consider the estimation performance in finding the rotation frequency in -3dB radar data cubes over $K = 50$ CPIs when the transmitter emits $N = 40$ pulses in

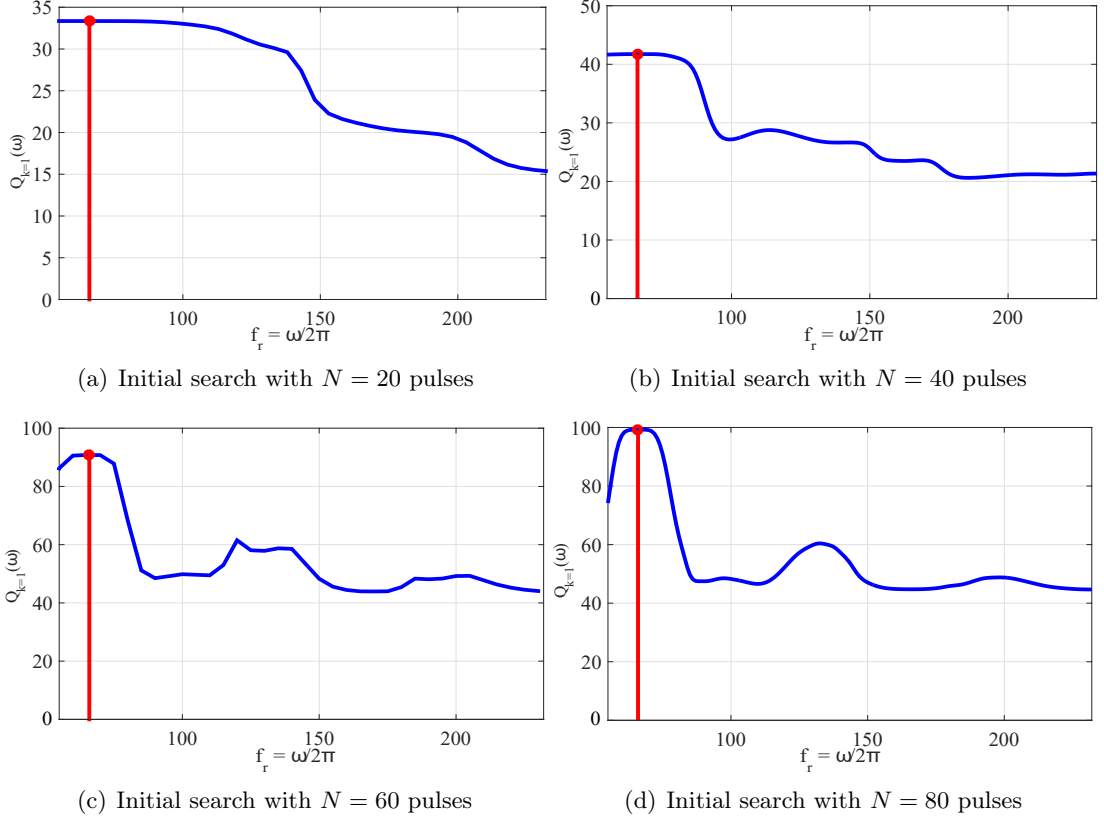


Figure 4.7: Initial search for the rotation frequency (i.e., $f_r = \frac{\omega}{2\pi}$) with -3dB reflections: (a) Initial search for the rotation frequency with $N = 20$ pulses. (b) Initial search for the rotation frequency with $N = 40$ pulses. (c) Initial search for the rotation frequency with $N = 60$ pulses. (d) Initial search for the rotation frequency with $N = 80$ pulses. All solid blue lines shows the output of the initial search with the ground truth value of the rotation frequency as solid red lines.

a CPI. For this purpose, Algorithm 4 and 5 within Algorithm 6 and 7 are used for 100 realisations. Figure 4.8 shows a typical estimate output via the golden section search using the radar data cubes over $k = 10$ CPIs. Here, the true value is depicted by the red line, and the estimated value is the blue line. The resulting estimate is reasonably close to the true value and is found after only $i_g = 8$ iterations (black crosses). Figure 4.9 presents estimates of the rotation frequency using the radar data cubes over $K = 50$ CPIs, where x axis indicates the number of the radar data cubes. These values (blue line) are compared with the true value (red line). Also, the $\pm\Delta f_r = \pm 3.6\text{Hz}$ found as a resolution of Fourier transform $\frac{2}{\text{PRI} \times N}$ when using $N = 2048$ pulses are given for comparison. Figure 4.9(a) shows the typical estimate of the rotation frequency (blue line), where the estimation error has considerably large at the initial estimate and stays small after $k = 10$ data cubes used. The averaged estimate

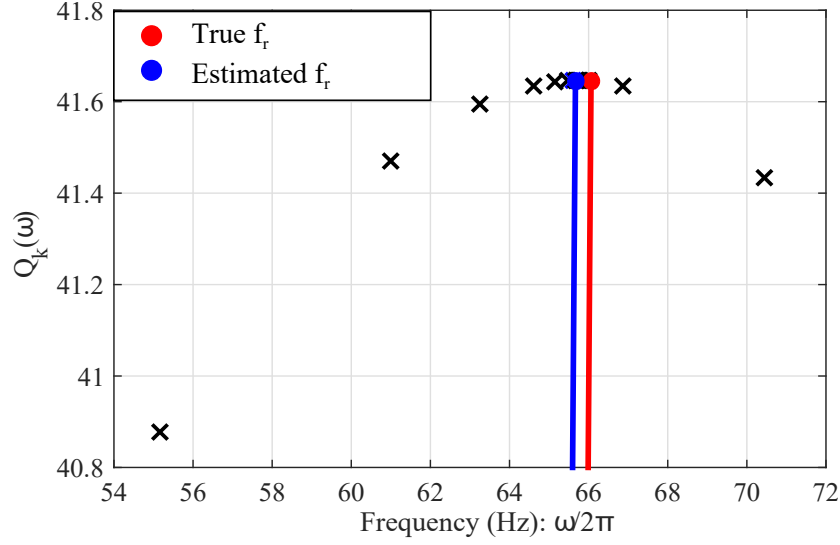


Figure 4.8: Typical rotation frequency estimation via the golden section search: A typical rotation frequency (blue dot) is estimated by using Algorithm 7 within Algorithm 6 in comparison with the true value (red dot). The black crosses indicates $i_g = 8$ iterations for finding the rotation frequency in Algorithm 7

of the rotation frequency (blue line) with $\pm\sigma$ bounds (dashed blue lines) is illustrated in Figure 4.9(b). It is seen that the estimation error stays within a small fraction of the Δf_r . For further comparison, Figure 4.9(c) gives the short-time Fourier Transform (STFT) of the estimated reflection coefficients obtained by using the algorithm proposed in Chapter 3. For this purpose, the EM algorithm in Section 3.4 is used with the same array measurements and then finds reflection coefficients based on the ground truth trajectory. The STFT result of the complex reflection coefficient estimates is illustrated in Figure 4.9(c). It is complicated to analyse/recognise the micro-Doppler components in the STFT. In order to further analyse this STFT result, a singular value decomposition method [116] is employed, and its results are illustrated in Figure 4.10. This method is the factorisation of a rectangular matrix, in which the matrix is factorised into left singular vectors, a diagonal matrix of singular values, and right singular vectors, and a higher singular value indicates a more dominant element in the data. Figure 4.10(a) shows the first three dominant frequencies selected by using the first three singular values. All the singular values are illustrated in Figure 4.10(b). It is shown that the second (red line) and the third (yellow line) dominant frequencies are not matched to the true rotation frequency, whereas the proposed estimator provides the correct estimate with fine accuracy (see, Figure 4.9).

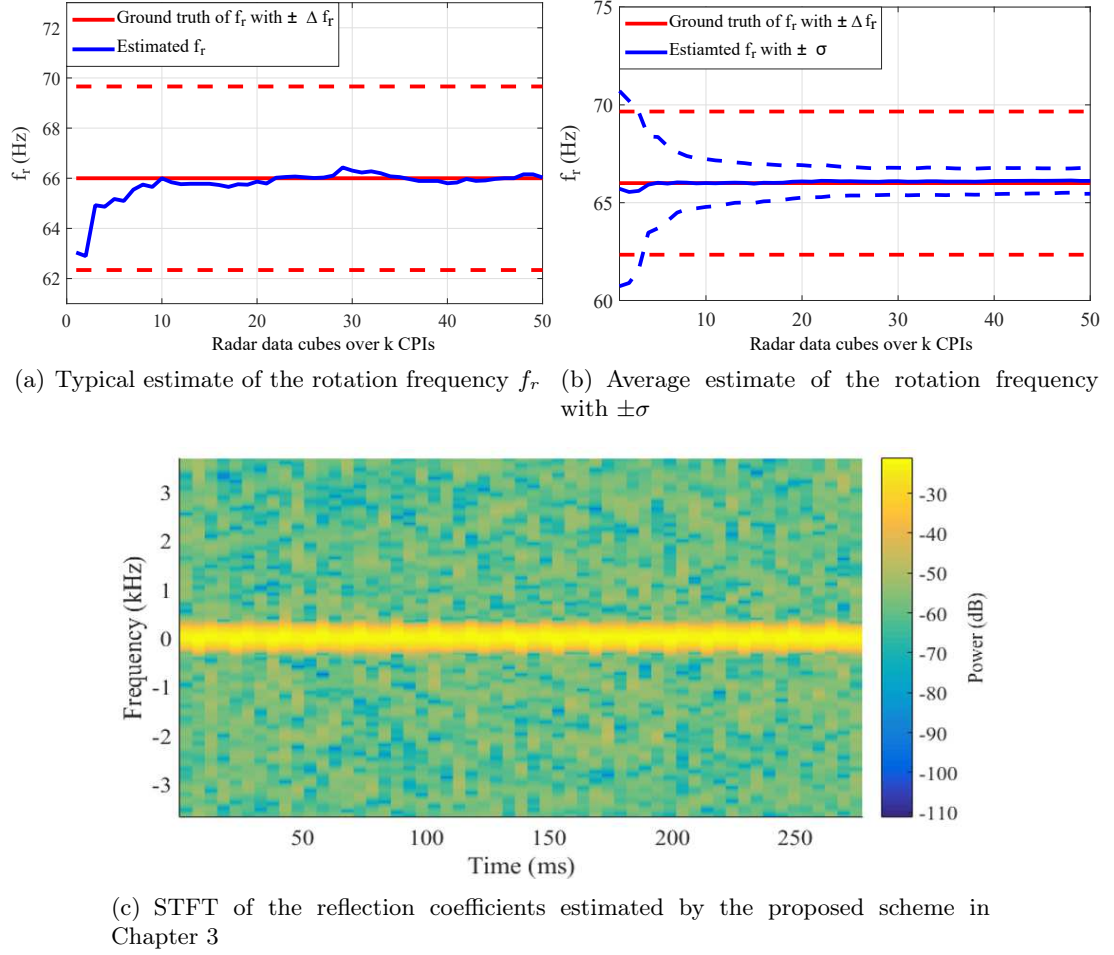


Figure 4.9: Rotation frequency estimation with the radar data cubes over k CPIs: (a) Typical estimate (blue solid line) of the rotation frequency using Algorithm 6. (b) Averaged estimates (blue solid line) with $\pm \sigma$ bounds (blue dashed lines) of the rotation frequency obtained by using Algorithm 6 for the 100 realisations. The red solid and dashed lines indicate the true value of the rotation frequency f_r and $\pm \Delta f_r$ bounds in conventional processing, respectively. (c) Short time Fourier transform (STFT) of the reflection coefficients estimated by the proposed scheme in Chapter 3

Next, consider the estimation performance in finding the complex reflection coefficients in the radar data cube. For this purpose, Algorithm 5 within Algorithm 4 is used. Figure 4.11 shows typical estimates of the complex reflection coefficients for the typical steps of Algorithm 5, where the x axis indicates the real part of the complex reflection coefficient and the y axis shows its imaginary part. The resulting estimates are compared with their ground truth values. Also, the \pm standard deviations of Cramér-Rao bound (CRB), $\pm \sigma_{\text{CRB}}$, are given for comparison. This quantity is obtained by using the ground truth values of the kinematic state and the angular rotation frequency (see, for example, [90, Chp.3]). In Figure 4.11(a), the estimated reflection coefficient (blue line) for the object body stays within $\pm \sigma_{\text{CRB}}$ (dashed red ellipse) after only a few iterations

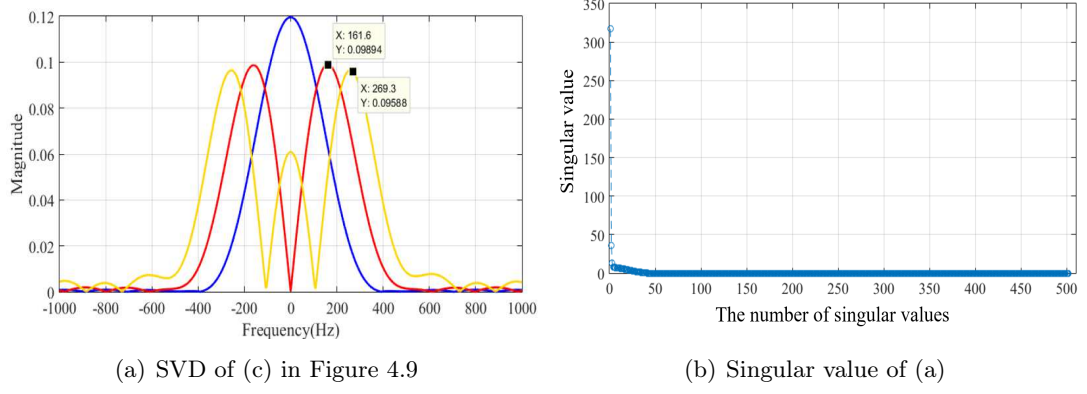


Figure 4.10: Singular value decomposition (SVD) of (c) in Figure 4.9: (a) Outputs of the first three singular values from the result of SVD. (b) Singular values of SVD.

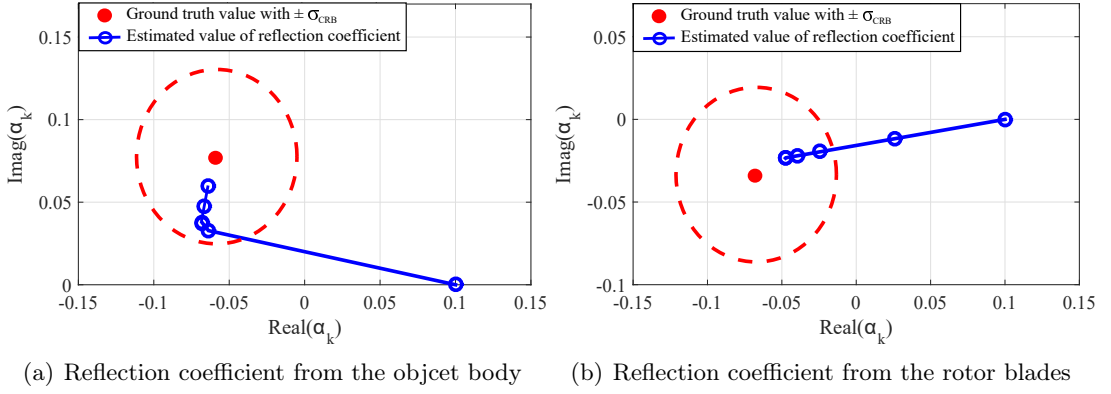


Figure 4.11: Complex reflection coefficient estimation with -3dB radar data cube: (a) A typical estimate of the complex reflection coefficient for the object body by using the proposed algorithm. The blue line indicates typical estimates of the object body reflection coefficient by using Algorithm 5 within Algorithm 4. The blue circles show $i = 5$ iterations for finding it. The resulting estimate is compared to the ground truth value (red dot) with the \pm standard deviation of Cramér-Rao bound (CRB), i.e., $\pm\sigma_{\text{CRB}}$ (dashed red ellipse). The x axis denotes the real part of the complex reflection coefficient and the y axis is its imaginary part. (b) A typical estimate of the complex reflection coefficient for the rotor blades by using Algorithm 5 within Algorithm 4 with the same colour codes in (a).

(solid blue circles), where the solid blue circles indicate the number of $i = 5$ iterations for finding the reflection coefficient in Algorithm 5. The resulting estimate is close to its ground-truth value (red dot). For the rotor blade reflection coefficient, Figure 4.11(b) presents the typical estimate of the complex reflection coefficient for the rotor blades. The resulting estimate (solid blue line) stays within $\pm\sigma_{\text{CRB}}$ (dashed red ellipse) and is close to the ground truth value (red dot). Note that both the body and the rotor blade reflection coefficients estimated by the proposed algorithm are close to the ground truth values. It is also seen that these estimation errors stay within $\pm\sigma_{\text{CRB}}$ after a few iterations.

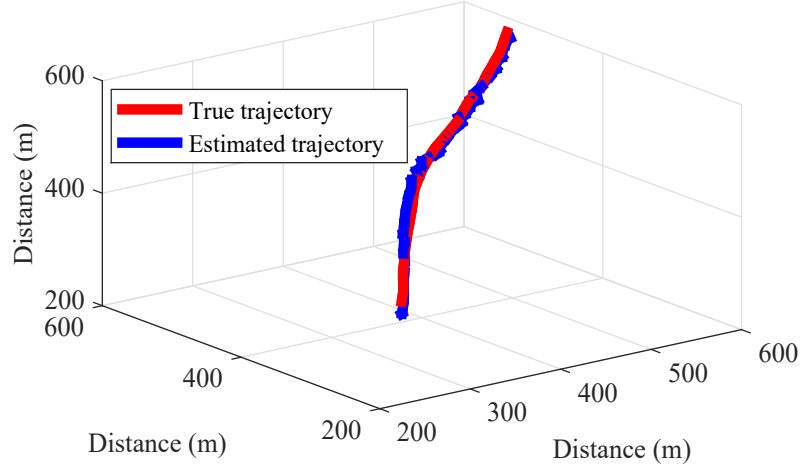


Figure 4.12: Typical trajectory estimation: The estimated trajectory by using Algorithm 4 is depicted as the blue solid line. This output is compared to its ground truth (red solid line).

For estimation performance in finding the object trajectory by using Algorithm 4. Figure 4.12 illustrates a typical trajectory (red line) which would lead to resolution bin migrations in conventional processing. The trajectory estimate output by the proposed algorithm is depicted as the blue solid line. Figure 4.13(a) shows the root mean squared error (RMSE) of the corresponding range estimate in comparison with the range resolution of ΔR (dashed red line). Note that the error reduces to the 10.6% of the range resolution after 3.3 s. Figure 4.13(b) presents the RMSE of the velocity component of the trajectory estimate in Figure 4.12. This estimate error is below the velocity resolution bin of ΔV (dashed red line), where the error between 0.5 s and 1.5 s shows a relatively large value due to the object's manoeuvres. Figure 4.13(c) illustrates the RMSE of the azimuth angle component of the trajectory estimate in Figure 4.12. The estimate error is a very small value compared to the azimuth resolution of $\Delta \theta$ (dashed red line). Figure 4.13(d) illustrates the RMSE of the elevation angle component of the trajectory estimate in Figure 4.12. Here, the estimate error shows a small error compared to the elevation resolution of $\Delta \phi$ (dashed red line). Note that the resolution bins of the system provides only a coarse view of the trajectory, whereas the proposed algorithm yields a super-resolution effect as discussed in Section 4.4.

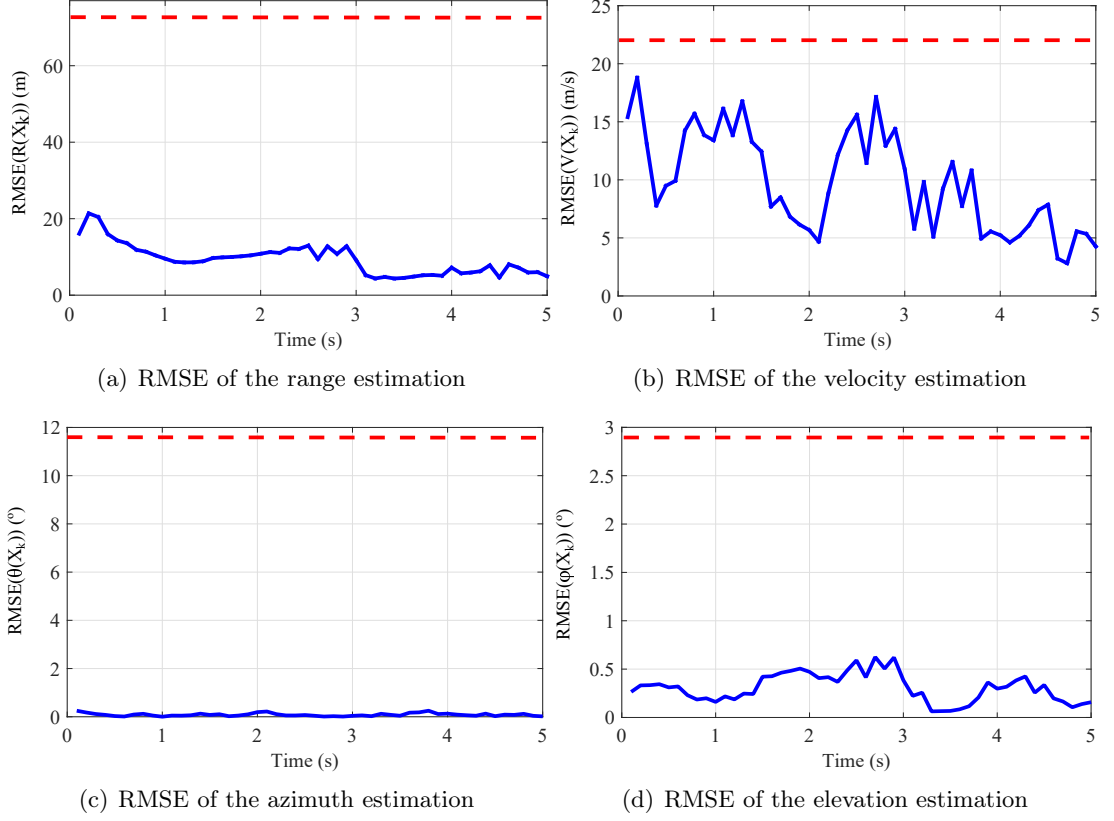


Figure 4.13: Root mean square error (RMSE) of the typical trajectory estimation: (a) RMSE of the range estimation obtained in Figure 4.12. (b) RMSE of the velocity estimation obtained in Figure 4.12. (c) RMSE of the azimuth angle estimation obtained in Figure 4.12. (d) RMSE of the elevation angle estimation obtained in Figure 4.12. The red dashed lines in all these figures indicate the range resolution ($\Delta R = 75\text{m}$) in (a), the velocity resolution ($\Delta V = 23.5\text{ms}^{-1}$) in (b), the azimuth resolution ($\Delta\theta = 11.81^\circ$) in (c), and the elevation resolution ($\Delta\phi = 2.93^\circ$) in (d), respectively.

Detection performance via the proposed scheme

Here, consider the hypothesis test for detection using the sufficient statistics of the likelihood ratio with an arbitrarily long time window as discussed in Section 4.6. For this purpose, Algorithm 4 and 5 within Algorithm 6 and 7 are used with 100 scenario realisations. The resulting long time integration performance is compared with those of the clairvoyant detector and the conventional one:

1. The clairvoyant detector: This detector uses the ground truth values of the unknown parameters (i.e., the object trajectory, the reflection coefficients, and the rotation frequency) when evaluating the logarithm of the likelihood ratio

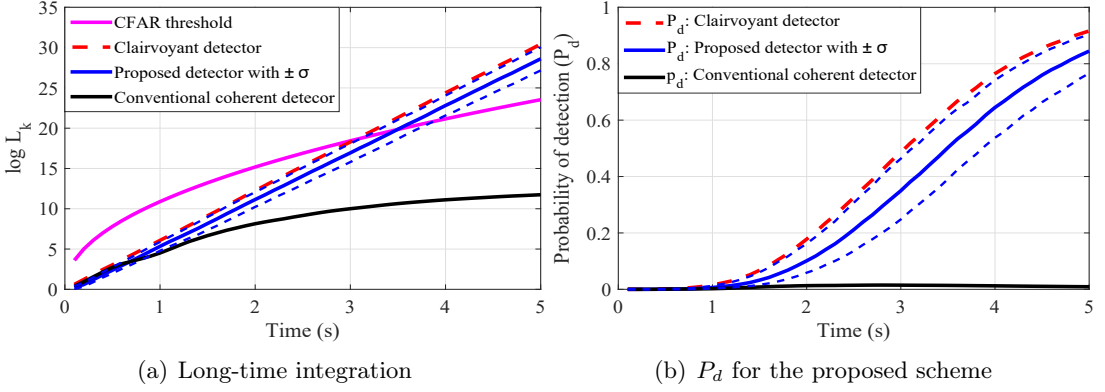


Figure 4.14: Detection performance of the proposed detector in comparison with the clairvoyant detector and the conventional detector: (a) Long-time integration using the proposed scheme, the clairvoyant integrator, and the conventional coherent integrator. The integrated sufficient statistics from the proposed integration averaged over 100 experiments is depicted by the solid blue line with $\pm \sigma$ (blue dashed lines). The integrated value from the clairvoyant integrator is the dashed red line and the clairvoyant (CFAR) threshold for $P_{fa} = 10^{-6}$ (averaged for 100 experiments) is the solid magenta line. The conventional scheme leads to the solid black line. (b) Probability of detection (P_d) for the proposed scheme compared to those of the clairvoyant detector and the conventional detector with the same colour codes in (a).

test in (4.74). The CFAR threshold, i.e, $\log \mathcal{T}_k$, for this detector is found using (3.56)–(3.59) for $M = 1$ transmitter case as discussed in Section 3.5.1.

2. Conventional coherent detector: This detector processes the measurements after mapping them over a grid of angles and Doppler bins. These corresponding resolution cells are defined in Figure 4.13. This detector integrates the mapped complex values for the same “cell under test” across time without taking account object manoeuvres [1]. This detector is defined in (3.76).

In Figure 4.14(a), the integration values are given as a function of time. The clairvoyant integrator sets an upper bound for the integrated sufficient statistics, the average of which is depicted by the dashed red line. Long time integration accuracy of the proposed algorithm is coupled to the trajectory estimation performance through the EM iterations for finding the reflection coefficients and the rotation frequency. Here, the proposed scheme’s performance is very close to the clairvoyant detector bound (solid blue line rendering the average with $\pm \sigma$ bounds shown with dotted blue lines). The proposed integration reaches to 27 at $t = 5$ s, which is relatively close to 31 achieved by the clairvoyant integration. This indicates that the estimation errors of unknowns are very

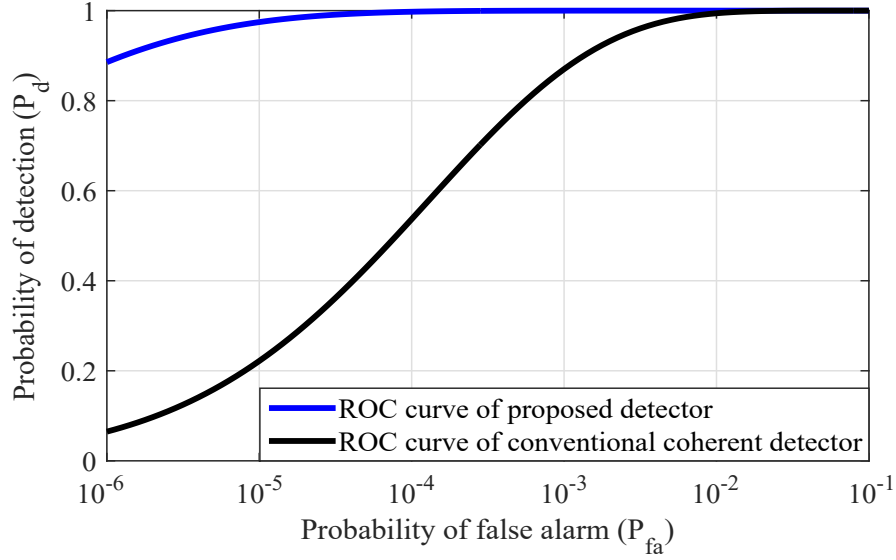


Figure 4.15: Receiver operating characteristic (ROC) curves: ROC curve of the proposed detector (blue solid line) is compared to ROC curve of the conventional coherent detector (black solid line).

small. The conventional scheme fails to continue the integration after the object leaves at the initial cell under test. This integration is shown with the solid black line in Figure 4.14(a). The clairvoyant CFAR detection threshold for $P_{fa} = 10^{-6}$ is depicted as the solid magenta line (averaged for the 100 experiments) in Figure 4.14(a). The detection for each detector is made by comparing its integration value against this threshold. The proposed scheme exceeds the CFAR threshold and enables one to decide on the object existence hypothesis ($H = H_1$) after $t = 3.5$ s, whereas the conventional scheme stays in the region for the noise only signal hypothesis ($H = H_0$).

Next, consider the probability of detection, P_d , as a function of the integration time in Figure 4.14(b). Here, the P_d of the proposed scheme is found using 3.60 and is averaged over the 100 experiments. The P_d of the clairvoyant detector (dashed red line) sets the upper performance bound. The P_d of the proposed scheme is drawn by the solid blue line in Figure 4.14(b). This quantity increases with time and reaches $P_d = 0.83$ at $t = 5$ s, which is relatively close to the $P_d = 0.92$ of the clairvoyant detector. The P_d of the conventional detector fails to detect the object in an overwhelming majority of the experiments (solid black line) in Figure 4.14(b). Furthermore, the probability of detection, P_d , is considered as a function of different false alarm (P_{fa}) values in the range of $P_{fa} = 10^{-6}$ to $P_{fa} = 10^{-1}$. This is illustrated in Figure 4.15 and referred to

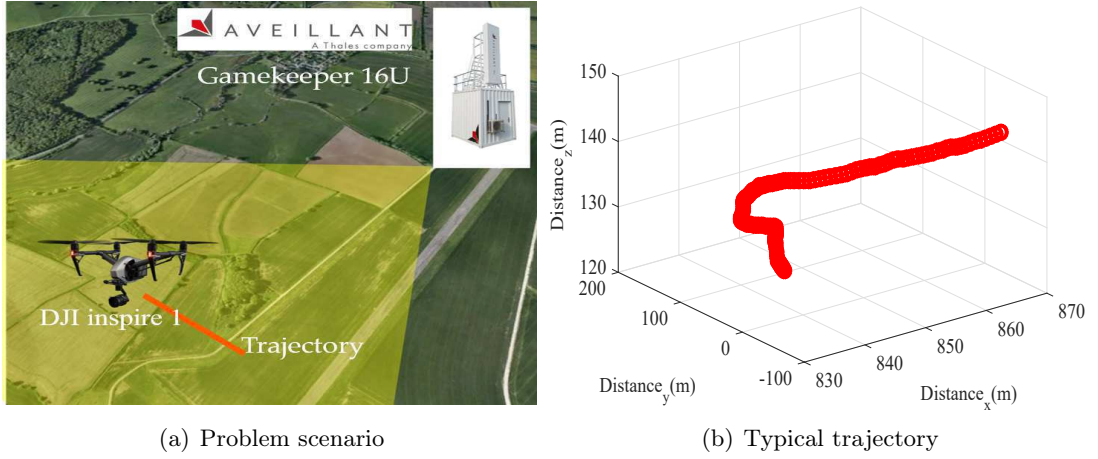


Figure 4.16: Experiment scenario: (a) Gamekeeper Thales/Aveillant radar system emits consecutive modulated pulses towards the surveillance region (light coloured region) and collects reflections from a DJI inspire 1 UAV with trajectory depicted by the solid red line. (b) UAV trajectory in the three-dimensional volume.

as the receiver operating characteristic (ROC) curve [18, Chp.3]. For this purpose, the integration value at $t = 5\text{s}$ is used for ROC calculation using (3.61). The ROC obtained by proposed scheme (solid blue line) is compared with that of the conventional coherent detector (solid black line). The ROC of the proposed detector provides almost $P_d = 1$ after $P_{fa} = 10^{-5}$, whereas the conventional coherent integration provides $P_d = 1$ after $P_{fa} = 10^{-2}$.

4.7.2 Real experiment result

This subsection demonstrates the efficacy of the proposed algorithm using real measurements. These measurements are collected by a recently developed Thales/Aveillant Gamekeeper system [109, 112]. In this experiment, the radar system is located at $[0\text{m}, 0\text{m}, 106\text{m}]^T$. This system continually emits fixed frequency pulse waveforms with the pulse duration of $1\text{ }\mu\text{s}$ towards the surveillance region as illustrated in Figure 4.16(a). $N = 40$ pulses are considered with a PRI of $133\text{ }\mu\text{s}$ and an illumination period is 0.2785s between two consecutive CPIs.

In the surveillance region, a small rotary-wing drone (a DJI inspire 1, in this experiment)

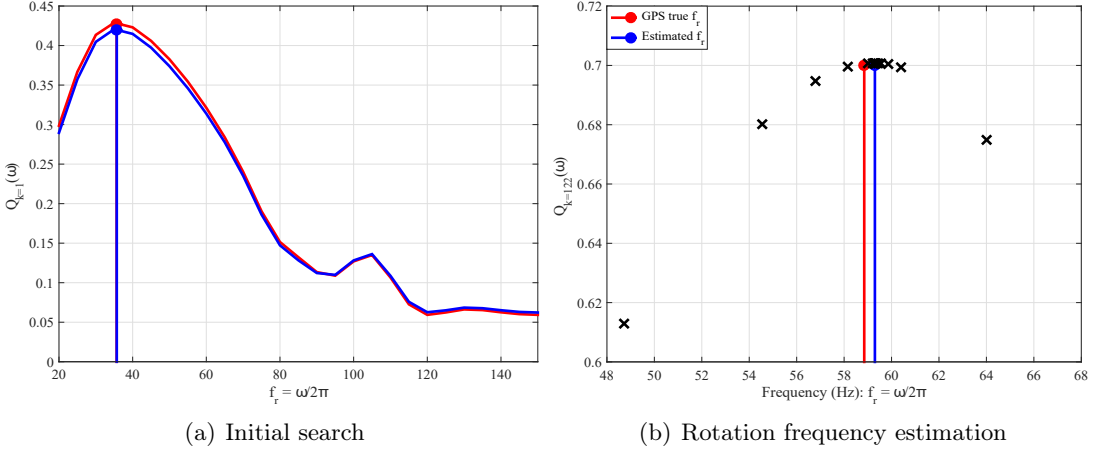


Figure 4.17: Typical rotation frequency estimation via the golden section search: (a) Initial search for the rotation frequency (i.e., $f_r = \frac{\omega}{2\pi}$). (b) Typical rotation frequency estimation via the golden section search when $k = 122$ CPIs. A typical rotation frequency (blue dot) is estimated by using Algorithm 7 within Algorithm 6 in comparison with the true value (red dot) based on the GPS ground truth. The black crosses indicates $i_g = 8$ iterations for finding the rotation frequency in Algorithm 7.

is flown. This drone consists of $M = 4$ rotor hubs and $\tilde{L} = 2$ blades on each rotor hub. The blade length is $B = 0.16\text{m}$, which is shorter than the carrier wavelength $\lambda_c = 0.25\text{m}$. The drone's initial state is $\mathbf{X}_0 = [847\text{m}, 103\text{m}, 119\text{m}, -0.22\text{m/s}, 0.06\text{m/s}, 0.48\text{m/s}]^T$ and it follows the ground truth drone trajectory depicted with the solid red line in Figure 4.16(b). Here, the ground truth drone trajectory is recorded by using the global positioning system (GPS) recordings. The other parameters and the algorithm setting are the same used in Section 4.7.1.

Performance in estimating unknowns

Here, demonstrate the inner workings of the proposed algorithms and show the estimation accuracy of unknowns using the real measurements. For the initial guess of the rotation frequency in Algorithm 6, Figure 4.17(a) illustrates the output of the initial searches. For comparison, the ground truth value is obtained by using the initial search with the GPS ground truth trajectory. The rotation frequency found using the GPS data is depicted with the red in Figure 4.17(a). The blue line indicates the output of the proposed scheme. Note that the outputs obtained by the initial search become narrower around the turn value.

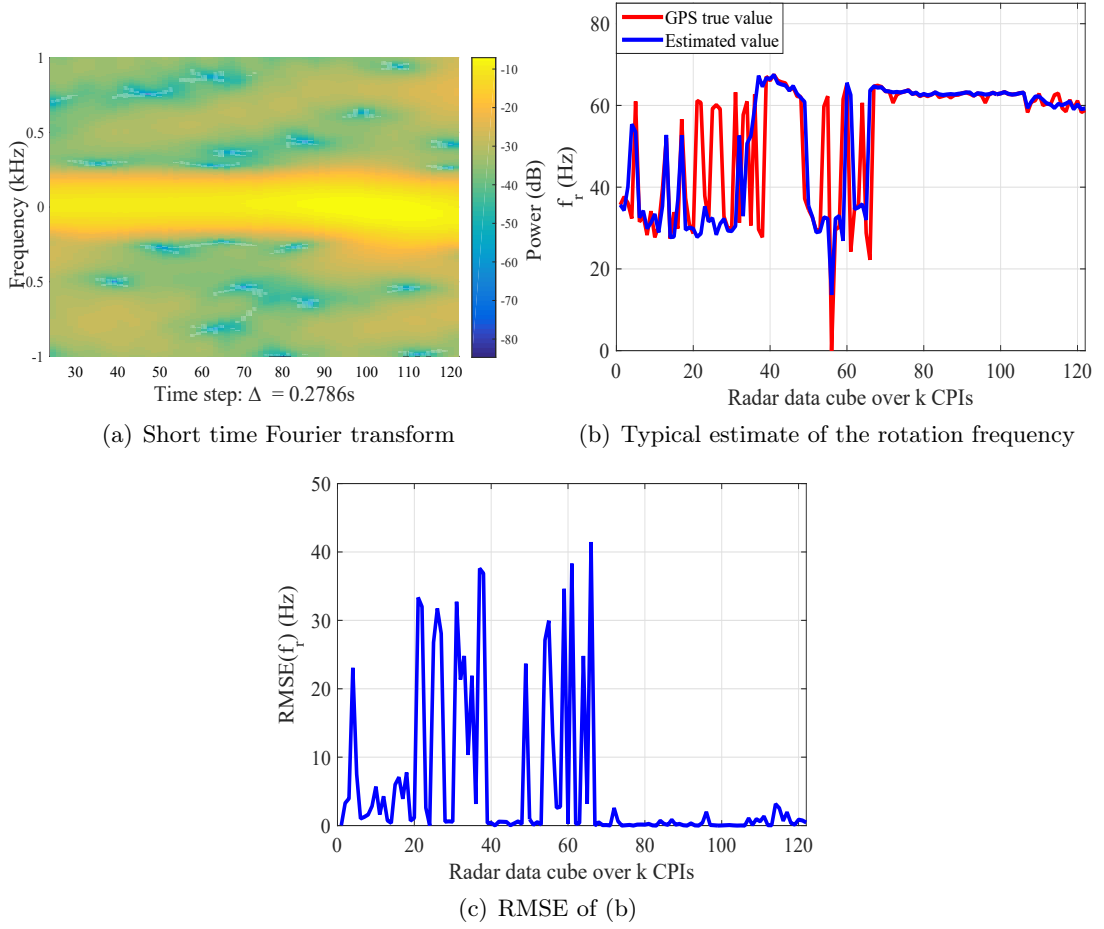


Figure 4.18: Rotation frequency estimation with the radar data cubes over k CPIs: (a) Short time Fourier transform (STFT) of the estimated reflection coefficients using the EM algorithm Section 3.4 (b) Typical estimate (blue solid line) of the rotation frequency using Algorithm 6. (c) Root mean square error (RMSE) of the estimated rotation frequency in (b).

Now, consider the estimation performance in finding the rotation frequency. Figure 4.17(b) illustrates the typical output from Algorithm 7 with $K = 122$ radar data cubes. The GPS ground truth, found as explained above, and the estimated values are depicted by the solid red and the solid blue lines, respectively. Here, the resulting estimate (blue line) is reasonably close to the GPS true value and is found after only $i_g = 8$ iterations (black crosses) in the golden section search.

Figure 4.18 shows the estimates of the rotation frequency obtained by using the proposed estimation scheme over $K = 122$ CPIs. These estimated values (blue line) are compared with the GPS true value (red line) obtained by using the GPS ground truth of the

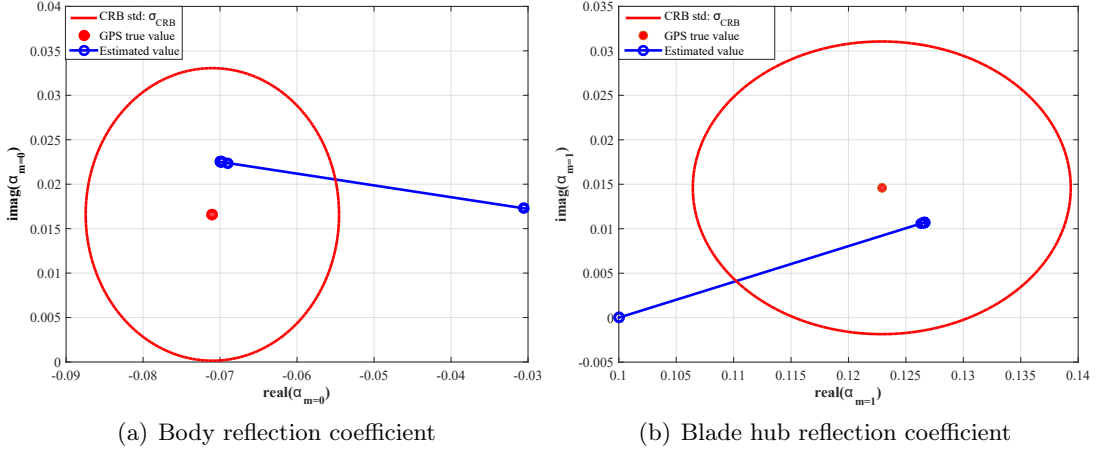


Figure 4.19: Typical estimate of complex reflection coefficients using our estimation scheme: (a) Typical estimate of the body reflection coefficient. (b) Typical estimate of the blade hub reflection coefficient. The blue circles show $i = 4$ iterations for finding these estimates. The resulting estimates are compared to the true value (red dot) based on GPS ground truth and with the \pm standard deviation of Cramér-Rao bound (CRB), σ_{CRB} (solid red ellipse).

drone kinematic state. Also, the short-time Fourier Transform (STFT) of the estimated reflection coefficients using the GPS ground truth is given. For this purpose, the EM algorithm in Section 3.4 is used with the same array measurements and then finds reflection coefficients based on the GPS ground truth trajectory. These reflections contain micro-Doppler signatures of the drone and are used for STFT. This output is illustrated in Figure 4.18(a). It is seen that the STFT output does not reveal the rotation frequency. Also note that when the blade length is less than the carrier wavelength, its STFT output does not produce frequency changes within a short time interval and is difficult to analyse/recognise micro-Doppler signatures from rotating blades.

Figure 4.18(b) shows the estimates of the rotation frequency (blue line) over $K = 122$ radar data cubes, where x axis indicates the number of the radar data cubes used for the estimation. Figure 4.18(c) illustrates the root mean square error (RMSE) of the estimated rotation frequency in (b). Here, the estimation error has considerably large at the initial estimate and stays small after $k = 68$ radar data cubes used. It is clearly seen that the estimation error stays within $< 2\text{Hz}$ after $k = 68$ radar data cubes used.

Next, consider the estimation performance in finding the complex reflection coefficients

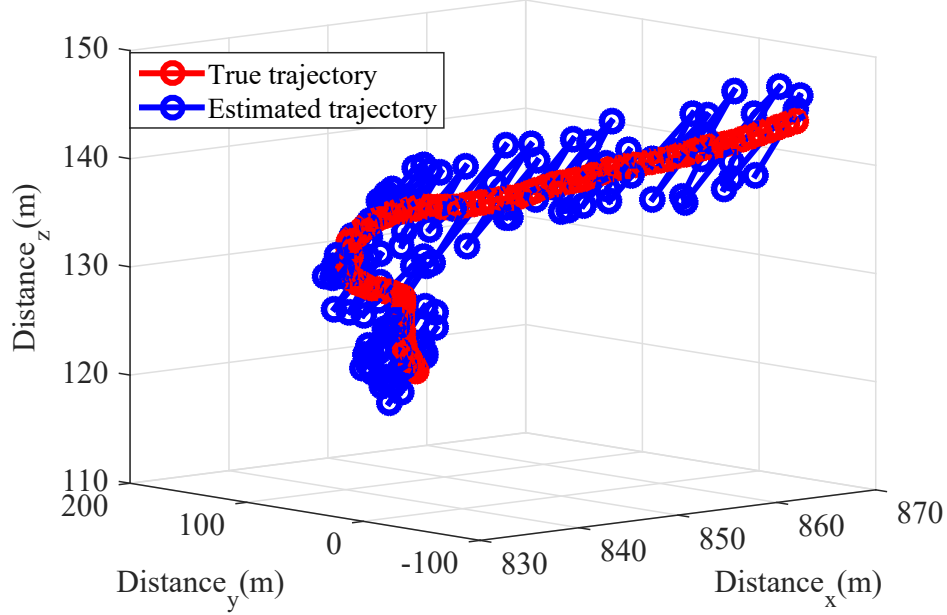


Figure 4.20: Trajectory estimation: The estimated trajectory obtained by using Algorithm 4 is depicted as the solid blue line. This output is compared to its ground truth depicted as the solid red line.

in the radar data cube. Figure 4.19 shows typical estimates of the complex reflection coefficients for the typical steps of Algorithm 5, where the x axis and the y axis indicate the real part of the complex reflection coefficient and its imaginary part, reflectively. The resulting estimates are compared with their GPS ground truth. Also, the \pm standard deviation of Cramér-Rao bound (CRB), $\pm\sigma_{\text{CRB}}$, are given for comparison. In Figure 4.19(a), the estimate of the body reflection coefficient (blue line) stays within $\pm\sigma_{\text{CRB}}$ (solid red ellipse) after $i = 4$ iterations (solid blue circles), where the solid blue circles indicate the number of i iterations for finding the reflection coefficient in Algorithm 5. Here, the resulting estimate is close to its GPS ground truth value (red dot). For the estimate of the blade hub reflection, the resulting estimate (solid blue line) stays within $\pm\sigma_{\text{CRB}}$ (solid red ellipse) and is close to the GPS ground truth value (red dot) as illustrated in Figure 4.19(b). Note that both the body and the blade hub reflection coefficients estimated by the proposed scheme are close to the ground truth values. It is also shown that these estimation errors stay within $\pm\sigma_{\text{CRB}}$ after a few iterations.

For estimation performance in finding the drone trajectory by using Algorithm 4.

Figure 4.20 illustrates the GPS ground truth trajectory (red line) which would lead to resolution bin migrations in conventional processing. The trajectory estimate output by the proposed algorithm is depicted as the solid blue line. Figure 4.21(a) shows the RMSE of the corresponding range estimate in comparison with the range resolution of ΔR (dashed red line). Note that the maximum error of the range estimation yields the 6.67% of the range resolution. Figure 4.21(b) presents the RMSE of the velocity component of the trajectory estimate in Figure 4.20. This estimation error is much lower than the velocity resolution bin of ΔV (dashed red line), where the maximum estimation error yields the 34% of the velocity resolution at the initial and is reduced to the 12.7% after 26 s. Figure 4.21(c) illustrates the RMSE of the azimuth angle component of the trajectory estimate in Figure 4.20. The estimation error is a very small value compared to the azimuth resolution of $\Delta\theta$ (dashed red line). Figure 4.21(d) shows the RMSE of the elevation angle component of the trajectory estimate in Figure 4.20. Here, the estimation error shows a small error compared to the elevation resolution of $\Delta\phi$ (dashed red line).

Detection performance via the proposed scheme

Here consider the hypothesis test for detection using the sufficient statistics of the likelihood ratio with an arbitrarily long-time window using the real measurements. In Figure 4.22, the integration values are given as a function of time. Here, the proposed integration reaches to 27 at $t = 34$ s, which is much higher than 15 achieved by the conventional integration. This also indicates that the estimation errors of unknowns are very small. For detection, the CFAR detection threshold for $P_{fa} = 10^{-7}$ is depicted by the red line in Figure 4.22. Detection for each detector is made by comparing its integration value against this threshold. The proposed scheme exceeds the CFAR threshold and enables one to decide on the object existence hypothesis ($H = H_1$) at $t = 5$ s, whereas the conventional scheme stays in the region for the noise only signal hypothesis ($H = H_0$).

4.8 Summary

This chapter has focused on the micro-Doppler estimation of manoeuvring and small rotary-wing aircraft using the monostatic radar. The micro-Doppler signature is considered as the rotation frequency generated by rotating rotor blades of the aircraft. In order to find this, the short-time Fourier transform (STFT) of a radar data cube collected in a CPI is commonly used as the time-frequency analysis technique. However, when the carrier wavelength is smaller than the blade length, the micro-Doppler signature is very close to the main Doppler shift, and this approach cannot discriminate this micro-Doppler signature from the main Doppler shift due to the limited frequency resolution. In order to achieve the fine resolution, this approach often requires more samples than those collected in a CPI.

In order to tackle this challenge, this chapter has proposed an algorithm capable of simultaneously tracking the object trajectory and estimating the rotation frequency before the detection decision is made. In particular, the expectation-maximisation (EM) approach is used: The expectation is approximated by using the state distributions generated from Bayesian recursive filtering for the trajectory estimation. The reflection coefficients and the rotation frequency are estimated by maximising this approximated expectation. It is demonstrated that the proposed scheme enables one to estimate the micro-Doppler shifts with high accuracy using simultaneously tracking the trajectory before the detection decision is made in both the simulated data and the actual measurements on manoeuvring and small rotary-wing aircraft, whereas the typical approach cannot find it. It is also shown that the detection scheme, which combines the proposed estimator and the coherent integration scheme proposed in Chapter 3, is proposed in order to detect manoeuvring and small rotary-wing aircraft.

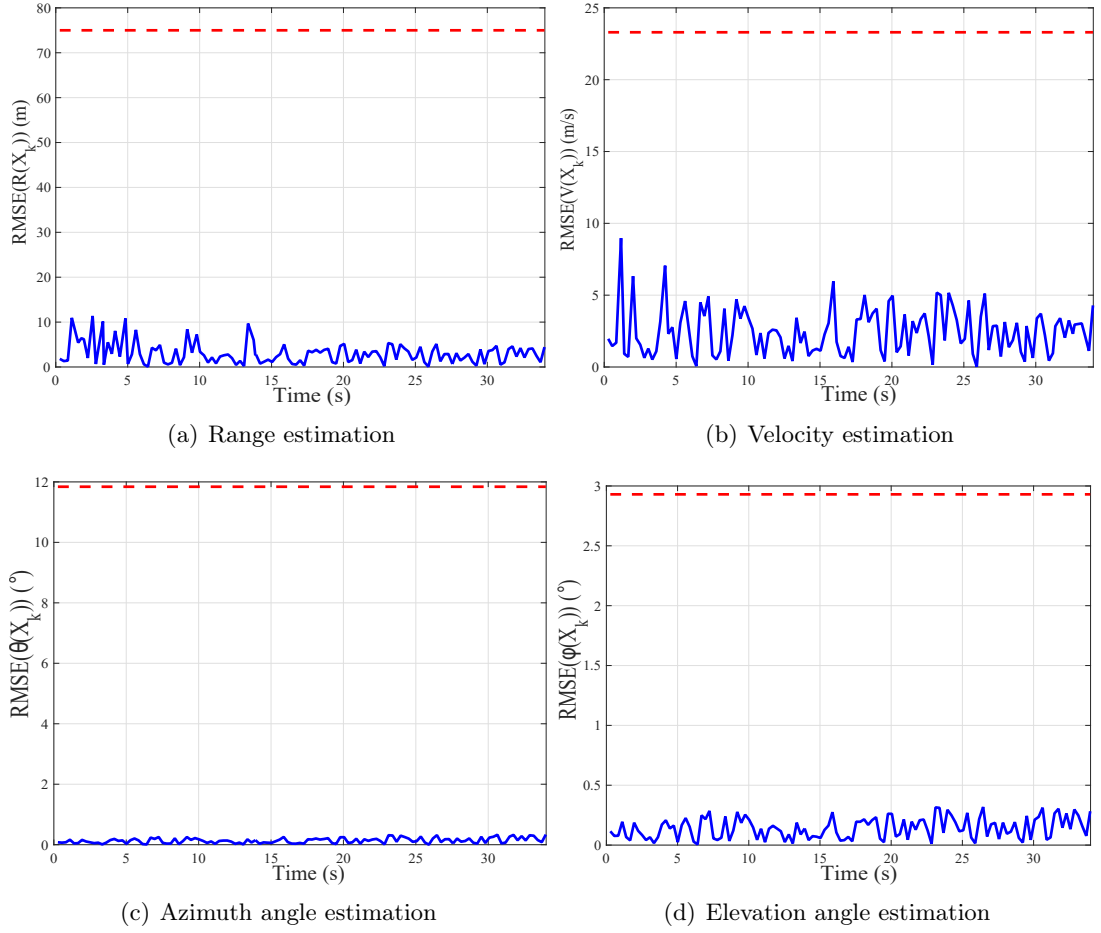


Figure 4.21: Root mean square error (RMSE) of the typical trajectory estimation: The trajectory estimation is obtained in Figure 4.20. (a) RMSE of the range estimation. (b) RMSE of the velocity estimation. (c) RMSE of the azimuth angle estimation. (d) RMSE of the elevation angle estimation. The red dashed lines in all these figures indicate the range resolution ($\Delta R = 75\text{m}$) in (a), the velocity resolution ($\Delta V = 23.5\text{ms}^{-1}$) in (b), the azimuth resolution ($\Delta \theta = 11.81^\circ$) in (c), and the elevation resolution ($\Delta \phi = 2.93^\circ$) in (d), respectively.

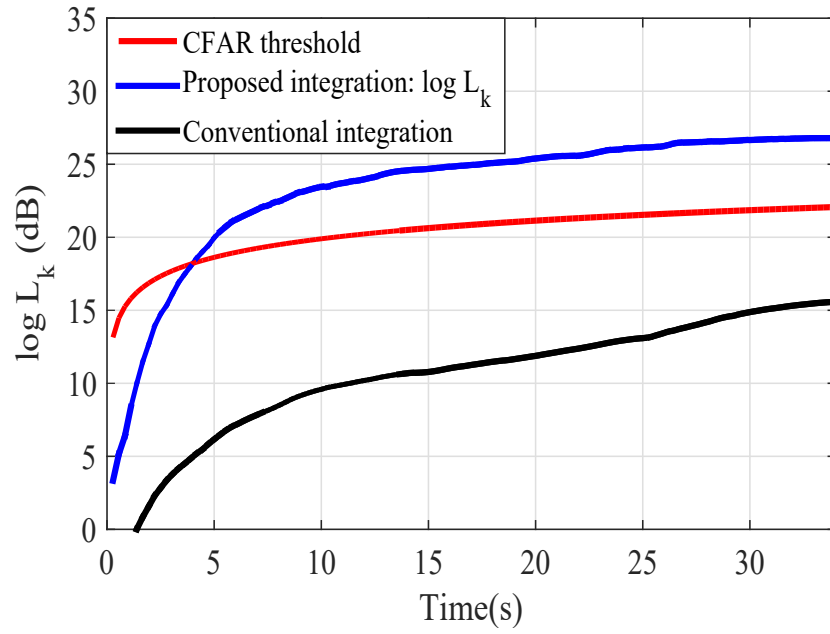


Figure 4.22: Detection performance of the proposed detector in comparison with the conventional detector: Long-time integration using the proposed scheme, and the conventional coherent integrator. The integrated sufficient statistics from the proposed integration is depicted by the blue line. The CFAR threshold for $P_{fa} = 10^{-7}$ is the red line, and, the conventional scheme is depicted by the black line.

Chapter 5

Conclusion

This thesis has addressed the problems in detecting manoeuvring and small objects in high noise background and estimating their micro-Doppler features. This is challenging because the level of reflected signals from such objects collected in a coherent processing interval (CPI) is less than that of noise only signals, and their reflections vary with the range-bearing and Doppler values over time. Conventional detectors and estimators are likely to fail in collecting sufficient evidence on the objects' presence and their relative parameters for a long time due to not taking into account their manoeuvres.

In order to tackle these challenges, this thesis provides a series of novel approaches that can detect manoeuvring and small objects by simultaneously performing long time integration and estimating their micro-Doppler signatures in order to achieve reliable detection and characterisation of them. Section 5.1 gives a summary of this thesis and highlights the contributions. The possible directions for future research that can further improve these contributions are provided in Section 5.3.

5.1 Summary

Chapter 1 has provided the brief introduction to the challenges and the limitations of object detection and micro-Doppler estimation for the manoeuvring and small objects. These give the motivation and identify the problems, which need to be solved in this thesis. The contributions and the thesis outline are presented at the end of this chapter.

Chapter 2 has reviewed the background materials, which are related to Chapter 3 and Chapter 4. This chapter introduces the advantages and disadvantages of radar configurations, which define the monostatic configuration, the bistatic setting, and the multistatic configuration. This also introduces the conventional detection processing chains, including beam-forming and Doppler processing, with the limitation of detection in manoeuvring and small objects. Then, it provides the brief introduction to time-frequency analysis methods for the micro-Doppler signatures and gives the overview of track-before-detect including the recent advanced in this topic.

Chapter 3 has presented the first major contribution: This chapter provides the new approach to a long-time coherent integration for detection of manoeuvring and small objects in the multistatic setting. The main differences compared to existing TBD algorithms are i) the evaluation of the complex likelihood ratio conditioned on object-related parameters, complex reflection coefficients, and synchronisation terms based on Bayesian recursive filtering in order to achieve the coherent processing, and ii) the detection test, which uses the coherent integration obtained by the resulting values of the complex likelihood ratios for an arbitrarily long time instead of the use of the probability of target existence used in the existing TBD algorithms. In particular, the long time integration is determined by evaluating the long time likelihood ratio test conditioned on a trajectory, reflection coefficients, and synchronisation terms as unknowns. The proposed scheme uses the Markov state-space model to find the unknown trajectory, which contains the object kinematics. The measurement model in this state-space model involves the radar ambiguity function parametrised on the aforementioned reflection coefficients. The reflection coefficients estimation is evaluated using the expectation-maximisation (EM) algorithm within the Bayesian filtering recursions for state trajectory estimate. For synchronisation, the proposed approach uses the digital beam-forming technique to simultaneously divert beams towards both the test points of detection and the locations of the separately located transmitters in order to find the respective time reference shifts in the bistatic channels. The resulting algorithm hence enables one to collect the entire evidence of the object's presence at the receiver by i) performing the coherent integration in both the monostatic channel

and the bistatic channels within a CPI, ii) non-coherently integrating across different (non-coherent) channels, and iii) continuing integration for an arbitrarily long interval that contains many CPIs. As a result, the proposed approaches enable one to detect manoeuvring and low SNR objects which cannot be detected using other detection techniques.

Chapter 4 has presented the second major contribution: This chapter provides the novel approach to the micro-Doppler estimation of manoeuvring and small rotary-wing unmanned aerial vehicles (UAVs) in the co-located transmitter/uniform planar array (UPA) receiver pair. The rotation frequency of rotor blades is considered as the micro-Doppler feature. This chapter proposes the estimation scheme that can estimate the rotation frequency by simultaneously tracking a single UAV and estimating its reflection coefficients from both the fuselage and the rotor blades before the detection decision is made. In particular, the proposed estimator uses the maximum likelihood (ML) approach that finds the rotation frequency to maximise the likelihood function conditioned on a trajectory, a rotation frequency, and reflection coefficients as unknowns. In order to evaluate this ML, the joint Bayesian recursive filtering and expectation-maximisation (EM) approach is proposed. This approach uses Bayesian recursive filtering with the Markov state-space model for estimating the trajectory. The measurement model in this state model captures both the reflection coefficients and the rotor rotation frequency together with the radar ambiguity function. The EM finds these parameters within the Bayesian recursive filtering. Hence, the resulting algorithm enables one to estimate the rotor rotation frequency with a favourable accuracy while simultaneously estimating both the trajectory and the reflection coefficients before deciding on the object's presence. Then, the detection scheme that utilises these estimates is proposed.

5.2 Limitations

In this thesis, the radar system is a ground-based security surveillance system for the small aircraft detection, where multiple transmitters and a single receiver are located at different regions on the ground and observe small aircraft in the sky. Regarding this system, Chapter 3 and 4 develop the algorithms in order to detect the small aircraft. These algorithms have the following limitations:

1. Multipath interference at the receiver is not considered.
2. Jammers are not considered.
3. Multiple target scenario is not considered
4. Radar clutter is not considered.
5. Noise samples are statistically independent.
6. For the micro-Doppler estimation, a rotary-wing aircraft is only considered.

5.3 Possible directions for future work

The overall detection and estimation approaches proposed in this thesis are developed regarding the assumptions and the problems given in Chapter 1. One important consideration is the multiple object detection and their micro-Doppler feature estimation. In this thesis, the proposed algorithms are developed regarding a single low SNR object presented in a surveillance region. The evaluation of the likelihood used for the object detection and the micro-Doppler estimation provides an accurate approximation. This benefit comes with an additional computational cost in comparison with the conventional methods. In the case of multiple objects presented in a surveillance region, the proposed schemes need to have a bank of the Bayesian filters, each of

which processes reflected signals from each object in order to detect it and estimate its micro-Doppler features. This can lead to high computational cost. Thus, one possible direction of adopting the proposed schemes for the multiple object case would be finding approaches that can improve computational efficiency.

For micro-Doppler estimation, the proposed estimator presented in Chapter 4 is developed in the monostatic radar configuration. It is interested in extending this approach in the bistatic configuration and the multistatic setting. In order to achieve this goal, the signal model used in Chapter 4 needs to adopt the signal model used in Chapter 3 and has extra unknowns as the synchronisation terms in the bistatic channels. This requires to solve an optimisation problem with many unknowns, which comes with its own set of challenges. Finding a solution to this problem can be a direction of further improving the proposed estimator using the bistatic/multistatic configurations.

Appendix A

The likelihood locality, Cramér-Rao bound, and computational complexity of the proposed detector

This appendix provides the derivations of likelihood locality, Cramér-Rao bound for the reflection coefficients, and computational complexity used in the proposed detection scheme in Chapter 3. This appendix starts with introducing the likelihood locality in Section A.1. Then, Section A.2 provides the Cramér-Rao bound for the reflection coefficients. Section A.3 details the computational complexity of the proposed detector.

A.1 The likelihood locality

This section explains the likelihood ratio test with the locality of the measurements. When a single object exists in the surveillance region, the m th channel measurement contains the reflections, $\mathbf{Z}_{m,k}(r) \in \mathcal{E}_m(\mathbf{X}_k)$, from the object state, \mathbf{X}_k . Let one define the complement of \mathcal{E}_m in the set of range bins, which is found as

$$\bar{\mathcal{E}}_m(\mathbf{X}_k) \triangleq \{1, 2, \dots, \Gamma\} \setminus \mathcal{E}_m(\mathbf{X}_k)$$

The likelihood locality, Cramér-Rao bound, and computational complexity of the proposed detector

. The numerator terms in (3.13) can be found using $\mathcal{E}_m(\mathbf{X}_k)$ and $\bar{\mathcal{E}}_m(\mathbf{X}_k)$:

$$l(\mathbf{Z}_{m,k}|\mathbf{X}_k, \alpha_{m,k}, \Delta t_m, H = H_1) = \prod_{r \in \mathcal{E}_m(\mathbf{X}_k)} l(\mathbf{Z}_{m,k}(r)|X_k, \alpha_{m,k}, \Delta t_m, H = H_1) \prod_{r' \in \bar{\mathcal{E}}_m(\mathbf{X}_k)} p(\mathbf{Z}_{m,k}(r')). \quad (\text{A.1})$$

Similarly, the likelihood for the noise-only signal hypothesis factorises as

$$l(\mathbf{Z}_{m,k}|X_k, H = H_0) = \prod_{r \in \mathcal{E}_m} l(\mathbf{Z}_{m,k}(r)|H = H_0) \prod_{r' \in \bar{\mathcal{E}}_m} p(\mathbf{Z}_{m,k}(r')), \quad (\text{A.2})$$

which, after substituting into (3.10) with (A.1) leads to (3.13).

A.2 Cramér-Rao bound (CRB) for complex reflection coefficients

Let this section consider the Cramér-Rao bound (CRB) for the complex reflection coefficient estimated by Algorithm 1. The CRB provides the theoretical minimum variance for an unbiased estimator and is found by using inverse Fisher information [90, Chp.3]. In the problem setting considered in Chapter 3, the Fisher information is found by taking the second order partial derivative of the logarithm of the likelihood with respect to the reflection coefficient. This processing is followed through Equation (3.6) and (3.7) in [90, Chp.3]:

$$\mathbf{I}(\alpha_{m,k}) = -\mathbb{E} \left\{ \frac{\partial^2 \log l(\mathbf{Z}_k|\alpha_k)}{\partial \alpha_{m,k}^2} \right\}, \quad (\text{A.3})$$

$$\log l(\mathbf{Z}_k|\alpha_k) = \log \left\{ \int \int_{\mathbf{X}_k \Delta \mathbf{t}} l(\mathbf{Z}_k|\mathbf{X}_k, \Delta \mathbf{t}, \alpha_k) \times p(\mathbf{X}_k, \Delta \mathbf{t}|\alpha_k) d\mathbf{X}_k d\Delta \mathbf{t} \right\}, \quad (\text{A.4})$$

where $\mathbf{I}(\alpha_{m,k})$ denotes the Fisher information of the m th reflection coefficient at the k th CPI, and $\mathbb{E}\{\cdot\}$ is the expectation of its input argument.

In order to evaluate $\log l(\cdot)$ in (A.4), the ground truth values of the object state, \mathbf{X}_k , and the synchronisation term, $\Delta \mathbf{t}$, are used. After substituting these true values into (A.4),

The likelihood locality, Cramér-Rao bound, and computational complexity of the proposed detector

the resulting expression is found as

$$\begin{aligned}
\log l(\mathbf{Z}_k|\boldsymbol{\alpha}_k) &= \log l(\mathbf{Z}_k|\mathbf{X}_k = \mathbf{X}_{\text{true},k}, \boldsymbol{\alpha}_k, \Delta\mathbf{t} = \Delta\mathbf{t}_{\text{true}}) \quad (\text{A.5}) \\
&= \sum_{r \in \mathcal{E}_m(\mathbf{X}_{\text{true},k})} \left(-\log(\pi^{LN} \det(\Sigma_m)) - \mathbf{Z}_{m,k}^H(r) \Sigma_m^{-1} \mathbf{Z}_{m,k}(r) \right. \\
&\quad \left. + 2 \operatorname{Re}\{\alpha_{m,k}^* \mathbf{s}_m^H(r, \mathbf{X}_{\text{true},k}, \Delta\mathbf{t}_{\text{true}}) \Sigma_m^{-1} \mathbf{Z}_{m,k}(r)\} \right. \\
&\quad \left. - |\alpha_{m,k}|^2 \mathbf{s}_m^H(r, \mathbf{X}_{\text{true},k}, \Delta\mathbf{t}_{\text{true}}) \Sigma_m^{-1} \mathbf{s}_m(r, \mathbf{X}_{\text{true},k}, \Delta\mathbf{t}_{\text{true}}) \right), \\
\frac{\partial^2 \log l(\mathbf{Z}_k|\boldsymbol{\alpha}_k)}{\partial \alpha_{m,k}^2} &= -2 \times \mathbf{s}_m^H(r, \mathbf{X}_{\text{true},k}, \Delta\mathbf{t}_{\text{true}}) \Sigma_m^{-1} \mathbf{s}_m(r, \mathbf{X}_{\text{true},k}, \Delta\mathbf{t}_{\text{true}}), \quad (\text{A.6})
\end{aligned}$$

where $\mathbf{X}_{\text{true},k}$ and $\Delta\mathbf{t}_{\text{true}}$ are the true values of \mathbf{X}_k and $\Delta\mathbf{t}$, respectively. As a result, the Fisher information of $\mathbf{I}(\alpha_{m,k})$ in (A.3) is given by

$$\mathbf{I}(\alpha_{m,k}) = \sum_{r \in \mathcal{E}_m(\mathbf{X}_{\text{true},k})} 2 \mathbf{s}_m^H(r, \mathbf{X}_{\text{true},k}, \Delta\mathbf{t}_{\text{true},m}) \Sigma_m^{-1} \mathbf{s}_m(r, \mathbf{X}_{\text{true},k}, \Delta\mathbf{t}_{\text{true},m}), \quad (\text{A.7})$$

and the CRB for the m th reflection coefficient at the k th CPI is found by using the inverse $\mathbf{I}(\alpha_{m,k})$:

$$\sigma_{\text{CRB}}^2 \triangleq \mathbf{I}(\alpha_{m,k})^{-1}. \quad (\text{A.8})$$

This quantity is the lower bound of the variance of the complex reflection coefficient:

$$\operatorname{Var}(\hat{\alpha}_{m,k}) \geq \sigma_{\text{CRB}}^2, \quad (\text{A.9})$$

where $\operatorname{Var}(\hat{\alpha}_{m,k}) = \mathbb{E}\{|\alpha_{m,k} - \hat{\alpha}_{m,k}|^2\}$ is the variance.

Note that Σ_m is Hermitian and positive definite. Therefore, the CRB for the real part of the complex reflection is equivalent to that for the imaginary part [90, Chp.15].

A.3 Computational complexity of the proposed detector

This section gives the computational complexity of the proposed detector compared to that of the conventional coherent detector. In order to find the computational complexity of the proposed algorithm for the cell under test at the K th CPI, let one consider

The likelihood locality, Cramér-Rao bound, and computational complexity of the proposed detector

Table A.1: Computational cost of the cell under test at the k th CPI

Equation	multiplications	additions	Algorithm
(3.30)	$2PN_{r(X)}M(LN)^2$	$2PN_{r(X)}MLN(LN - 1)$	Algorithm 3
(3.32)	P	$(P - 1)$	Algorithm 3
(3.35)	PN_X	$(P - 1)N_X$	Algorithm 3
(3.53)	$4N_{r(X)}M(LN)^2$	$4N_{r(X)}MLN(LN - 1)$	Algorithm 3
(3.43)	$2N_{I_1}PN_{r(X)}M(LN)^2$	$2N_{I_1}PN_{r(X)}MLN(LN - 1)$	Algorithm 1
(3.45)	$4N_{I_1}PN_{r(X)}M(LN)^2$	$4N_{I_1}PN_{r(X)}MLN(LN - 1)$	Algorithm 1
(3.51)	$kN_{I_2}N_{r(\Delta t)}$	$N_{I_2}(kN_{r(\Delta t)} - 1)$	Algorithm 2

the total number of multiplications and additions for Algorithm 1, Algorithm 2, and Algorithm 3.

Table A.1 shows the number of multiplications and additions for each step of Algorithm 1, Algorithm 2, and Algorithm 3, respectively, where N_X denotes the dimensionality of the object state in (3.17), and $N_{r(X)}$ and $N_{r(\Delta t)}$ indicate the length of $\mathcal{E}(X_k)$ and $\mathcal{E}(\Delta t)$. Here, N_{I_1} and N_{I_2} denote the number of iterations for the EM algorithm in Algorithm 1 and the golden section search in Algorithm 2, respectively.

The total cost at the K th CPI is hence found by using the sum of all multiplications and additions in Table A.1: The total multiplications are

$$2PN_{r(X)}M(LN)^2(3N_{I_1} + \frac{N_X}{2} + 3) + P + kN_{I_2}N_{r(\Delta t)},$$

and the total additions are

$$2PN_{r(X)}M(LN + 1)(3N_{I_1} + 2) + (P - 1) + (P - 1)N_X + N_{I_2}(kN_{r(\Delta t)} - 1).$$

The conventional coherent detector over a grid of bearing and Doppler bins is found in [18, Chp.13]:

$$T_K(r, X(i, j)) = \sum_{k=1}^K \sum_{m=1}^M \text{Re}\{\mathbf{s}_m(r, X(i, j))\Sigma_m^{-1}\mathbf{Z}_{m,k}(r)\} \underset{H_0}{\overset{H_1}{\geq}} \log \mathcal{J}_k. \quad (\text{A.10})$$

Here, $X(i, j)$ denotes a location (i.e., range and bearing) and velocity associated with

The likelihood locality, Cramér-Rao bound, and computational complexity of the proposed detector

the i th bearing bin and the j th Doppler bin at the r th range bin. The computational cost of this conventional detector for the cell under test at the K th CPI hence has $2KM(LN)^2$ multiplications and $2LN(LN - 1)(KM - K - M)$ additions.

As a result, the computational complexity of the proposed detector for the cell under test for K CPIs is $\mathcal{O}(PN_I)$, whereas the conventional coherent detector requires $\mathcal{O}(K)$.

Appendix B

Original publications

- K. Kim, M. Uney, and B. Mulgrew, “Detection of manoeuvring low SNR objects in receiver arrays,” *2016 Sensor Signal Processing for Defence (SSPD)*, Sept 2016, pp. 1 – 5.
- K. Kim, M. Uney, and B. Mulgrew, “Simultaneous tracking and long time integration for detection in collaborative array radars,” *2017 IEEE Radar Conference (RadarConf)*, May 2017, pp. 0200 – 0205.
- K. Kim, M. Uney, and B. Mulgrew, “OPPORTUNISTIC SYNCHRONISATION OF MULTI-STATIC STARING ARRAY RADARS VIA TRACK-BEFORE-DETECT,” *2018 IEEE International Conference on Acoustics, Speech and Signal Processing (ICASSP)*, April 2018, pp. 3320 – 3324.
- K. Kim, M. Uney, and B. Mulgrew, “ESTIMATION OF DRONE MICRO-DOPPLER SIGNATURES VIA TRACK-BEFORE-DETECT IN ARRAY RADARS,” *International Radar Conference (Radar 2019)*, Sep 2019.
- K. Kim, M. Uney, and B. Mulgrew, “Coherent track-before-detect with micro-Doppler signature estimation in array radars,” *IET Radar, Sonar and Navigation*, accepted Feb 2020.

Bibliography

- [1] M. Richards, *Fundamentals of Radar Signal Processing*, ser. Professional Engineering. McGraw-hill, 2005.
- [2] C. Alabaster, *Pulse Doppler Radar: Principles, Technology, Applications*, ser. Electromagnetics and Radar. Institution of Engineering and Technology, 2012.
- [3] A. V. Oppenheim, R. W. Schaffer, and J. R. Buck, *Discrete-time Signal Processing*, 2nd ed. Upper Saddle River, NJ, USA: Prentice-Hall, Inc., 1999.
- [4] M. Uney, B. Mulgrew, and D. Clark, “Maximum likelihood signal parameter estimation via track before detect,” in *2015 Sensor Signal Processing for Defence (SSPD)*, Sept 2015, pp. 1–5.
- [5] M. Richards, W. Melvin, J. Scheer, J. Scheer, and W. Holm, *Principles of Modern Radar: Radar Applications*, ser. Electromagnetics and Radar. Institution of Engineering and Technology, 2014.
- [6] C. M. Johnson, “Ballistic-missile defense radars,” *IEEE Spectrum*, vol. 7, no. 3, pp. 32–41, March 1970.
- [7] P. Meischner, *Weather Radar: Principles and Advanced Applications*, ser. Physics of Earth and Space Environments. Springer Berlin Heidelberg, 2013.
- [8] T. S. Perry, “In search of the future of air traffic control,” *IEEE Spectrum*, vol. 34, no. 8, pp. 18–35, Aug 1997.
- [9] E. Lissel, H. Rohling, and W. Plagge, “Radar sensor for car applications,” in *Proceedings of IEEE Vehicular Technology Conference (VTC)*, June 1994, pp. 438–442 vol.1.
- [10] M. Rameez, M. Dahl, and M. I. Pettersson, “Adaptive digital beamforming for interference suppression in automotive FMCW radars,” in *2018 IEEE Radar Conference (RadarConf18)*, April 2018, pp. 0252–0256.

- [11] F. H. Sanders, R. L. Sole, J. E. Carroll, G. S. Secrest, and T. L. Allmon, "Analysis and resolution of RF interference to radars operating in the band 2700-2900 MHz from broadband communication transmitters," US Dept. Commerce, NTIA, Washington, D.C., USA, Tech. Rep. TR-13-490, 2012. [Online]. Available: https://www.ntia.doc.gov/files/ntia/publications/13-490_1_.pdf
- [12] P. Peebles, *Radar Principles*. Wiley India Pvt. Limited, 2007.
- [13] H. L. Van Trees, *Detection, Estimation, and Modulation Theory: Radar-Sonar Signal Processing and Gaussian Signals in Noise*. Melbourne, FL, USA: Krieger Publishing Co., Inc., 1992.
- [14] Y. Barniv, "Dynamic programming solution for detecting dim moving targets," *IEEE Transactions on Aerospace and Electronic Systems*, vol. AES-21, no. 1, pp. 144–156, Jan 1985.
- [15] Y. Barniv and O. Kella, "Dynamic programming solution for detecting dim moving targets part ii: Analysis," *IEEE Transactions on Aerospace and Electronic Systems*, vol. AES-23, no. 6, pp. 776–788, Nov 1987.
- [16] P. Huang, G. Liao, Z. Yang, X. Xia, J. Ma, and J. Ma, "Long-time coherent integration for weak maneuvering target detection and high-order motion parameter estimation based on keystone transform," *IEEE Transactions on Signal Processing*, vol. 64, no. 15, pp. 4013–4026, Aug 2016.
- [17] M. Richards, W. Holm, and J. Scheer, *Principles of Modern Radar: Basic Principles*, ser. Electromagnetics and Radar. Institution of Engineering and Technology, 2010.
- [18] S. Kay, *Fundamentals of Statistical Signal Processing: Detection theory*, ser. Prentice Hall Signal Processing Series. Prentice-Hall PTR, 1998.
- [19] S. sheng Zhang, T. Zeng, T. Long, and H. peng Yuan, "Dim target detection based on keystone transform," in *2005 IEEE International Radar Conference*, May 2005, pp. 889–894.
- [20] X. Chen, J. Guan, N. Liu, and Y. He, "Maneuvering target detection via Radon-Fractional Fourier Transform-based long-time coherent integration," *IEEE Transactions on Signal Processing*, vol. 62, no. 4, pp. 939–953, Feb 2014.
- [21] L. Kong, X. Li, G. Cui, W. Yi, and Y. Yang, "Coherent integration algorithm for a maneuvering target with high-order range migration," *IEEE Transactions on Signal Processing*, vol. 63, no. 17, pp. 4474–4486, Sept 2015.

- [22] X. Li, G. Cui, W. Yi, and L. Kong, "Manoeuvring target detection based on keystone transform and lv's distribution," *IET Radar, Sonar Navigation*, vol. 10, no. 7, pp. 1234–1242, 2016.
- [23] J. Zheng, J. Zhang, S. Xu, H. Liu, and Q. H. Liu, "Radar detection and motion parameters estimation of maneuvering target based on the extended keystone transform," *IEEE Access*, pp. 1–1, 2018.
- [24] S. A. B. Ristic and N. Gordon, *Beyond the Kalman Filter: Particle Filters for Tracking Applications*. Artech House, 2004.
- [25] X. Deng, Y. Pi, M. Morelande, and B. Moran, "Track-before-detect procedures for low pulse repetition frequency surveillance radars," *IET Radar, Sonar Navigation*, vol. 5, no. 1, pp. 65–73, January 2011.
- [26] M. G. Rutten, N. J. Gordon, and S. Maskell, "Recursive track-before-detect with target amplitude fluctuations," *IEEE Proceedings - Radar, Sonar and Navigation*, vol. 152, no. 5, pp. 345–352, October 2005.
- [27] S. Davey, M. Rutten, and B. Cheung, "Using phase to improve track-before-detect," *IEEE Transactions on Aerospace and Electronic Systems*, vol. 48, no. 1, pp. 832–849, Jan 2012.
- [28] W. H. V. Aulock, "Properties of phased arrays," *Proceedings of the IRE*, vol. 48, no. 10, pp. 1715–1727, Oct 1960.
- [29] N. Willis and H. Griffiths, *Advances in Bistatic Radar*, ser. Electromagnetics and Radar. Institution of Engineering and Technology, 2007.
- [30] H. Griffiths, "Multistatic, MIMO and networked radar: The future of radar sensors?" in *The 7th European Radar Conference*, Sept 2010, pp. 81–84.
- [31] P. Tait and I. of Electrical Engineers, *Introduction to Radar Target Recognition*, ser. Electromagnetics and Radar Series. Institution of Engineering and Technology, 2005.
- [32] A. Rihaczek and S. Hershkowitz, *Theory and Practice of Radar Target Identification*, ser. Artech House radar library. Artech House, 2000.
- [33] V. Chen, *The Micro-Doppler Effect in Radar*, ser. Artech House radar library. Artech House, 2011.
- [34] V. C. Chen, F. Li, S. S. Ho, and H. Wechsler, "Micro-Doppler effect in radar: phenomenon, model, and simulation study," *IEEE Transactions on Aerospace and*

- Electronic Systems*, vol. 42, no. 1, pp. 2–21, Jan 2006.
- [35] P. Molchanov, K. Egiazarian, J. Astola, R. I. A. Harmanny, and J. J. M. de Wit, “Classification of small UAVs and birds by micro-Doppler signatures,” in *2013 European Radar Conference*, Oct 2013, pp. 172–175.
 - [36] M. Ritchie, F. Fioranelli, H. Borrión, and H. Griffiths, “Multistatic micro-Doppler radar feature extraction for classification of unloaded/loaded micro-drones,” *IET Radar, Sonar Navigation*, vol. 11, no. 1, pp. 116–124, 2017.
 - [37] J. Li and P. Stoica, *MIMO Radar Signal Processing*. John Wiley & Sons, Inc., Hoboken, NJ, 2009.
 - [38] A. Haimovich, R. Blum, and L. Cimini, “MIMO radar with widely separated antennas,” *IEEE Signal Processing Magazine*, vol. 25, no. 1, pp. 116–129, 2008.
 - [39] P. F. Sammartino, “A comparison of processing approaches for distributed radar sensing,” Ph.D. dissertation, University College London, 2009.
 - [40] H. Griffiths and C. J. Baker, “Towards the intelligent adaptive radar network,” in *2013 IEEE Radar Conference (RadarCon13)*, April 2013, pp. 1–5.
 - [41] Y. Pailhas, Y. Petillot, K. Brown, and B. Mulgrew, “Spatially distributed MIMO sonar systems: Principles and capabilities,” *IEEE Journal of Oceanic Engineering*, vol. 42, no. 3, pp. 738–751, July 2017.
 - [42] A. Gorji, R. Tharmarasa, and T. Kirubarajan, “Widely separated MIMO versus multistatic radars for target localization and tracking,” *IEEE Transactions on Aerospace and Electronic Systems*, vol. 49, no. 4, pp. 2179–2194, OCTOBER 2013.
 - [43] S. Buzzi, M. Lops, and L. Venturino, “Track-before-detect procedures for early detection of moving target from airborne radars,” *IEEE Transactions on Aerospace and Electronic Systems*, vol. 41, no. 3, pp. 937–954, July 2005.
 - [44] M. Mallick, V. Krishnamurthy, and B. Vo, *Integrated Tracking, Classification, and Sensor Management: Theory and Applications*. Wiley, 2012.
 - [45] M. Richards, W. Holm, and J. Scheer, *Principles of Modern Radar: Basic Principles*, ser. Electromagnetics and Radar. Institution of Engineering and Technology, 2010.
 - [46] “Analysis and Resolution of RF Interference to Radars Operating in the Band 2700-2900 MHz from Broadband Communication Transmitters,”

- accessed February 2020. [Online]. Available: https://www.ntia.doc.gov/files/ntia/publications/compendium/1215.00-1240.00_01SEP14.pdf
- [47] “IEEE standard for radar definitions,” *IEEE P686/D2, 2017 (Revision of IEEE Std 686-2008)*, pp. 1–62, Jan 2017.
 - [48] H. L. Van Trees, *Optimum Array Processing*. New York: Wiley-Interscience, 2002.
 - [49] W. Rees and W. Rees, *Physical Principles of Remote Sensing*, ser. Topics in remote sensing. Cambridge University Press, 2001.
 - [50] B. Mahafza, *Radar Systems Analysis and Design Using MATLAB Third Edition*. Taylor & Francis, 2013.
 - [51] B. Shtarkalev, “Single data set detection for multistatic doppler radar,” Ph.D. dissertation, The University of Edinburgh, 2015.
 - [52] P. Wang, H. Li, and B. Himed, “Moving target detection using distributed MIMO radar in clutter with nonhomogeneous power,” *IEEE Transactions on Signal Processing*, vol. 59, no. 10, pp. 4809–4820, Oct 2011.
 - [53] P. Wang, H. Li, and B. Himed, “Distributed detection of moving target using MIMO radar in clutter with non-homogeneous power,” in *International Workshop on Systems, Signal Processing and their Applications, WOSSPA*, May 2011, pp. 383–387.
 - [54] M. Akcakaya and A. Nehorai, “MIMO radar detection and adaptive design under a phase synchronization mismatch,” *IEEE Transactions on Signal Processing*, vol. 58, no. 10, pp. 4994–5005, Oct 2010.
 - [55] M. Weib, “Synchronisation of bistatic radar systems,” in *IGARSS 2004. 2004 IEEE International Geoscience and Remote Sensing Symposium*, vol. 3, Sept 2004, pp. 1750–1753 vol.3.
 - [56] W. Melvin, “A STAP overview,” *IEEE Aerospace and Electronic Systems Magazine*, vol. 19, no. 1, pp. 19–35, Jan 2004.
 - [57] J. Ward, *Space-time Adaptive Processing for Airborne Radar*, ser. Technical report (Lincoln Laboratory). Massachusetts Institute of Technology, Lincoln Laboratory, 1994.
 - [58] F. C. Robey, D. R. Fuhrmann, E. J. Kelly, and R. Nitzberg, “A CFAR adaptive matched filter detector,” *IEEE Transactions on Aerospace and Electronic Systems*,

- vol. 28, no. 1, pp. 208–216, Jan 1992.
- [59] E. J. Kelly, “An adaptive detection algorithm,” *IEEE Transactions on Aerospace and Electronic Systems*, vol. AES-22, no. 2, pp. 115–127, March 1986.
 - [60] M. R. Bell and R. A. Grubbs, “Jem modeling and measurement for radar target identification,” *IEEE Transactions on Aerospace and Electronic Systems*, vol. 29, no. 1, pp. 73–87, Jan 1993.
 - [61] T. Thayaparan, S. Abrol, E. Riseborough, L. Stankovic, D. Lamothe, and G. Duff, “Analysis of radar micro-Doppler signatures from experimental helicopter and human data,” *IET Radar, Sonar Navigation*, vol. 1, no. 4, pp. 289–299, Aug 2007.
 - [62] J. Martin and B. Mulgrew, “Analysis of the theoretical radar return signal form aircraft propeller blades,” in *IEEE International Conference on Radar*, May 1990, pp. 569–572.
 - [63] C. Clemente and J. J. Soraghan, “GNSS-based passive bistatic radar for micro-doppler analysis of helicopter rotor blades,” *IEEE Transactions on Aerospace and Electronic Systems*, vol. 50, no. 1, pp. 491–500, January 2014.
 - [64] V. Chen and H. Ling, *Time-frequency Transforms for Radar Imaging and Signal Analysis*, ser. Artech House Mobile Communications Series. Artech House, 2002.
 - [65] I. Guvenc, F. Koohifar, S. Singh, M. L. Sichitiu, and D. Matolak, “Detection, tracking, and interdiction for amateur drones,” *IEEE Communications Magazine*, vol. 56, no. 4, pp. 75–81, April 2018.
 - [66] M. A. Govoni, “Micro-Doppler signal decomposition of small commercial drones,” in *2017 IEEE Radar Conference (RadarConf)*, May 2017, pp. 0425–0429.
 - [67] B. K. Kim, H. Kang, and S. Park, “Drone classification using convolutional neural networks with merged doppler images,” *IEEE Geoscience and Remote Sensing Letters*, vol. 14, no. 1, pp. 38–42, Jan 2017.
 - [68] Q. He and R. S. Blum, “Noncoherent versus coherent MIMO radar: Performance and simplicity analysis,” *Signal Processing*, vol. 92, no. 10, pp. 2454 – 2463, 2012.
 - [69] L. Āžbeda-Medina, . F. GarcĀąa-FernĀądez, and J. Grajal, “Adaptive auxiliary particle filter for track-before-detect with multiple targets,” *IEEE Transactions on Aerospace and Electronic Systems*, vol. 53, no. 5, pp. 2317–2330, Oct 2017.
 - [70] L. Moyer, J. Spak, and P. Lamanna, “A multi-dimensional Hough Transform-based

- track-before-detect technique for detecting weak targets in strong clutter backgrounds,” *IEEE Transactions on Aerospace and Electronic Systems*, vol. 47, no. 4, pp. 3062–3068, OCTOBER 2011.
- [71] S. M. Tonissen and Y. Bar-Shalom, “Maximum likelihood track-before-detect with fluctuating target amplitude,” *IEEE Transactions on Aerospace and Electronic Systems*, vol. 34, no. 3, pp. 796–809, July 1998.
- [72] S. Buzzi, M. Lops, L. Venturino, and M. Ferri, “Track-before-detect procedures in a multi-target environment,” *IEEE Transactions on Aerospace and Electronic Systems*, vol. 44, no. 3, pp. 1135–1150, July 2008.
- [73] L. Fan, J. Wang, D. Yan, and B. Wang, “Target detection using radar with dynamic programming approach,” in *2009 IITA International Conference on Control, Automation and Systems Engineering (CASE 2009)*, July 2009, pp. 442–445.
- [74] Y. Boers and H. Driessen, “Particle filter-based track before detect algorithms,” in *Proc. SPIE*, vol. 5204, 2003, pp. 20–30.
- [75] B. Ristic and S. Arulampalam, “Bernoulli particle filter with observer control for bearings-only tracking in clutter,” *IEEE Transactions on Aerospace and Electronic Systems*, vol. 48, no. 3, pp. 2405–2415, JULY 2012.
- [76] A. Lepoutre, O. Rabaste, and F. L. Gland, “Multitarget likelihood computation for track-before-detect applications with amplitude fluctuations of type swerling 0, 1, and 3,” *IEEE Transactions on Aerospace and Electronic Systems*, vol. 52, no. 3, pp. 1089–1107, June 2016.
- [77] M. Arulampalam, S. Maskell, N. Gordon, and T. Clapp, “A tutorial on particle filters for online nonlinear/non-Gaussian Bayesian tracking,” *IEEE Transactions on Signal Processing*, vol. 50, no. 2, pp. 174–188, Feb 2002.
- [78] E. H. Aoki, P. K. Mandal, L. Svensson, Y. Boers, and A. Bagchi, “Labeling uncertainty in multitarget tracking,” *IEEE Transactions on Aerospace and Electronic Systems*, vol. 52, no. 3, pp. 1006–1020, June 2016.
- [79] Y. Boers and P. K. Mandal, “Optimal particle-filter-based detector,” *IEEE Signal Processing Letters*, vol. 26, no. 3, pp. 435–439, March 2019.
- [80] J. Kwon, N. Kwak, E. Yang, and K. Kim, “Particle filter based track-before-detect method in the range-doppler domain,” in *2019 IEEE Radar Conference (RadarConf)*, April 2019, pp. 1–5.
- [81] M. Wen, W. Yi, and W. Li, “Multi-frame track-before-detect algorithm for

- disambiguation,” *The Journal of Engineering*, vol. 2019, no. 21, pp. 7726–7729, 2019.
- [82] S. P. Ebenezer and A. Papandreou-Suppappola, “Generalized recursive track-before-detect with proposal partitioning for tracking varying number of multiple targets in low snr,” *IEEE Transactions on Signal Processing*, vol. 64, no. 11, pp. 2819–2834, June 2016.
- [83] H. Wang, J. Yi, and X. Wan, “Greedy algorithm-based track-before-detect in radar systems,” *IEEE Sensors Journal*, vol. 18, no. 17, pp. 7158–7165, Sep. 2018.
- [84] W. Yi, H. Jiang, T. Kirubarajan, L. Kong, and X. Yang, “Track-before-detect strategies for radar detection in g0-distributed clutter,” *IEEE Transactions on Aerospace and Electronic Systems*, vol. 53, no. 5, pp. 2516–2533, Oct 2017.
- [85] F. Papi, V. Kyovtorov, R. Giuliani, F. Oliveri, and D. Tarchi, “Bernoulli filter for track-before-detect using mimo radar,” *IEEE Signal Processing Letters*, vol. 21, no. 9, pp. 1145–1149, Sep. 2014.
- [86] H. V. Nguyen, H. Rezatofighi, B. Vo, and D. C. Ranasinghe, “Online uav path planning for joint detection and tracking of multiple radio-tagged objects,” *IEEE Transactions on Signal Processing*, vol. 67, no. 20, pp. 5365–5379, Oct 2019.
- [87] B. Ristic, L. Rosenberg, D. Y. Kim, X. Wang, and J. Williams, “Bernoulli track-before-detect filter for maritime radar,” *IET Radar, Sonar Navigation*, vol. 14, no. 3, pp. 356–363, 2020.
- [88] O. Rabaste, C. Riche, and A. Lepoutre, “Long-time coherent integration for low SNR target via particle filter in track-before-detect,” in *2012 15th International Conference on Information Fusion (FUSION)*, July 2012, pp. 127–134.
- [89] S. Davey, N. Gordon, and M. Sabordo, “Multi-sensor track-before-detect for complementary sensors,” *Digital Signal Processing*, vol. 21, no. 5, pp. 600–607, 2011.
- [90] S. M. Kay, *Fundamentals of Statistical Signal Processing: Estimation Theory*. Upper Saddle River, NJ, USA: Prentice-Hall, Inc., 1993.
- [91] K. Thai, O. Rabaste, J. Bosse, and T. Chonavel, “Glrt particle filter for tracking nlos target in around-the-corner radar,” in *2018 IEEE International Conference on Acoustics, Speech and Signal Processing (ICASSP)*, April 2018, pp. 3216–3220.
- [92] B. Carlin and T. Louis, *Bayes and Empirical Bayes Methods for Data Analysis, Second Edition*, ser. Chapman & Hall/CRC Texts in Statistical Science. Taylor

- & Francis, 2010.
- [93] A. De Maio and M. Lops, “Design principles of MIMO radar detectors,” *IEEE Transactions on Aerospace and Electronic Systems*, vol. 43, no. 3, pp. 886–898, July 2007.
 - [94] Y. Yang and R. S. Blum, “MIMO radar waveform design based on mutual information and minimum mean-square error estimation,” *IEEE Transactions on Aerospace and Electronic Systems*, vol. 43, no. 1, pp. 330–343, January 2007.
 - [95] W.-K. Chen, *The electrical engineering handbook*. Elsevier Academic Press, 2005.
 - [96] T. K. Yaakov Bar-Shalom, X. Rong Li, *Estimation with Applications To Tracking and Navigation: Theory algorithm and Software*. John Wiley & Sons, 2001.
 - [97] X. Rong Li and V. P. Jilkov, “Survey of maneuvering target tracking. Part I. Dynamic models,” *IEEE Transactions on Aerospace and Electronic Systems*, vol. 39, no. 4, pp. 1333–1364, Oct 2003.
 - [98] P. A. Kountouriotis and S. Maskell, “Maneuvering target tracking using an unbiased nearly constant heading model,” in *2012 15th International Conference on Information Fusion*, July 2012, pp. 2249–2255.
 - [99] K. Murphy, *Machine Learning: A Probabilistic Perspective*, ser. Adaptive computation and machine learning. MIT Press.
 - [100] M. Orton and W. Fitzgerald, “A Bayesian approach to tracking multiple targets using sensor arrays and particle filters,” *IEEE Transactions on Signal Processing*, vol. 50, no. 2, pp. 216–223, Feb 2002.
 - [101] C. Robert and G. Casella, *Monte Carlo Statistical Methods*. Springer, 2014.
 - [102] A. Doucet, A. Smith, N. de Freitas, and N. Gordon, *Sequential Monte Carlo Methods in Practice*, ser. Information Science and Statistics. Springer New York, 2001.
 - [103] T. K. Moon, “The Expectation-Maximization Algorithm,” *IEEE Signal Processing Magazine*, vol. 13, no. 6, pp. 47–60, Nov 1996.
 - [104] Y. Gu, J. Liu, X. Li, Y. Ch, and Y. Ji, “State space model identification of multirate processes with time-delay using the expectation maximization,” *Journal of the Franklin Institute*, vol. 356, no. Issue 3, pp. 1623–1639, February 2019.
 - [105] K. Weisberg, S. Gannot, and O. Schwartz, “An online multiple-speaker

- doa tracking using the capped-EM algorithm,” in *ICASSP 2019 - 2019 IEEE International Conference on Acoustics, Speech and Signal Processing (ICASSP)*, May 2019, pp. 656–660.
- [106] M. Bazaraa, H. Sherali, and C. Shetty, *Nonlinear programming: theory and algorithms*, ser. Wiley-Interscience series in discrete mathematics and optimization. Wiley, 1993.
- [107] “Gatwick Airport: Drones ground flights,” accessed February 2020. [Online]. Available: <https://www.bbc.com/news/uk-england-sussex-46623754>
- [108] “NK sent spy drones,” accessed February 2020. [Online]. Available: http://www.koreatimes.co.kr/www/nation/2014/05/113_156790.html
- [109] “Gamekeeper 16U Product Sheet,” accessed May 2019. [Online]. Available: <http://www.aveillant.com/products/gamekeeper-16u>
- [110] N. McLachlan, *Bessel Functions for Engineers*, ser. The Oxford engineering science series. Clarendon Press, 1961.
- [111] A. K. Singh and Y. Kim, “Automatic measurement of blade length and rotation rate of drone using w-band micro-Doppler radar,” *IEEE Sensors Journal*, vol. 18, no. 5, pp. 1895–1902, March 2018.
- [112] M. Jahangir, C. J. Baker, and G. A. Oswald, “Doppler characteristics of micro-drones with l-band multibeam staring radar,” in *2017 IEEE Radar Conference (RadarConf)*, May 2017, pp. 1052–1057.
- [113] B. Oh, X. Guo, F. Wan, K. Toh, and Z. Lin, “Micro-doppler mini-UAV classification using empirical-mode decomposition features,” *IEEE Geoscience and Remote Sensing Letters*, vol. 15, no. 2, pp. 227–231, Feb 2018.
- [114] J. L. Garry and G. E. Smith, “Experimental observations of micro-doppler signatures with passive radar,” *IEEE Transactions on Aerospace and Electronic Systems*, vol. 55, no. 2, pp. 1045–1052, April 2019.
- [115] S. J. Godsill, A. Doucet, and M. West, “Monte Carlo smoothing for non-linear time series,” *Journal of the American Statistical Association*, vol. 99, pp. 156–168, 2004.
- [116] “Singular Value Decomposition,” accessed March 2020. [Online]. Available: https://web.mit.edu/be.400/www/SVD/Singular_Value_Decomposition.htm